Applications of Double-Difference Tomography for a Deep Hard Rock Mine

Jeffrey Kerr

Thesis submitted to the faculty of the Virginia Polytechnic Institute and State University in partial fulfillment of the requirements for the degree of

Masters of Science

In

Mining and Minerals Engineering

Erik C. Westman, Chairman

Martin C. Chapman

Mario G. Karfakis

Denis Thibodeau

November 16, 2011

Blacksburg, VA 24060

Keywords: Tomography, Hard Rock, Mining

Applications of Double-Difference Tomography for a Deep Hard Rock Mine

Jeffrey Kerr

Abstract

Seismicity at a deep hard rock mine can be a precursor to ground failure events. Seismicity data can be used in double-difference tomography, which produce tomograms showing velocity distributions in the rock mass that can be used to infer relative stress of the rock mass. The data set used for the double-difference tomography inversion was from Creighton Mine in Sudbury, Ontario, Canada, and consisted of two months of data averaging 150 microseismic events per day. Three separate studies were conducted to evaluate the applications of double-difference tomography on a deep hard rock mine. These studies produced mine scale tomograms, stope scale tomograms of two active stopes, and stope scale tomograms for a cluster of events. TomoDD was used for the tomographic inversion, with other commercial programs used to view the results. All three studies produced results consistent with prior mine knowledge and basic concepts of rock mass stress redistribution. Mine scale tomograms accurately displayed a low velocity where the mined ore body is known to be with adjacent high velocity, stope scale tomograms of the two stopes both correctly demonstrated a low velocity relaxed zone near the stope following a production blast, and stope scale tomograms of an event cluster displayed consistency in results for two clusters in periods before, during, and after each cluster. The three studies show that double-difference tomography is a promising tool for observing rock mass stress redistribution that provides a baseline evaluation for the potential uses of the technology in a deep hard rock mine.

Acknowledgments

First, I would like to thank my advisor, Dr. Westman, for his guidance and help throughout the graduate and research process, beginning to end. In addition, I would like to thank Dr. Karfakis for his motivational support and his spontaneous rock mechanics lectures throughout my research. I would also like to extend my gratitude towards the Mining and Minerals Engineering Department at Virginia Tech for allowing me the opportunity to stay here at Virginia Tech for graduate studies (and two more seasons of Hokie football) and to the Mining and Minerals office staff for offering me opportunities to take a break from my studies when help was required. I would also like to thank the National Science Foundation for their role in providing me this opportunity.

I would like to thank Vale and Creighton Mine for providing the data required for this research. In addition, I would like to thank Dr. Thibodeau for his role in data acquisition, his invaluable input into mine conditions, and common observations underground at Creighton Mine. Finally, I would like to thank the rock mechanics group at Creighton Mine for the additional informational resources provided to me that I needed to complete my graduate studies.

Table of Contents

List of Figures

List of Tables

Chapter 1 – Introduction

Mining is often considered one of the highest risk jobs in the world. While mining does not rank in the top ten most dangerous jobs by fatality in the United States by Forbes magazine, it is noted that with just over one hundred fatalities in the United States in 2009, mining is in the top twenty (Whelan 2011). Most years in the United States, the majority of fatalities related to mining occur in or around coal mines. Coal mining accounts for numerous fatalities due to the numerous hazards such as enclosed spaces, the explosive nature of the material, and the laminated rock types encountered in a coal mine (Mark 2010). The trend of more coal mining fatalities compared to metal mining is evident worldwide also, with thousands of deaths occurring in coal mines each year in China and other major countries that are prominent in coal mining.

Although metal mining consistently has less fatal accidents than coal mining annually, this does not mean that metal mining is necessarily safer. Like coal mining, metal mines have numerous inherent hazards. Metal mines present a variety of hazards ranging from health issues caused by drilling to safety issues due to temperature and ground control.

From a safety standpoint, temperature in metal mines around the world is of concern. With virgin rock temperatures reaching up to 150 degrees Fahrenheit in some metal mines, heat fatigue can become a significant issue in metal mines. The temperatures in metal mines reach such high temperatures due to the geothermal gradient, which is the rate of change in temperature with depth (Merriam-Webster 2004). The key factor involved with the geothermal gradient is depth, which is also one of the areas of greatest concern in metal mining from a rock mechanics standpoint.

Metal mines are some of the deepest manmade structures in the World, with bottom depths reaching from 6,000 feet to 10,000 feet in some mines in the United States, Canada, and South Africa (Urbancic 2000; Stoddard 2011). With depth come numerous other rock mechanics issues that are prevalent in deep metal mines around the World. The major rock mechanics issues from a safety standpoint include roof failures, rock bursts, and seismic activity.

A rock burst is defined as the rapid release of strain energy in an often violent outburst of rock from the main rock mass. A rock burst can result in injuries, fatalities, mine opening closure, lost production, and equipment damage (Caldwell 2011). With hundreds to thousands of

rock bursts estimated in metal mines per year with varying degrees of damage, rock bursts are considered one of the largest areas of concern in relation to metal mining.

Seismic activity accompanies rock bursts in metal mines, especially deep metal mines. Rock bursts are often preceded and followed by an increase in seismic activity (Caldwell 2011). However, with or without a rock burst, deep metal mines still experience seismic activity. This seismic activity, often microseismic energy releases, typically indicate fracture formation or faults slipping along themselves. While most seismic activity is considered small, there are some large scale events that occur; microseismic events are described as events below a magnitude 0.0 on the moment magnitude scale. These large scale, seismic events can lead to structural integrity issues as well as catastrophic failures (Trifu 2009).

With the threat of rock bursts, fault slips, roof falls, and catastrophic failure due to the rock mass structure and depth of the mine workings, there exists a multitude of safety checks and controls. For most mines, the first option chosen to handle ground control issues is to install enhanced support in areas that have visual indications of poor ground conditions. Some enhanced supports commonly used in the metal mining industry include shotcrete, wire mesh, and specialized rock bolts. If enhanced supports are not effective in controlling the ground, then de-stressing the area with blasting is employed (Malek 2009).

If active approaches towards ground control in mines are not successful, one option employed by mine sites is to alter the mine design and development to better accommodate the ground issues (Trifu 2009). Mine designs can be altered to employ smaller openings, smaller stopes, or changing directions to mitigate horizontal stresses. Mine designs are often evaluated prior to implementation through numerical modeling, another commonly used tool employed to evaluate safety conditions for a mine site (Malek 2009).

Another tool utilized in evaluating safety at mine sites in relation to ground control is seismic monitoring. Seismic monitoring is commonplace for many deep metal mines around the World. Seismic monitoring can be used to determine when and where an event near the mine has occurred, allowing for proper measures to be taken. In addition, seismic monitoring can be used to determine re-entry status for a mine after events (Trifu 2009).

Seismic information obtained through monitoring can further be used in determining ground conditions through seismic tomography methods. Seismic tomography is a non-invasive technique that images the velocity distribution over a volume of interest. The velocity

distribution can be used to determine areas of high or low velocity distributions (IRIS 2011). The distribution of high or low velocity is an important rock mass characteristic from a ground control standpoint. High velocity areas are interpreted as highly stressed areas of a rock mass and low velocity areas are interpreted as low stressed areas such as fracture zones. In addition, high and low velocity areas could also be interpreted as high and low stiffness, respectively. These relations are only valid in an assumed lithological homogenous rock mass. The knowledge of highly stressed areas, as well as fractured zones, is important to understanding the rock mass, in addition to the changes that the rock mass is undergoing.

Seismic tomography has successfully imaged underground mining environments and their local rock masses. In 2009, research conducted on a western United States coal mine showed that seismic tomography could more accurately locate seismic event locations in the proximity of a mine (Lurka 2009). In 2005, a study conducted on a longwall coal mine in Colorado successfully observed the front and side abutments for the longwall face (Luxbacher 2005). Accurate event locations, as well as the knowledge of how expansive the front and side abutment are, allow for proper planning and ground control measures to be put in place.

While seismic tomography has been utilized in a variety of ways in relation to underground coal mining, there have been few studies related to seismic tomography and its application to a deep metal mine. The research presented utilizes a seismic tomography variation, double-difference tomography, to generate tomograms for a deep metal mine in Sudbury, Ontario, Canada. The data utilized for the double-difference tomographic inversion were recorded from an in-place seismic monitoring system over a two month time period.

Tomograms were created for both mine scale and stope scale sized areas. Mine scale tomograms were generated first and were utilized in the selection of stope scale sized areas. Stope scale tomograms were generated and evaluated on by location basis.

The purpose of double-difference tomography research in relation to a deep metal mine is to improve safety from a ground control prospective. Possible uses for double-difference tomography could range from hazard mappings used on a timed interval to a model to be updated periodically to observe rock mass changes. While the goal regarding double-difference tomography and metal mines is to improve safety, the goal of the research presented is to provide a baseline exploration of the possible uses of double-difference tomography in a deep metal mine setting utilizing both large and small scale observations.

Chapter 2 – Literature Review

In order to explore the uses of double-difference tomography as it is related to hard rock mining, an understanding of rock mechanics, elasticity theory, and the method of seismic tomography itself is needed; the following sections will discuss these topics.

2.1 - Rock Mechanics

2.1.1 – Stress

A common misconception about stress is that stress is equivalent to force. Pressure and force are scalar and vector quantities, which have magnitude and are independent of direction, whereas stress is a tensor. A tensor is a multi-dimensional array of numerical values that describe linear relations between vectors, scalars, and other tensors. In relation to stress, a tensor is used to represent correspondences between sets of stress vectors on the faces of a cube (Hudson 2003).

Stress at a single point can be defined by three normal stresses and six shear stresses. Figure 2.1, below, shows all possible stress states on an element. A normal stress is defined by stress acting perpendicularly on a plane which has force being applied to it, and shear stress is defined as stress acting parallel to a plane which has a force being applied to it. Stress states can also be defined as three normal stresses and three shear stresses acting on a plane, or by the magnitude and direction of the three principal stresses, $\sigma_1, \sigma_2, \sigma_3$ (Hudson 2003). A stress state can be defined by only three principal stresses because at that point, the shear stress is equal to zero.

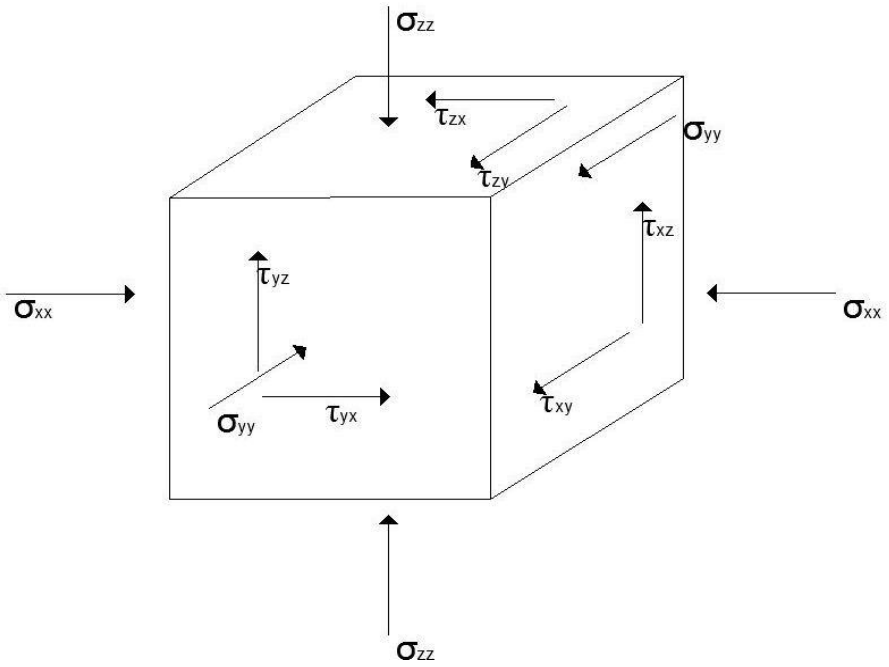

Figure 2.1: Stress components on an element. After Hudson 2003.

In testing terms, there are multiple variations of stress used to obtain different strength and stress quantities. Uniaxial stress is used to obtain the uniaxial compressive strength of a material and is found using only one principal stress with all others being equal to zero. Biaxial stress, which is used less often, is defined as two principal stresses acting on an object. More commonly used to determine strength and stress, especially for rock strength, is the tri-axial test. The tri-axial test uses the tri-axial state of stress, which has all three principal stresses involved, but two of the stresses are equal in magnitude. Most objects, including rock, are subjected to true tri-axial stress, albeit some stress differences may be miniscule, which occurs when all three principal stresses are applied at different magnitudes (Hudson 2003).

Beyond the differing states of stress, according to Hudson there are eleven different types of stress that can be applied to rock masses (Hudson 2003). In relation to rock masses, the three most common stresses encountered are gravitational stress, such as lithostatic pressure, which incorporates the weight of overlying rock, natural stress which involves only in situ, or in place, stress, and induced, deviatoric stress which comprises stresses caused by other factors. According to Amadei, all rock stresses can be categorized into two of Hudson's classifications, in situ and induced. Amadei states that in situ stress is all stresses that existed in rock prior to any disturbance and induced stress is all stresses caused by artificial disturbances or from the natural system from swelling, consolidation, or other natural processes (Amadei 1997).

In 2003, Hudson presented a systematic approach used for gaining knowledge of stresses in rock masses. Initially, it is important to gain all preexisting knowledge of the area, including all known in situ stresses or possible causes for induced stresses. If more information needs to be obtained, it should be determined whether the gravitational stress is a principal stress along with its magnitude. After the gravitational stress has been determined, drilling should be used to determine directions for the three principal stresses. Using borehole and over coring testing methods, stress tensors for the area could be calculated. In addition, stress tensors may be obtained in boreholes through the use of hydraulic fracturing (Ljunggren 2003). This process should be used multiple times in order to later interpolate stress variations across the rock mass in question (Hudson 2003).

2.1.2 - Rock Stress Measurements

As seen from the systematic approach to determine stress in rock by Hudson, it is necessary to use various tests to determine in situ stresses. All in situ stresses must be determined with high precision as engineering calculations will be based on such quantities. In order to obtain the high precision needed to do engineering calculations the technique and equipment used for rock measurements must be reliable, as the measurements are only as dependable as the equipment used (Ljunggren 2003).

There are two methods of stress measurement; disturbing of in situ rock masses and observation of rock behavior. There are multiple methods that disturb the in situ rock mass, including hydraulic methods, borehole relief methods, and surface relief methods. For hydraulic methods, the primary tool used is hydraulic fracturing, which measures minimum and maximum normal stresses based on fluid injection in a sealed area of a borehole. A secondary hydraulic method is hydraulic fracturing of preexisting fractures, which is the same concept as hydraulic fracturing; it is a measure of fracture propagation in lieu of fracturing. Borehole relief methods include over coring of cells in both pilot holes and the bottom of the borehole, as well as borehole slotting for constant strain measurements. Surface relief methods are basic measurements, such as deformation, that measure the rock response to stress relief.

Observation of rock behavior methods utilizes both in situ known characteristics as well as measurements from boreholes. Common tools used include previous statistical knowledge and interpolation of that data, relief or large rock masses, borehole breakouts, and specific focal mechanisms (Ljunggren 2003). In addition, another well-known tool used is monitoring of

acoustic emissions, which analyzes brittle failure by recording spontaneous acoustic emissions from crack failures (Lockner 1995). Rock quality also can be used as an observation based stress measurement; rock quality is often measured by core hole discing in relation to stress measurement (Ljunggren 2003).

2.1.3 - Rock Failure Criterion

Numerous failure criteria are used to predict rock failure, including the Hoek-Brown failure criterion, the Griffith crack theory, and the Mohr-Coulomb failure criterion. The Hoek-Brown theory was originally derived in 1980 from research of brittle failure for intact rock by Hoek and jointed rock behavior studies by Brown. The Hoek-Brown criterion was one of the first to use empirical relationships, later connecting geologic observations to the empirical relations using the Geologic Strength Index created by Hoek. Every few years, the original Hoek-Brown failure criterion, shown below in Equation 2.1, is re-derived to enhance its rock coverage range, most recently altered to include ideas related to undisturbed and disturbed rock (Hoek 2002).

$$\sigma_1' = \sigma_3' + \sigma_{ci}(m\frac{\sigma_3'}{\sigma_{ci}} + s)^{0.5} \qquad (2.1)$$

Where σ_1' and σ_3' are the maximum and minimum principal stresses respectively and σ_{ci} is the uniaxial compressive strength. The variables *m* and *s* are material constants with ranges for *m* between seven and seventeen, with seven being used for platy rocks with many interfaces and seventeen representing a strong, solid rock with *s* assumed to be one to represent intact rock (Hoek 2002).

The Griffith crack theory does not predict total rock failure, but how a crack will propagate and grow. According to the theory, a crack will grow when the crack reduces the potential energy of the crack, and the crack can also grow if the rate of elastic energy release from the crack growth is more than the surface energy of the crack. In conjunction with the Griffith crack theory, common knowledge extends the knowledge of cracks and how they will fail. Some common knowledge related to cracks are that cracks in tension are more unstable than when in compression, under normal compression friction helps crack stability, and that cracks can still propagate in normal compression if the shear stress is large. With the Griffith crack theory and knowledge of how a crack fails, Equation 2.2, below, can be used to predict failure of a rock mass (Margolin 1984).

$$(\sigma_1 - \sigma_3)^2 = 8\tau_0(\sigma_1 + \sigma_3) \qquad (2.2)$$

Where σ_1 and σ_3 are the maximum and minimum principal stresses respectively and τ_0 is the tensile strength (Margolin 1984).

The Mohr-Coulomb failure criterion is currently one of the most widely used criteria employed in rock mechanics. The idea of the Mohr-Coulomb failure criterion was first broached by Coulomb with his research into shear fracturing of a material in uniaxial compression. Mohr later improved Coulomb's theory to handle triaxial stresses by recognizing that material properties are functions of differing stress states (Handin 1969). The Mohr-Coulomb criterion, which is used to determine shear strength, states that cohesion value for a rock remains constant, and friction varies with normal stress, is shown below in Equation 2.3.

$$\tau = c + \sigma_n \tan\varphi \qquad (2.3)$$

Where τ is the shear strength of the rock, c is the cohesion of the rock, σ_n is the normal stress acting on the rock sample, and φ is the angle of internal friction for the rock (Zhao 2000). In compression, the Mohr-Coulomb rock strength coincides with the Griffith crack theory to describe crack closure (Cook 1965).

The Mohr-Coulomb failure criterion is commonly shown graphically. Figure 2.2, below, shows the Mohr-Coulomb failure criterion graphically.

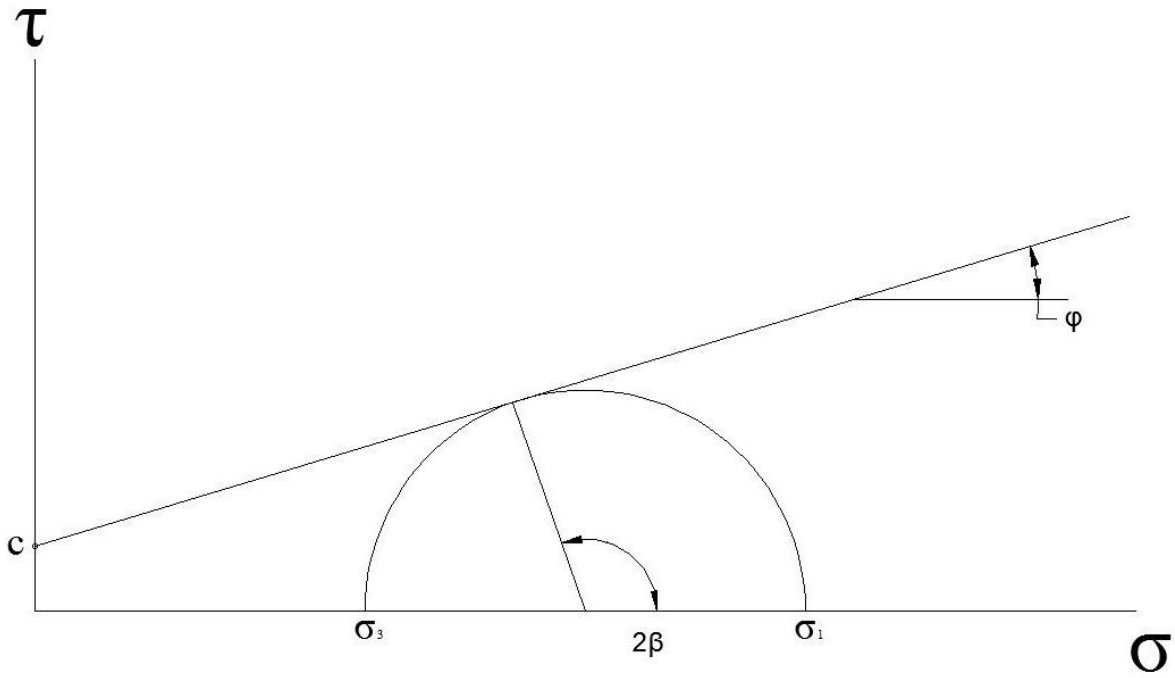

Figure 2.2: Mohr-Coulomb Failure Criterion.

As shown in Figure 2.2, above, the Mohr-Coulomb criterion encompasses the use of a Mohr circle and the failure criterion. The failure criterion is the line tangent to 2β, with β representing the jointed failure plane that intersects the initial cohesion value along the τ axis; the tangent failure criterion is oriented at the angle of internal friction. The failure criterion in the graphical form allows one to see σ_1 and σ_3 pairs and their respective point of failure (Zhao 2000).

2.1.4 – Seismic Velocity

Seismic waves, a class of elastic waves, are formed from a displacement or distortion in the Earth (Lindsay 2010). The rate at which elastic waves travel through the Earth is known as the seismic velocity. Seismic velocity can be determined by utilizing the known distance traveled of the elastic wave and the duration of the seismic wave as recorded by a seismograph.

2.1.5 – Seismic Waves

There are two main types of seismic waves for isotropic materials with a free surface, surface and body, each consisting of two different waves. The two types of surface waves include Love and Rayleigh waves, both named for the individuals who described them (Endsley 2007). The Love wave exists only for layered material in which velocity increases with depth and displacement occurs in the horizontal plane. Love waves in the crust typically have a velocity of two to six kilometers per second. Rayleigh waves are the slowest of all seismic waves with typical velocities of one to five kilometers per second (Ammon 2001). Rayleigh wave motion is an up and down oscillation, similar to ocean waves.

The two types of body waves are P and S waves, respectively. The P wave is the fastest traveling seismic wave, partly due to the way in which it propagates; P waves result in compressing and expanding of the ground as the wave passes. P waves are the only waves that can travel through both solid material, such as rock in the Earth, and liquid material, such as water. Due to the ability to travel through all types of materials, P wave velocities can range in speed from one to fourteen kilometers per second, with the lowest velocities typically recorded when water is encountered for the majority of the wave travel time and the highest occurring when the wave travels through the Earth's mantle (Ammon 2001). For an isotropic material the P wave velocity is known by Equation 2.4, below,

$$V_p = \sqrt{\frac{k+\frac{4}{3}\mu}{\rho}} \qquad (2.4)$$

where V_p is the P wave velocity, k is the bulk modulus of the rock mass, μ is the shear modulus of the rock mass, and ρ is the density of the rock mass the wave traverses (Lawerence).

S wave motion is in the plane perpendicular to the direction of wave propagation. S wave amplitudes are usually larger than P wave amplitudes for seismic sources due to shear distributions. Like P waves, the highest S wave velocities occur in the Earth's mantle, but the lowest velocities occur in unconsolidated sediments as S waves are unable to travel in water like P waves (Ammon 2001). For isotropic materials, S wave velocities can be calculated from Equation 2.5, below,

$$V_s = \sqrt{\frac{\mu}{\rho}} \qquad (2.5)$$

where V_s is the S wave velocity, μ is the shear modulus of the rock mass, and ρ is the density of the rock mass the wave traverses (Lawerence).

2.1.6 – Determining Seismic Velocities

Seismic velocity, while not a defining characteristic of a rock mass, is an important attribute of a rock mass. As shown in Equations 2.4 and 2.5, it is possible to determine P and S wave velocities if density and elastic moduli are known, but usually there are variations of these quantities in a rock mass. In order to obtain the accurate velocity readings testing must be completed on the rock mass in question.

Testing rock samples in a lab is a common form of determining seismic velocities. Seismic velocity lab testing is a simple process, requiring only a few instruments and a rock core sample. The rock core sample is typically a cylindrical sample, allowing for only unidirectional measurements; in order to obtain multiple measurement directions a cubic sample can be used (Kern 2011). One process to determine seismic velocities in the lab is placing a rock core in a sample holder between a source and receiver. The source sends a transduced wave through the rock core with the aid of a piezoelectric crystal; the receiver picks up the wave source. The wave is then viewed using a seismic viewer to determine the travel time through the known dimensions of the core sample, allowing for seismic velocity to be calculated with all other rock properties known (Karfakis 2008).

Lab testing is a cheap and effective way for determining seismic velocities, but rarely do velocities determined in the lab correspond to field measurements for the same rock mass (Moos 1983). In order to obtain the most accurate seismic velocities for a rock type, *in situ* testing must

be conducted on the rock mass. Numerous tests exist to determine seismic velocities including down hole seismic surveys and cross hole seismic surveys, but in order to obtain a complete seismic profile from *in situ* measurements, a seismic survey must be conducted. The concept of a seismic survey is simple; a wave is produced by a source, anything ranging from a sledgehammer to a small explosion and received by numerous receivers positioned along a specific geometry. The data received is then transmitted to a seismograph (Park 2007). In order to determine the specific seismic velocity from the seismic survey, wave propagation effects, reflection and refraction, must be taken into account to determine the wave paths taken through the rock mass.

2.1.7 – Rock Mass Properties from Seismic Waves and Velocities

Seismic velocities themselves are considered properties of a rock mass, but seismic velocities can also be utilized to determine numerous rock mass properties. Due to extensive research conducted on differing rock types, the seismic velocity of an unknown rock mass can be used to narrow the possible types of rock mass. Additionally, the reaction of the elastic waves that determine seismic velocity can identify changes in rock mass through reflection or refraction. With seismic wave reflection and refraction it is also possible to classify differing deposits within a rock mass such as an oil or natural gas deposit (Moos 1983).

Seismic velocities can be used to identify overall rock mass classifications, but more importantly, seismic velocities can identify unique variations inside of a rock mass. P and S waves can both travel through solid objects, whereas only P waves can travel through liquids. This makes the seismic velocity a useful tool in determining voids and fractures in the rock mass. Voids and fractures can cause seismic velocity to reach slow speeds, making it possible to determine fracture zones and voids in the rock mass. It is possible to locate the exact area of fractures through down hole surveys or cross well seismic surveys. The fracture zones typically observed are on the macro, or large scale, but micro, or small scale, fractures also play a role in seismic velocity; groupings of micro fractures can also be observed through seismic surveys (Moos 1983).

2.1.8 – Stress from Seismic Velocity

Although seismic velocities can show many different attributes about a rock mass, the most important consideration from a mining prospective is the stress on the rock mass. Seismic

velocity can show relative stress variations throughout the rock mass, with higher velocities corresponding to highly stressed areas, and lower velocities corresponding to lower stressed areas by taking into account the presence of void spaces and compaction. Higher velocities in addition can show areas of great stiffness and low velocities can also show areas of low stiffness (Blum 1997). Velocities generally increase with depth, which corresponds well to higher velocities being shown in highly stressed areas, as deeper locations and rock masses are subjected to greater overburden and confining pressures (Lawerence).

In addition to the basic relationship of high velocity is high stress and low velocity is low stress, seismic velocities can show unique stress features such a pore pressures. An increase in pore pressure opens cracks and voids in rock mass, causing velocity to drop in that area. Once an increase in pore pressure has opened fractures, remaining high pore pressures can keep cracks open, retaining the low velocity readings in that zone (Mavko).

Overall, the most important characteristic shown from seismic velocity is the effective stress, as it has the most effect on velocity readings. Velocity typically increases, or decreases, in a similar fashion to the effective stress of the region it is located in, making it either a highly stressed or lower stressed zone (Mavko), which is an important property to know from a mining standpoint. Effective pressure, or the difference between the confining pressure and pore pressure in an area (Hoffman 2005). High pore pressure lowers the effective stress in a mass and weakens fractures.

2.2 – Seismic Monitoring

2.2.1 - Seismicity

The topic of rock deformation has been subject to much debate since the late 1930s when Obert and Duvall discovered that rocks emit acoustic emissions, or micro-level sounds, under stressed conditions. Obert and Duvall revealed that an acoustic emission event, also known as "rock talk," increases with intensity as more load is applied until a state of equilibrium is met (Gray 1981). A seismic event is defined as an event with a moment magnitude greater than or equal to zero, caused by an outside force acting within the Earth according to Merriam-Webster (Merriam-Webster 2004). In addition to seismic research, microseismic research, or a vibration of the Earth with a magnitude of less than zero, is also a common research topic (Urbancic 1997).

Seismic research has been incorporated into modern mining since the 1960s when numerous studies commenced that would produce sophisticated monitoring equipment that could monitor vast frequency levels (Gray 1981). Additionally, numerous mining operations and government research agencies have been using seismic monitoring equipment commencing in the early 2000s, in an effort to better understand seismic and microseismic influence on the mining environment. Common uses for seismic monitoring related to mining include locating ore deposits, locating fractures in rock formations, and determining velocities (and consequently stress) of rock formations (Chang 2000). Monitoring can be used to discover pertinent information related to rock failure. Microseismic and seismic monitoring has been used to discern between progressive, continuous, and episodic rock failure mechanisms at mines. Progressive failure is shown through seismic monitoring as having the distinct characteristic of a stable roof (little seismic activity) which deteriorates with failures (increased seismic activity) and eventually restores to a stable condition. Continuous failure shown through seismic monitoring is discernible from progressive failure as there is always seismic activity occurring in continuous failure; sizes of the event can be determined from recorded magnitudes. Episodic rock failure is a combination of both continuous and progressive failure and thus is hard to view through seismic monitoring (Iannacchione 2005).

2.2.2 - Equipment

Seismic monitoring is only as effective as the equipment and deployed at the underground mine site. The first level of equipment used for monitoring is of the data acquisition variety. Sensitive seismometers, or geophones, are used to detect movements of underground material. Accelerometers are seismometers that can record strong ground motion and may be used in more seismically active volumes as they are more adapted to withstand violent movements (Hons 2008). Data obtained from the seismometers is transferred to a central data recording location through various transmission media. Standard transmission media are fiber optic, coaxial, and Ethernet wired from the data acquisition source (i.e. geophone) to the central datum server. Other less common modes of transmission involve radio frequencies. North Fork Valley, a longwall mine in western Colorado, employed the use of spread spectrum radios and the internet to remotely monitor and control their surface and underground seismic network (Swanson 2008). A basic data receiving station consists of a standard computer

connected to the network; the software packages on the computer act as the receiving station and processing core.

Some monitoring systems use integrated software in conjunction with the equipment for a complete package for seismic monitoring. The 'Earthworm' seismic monitoring system can determine wave arrival times, epicenter locations, and magnitudes, and was used successfully in 2003 at the Stillwater complex in the United States. Earthworm was one of the first seismic monitoring systems to utilize the internet to provide both real time seismic monitoring as well as seismic data retrieval/alteration (Denton 2003).

Like the Earthworm system, the Engineering Seismology Group's (ESG) Paladin system is an internet based real time seismic monitoring system. Unlike many other seismic monitoring systems, the Paladin is a Mine Health and Safety Administration (MSHA) approved permissible system that works in conjunction with other ESG products to provide real time monitoring, processing, and analysis for underground mines (Elliot 2008). The Paladin system is a versatile monitoring system, able to be customized to fit in any mining scenario encountered, with all data communication being sent through Ethernet or wireless communication from the Paladin seismic recorders to a central data receiver. The Paladin, in conjunction with the ESG software package, Hyperion, maps all received data into a three dimensional model in order to supply event location maps to researchers or mine personnel (ESG 2010). Another common system used throughout the mining industry for seismic monitoring is the ISS International Seismic Monitoring System. The ISS system, like the Paladin, provides both real time monitoring and three dimensional realizations for one-hundred forty mines throughout the World. The ISS system is an adaptable system, able to work in any underground situation as well as with any base computing platform, language, and geology (International 2010).

2.2.3 - Discoveries

According to multiple research studies and mine experience, the prevalent observation has been that roof falls and impacts generate a much higher magnitude than any other mining related seismic event, outside of an air blast. Most recently, a study by Iannacchoine at an underground limestone quarry in 2005 discovered that roof falls have higher seismic moments, are longer in duration, and are more emergent in nature than typical seismic or microseismic events (Iannacchione 2005). In addition to Iannacchione's work, in 2008 Bajpayee determined that microseismic systems could detect seismic activity prior to a roof fall in the general location.

The increase in seismic activity is apparent compared to a non-failure event, however, the arrival time of seismic energy prior to a roof fall is dependent on local conditions and active mining (Bajpayee 2008).

Prior to Iannacchoine and Bajpayee's work, seismic monitoring at Canadian mines demonstrated that the intact rock formation in advance of the mining face produces the most seismic activity on a consistent basis. The seismic activity ahead of the mining face is attributed to the high stress values in the area (Urbancic 2000). Highly stressed areas in advance of the mining face are also a usual occurrence in longwall mines. Ellenberger observed a deep coal longwall mine in Utah noting that the longwall face, in addition to both the headgate and tailgate, are the most stressed areas of the coal mine. Ellenberger also noted that there is significantly less stress on the gob area behind the longwall, as shown by low seismic velocities and a low number of microseismic events away from the face after a successful cave; however some of the largest seismic events are associated with caving in the gob. The combination of the presence of a well-defined gob area and wider longwall panels generate much of the stress and seismic activity at the longwall face (Ellenberger 2001).

While much of the seismic monitoring technology has been used to study rock failures and stress concentrations, Murphy used seismic monitoring in order to determine the seismic signature of an explosion. According to Murphy, his study was motivated by the Sago mine disaster; seismic monitoring stations received waves that place Sago at the center of the error ellipse for epicenter location. Murphy learned from experiments at the Lake Lynn mine in Pennsylvania that explosions do create obvious seismic events that can be differentiated from other seismic events caused by air blasts following an initial explosion by comparing their seismic waves, frequencies, and the arrival time of seismic waves. In addition to independent seismic events from the blast, the Lake Lynn experiment also exhibited a trend in the seismic energy from the explosions. Explosions that are located in a confined area, such as behind a seal, show greater seismic energy than if the explosion were unconfined (Murphy 2008).

2.2.4 - Applications

Many of the discoveries related to seismic monitoring of mines are research related, but the mining industry has also had success with seismic monitoring. Multiple locations around the world have used seismic monitoring to warn of immediately impending roof falls, rock bursts, and/or air blasts. Salt mines in Eastern Europe have used seismic monitoring to determine pillar

degradation where pillars are prone to rock bursts as well as zones of high stress on manmade underground structures which could be reinforced for increased safety (Thoma 2003). At the Moonee Colliery mine in Australia, an underground longwall operation, seismic monitoring has been used to forecast impending roof falls behind the longwall face. Moonie Colliery has the unique feature of massive, competent roof strata, causing the roof to remain stable for an extended period of time. With seismic monitoring, Moonie Colliery has been able to approximately determine when a fall is going to occur, based on an increase in seismic activity with a specific signature, allowing for workers to evacuate the face area to escape any residual air blast (Iannacchione 2005).

Seismic monitoring has been used to locate underground structures such as abandoned mines. Kase (2004) performed seismic surveys under an interstate highway in Kansas to determine if structures underground were causing the deterioration of the road. Kase's study used seismic signals to image the rock mass underground, a process known as seismic imaging. Seismic imaging employs seismic tomography, which is used to create a velocity model of a rock mass in order to determine zones that represent stress characterization of the area. The study on the Kansas interstate of the use of seismic imaging and tomography can provide a general view of underground works and rock structures that will increase safety and stability concerns (Kase 2004).

2.2.5 - Future

Like any technology, seismic monitoring has limitations. Researchers, manufactures, and the mining industry have worked and continue to improve the future of seismic monitoring. According to research and conclusions provided by Westman in 2001, with more correlated data it could be possible to forecast high stress zones in order to provide more support to those areas (Westman 2001). The ability to forecast high stress zones has potential to lead to further developments in seismic monitoring. Prior to Westman's research, Srinivason's analysis of the South African Kolar Gold Fields determined that with more stress data, forecasting could be utilized from seismic monitoring. Srinivason stated that further seismic monitoring could be used to predict rock bursts from a widely spanning area (Srinivasan 1995). Urbanic's research in 1997 concluded that the ability to forecast stress, rock bursts, or other mining related seismic events could lead to spatial information on mine maps to guide future mining plans (Urbancic 1997).

With future goals and applications of seismic monitoring for underground mining established by researchers, the current limitation on monitoring lies within equipment. Seismic equipment has begun the process of improving as of the early 2000's with manufactures working to develop more versatile equipment, capable of working in underground coal mine environments with MSHA permissibility; currently there are few MSHA approved monitoring systems. In order to truly reach the pinnacle of seismic monitoring, manufactures aim to enhance performance, enable more systems to use remote monitoring, increase the integration rate of multiple pieces of equipment, and improve the real time monitoring capabilities (Elliot 2008).

2.3 – Tomography

2.3.1 – History of Tomography

Tomography, a technique used to display a cross section of a solid body through the use of x-ray or ultrasonic waves, is not a novel concept in the scientific community. The mathematics for tomography was developed in the early 1900's by Johann Radon (Radon 1917); at the time, the technology was considered irrelevant. Radon's work was dismissed for half a century, but in 1963 Allan Cormack successfully utilized Radon's mathematical theorems to develop a tomographic technology (Shepp 1983).

Building off of the tomographic technique that Cormack developed, Godfrey Hounsfield advanced tomography to a modernized technology in 1968. Hounsfield pioneered the development of Computer Assisted Tomography (CAT) through the transmission of Bremsstrahlung x-rays to image a human head. Hounsfield and Cormack were both acknowledged in the late 1970's for their work in tomography, winning the Nobel Prize in 1979 (Shepp 1983).

Using the tomographic mathematical derivations of Radon, and the pioneering work of Cormack and Hounsfield, numerous tomographic technologies have been created for various scientific communities. Tomography revolutionized the medical field, allowing for non-invasive testing and scanning of the human body (Cesareo 1989). Research foundations use tomography to image any number of objects ranging, from the human body to plant makeup to rock sample structures.

2.3.2 – Seismic Tomography

Tomography has been used for a number of years in the medical industry; the same is true in regards to seismic tomography and the geophysics community. Unlike the medical industry, where advances were already being made in the 1970s, tomography to image the interior of the Earth did not begin until the middle of the 1970's (Monteiller 2005). Improvements have been made throughout the years, but the original work conducted by Keilti Aki and William Lee in 1976 has remained the foundation for seismic tomography.

Aki and Lee believed that it would be possible to image *in situ* rock masses much like the medical field does for a body. In place of x-ray waves and magnetic fields, Aki and Lee used seismic waves, P and S waves, caused by earthquake and micro-earthquake events to extract information from the Earth's crust. The original goal of Aki and Lee's project was to image a three by four by five kilometer area that included a fault in California through seismic tomography. In addition to imaging a seismic zone, Aki and Lee also sought to define a set of parameters to characterize the P and S wave ray paths to later improve spatial resolution (Aki 1976).

The basis of Aki and Lee's study is still commonly used in the simplest of seismic tomography methods. Aki and Lee determined that the initial step in utilizing tomography on a seismic study would be to divide the network into smaller meshes and give each mesh an initial velocity model to adjust using mathematical derivations. Once the seismic area had been meshed, the P and S wave travel times were utilized to recreate the velocity model, adjusting areas as necessary to correlate to know travel times (Aki 1976).

The success of Aki and Lee in imaging a fault zone led to additional tomographic research in the following decades. Currently, seismic tomography is used to image numerous underground structures, ranging from underground mines to subducting slab movements, known fault planes in a seismically active area, and fault planes under volcanoes (Zhang 2003; Westman 2004; Monteiller 2005; Hirose 2008). In addition to imaging massive underground structures tomography has been used to image fracture systems from hydraulic fracturing and monitor tracer fluids to evaluate underground fracturing (Lane Jr. ; Fehler 1995).

Results from tomographic studies provide an in-depth look into the subsurface of the region, such as fractures and structures, but the quality of the results may not always be acceptable. Aki and Lee's study, which utilized P and S wave data from seismic networks,

showed that it was not possible to change the amount of source events, but it was possible to change the number of receivers in an array (Aki 1976). An increase in the number of sources and receivers greatly improves the quality and resolution of tomographic results. In addition, for the best results the location of the receivers is an important factor. While it may not be possible to have complete coverage around the imaging body, 360 degree coverage around the body will produce the best results (Song 1998).

Due to the increasing number of studies utilizing seismic tomography, various alterations have been made to Aki and Lee's original seismic tomographic methods. One current study, the National Science Foundation's Earthscope program, is utilizing a variation of Aki and Lee's seismic tomography methods in an attempt to image the entire North American Continental lithosphere. Earthscope plans on utilizing a double difference inversion technique with only P wave arrival times (IRIS 2011).

2.3.3 – Common Methods for Seismic Tomography

Seismic tomography makes use of P, S, and surface waves travel times, as well as amplitudes. Some common seismic tomographic methods include Transmission Tomography, Attenuation Tomography, and Travel Time Tomography. Transmission Tomography utilizes P wave travel times as the source of data for the tomographic inversion. Transmission Tomography differs from most tomographic methods in the aspect that the observed P wave data is used simply as a back comparison to computer generated ray paths. Expansive sets of rays are back projected in order to estimate the velocity distribution required to recreate the observed travel times. The calculated travel times and ray paths are compared to the observed travel times through a least squares linear regression inversion (Peterson Jr. 1989).

Like all methods, there are positive and negative features to Transmission Tomography. Transmission Tomography was a commonly used method during the late 1980's and early 1990's due to its simplicity. However, due to the simplicity of the method, numerous errors can be generated. Background anisotropy in the data set can produce large errors in the tomographic process, causing the method to take more time than other methods as all background anisotropy must be removed from the travel times before the least squares inversion is applied (Peterson Jr. 1989).

Amplitude Attenuation Tomography is another seismic tomography method. Amplitude Attenuation Tomography shows the distribution of attenuation of seismic waves through a rock

mass by using a viscous attenuation theory (Watanabe 1996). Unlike Transmission Tomography, Amplitude Attenuation Tomography is not used as a standalone tomographic method as a velocity model is required for accurate results (Watanabe 1996; Bauer 2005).

While the major drawback of Amplitude Attenuation Tomography is that it must be used in tandem with other tomographic methods to be applied, there are other negatives involved with the method. The data required for Amplitude Attenuation Tomography, waveform data, may be more difficult to obtain from seismic monitoring organizations than simple arrival times. If the waveform data can be obtained, the use and analysis of it is more difficult than the arrival times utilized by most tomographic methods (Bauer 2005). All negative features are mitigated with Amplitude Attenuation Tomography due to the detail of the results that can be obtained through the method. Amplitude Attenuation Tomography can locate fracture zones very well in a rock mass because seismic waves' amplitude becomes very attenuated when it encounters cracks and fractures (Watanabe 1996).

The most common tomographic methods for velocity modeling are variants of Travel Time Tomography. Travel Time Tomography utilizes both active methods including blasts or hammer strikes, as well as passive methods such as natural seismicity where seismic waves are used to obtain travel times for the tomographic inversion (Fehler 1995). Active methods to obtain travel times to run tomographic inversions are used in areas with typically low seismic activity as well as instances in which a known distance is required for accurate velocity modeling. Passive methods are the most common used for Travel Time Tomography as travel time data can be easily obtained from in place seismic monitoring equipment (Lurka 2009).

Travel Time Tomography consists of a well-defined procedure utilized in most variations that is primarily independent of the data. Once the area covered by the data is known, the dimensions of the area involved in the tomographic imaging are divided into small rectangular cells. For the initial data inversion, velocity and attenuation is assumed to be homogenous and isotropic, as no data is originally known; if velocity and attenuation properties are already known, then known properties are used. With an assumed velocity and attenuation model, an iterative process is used to determine the accurate velocity model. An iterative process is used because the ray paths required to generate the velocity model also use the velocity model as it is generated (Watanabe 1996).

The iterative process undertaken in most Travel Time Tomography variations includes a four step process. The first step of the iterative process is to determine the initial velocity model for that step of the iteration. The second part of the iteration includes determining the theoretical travel times calculated from the applied ray tracing technique. Once the theoretical travel times are calculated, they are compared to the observed travel times from the data set. If the comparison between the theoretical and observed travel times is not within acceptable limits, the velocity model is adjusted to within acceptable limits. The entire iterative process is repeated with the new velocity model until the theoretical and observed travel times indicate the velocity model is within acceptable limits (Watanabe 1996).

There are numerous variations of travel time tomography used for seismic tomography including passive travel time tomography and double-difference tomography. The variations for travel time tomography differ through various modes including input data, ray tracing methods, and the inversion technique. Input data, while all based on travel times, can either consist of P or S waves, or both (Lurka 2009). Multiple inversion techniques are employed in travel time tomography, each having specific applications or positives and negatives to the methods. Some inversion techniques include least squares regression, hyperbolic and parabolic inversions (Fehler 1995).

2.3.4 – Double-Difference Tomography

Double-difference tomography is a tomographic method created by Haijiang Zhang and Clifford Thurber in the early 2000's. Double-difference tomography utilizes two separate, but near, events to provide an accurate event location as well as accurate tomographic results. The double difference algorithm, named for its mathematical base, uses the difference of observed and calculated travel times for two separate events for the tomographic inversion. Equation 2.7, below, is the most basic mathematical interpretation for double-difference tomography,

$$dr_{k^{ij}} = (T_{k^i} - T_{k^j})^{obs} - \left(T_{k^i} - T_{k^j}\right)^{cal} \qquad (2.7)$$

where $dr_{k^{ij}}$ is the double difference between the observed and calculated travel times, T_k for events i and j. The travel times used through the double difference algorithm can either be absolute or relative. The pairs of events used with the double difference algorithm solve both a three dimensional velocity structure, as well as seismic event locations simultaneously (Zhang 2003).

Zhang and Thurber's double-difference tomography consists of a variety of methodologies from various former tomographic methods. The governing concept behind double-difference tomography was developed by Dodge in 1995. Dodge's seismic tomography methodology was based around adjusting differing arrival times to minimize the discrepancy between close events and their arrival times. While Dodge only used absolute travel times in his calculations, Fremont and Malone had previously noted that the ray paths of all close events would have approximately the same takeoff angle and azimuth in relation to further spaced events; this concept introduced the possible use of relative travel times. In 2000, utilizing previous studies, Waldhauser and Ellsworth began to change event locations during the tomographic inversion. As the event locations changed during the inversion, all properties determined and utilized for seismic tomography were changed and evaluated for each location. The changing of multiple properties and locations through numerous inversion iterations essentially found absolute travel times and locations for events by utilizing relative arrival times initially. In 2003, Zhang and Thurber combined the ideals of using relative and absolute travel times, as well as optimizing the travel times for similar events to develop double-difference tomography (Zhang 2003).

Using both relative and absolute travel times, more accurate travel times, as well as differential times between paired events, the double-difference tomography algorithm provides precise relocation and velocity reconstruction models. Accurate travel times and locations are established by using a pseudo ray bending and ray tracing code, to find multiple rays and travel time pairs. The ray paths established through the pseudo bending code is interpolated into a three dimensional environment through tri-linear interpolation. Each ray path is then divided into segments throughout the zone of interest, with partial derivatives taken and evaluated from the surrounding eight nodes near the ray path (Zhang 2003). Since the double-difference tomography algorithm uses a regular inversion grid with regular grid spacing, some nodes in the model may never be evaluated because of traversed ray paths (Zhang 2006). Nodes that are traversed by ray paths, or in the surrounding eight nodes near a traversed node, are used to interpolate the velocity structure and event locations (Zhang 2003).

The double-difference tomography algorithm evaluates each node, either traversed or interpolated, and then smooths the velocity model where necessary to provide a sharper image. Smoothing of the velocity structure is accomplished through simultaneous solving of first and

second order modeling equations built into the double-difference tomography code. In order to keep velocity structure and event locations from changing each iteration of the algorithm, the code alternates joint inversion of velocity structure and event location. When the double-difference tomography code is not jointly evaluating velocity and event locations, it only evaluates the velocity; event locations are never standalone. All equations and models during the double-difference tomography algorithm for velocity and event locating are linear equation systems in a least squares regression with each equation weighted based on its' own factor (Zhang 2003).

The process utilized during the double-difference tomography method provides for extremely accurate results relating to event locating and velocity structure for near events (Zhang 2006). The accuracy of the results is in part due to the methodical use of P and S waves. Ray paths obtained from the use of P and S waves are checked through various methods to see if the magnitude and direction of the ray paths are within acceptable limits in comparison to each other. If the ray paths prove to not be within acceptable limits, the ray paths are disregarded and the corresponding P and S wave data are removed from the algorithm (Zhang 2009). With ray paths for poorly correlated P and S waves removed and the small area that ray paths influence during the double-difference tomography method, the ray path derivatives created during interpolations are concentrated around the source of ray paths, making outside ambiguity in the velocity model nonexistent (Zhang 2006).

Like all tomographic methods, double-difference tomography has some inherent problems. The primary problems of double-difference tomography come from the inflexibility in events that can be used. All events used during the algorithm must be closely spaced, as double-difference tomography is only able to improve the event location of closely spaced events. Due to the close proximity of events used, all path anomalies are considered to be the same for paired travel times and events. If the velocity changes are too extreme in the velocity reconstruction, the locations for one, or both, events could potentially be wrong because the same ray path factors affect both (Zhang 2003).

Aside from the inflexibility of the events, another issue with double-difference tomography is the weighting scheme for events used throughout the inversion process. The weighting scheme is not predefined. The weighting scheme changes throughout the inversion process, depending on several factors in the algorithm. In addition, the weighting scheme is

characteristically biased during the combination of absolute arrival times, catalog differential times, and waveform cross correlation (Zhang 2003).

The inflexibility of events and the biased weighting schemes both contribute to other problems that can be encountered in double-difference tomography. The regular grid used for the algorithm, in conjunction with the close proximity of events to one another, can cause many zones of an imaging area to not be traversed. The areas not traversed by a ray still often show some kind of results due to the damping and smoothing parameters used in double-difference tomography, thus introducing bias into the results (Zhang 2006). In conjunction with potentially biased results and areas displaying results when there may be none, the confidence weighting for the method only shows how many ray paths were traversed a voxel. The length of the ray path, as well as the velocity correlation to other ray paths within a voxel, is not factored into the confidence calculation through the method.

2.3.5 – Double-Difference Tomography Codes

There are several codes written to perform double-difference tomography inversions. The most commonly used code is TomoDD by Zhang. TomoDD assumes a flat Earth model; therefore, the software is appropriate to be used only for tens to hundreds of kilometer zones. The pseudo bending and ray tracing techniques in TomoDD assume a continuous velocity structure with only slight variations. Due to the continuous velocity structure, TomoDD cannot handle velocity discontinuities (Zhang 2006).

If the area being imaged tomographically has known velocity discontinuities and cannot utilize TomoDD, another option is TomoFDD. TomoFDD can readily handle velocity discontinuities. Moreover, TomoFDD assumes a spherical Earth model, allowing for a great deal of accuracy over hundreds to thousands of kilometers viewing areas. TomoFDD uses the same basis as TomoDD as far as the double-difference algorithm, but it also incorporates finite difference algorithms (Zhang 2006).

To supplement TomoDD and TomoFDD, another code utilizing the same double difference principals exists; TomoADD. TomoADD is an adaptive mesh double difference tomographic algorithm. TomoADD allows the inversion mesh to be closely matched to the distribution of the data set used for the tomographic imaging (Zhang 2006).

Chapters 1 and 2 References

Aki, K., W. H. K. Lee (1976). "Determination of Three-Dimensional Velocity Anomalies Under a Seismic Array Using First P Arrival Times from Local Earthquakes." Journal of Geophysical Research 81(23): 4381-4399.

Amadei, B., O. Stephansson (1997). Rock Stress and its Measurement London, Chapman & Hall.

Ammon, C. J. (2001). "Seismic Waves and Earth's Interior." Retrieved August 17, 2011, from http://eqseis.geosc.psu.edu/~cammon/HTML/Classes/IntroQuakes/Notes/waves_and_interior.html.

Bajpayee, T. S., A.T. Iannacchione, S.R. Schilling (2008). Detecting Strata Fracturing and Roof Failures from a Borehole Based Microseismic System. 27th International Conference on Ground Control in Mining. Morgantown, WV: 313-318.

Bauer, K., C. Haberland, R..G Pratt, F. Hou, B.E. Medioli, M.H. Weber (2005). Ray-Based Cross-Well Tomography for P-Wave Velocity, Anisotropy, and Attenuation Structure Around the JAPEX/JNOC/GSC et. al. Mallik 5L-38 Gas Hydrate Production Research Well. Northwest Territories, Canada, Geologic Survey of Canada. Bulletin 585: 21.

Blum, P. (1997). P Wave Velocity. Physical Properties Handbook.

Caldwell, J. (2011). "Rock Burst." Retrieved September 7, 2011.

Cesareo, R., S. Mascarenhas (1989). "A New Tomographic Device based on the Detection of Fluorescent X-Rays." Nuclear Instruments and Methods in Physics Research A277: 669-672.

Chang, X., Y. Liu , H. Wang, X. Gao (2000). "Rock Mass Structure Analysis Based on Seismic Velocity and Attenuation Images." CHINESE SCIENCE BULLETIN 45(13): 1211-1216.

Cook, N. G. W., K. Hodgson (1965). "Some Detailed Stress Strain Curves for Rock." Journal of Geophysical Research 70(12): 6.

Cormack, A. M. (1963). Journal of Applied Physics 34.

Denton, D., M. Stickney, T. Williams, R. Langston (2003). Remote Monitoring of Mine Seismicity and Earthquakes Using Radio Telemetry, Computers, and the Internet. Fourth International Conference on Computer Applications in the Minerals Industries. Calgary.

Ellenberger, J. L., K.A. Heasley, P.L. Swanson, J. Mercier (2001). Three Dimensional Microseismic Monitoring of a Utah Longwall. 38th U.S. Rock Mechanics Symposium. Lisse, Netherlands. II: 1321-1326.

Elliot, A. (2008, May 30). "Mining Ground Support." Mining-Technology. Retrieved August 30, 2010, from http://www.mining-technology.com/features/feature2017/.

Endsley, K. A. (2007). "What is Seismology and What are Seismic Waves?". Retrieved August 18, 2011, from http://www.geo.mtu.edu/UPSeis/waves.html.

ESG (2010). "Paladin - How it Works." Mining. Retrieved August 31, 2010, from http://www.esg.ca/content/how-it-works.

Fehler, M., J. Rutledge (1995). Using Seismic Tomography to Characterize Fracture Systems Induced by Hydraulic Fracturing. SEGF/SEG Third International Symposium on Geotomography. Tokyo, Japan.

Gray, R. E. (1981). Accoustic Emissions in Geotechnical Engineering Practice, ASTM International.

Handin, J. (1969). "On the Coulomb-Mohr Failure Criterion." Journal of Geophysical Research 74(22): 5343-5349.

Hirose, F., J. Nakajima, A. Hasegawa (2008). "Three-Dimensional Seismic Velocity Structure and Configuration of the Philippine Sea Slab in Southwestern Japan Estimated by Double-difference tomography." Journal of Geophysical Research 113: 26.

Hoek, E., C.C. Torres, B. Corkum (2002). Hoek-Brown Failure Criterion - 2002 Edition. Vancouver.

Hoffman, R., X. Xu, M. Batzle (2005). "Effective Pressure of What is the Effect of Pressure?" The Leading Edge 24.

Hons, M., R. Stewart, D. Lawton, M. Bertram, G. Hauer (2008). Accelerometer vs. Geophone Response: A Field Case History. Canadian Society of Petroleum Geologists Convention. Calgary, Canada.

Hudson, J. A., F.H. Cornet, R. Christainsson (2003). "ISRM Suggested Methods for Rock Stress Estimation—Part 1: Strategy for Rock Stress Estimation." International Journal of Rock Mechanics & Mining Sciences 40: 991-998.

Iannacchione, A. T., G.S. Esterhuizen, T.S Bajpayee, P.L Swanson, M.C. Chapman (2005). Characteristics of Mining Induced Seismicity Associated with Roof Falls and Roof Caving Events. 40th U.S. Rock Mechanics Symposium. Anchorage, AK, American Rock Mechanics Association: 1-10.

Iannacchione, A. T., T.S Bajpayee, J.L. Edwards (2005). Forecasting Roof Falls with Monitoring Technologies – A Look at the Moonee Colliery Experience. 24th International Conference on Ground Control in Mining. Morgantown, WV, West Virginia University: 44-51.

International, I. S. S. (2010). "I.S.S. International." Retrieved September 1, 2010, from http://www.issi.co.za/.

IRIS (2011). Seismic Tomography, National Science Foundation; Earthscope.

Karfakis, M. (2008). Rock Classifications. Blacksburg VA, Virginia Tech.

Kase, E. J., T.A. Ross, R.W. Henthorne, S.R. Jacoby (2004). Seismic Imaging as a Means to Investigate Abandoned Underground Mines. Interstate Technical Group on Abandoned Underground Mines. Tucson, AZ.

Kern, H. (2011). "Measuring and Modeling of P- and S-Wave Velocities on Crustal Rocks: A Key for the Interpretation of Seismic Reflection and Refraction Data." International Journal of Geophysics 2011.

Lane Jr., J. W., F.P. Haeni, F.D. Day-Lewis Use of Time-Lapse Attenuation-Difference Radar Tomography Methods to Monitor Saline Tracer Transport in Fractured Crystalline Bedrock.

Lawerence, Berkeley Seismic Velocity, Attenuation and Rock Properties.

Lindsay, T. (2010). "Elastic Waves." Retrieved August 18, 2011, from http://www.earthsci.unimelb.edu.au/ES304/MODULES/SEIS/NOTES/waves.html.

Ljunggren, C., Y. Chang, T. Janson, R. Christainsson (2003). "An Overview of Rock Stress Measurement Methods." International Journal of Rock Mechanics & Mining Sciences 40: 975-989.

Lockner, D. A. (1995). Rock Failure. Rock Physics and Phase Relations: A Handbook of Physical Constants. Menio Park, CA, American Geophysical Union.

Lurka, A., P. Swanson (2009). "Improvements in Seismic Event Locations in a Deep Western US Coal Mine Using Tomographic Velocity Models and an Evolutionary Search Algorithm." Mining Science and Technology 19(5): 599-603.

Luxbacher, K. D. (2005). Four-Dimensional Passive Velocity Tomography of a Longwall Panel. Mining and Minerals Engineering. Blacksburg, VA, Virginia Tech. Masters of Science.

Malek, F., F.T. Surorineni, P. Vasak (2009). Geomechanics Strategies for Rockburst Management at Vale Inco Creighton Mine. 3rd CANUS Rock Mechanics Symposium. Toronto, Ontario, Canada.

Margolin, L. G. (1984). "A Generalized Griffith Criterion for Crack Propagation." Engineering Fracture Mechanics 19(3): 539-543.

Mark, C., A.T. Iannacchione (2010). Ground Control Issues for Safety Professionals. Pittsburgh, PA, NIOSH.

Mavko, G. Conceptual Overview of Rock and Fluid Factors that Impact Seismic Velocity and Impedance, Stanford University.

Merriam-Webster (2004). The Merriam-Webster English Dictionary. New Edition, Merriam-Webster.

Monteiller, V., J. Got, J. Virieux, P. Okubo (2005). "An Efficient Algorithm for Double-difference tomography and Location in Heterogeneous Media, with an Application to the Kilauea Volcano." Journal of Geophysical Research 110: 22.

Moos, D., M.D. Zoback (1983). "In Situ Studies of Velocity in Fractured Crystalline Rocks." Journal of Geophysical Research 88(B3): 2345-2358.

Murphy, M. M., A.T. Iannacchoine, E.C. Westman, M.C. Chapman (2008). Analysis of Seismic Signatures from Gas and Dust Based Explosions at the Lake Lynn Experimental Mine. SME Annual Meeting and Exhibit. Salt Lake CIty, Utah, SME: 1-7.

Obert, L. and W. Duvall (1945). Microseismic Method of Predicting Rock Failure in Underground Mining. Part II. Laboratory Experiments: Medium: X; Size: Pages: 14.

Park, C. (2007). "What is Seismic Survey?". Retrieved August 21, 2011, from http://www.parkseismic.com/Whatisseismicsurvey.html.

Peterson Jr., J. E., E.L. Majer, A. Tura, A. Davey (1989). Practical Aspects of Crosswell Tomographic Surveys. Berkeley, CA, University of California.

Radon, J. (1917). Reprinted in Proceedings of Symposia in Applied Mathematics (1983): 27, 71.

Shepp, L. A. (1983). Computed Tomography. Symposia in Applied Mathematics, Cincinnati, Ohio.

Song, L., H. Liu, S. Chun, Z. Song, S. Zhang (1998). "Mapping an Underground Rock Mass by Anisotropic Acoustical Transmission Tomography." Ultrasonics 36: 1009-1012.

Srinivasan, C. (1995). Seismic Monitoring of Rockburts and Underground Blastings for Assessing the Stability of Deep Mine Workings at Kolar Gold Fields. 17th Annual Seismic Research Symposium. Arizona: 581-591.

Stoddard, E. (2011). Depth for South Africa's Gold Mines. Reuters. Carletonville, South Africa.

Swanson, P. L., C. Stewart, W. Koontz (2008). Monitoring Coal Mine Seismicity with an Automated Wireless Digital Strong-Motion Network. 27th International Conference on Ground Control in Mining. Morgantown, WV: 79-86.

Thoma, H., B. Bode, O. Klippel (2003). Continuous Seismic Monitoring as One Way to Assess Sources of Danger in Potash and Rock Salt Mining. Seismic Monitoring. Sondershausen, Germany, Kali – Umwelttechnik.

Trifu, C. I., F.T. Sourineni (2009). Use of Microseismic Monitoring for Rockburst Management at Vale Inco Mines. Sudbury, Ontario, Canada, Engineering Seismology Group: 12.

Urbancic, T., C. Trifu (1997). Seismic Monitoring of Mine Enviroments. Exploration 97: Fourth Decennial International Conference on Mineral Exploration, Toronto, Prospectors and Developers Associaton.

Urbancic, T., C. Trifu (2000). "Recent advances in seismic monitoring technology at Canadian mines." Journal of Applied Geophysics 45: 225-237.

Watanabe, T., K. Sassa (1996). "Seismic Attenuation Tomography and its Application to Rock Mass Evaluation." International Journal of Rock Mechanics, Mining Sciences, and Geomechanics 33(5): 467-477.

Westman, E. (2004). "Use of Tomography for Inference of Stress Redistribution in Rock." IEEE Transactions on Industry Applications 40(5): 1413-1418.

Westman, E. C., K.A. Heasley, P.L. Swanson, S. Peterson (2001). A Correlation Between Seismic Tomography, Seismic Events and Support Pressure. DC Rocks 2001, The 38th U.S. Symposium on Rock Mechanics. Washington D.C, Swets & Zeitlinger Lisse.

Whelan, D. (2011) America's Most Dangerous Jobs. Forbes

Zhang, H. (2003). Double-Difference Seismic Tomography Method and its Applications. Geophysics. Madison, WI, University of Wisconsin. Ph.D.

Zhang, H., C. Thurber (2006). "Development and Applications of Double-difference Seismic Tomography." Pure and Applied Geophysics 163: 373-403.

Zhang, H., C.H. Thurber (2003). "Double-difference tomography: The Method and Its Application to the Hayward Fault, California." Bulletin of the Seismological Society of America 93(5): 1875-1889.

Zhang, H., S. Sarkar, M.N. Toksoz, H.S. Kuleli, F. Al-kindy (2009). "Passive Seismic Tomography Using Induced Seismicity at a Petroleum Field in Oman." Geophysics 74(6): 57-69.

Zhao, J. (2000). "Applicability of Mohr-Coulomb and Hoek-Brown Strength Criteria to the Dynamic Strength of Brittle Rock." International Journal of Rock Mechanics & Mining Sciences 37: 115-1121.

Chapter 3 - Applications of Double-Difference Tomography for a Deep Metal Mine

Abstract

Seismicity at a deep hard rock mine can be a precursor to ground failure events. Seismicity data can be used in double-difference tomography, which produce tomograms showing velocity distributions in the rock mass that can be used to infer relative stress of the rock mass. The data set used for the double-difference tomography inversion was from Creighton Mine in Sudbury, Ontario, Canada, and consisted of two months of data averaging 150 seismic events per day. Three separate studies were conducted to evaluate the applications of double-difference tomography on a deep hard rock mine. These studies produced mine scale tomograms, stope scale tomograms of two active stopes, and stope scale tomograms for a cluster of events. TomoDD was used for the tomographic inversion, with other commercial programs used to view the results. All three studies produced results consistent with prior mine knowledge and basic concepts of rock mass stress redistribution. Mine scale tomograms accurately displayed a low velocity where the mined ore body is known to be with adjacent high velocity, stope scale tomograms of the two stopes both correctly demonstrated a low velocity relaxed zone near the stope following a production blast, and stope scale tomograms of an event cluster displayed consistency in results for two clusters in periods before, during, and after each cluster. The three studies show that double-difference tomography is a promising tool for observing rock mass stress redistribution that provides a baseline evaluation for the potential uses of the technology in a deep hard rock mine.

3.1 - Introduction

The mining industry is considered one of the highest risk industries in the World regardless of surface or underground, metal or coal mining. Underground metal mining has some of the deepest structures in the World, with mines in Canada and South Africa reaching depths of up to 10,000 feet (Urbancic 2000; Stoddard 2011). With extreme depths, numerous rock mechanics related issues arise including rock bursts and seismicity.

Rock bursts, the rapid release of strain energy in a violent outburst of rock from a main rock mass, can result in injuries as severe as fatalities, mine opening closures, and lost production (Caldwell 2011). Rock bursts are often preceded and followed by an increase in seismicity. Seismicity is defined as acoustic emissions from rock mass movement or deformation under stressed conditions (Gray 1981).

Depth, rock bursts, and seismicity are all controlled by various methods at mine sites. To prevent, or mitigate damage from rock bursts, mines actively employ the use of enhanced supports (Mark 2010) or de-stress blasting (Malek 2009). Seismicity is handled on a more passive approach than rock bursts through the use of seismic monitoring equipment to determine seismically active zones and when a mine is safe after an increase in seismic activity (Trifu 2009).

With seismic monitoring equipment already in place at some mine sites, one application easily employed is seismic tomography (Rawlinson 2010). Seismic tomography can be used to show areas of high and low velocity, or high and low stress, in a rock mass (Blum 1997). In addition, seismic tomography, can be used to locate fracture and void spaces in underground environments (Moos 1983; Watanabe 1996). With high and low stress zones known, as well as fracture zones, seismic tomography can be used to characterize a rock mass (Song 1998; Westman 2004) and further improve safety at mine sites.

Creighton Mine, in Sudbury, Ontario, Canada, is well known for its depth and seismic activity. The mine began underground operations in 1905 and is currently owned and operated by Vale (Caterpillar 2008). Since 1905, Creighton Mine has progressed to a depth of nearly 8,000 feet. With the increasing depth at Creighton Mine, seismicity has been an issue since the 1930's, really becoming a safety concern in the 1980's. In 1980, Creighton Mine installed the first microseismic monitoring program at the mine site; the program is still in operation (Malek 2009).

Using seismic events recorded at Creighton Mine, a seismic tomography study was conducted for the mine site. Double-difference tomography was chosen for the tomographic inversion. Tomograms were generated on both mine and stope scale sized zones. Using both the mine and stope scale size tomograms, the goal of the study was to provide a baseline exploration for the accuracy, precision, and applications of double-difference tomography at a deep metal mine.

This paper will first introduce the basic concepts behind the double-difference tomography method, as well as the advantages and disadvantages to the method. An overview of the mine site and the microseismic monitoring program will follow. Third, the data set used for the tomographic inversion with the research methods will be discussed; all locational data follows the local mine coordinate system, which introduces all locations in feet, whereas all velocity measurements will follow standard SI units of kilometers and seconds. Specific results will then be introduced and discussed. Finally, conclusions will be summarized to show applications of double-difference tomography to a deep metal mine.

3.2 – Double-Difference Method

Double-difference tomography is a tomographic method created by Haijiang Zhang and Clifford Thurber in the early 2000's. Double-difference tomography utilizes two separate, but near, events to provide an accurate event location as well as accurate tomographic results. The double-difference algorithm, named for its mathematical base, uses the difference of observed and calculated travel times for two separate events for the tomographic inversion. Equation 3.1, below, is the most basic mathematical interpretation for double-difference tomography,

$$dr_{k^{ij}} = (T_{k^i} - T_{k^j})^{obs} - \left(T_{k^i} - T_{k^j}\right)^{cal} \qquad (3.1)$$

where $dr_{k^{ij}}$ is the double difference between the observed and calculated travel times, T_k, for events i and j. The travel times used through the double-difference algorithm can either be absolute or relative. The pairs of events used with the double difference algorithm solve both a three dimensional velocity structure, as well as seismic event locations simultaneously (Zhang 2003).

Zhang and Thurber's double-difference tomography consists of a variety of methodologies from various former tomographic methods. The governing concept behind Double-difference tomography was developed by Dodge in 1995. Dodge's seismic tomography methodology was based around adjusting differing arrival times to minimize the discrepancy between close events and their arrival times. While Dodge only used absolute travel times in his calculations, Fremont and Malone had previously noted that all close events' ray paths would have approximately the same takeoff angle and azimuth in relation to further spaced events; this concept introduced the possible use of relative travel times (Zhang 2003).

Utilizing previous studies, Waldhauser and Ellsworth in 2000 began to change event locations during the tomographic inversion. As the event locations changed during the inversion, all properties determined and utilized for seismic tomography were changed and evaluated for each location. The changing of multiple properties and locations through numerous inversion iterations essentially found absolute travel times and locations for events by utilizing relative arrival times initially. In 2003, Zhang and Thurber combined the ideals of using relative and absolute travel times, as well as optimizing the travel times for similar events to develop double-difference tomography (Zhang 2003).

Using both relative and absolute travel times, more accurate travel times, as well as differential times between paired events, the double-difference tomography algorithm provides precise relocation and velocity reconstruction models. Accurate travel times and locations are established by using a pseudo ray bending and ray tracing code, to find multiple rays and travel time pairs. The ray paths established through the pseudo bending code is interpolated into a three dimensional environment through tri-linear interpolation. Each ray path is then divided into segments throughout the zone of interest, with partial derivatives taken and evaluated from the surrounding eight nodes near the ray path (Zhang 2003). Since the Double-difference tomography algorithm uses a regular inversion grid with regular grid spacing, some nodes in the model may never be evaluated because of traversed ray paths (Zhang 2006). Nodes that are traversed by ray paths, or in the surrounding eight nodes near a traversed node, are used to interpolate the velocity structure and event locations (Zhang 2003).

The double-difference tomography algorithm evaluates each node, either traversed or interpolated, and then smooths the velocity model where necessary to provide a sharper image. Smoothing of the velocity structure is accomplished through simultaneous solving of first and second order modeling equations built into the double-difference tomography code. In order to keep velocity structure and event locations from changing each iteration of the algorithm, the code alternates joint inversion of velocity structure and event location. When the double-difference tomography code is not jointly evaluating velocity and event locations, it only evaluates the velocity; event locations are never standalone. All equations and models during the double-difference tomography algorithm for velocity and event locating are linear equation systems in a least squares regression with each equation weighted based on its' own factor (Zhang 2003).

The process utilized during the double-difference tomography method provides for extremely accurate results relating to event locating and velocity structure for near events (Zhang 2006). The accuracy of the results is in part due to the methodical use of P and S waves. Ray paths obtained from the use of P and S waves are checked through various methods to see if the magnitude and direction of the ray path are within acceptable limits in comparison to each other. If the ray paths prove to not be within acceptable limits, the ray paths are disregarded and the corresponding P and S wave data is removed from the algorithm (Zhang 2009). With ray paths for poorly correlated P and S waves removed and the small area that ray paths influence during the double-difference tomography method, the ray path derivatives created during interpolations are concentrated around the source of ray paths, making outside ambiguity in the velocity model nonexistent (Zhang 2006).

Like all tomographic methods, double-difference tomography has some inherent limitations. The primary limitation to double-difference tomography stems from the inflexibility in events that can be used. All events used during the algorithm must be closely spaced, as double-difference tomography is only able to improve the event location of closely spaced events (Got 2008). Due to the close proximity of events used, all path anomalies are considered to be the same for paired travel times and events; therefore, if the velocity changes are too extreme in the velocity reconstruction, then the locations for one or both events could potentially be wrong because the same ray path factors are affecting both (Zhang 2003).

Aside from the limitations imposed by the proximity of events, another issue with double-difference tomography is the weighting scheme for events used throughout the inversion process. The weighting scheme is not predefined. The weighting scheme changes throughout the inversion process, depending on several factors in the algorithm. In addition, the weighting scheme is characteristically biased during the combination of absolute arrival times, catalog differential times, and waveform cross correlation; the weighting itself imposes differing constrains on the data that are more well located than not (Zhang 2003).

The inflexibility of events and the biased weighting schemes both contribute to other problems that can be encountered in double-difference tomography. The regular grid used for the algorithm, in conjunction with the close proximity of events to one another, can cause many zones of an imaging area to not be traversed. The areas not traversed by a ray still often show some kind of results due to the damping and smoothing parameters used in double-difference

tomography, thus introducing bias into the results (Zhang 2006). In conjunction with potentially biased results and areas displaying results when there may be none, the confidence weighting for the method only shows how many ray paths were traversed by a voxel. The length of the ray path, as well as the velocity correlation to other ray paths within a voxel, is not factored into the confidence calculation through the method.

There are several codes written to perform double-difference tomography inversions. The most commonly used code is TomoDD by Zhang. TomoDD assumes a flat Earth model, therefore it is appropriate to use only for tens to hundreds of kilometer zones. The pseudo bending and ray tracing techniques in TomoDD assume a continuous velocity structure with only slight variations. Due to the continuous velocity structure, TomoDD cannot handle velocity discontinuities (Zhang 2006).

3.3 - Creighton Mines' Seismicity

Creighton Mine is situated on the southern edge of the Sudbury Igneous Complex, just outside of Sudbury, Ontario, Canada (Wiles 1988). There are three major rock masses located within Creighton Mine including granite, norite, and the ore. The granite is the footwall of Creighton Mine, with the Norite being the hanging wall and the host of the sulphide orebodies; the footwall also consists of gabbro intrusions (Malek 2009). Norite is a mafic igneous rock that is difficult to differentiate between gabbro in the footwall. Norite is consistently located near platinum and other precious metal orebodies. The orebody consists of both copper and nickel, individually representing 1.5 to 2.0% of the mined products (Snelling 2009).

Creighton Mine is characterized by extensive faults as well as extremely high gravitational, regional, and local domain stresses. There are four major fault groupings: the footwall shear system, east-west striking system, south-west striking of the 118 shear system, and minor faults on the boundaries of the 118 shear system (Snelling 2009). 118 refers to the orebody that the faulting is predominantly noted; Creighton Mine consists of five active ore bodies currently (Trifu 2009). Past studies have produced empirical relationships between the depth and stress tensors at Creighton Mine. Using empirical relations, stress values around the 7,800 level, current mining depth, are 110 to 128 MPa for the major stress, 87 MPa for the intermediate stress, and 70 MPa for the minor (Malek 2009; Trifu 2009). The major and intermediate principal stresses are horizontal, with the minor principal stress being the vertical

stress (Snelling 2009). Stress measurements previously conducted at Creighton Mine confirm the empirical relations for stress measurements.

High stress concentrations in addition to numerous fault zones lends to Creighton Mine's high frequency of seismicity. In place microseismic monitoring systems record approximately 70 events per day at Creighton Mine (Snelling 2009), with the most events following blasting operations (Caterpillar 2008). The majority of the approximate 26,000 events per year are below a 2.0 moment magnitude, but there are between 30 to 40 events per year that are above a 2.0 on the local moment magnitude scale (Trifu 2009).

Events are classified into two categories: blast related and stress related events. While most events are mining induced to an extent, meaning the events would not occur without the mining operation, blast related events are described as events that can be correlated directly to blasting. Stress related events are described as events that are caused through stress relief from the rock mass.

Blast related events occur in or around crown and sill pillars, in single development headings, and sill accesses following blasting. Blast related events are predominantly in the form of rock bursts, while stress related events are in the form of fault slips and strain bursts (Trifu 2009). Approximately 80% of the seismic events recorded at Creighton Mine are considered to be fault slip events (Snelling 2009).

Blast related events can be easily determined and planned for, but the random nature of stress related events necessitated the need for a microseismic monitoring program. The original instrumentation for Creighton Mine's microseismic system was installed in 1980 and has subsequently been upgraded numerous times (Malek 2009). Currently, Creighton Mine operates a 16-bit Hyperion system from Engineering Seismology Group (ESG) for the microseismic monitoring, consisting of a 104 channel capacity. The array consists of both uniaxial and triaxial accelerometers with sensitivities of 30 volts per unit gravity and 0.5 volts per unit gravity, respectively. The accelerometers used at Creighton Mine have wide frequency ranges also, with uniaxial units having a 50 to 5,000 Hz range, and triaxial units having 3 to 8,000 Hz. The Hyperion microseismic system detects estimated magnitude events of -2.0 to 1.0 on the local magnitude scale (Trifu 2009).

For local magnitudes greater than 1.0, Creighton Mine employs the use of a 24-bit Paladin system, also from ESG. The Paladin system consists of four triaxial geophones placed underground. The geophones used operate at a frequency of 4.5 Hz (Trifu 2009).

The Hyperion and Paladin systems work in unison to record event locations, times, magnitudes, energy releases, and dynamic properties of the events. Full waveforms are recorded by the systems. Both the Hyperion and Paladin seismic arrays are located entirely underground. The receivers are arranged to cover the entirety of the active mine works from 3,500 feet deep to the current level of 7,800 feet deep (Malek 2009; Trifu 2009).

3.4 - Data Set

For this study, Creighton Mine supplied two months of seismic data. The data began on January 14, 2009, and ended on March 16, 2009. During the two months, 9,270 events occurred for an average of 150 events per day. 150 events per day during the two months of data is higher than the typical 70 events per day; this elevated average exists because on March 14, there were 1,199 events.

During the two months of data, only 36 events were recorded with a moment magnitude higher than zero. The highest moment magnitude recorded during the time period was 0.7. Of the 36 events above zero, all but two events occurred between a depth of 7,300 and 7,600 feet. Figure 3.1, shown below, is a histogram of the moment magnitude distribution.

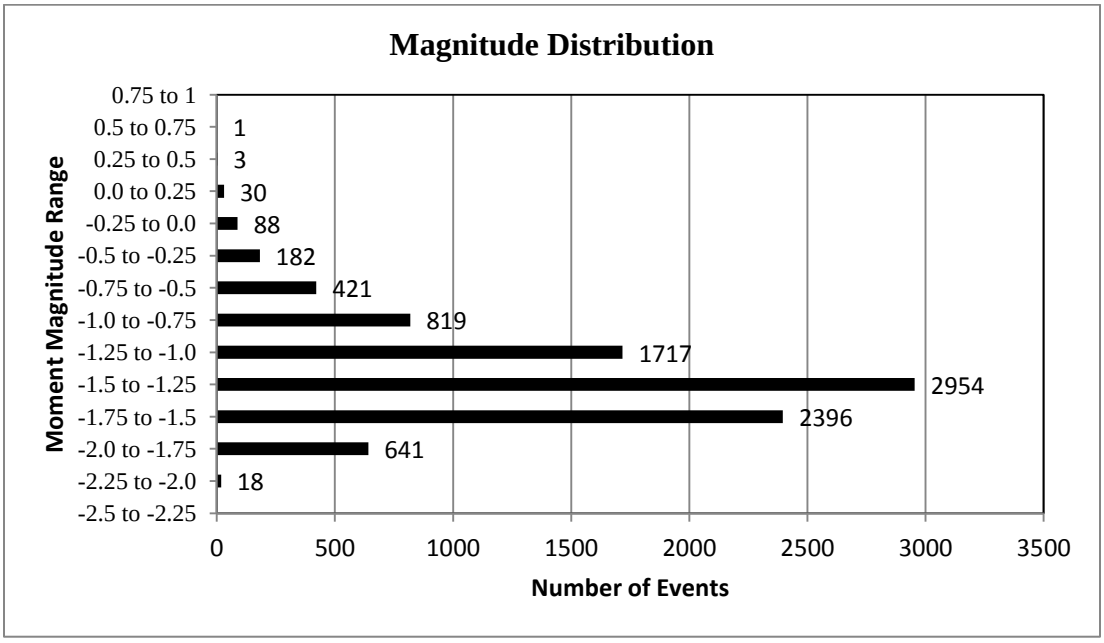

Figure 3.1: Histogram of moment magnitude distributions from Creighton Mine dataset.

In accordance with Figure 3.1, a typical representation of the distribution of magnitudes is shown by plotting the logarithm of the number of events against the magnitude of those events. This plot is the basis of an empirical relationship between frequency of events and the magnitude of these events proposed by Gutenberg and Richter. Gutenberg and Richter's empirical relationship is shown below in Equation 3.2,

$$\log N = a - b(M) \qquad (3.2)$$

where N is the number of events at magnitude M, a is a constant representing the level of seismicity, and b is a constant representing slope and is near a value of one (Gutenberg 1944). Figure 3.2, below, shows the plot of the logarithm of the number of events against the magnitude for the dataset received from Creighton Mine as well as the linear empirical relationship.

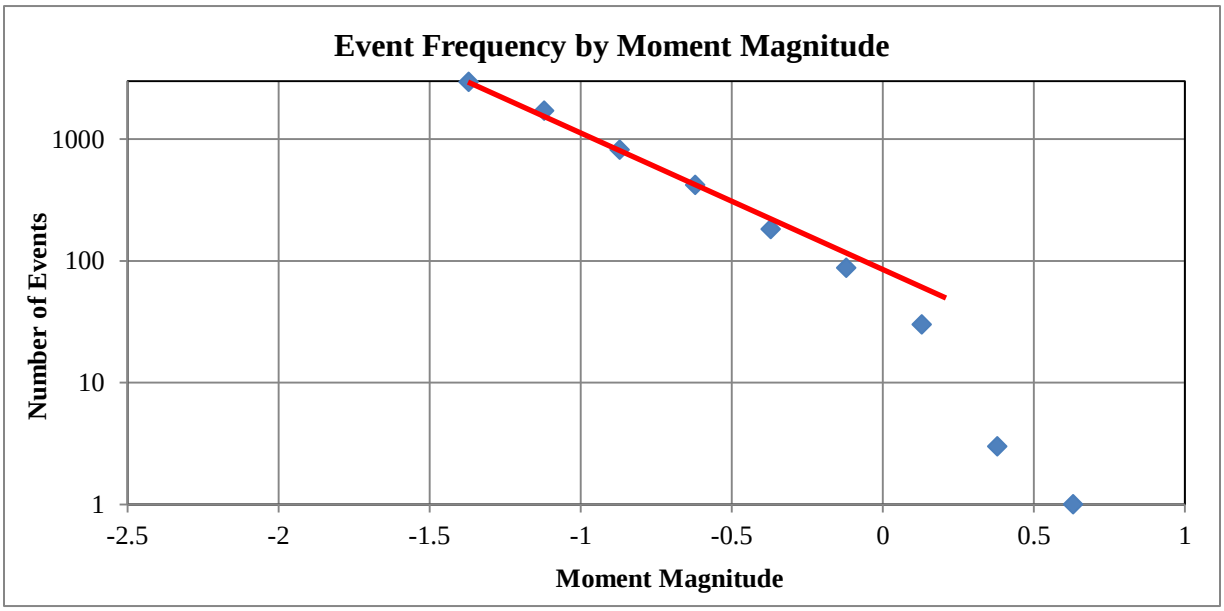

Figure 3.2: Logarithm of number of events at a given moment magnitude for the Creighton Mine dataset. The linear line produced from Gutenberg and Richter's empirical relationship is shown in red.

As shown in Figure 3.2, the dataset received from Creighton Mine produces a b value near the anticipated value of one for the majority of the microseismic events. A b value of near one indicates a constant stress drop throughout the region. Typically, lower magnitude events produce a non-constant b value (Gutenberg 1944), as shown by the change in slope in Figure 3.2, due to the sensitivity of recording equipment.

While most events of higher magnitude are confined to a 300 foot depth region, the majority of the events, close to 80%, are located in a 1,000 foot region between 7,000 and 8,000

feet. This distribution for the events is to be expected as all mining operations during the two month time period took place below 7,000 feet. From a horizontal prospective rather than vertical, most events took place in the footwall of Creighton Mine. Again, events in the footwall are to be expected as the material is a brittle granite. Figure 3.3, below, shows the event locations by depth for both the Northing and Easting. Northing and Easting coordinates were obtained through a mine coordinate system beginning at zero feet in both directions and extending outward in units of feet.

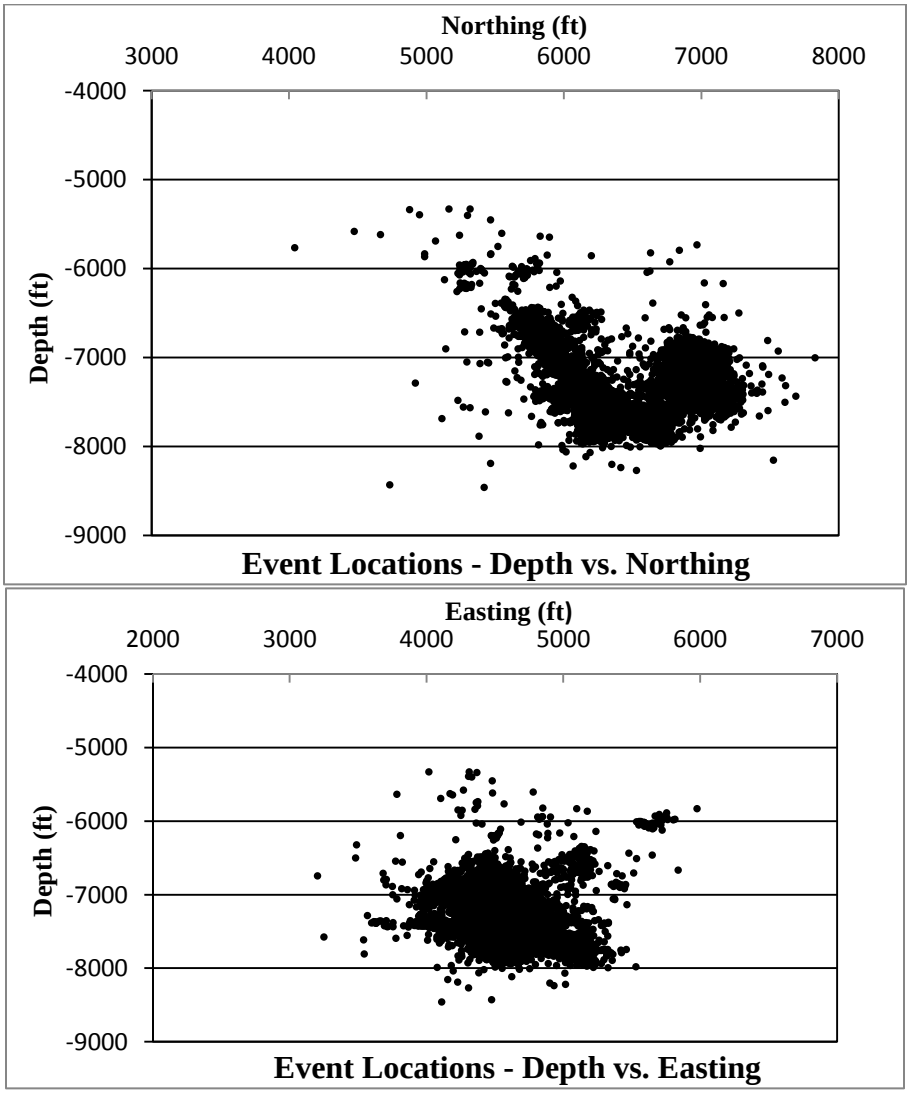

Figure 3.3: Event locations for the two months of seismic data at Creighton Mine.

For the two months of data received, the background velocity was determined to be approximately 6.25 kilometers per second. The background velocity was calculated utilizing all travel time and station receiver combinations recorded for the 9,270 events. All values were

normalized to indicate at zero time, there would be zero distance traveled. For background velocity calculations, all source and receiver pairs that indicate the receiver did not detect the source were ignored. Figure 3.4, below, shows the time vs. distance plot used to determine the background velocity for the data set from Creighton Mine. Figure 3.4 only shows times up to 0.1 seconds and distances up to 500 meters to demonstrate the linearity, and amount of the travel time and distance pairs used to determine the background velocity. Figure 3.5, also below, shows the entirety of the data sets travel time and distance pairs in order to demonstrate both the background velocity and the data sets expected low velocity threshold; the low velocity threshold for the data set is approximately 1.75 kilometers per second.

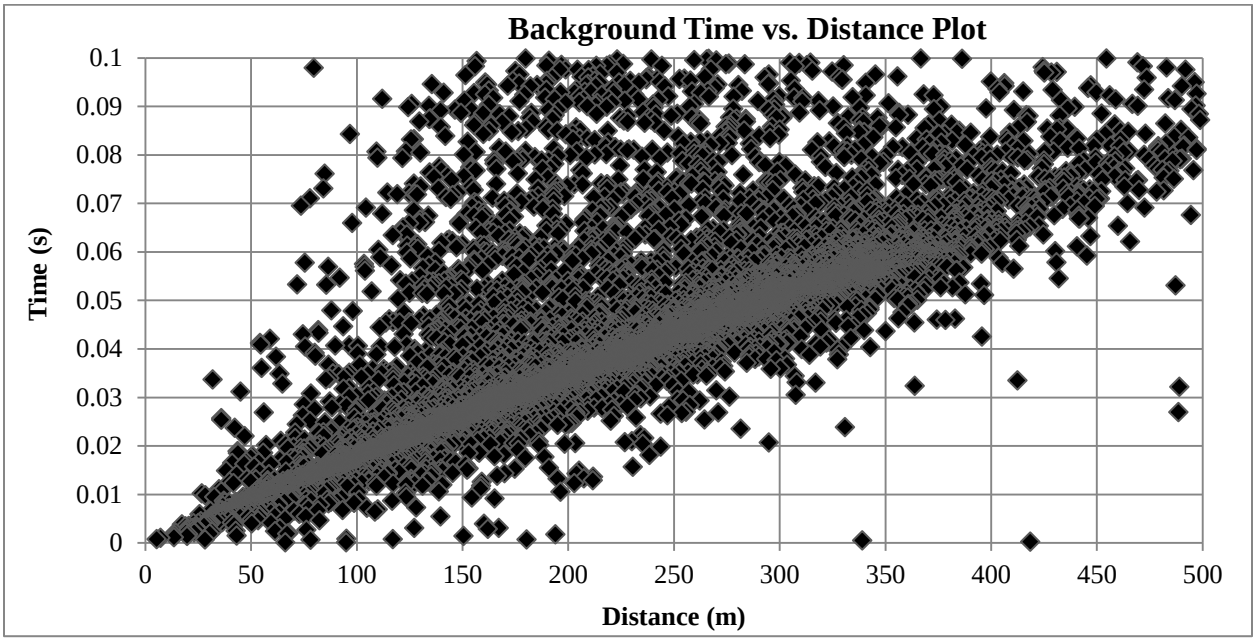

Figure 3.4: Time vs. Distance plot with a maximum travel time of 0.1 seconds and maximum distance of 500 meters to determine the background velocity of the data set from Creighton Mine.

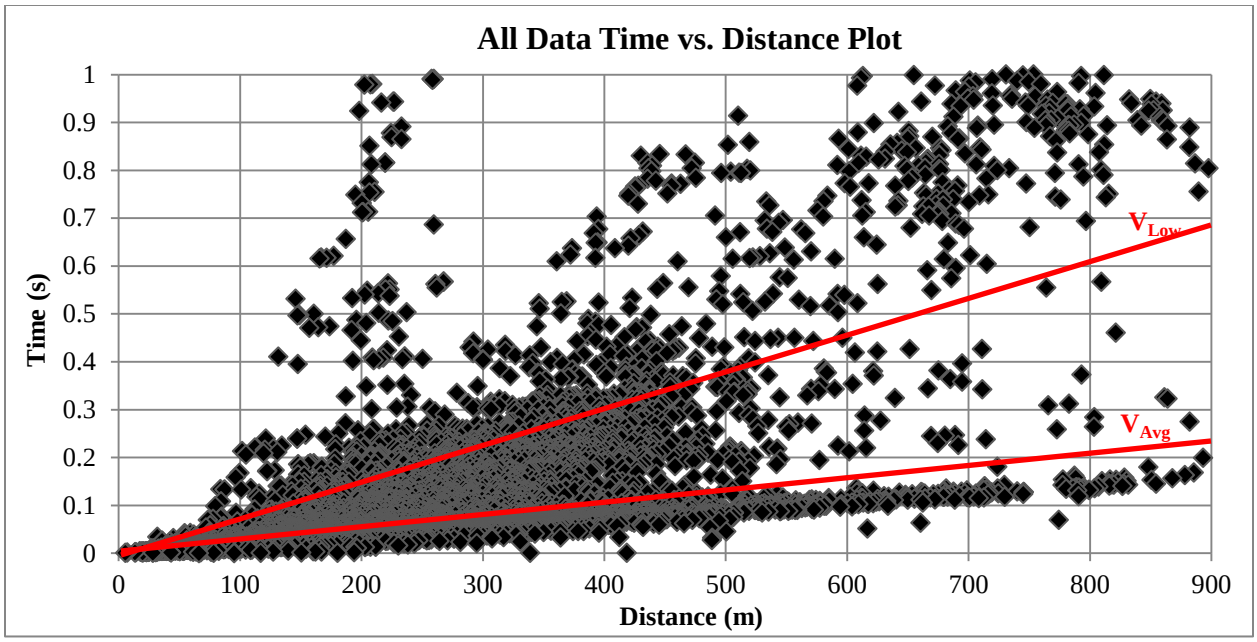

Figure 3.5: Time vs. Distance plot of all data with both the low velocity threshold and background velocity of the data set from Creighton Mine.

3.5 - Methods

For this study, three major areas of interest for Creighton Mine were analyzed. These areas include mine scale imaging to view entire site characteristics, stope scale imaging to view characteristics around mining fronts, and stope scale imaging to view changes due to groupings of above magnitude zero events. Each area of interest required different setups for the tomographic inversion through TomoDD. All locations are referred to in the mine coordinate system, which has all locations as feet; all velocities are in kilometers per second (km/s).

3.5.1 - Mine Scale Imaging

In order to obtain an overall understanding of Creighton Mine, tomographic imaging of the entire mine site was conducted. For the mine scale imaging, the two months of data were broken into four different time periods based on number of events. The four time periods were January 14 to February 13, February 14 to February 18, February 19 to March 13, and March 14 to March 16.

The first time period had the most events at 2,470, with the least events occurring in the second time period at 2,147. Over the four time periods, there was an average of 2,318 events.

All four time periods had too many events for the tomographic inversion to run based on the number of P-wave arrival times.

To select only events with a high amount of P-wave arrival times, the event files underwent a thinning process. This thinning process evaluated each event based on the number of source and receiver P-wave pairings. The events with the most pairings were retained for the tomographic inversion while the least paired events were not included in the inversion. In total, approximately 55,000 P-wave arrival times were utilized in the tomographic inversion.

The four time periods for the mine scale analysis were chosen in order to ensure events were well distributed throughout the imaging zone. Well distributed events allow for the best possible imaging over a large area. Through the event distribution of the four time period analysis, as well as the broad scope of the time periods, the majority of the mining area can be imaged to show rock mass characterization while ignoring small scale changes in the rock mass.

In order to view subtle changes in the entirety of the rock mass, twenty time periods were used. The twenty time periods cover the two months of data. Each time period consists of six days, with three days overlapping time periods, i.e. the first time period is January 14 to 19, and the second time period is January 17 to 22. The final time period is only five days.

Of the twenty time periods, the least amount of events in a time period is 333 while the maximum number of events is 2,683; the maximum events occurred during the five day time period. The twenty periods averaged 855 events. Of the twenty periods, seven require thinning due to excessive P-wave source and receiver pairings.

The breakdown of the twenty time periods was chosen to provide each time period with enough events for a successful tomographic inversion. The purpose of the twenty time period concept for the mine scale analysis was to show isolated changes in the rock mass, as the smaller time periods will reduce specific coverage areas. The overlap in the time periods was used in order to create a smooth animation to observe changes in the rock mass in a flipbook sequence.

While the time periods for observation were distributed so to allow for complete viewing of the mining locations, TomoDD requires a base velocity model covering all areas to be modeled during the inversion. This velocity model is set using a grid method with up to 40 nodes in the X, Y, and Z directions. The spacing between nodes on the grid are set using units of meters divided by 100 for Creighton Mine.

For the mine scale imaging of Creighton Mine, a 40 by 40 by 40 node grid, with 50 feet per node was used. The grid was set to model the area in the X direction of 3,900 to 5,650 feet, in the Y direction of 5,350 to 7,075 feet, and in the Z direction of 6,250 to 8,000 feet. The X direction represents the Easting associated with Creighton Mine, while the Y direction represents the Northing, and the Z direction is the depth at the mine.

While the region is small in comparison to many usages for TomoDD, it allows for complete mine coverage. All area utilized by the production drifts can be imaged in the 1,700 feet set by the grid spacing. The 1,700 feet of depth covers the active mining sections of Creighton Mine at the time of the study also.

In addition to the basic MOD file, TomoDD also requires the use of various parameters including weighting and damping of arrival times. Weighting refers to the first order smoothing constraints employed in the program in relation to slowness in the X, Y, and Z directions. The weighting eliminates sharp edges in the velocity model. Damping is used to identify poorly constrained events with high residuals. The damping value is the radius that an event can be relocated through the double-difference inversion.

For the mine scale imaging of Creighton Mine, weighting values of 35 in each direction were used. Damping values for mine scale imaging ranges from 60 to 90, depending on inversion iteration. These combinations of weighting and damping values were used to obtain a condition number between 60 and 80 after running TomoDD. The condition number is an output established during the double-difference inversion related to the range of damping of the least square linear regression equations.

With appropriate condition numbers met, another source of confidence output from TomoDD is the Derivative Weight Sum, or DWS. The DWS is a statistical parameter that assesses the density of rays that passes near a grid point. In order to ensure that areas not traversed by ray paths were used in the final tomogram, any DWS value below 1.0 was excluded in the mine scale imaging tomogram interpolation. 1.0 was chosen as the cutoff in order to eliminate any zero point, while leaving sufficient data points to cover the entirety of mine image.

3.5.2 - Stope Scale Imaging

In order to evaluate Creighton Mine on a more localized level, tomographic imaging was conducted on the stope level. For the small scale study, two stopes were evaluated; Stope 5078 and Stope 4448. Stope 5078 is located at approximately 5,080 East and 6,700 North on the mine

coordinate system, between the depths of 7,680 and 7,810 feet. Stope 5078 was in production for six months spanning from November 2008 to April 2009. The final production blast occurred during the two month data set on February 16. The blast was 14,500 pounds, the largest during the two month data set.

Stope 4448 is located at approximately 4,440 East and 6,740 North, between the depths of 7,530 and 7,680 feet. Stope 4448 was in production from January 2009 to February 2009. Each of the 11 production blasts occurred during the two month data set, with the largest blast occurring on February 16 at 9,500 pounds.

The two stopes, 5078 and 4448, were chosen as evaluation stopes due to their unique properties, such as utilizing the two largest blasts of the data set and the amount of activity at the stopes during the data set. Stope 5078 was chosen particularly because it was imaged in the mine scale imaging due to the unique mining sequence. Stope 4448 was chosen particularly because the stope was only in production during the two months of seismic data. In addition, the two stopes were chosen based on a confidence analysis of the mine scale imaging. Both Stope 5078 and Stope 4448 had DWS coverage surrounding the entirety of the stope area.

For both Stope 5078 and Stope 4448, a grouping of ten time periods was used. The ten time periods were based on a Sunday to Saturday time frame with the first time period beginning on Wednesday, January 14, and consisting of only four days. Due to limitations in TomoDD, three other time periods were shorter than the standard seven days. The period of February 15 to 21 was split into two time periods consisting of February 15 to February 17 before noon, and February 17 after noon until February 21. In addition, the final time period was shortened to six days as the seventh day included nearly 2,000 events itself.

The ten time periods were created in a Sunday to Saturday manner in order to facilitate enough events per time period to run a tomographic inversion. The minimum amount of events in one period was 302, while the maximum number of events was 1,278. Overall, there were 685 events per time period on average. Appendix A shows the time period breakdown for Stopes 5078 and Stope 4448.

For the stope scale imaging, a base velocity model with a grid consisting of 40 by 40 by 40 nodes was used. The spacing between nodes was 16.4 feet, or five meters. Two separate models were used for the two stopes to allow for each stope to have a unique viewing zone.

The velocity model of Stope 5078 spanned from approximately 4,800 to 5,450 feet in the west to east direction, 6.300 to 6,975 feet in the south to north direction, and 7,450 to 8,000 feet of depth. Stope 4448 spanned from 4,180 to 4,720 feet in the west to east direction, 6,480 to 7,020 feet in the south to north direction, and 7,350 to 7,900 feet of depth. The dimensions used for the velocity models allow for each stope to have approximately a 250 foot radius extending from the center of the stope, thus isolating the stope for small scale observations.

Due to the size discrepancy between the mine scale imaging and the stope scale imaging, a different approach to obtaining weighting and damping values, as well as the correct number of iterations was used. The stope scale imaging requires a fine tuned image over a small area, thus requiring the bias towards certain events to be reduced. In order to reduce the bias, an iterative process was used to determine the optimum weighting and damping values simultaneously. Using optimum values for weighting and damping, the number of iterations was determined.

In order to determine all optimum values for the TomoDD runs, it was necessary to run TomoDD on three different groupings of inputs. For the first grouping, which determined the correct weighting and damping, TomoDD was run 35 times per time period, at only two iterations per inversion group. The 35 instances represented the 35 different combinations of weighting and damping values tested. The values included weightings of 5, 10, 25, 50, and 100. Damping values ranged from 10 to 1,000, including 10, 25, 50, 100, 250, 500, and 1,000.

For each combination, a different input file was utilized, allowing for all 35 instances to be ran using an automated process. With all 35 instances processed, the resulting log files from each were analyzed. From the log files, the values of absolute mean, absolute variance, absolute CTRMS, and condition were extracted. Absolute mean and absolute variance values are both statistical parameters with the absolute mean being the mean travel time of the weighted pairs and the absolute variance being the variance from the mean for the absolute travel times. Absolute CTRMS is the double difference residuals from the catalog travel times.

Using absolute variance and absolute mean values for each of the weighting groupings, curves were generated to determine the correct weighting and damping values. On the curves, the optimum weighting values are defined as where the curves begin to converge at the higher absolute variance and absolute mean values. With the optimum weighting curve known, the optimum damping value occurs in the elbow of the curve.

Figure 3.6, below, shows the absolute variance versus absolute mean curve for the first time period of Stope 5078. The optimum weighting established from this curve occurred at 25. The optimum damping was situated at 100. Each damping value is located in Figure 3.6, as well as the locations that were used in selecting the appropriate weighting and damping values of 25 and 100, respectively. All absolute variance versus absolute mean plots for Stope 5078 are shown in Appendix A, with all absolute variance versus absolute mean plots for Stope 4448 shown in Appendix B.

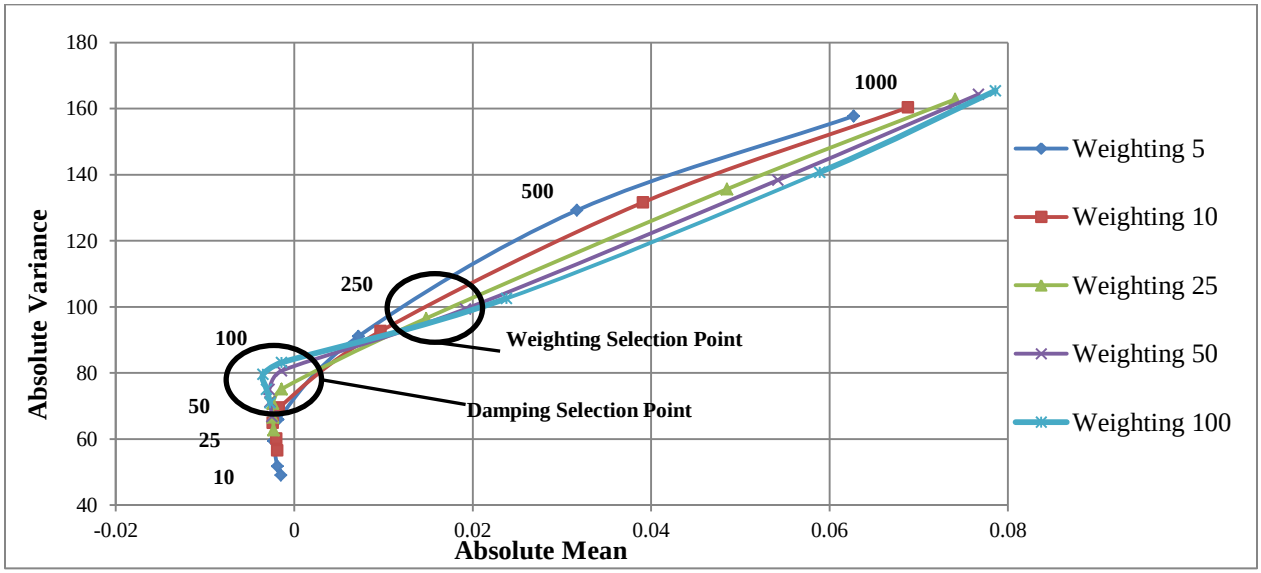

Figure 3.6: Stope 5078 absolute variance versus absolute mean for the first time period.

With the optimum weighting and damping determined, each of the ten time periods were run in TomoDD with five iterations per inversion group, for a total of 40 iterations. The resulting log files were analyzed and the absolute CTRMS value for each iteration extracted. The optimum number of iterations was determined by evaluating the CTRMS value per iteration plot. On the plot, the optimum number of iterations was evaluated as the point where the CTRMS value was changing very little from the previous iteration.

Figure 3.7, below, shows the absolute CTRMS per iteration plot for the first time period of Stope 5078. The absolute CTRMS per iteration plot shows that the values continuously decrease throughout the five iterations per grouping. However, the difference between iterations four and six is negligible, with iteration five displaying an unexplained drop in the CTRMS. Due to the negligible change from iteration four and six, the optimum number of iterations was chosen as four. All absolute CTRMS per iteration plots for Stope 5078 are shown in Appendix A and Appendix B for Stope 4448.

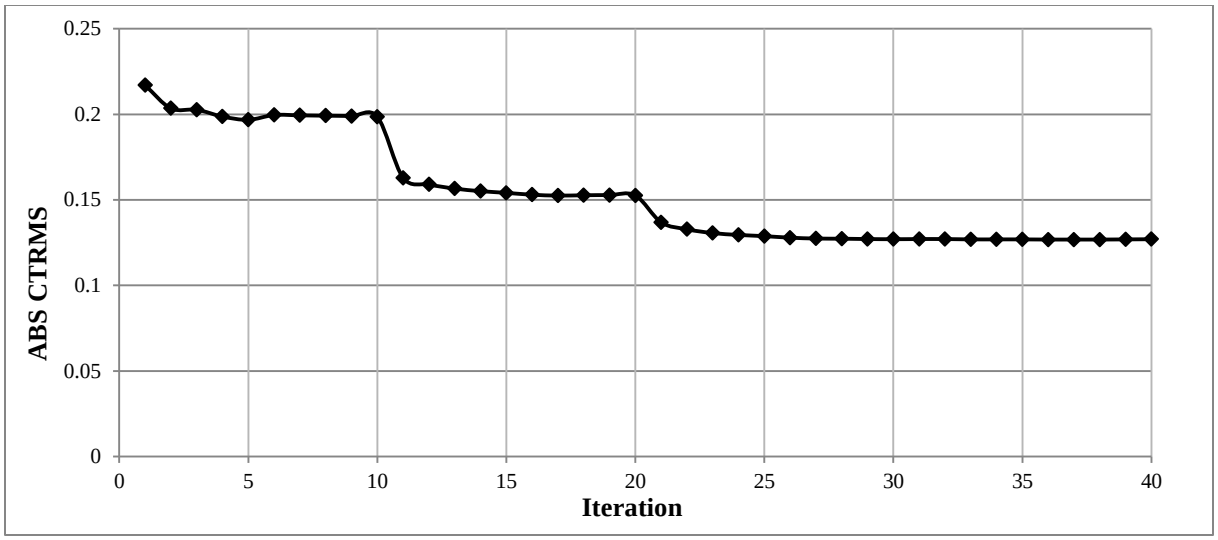

Figure 3.7: Stope 5078 absolute CTRMS per iteration plot for the first time period.

Table 3.1, below, is the optimum values for weighting and damping for both Stope 5078 and Stope 4448. The optimum number of iterations for each time period is also shown. All weighting values were either 25 or 50, with all damping values ranging between 75 and 100 for Stope 5078 and 50 and 100 for Stope 4448.

Table 3. 1: Weighting, damping, and iterations for each time period for both Stope 5078 and Stope 4448.

	Stope 5078			Stope 4448		
Period	**Weight**	**Damping**	**Iterations**	**Weight**	**Damping**	**Iteration**
1	25	100	4	50	50	4
2	25	100	5	50	75	5
3	25	85	5	25	85	4
4	25	75	4	25	90	5
5	50	100	4	50	90	5
6	50	100	5	50	90	4
7	50	100	3	50	85	3
8	25	75	4	50	50	5
9	50	75	4	25	100	5
10	50	75	5	50	65	3

With weighting and damping values optimized and condition numbers within the appropriate ranges, the optimum DWS cutoff was determined. To ensure enough data points were left to produce tomograms, the DWS cutoff point was set to be the top 75% of the data points. Zeroes

were excluded from the top 75% data calculation, as the top 75% with zeroes included would often still be zero.

In order to determine the top 75% DWS values once all zero points were removed, a frequency distribution over 0.01 and 0.1 increments was used. Using the frequency distribution, the percentage of DWS values that fell into its specific categories was determined, as well as a cumulative percentage. When the cumulative percentage reached 25%, that value was used as the cutoff. In addition, the cumulative 25% was also evaluated graphically. Figure 3.8 shows how the top 75% is determined graphically, in addition to the distribution of DWS values for Stope 5078 during the first time period. All histograms used in determining DWS cut off values for Stope 5078 are shown in Appendix A and Appendix B for Stope 4448.

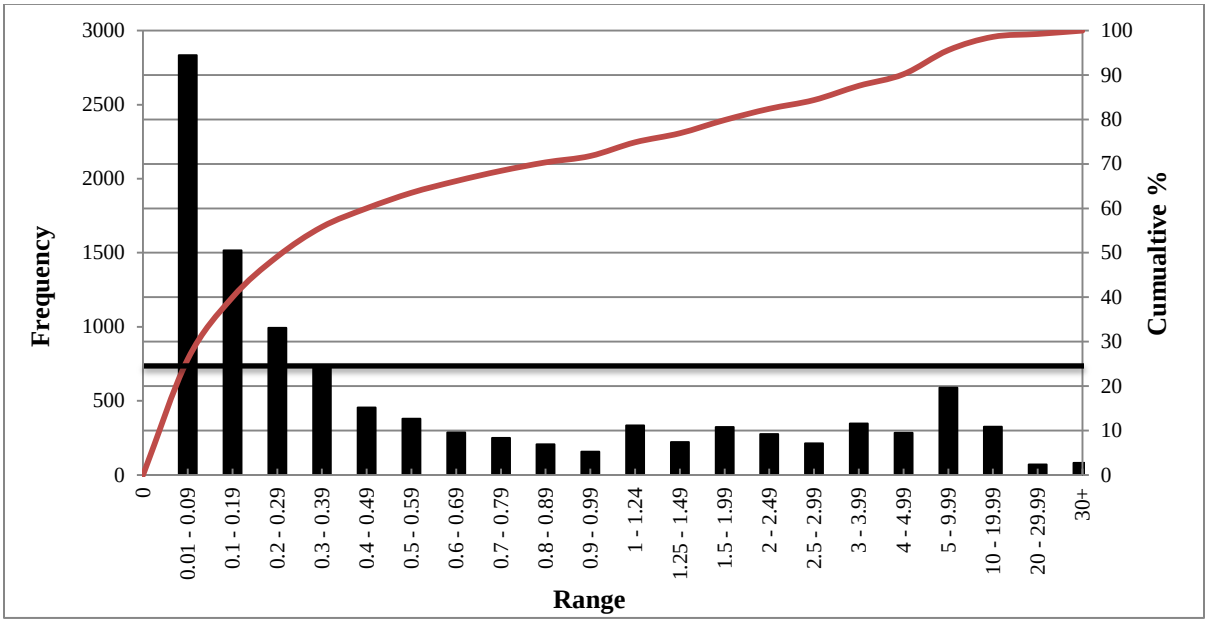

Figure 3.8: Histogram for DWS frequency with cumulative percentage plotted on the secondary axis for the first time period of Stope 5078.

Table 3.2, below, is the DWS value used as the top 75% cutoff for all time periods for both Stope 5078 and Stope 4448. In addition, Table 3.2 shows the percentage of data points remaining for the top 75% calculation after all zeroes were removed. Stope 4448 consistently had a higher percentage of data points remaining after all zeroes were removed.

Table 3.2: Top 75% DWS cutoff point and the total data points remaining after the elimination of zeroes for both Stope 5078 and 4448.

	Stope 5078		Stope 4448	
Period	**Top 75% DWS**	**% Above Zero**	**Top 75% DWS**	**% Above Zero**
1	0.09	23.31	0.09	43.25
2	0.17	26.79	0.19	51.77
3	0.14	29.27	0.22	53.60
4	0.14	30.75	0.20	64.78
5	0.50	46.89	1.15	75.37
6	0.60	52.65	0.40	72.04
7	0.15	41.48	0.15	54.75
8	0.15	38.15	0.17	53.74
9	0.12	36.06	0.19	56.04
10	0.09	29.34	0.13	44.95

3.5.3 - Stope Scale Imaging for an Event Cluster

In addition to evaluating stress redistribution near a stope, stress redistribution near a cluster of events was also evaluated. Seven events were chosen in order to view the stress redistribution of clustered events. These events were chosen because all have a magnitude higher than zero, are in close proximity of one another, and are contained within two small time periods.

For the stope scale imaging on a cluster of events, five time periods were used. Like the stope imaging, a Sunday to Monday breakdown was utilized beginning on Sunday, January 18. The final time period was limited to two full days and a quarter of another, February 14 through February 16 at six AM due to limitations in TomoDD. The five time periods had an average of 616 events.

Like the previous time period breakdowns, the five time periods are continuous, however the five time periods act as two distinct groups that utilize time period three in each. Group one focuses on a set of five events and utilizes the first three time periods as a before the event cluster, during the event cluster, and after the event cluster focus. Group two focuses on a set of two events with the third time period acting as the prior to the events cluster period and time period five acting as the after events cluster period. The time period distribution can be seen in Appendix C.

As with both the mine and stope imaging, the event cluster velocity model is set on a 40 by 40 by 40 node grid. The spacing between nodes is 16.4 feet, 16.4 feet was based off of the smallest spacing possible of five meters. In order to determine the exact area covered by the seven events, the average Northing, Easting, and Depth coordinates was taken for the seven events, with the average acting as the center of the velocity model grid locations.

A 250 foot radius from the average event locations was utilized. The model covered from 4,150 to 4,690 feet in the west to east direction and 6,350 to 6,890 feet in the south to north direction. To cover the depth of the events, 7,380 to 7,920 feet was modeled.

The same procedure to determine the optimum weighting, damping, and iterations as the stope imaging was conducted. Table 3.3, below, is the damping, smoothing, and iterations for each of the five time periods of the event clusters. All weighting values are either 25 or 50 with damping values ranging from 50 to 90. All absolute variance versus absolute mean plots, as well as absolute CTRMS per iterations plots, used in determining damping values, weighing values, and number of iterations for the cluster of events are shown in Appendix C.

Table 3.3: Weighting, damping, and number of iterations for the event clusters for each time period.

	Event Cluster		
Period	**Weight**	**Damping**	**Iteration**
1	50	60	3
2	25	85	4
3	25	50	4
4	25	90	4
5	50	90	5

For the event clustering, the same procedure for eliminating events with poor DWS confidence as the stope imaging was utilized. Table 3.4 shows the top 75% DWS value cutoff point as well as the percentage of data points remaining after all zeroes were eliminated. At worst, approximately 50% of the data points were removed with zero DWS. All histograms used in determining DWS cut off values for the cluster of events is located in Appendix C.

Table 3.4: Top 75% DWS and percent of data points with above zero DWS for the event cluster at each time period.

	Event Cluster	
Period	**Top 75% DWS**	**% Above Zero**
1	0.20	52.00
2	0.20	53.60
3	0.11	49.05
4	0.30	71.02
5	0.60	74.44

3.6 - Results and Discussion

Results for the three studies were evaluated using four dimensional, X, Y, Z, and various data components, imaging software. To interpolate tomograms between nodes, the Inverse Distance method to the first power was utilized. Only nodes within a distance of two times the node spacing were used in interpolating the tomograms. Any areas of the tomograms shown as white indicate that there was not sufficient data coverage.

3.6.1 – Mine Scale Imaging

The mine scale study provided tomograms for the majority of Creighton Mine. The first set of tomograms produced was based on the four time periods with the second set based on twenty time periods. These tomograms covered all sections of Creighton Mine below 5,000 feet of depth.

From the four time periods, a well-defined zone of interest is consistently shown from approximately 6,500 feet to 7,800 feet of depth. This zone of interest includes a massive low velocity bulb with high velocity lobes on south eastern and north western sides of the low velocity bulb. The low velocity bulb with high velocity lobes is shown by isosurfaces, presented in Figure 3.9. The low velocity bulb is represented by the blue isosurfaces with the high velocity bulb is represented by the red isosurfaces. All isosurfaces and tomograms presented are in relation to depth, shown as a blue axis, and easting or nothing, shown as a red or green axis, respectively. All axes are in feet.

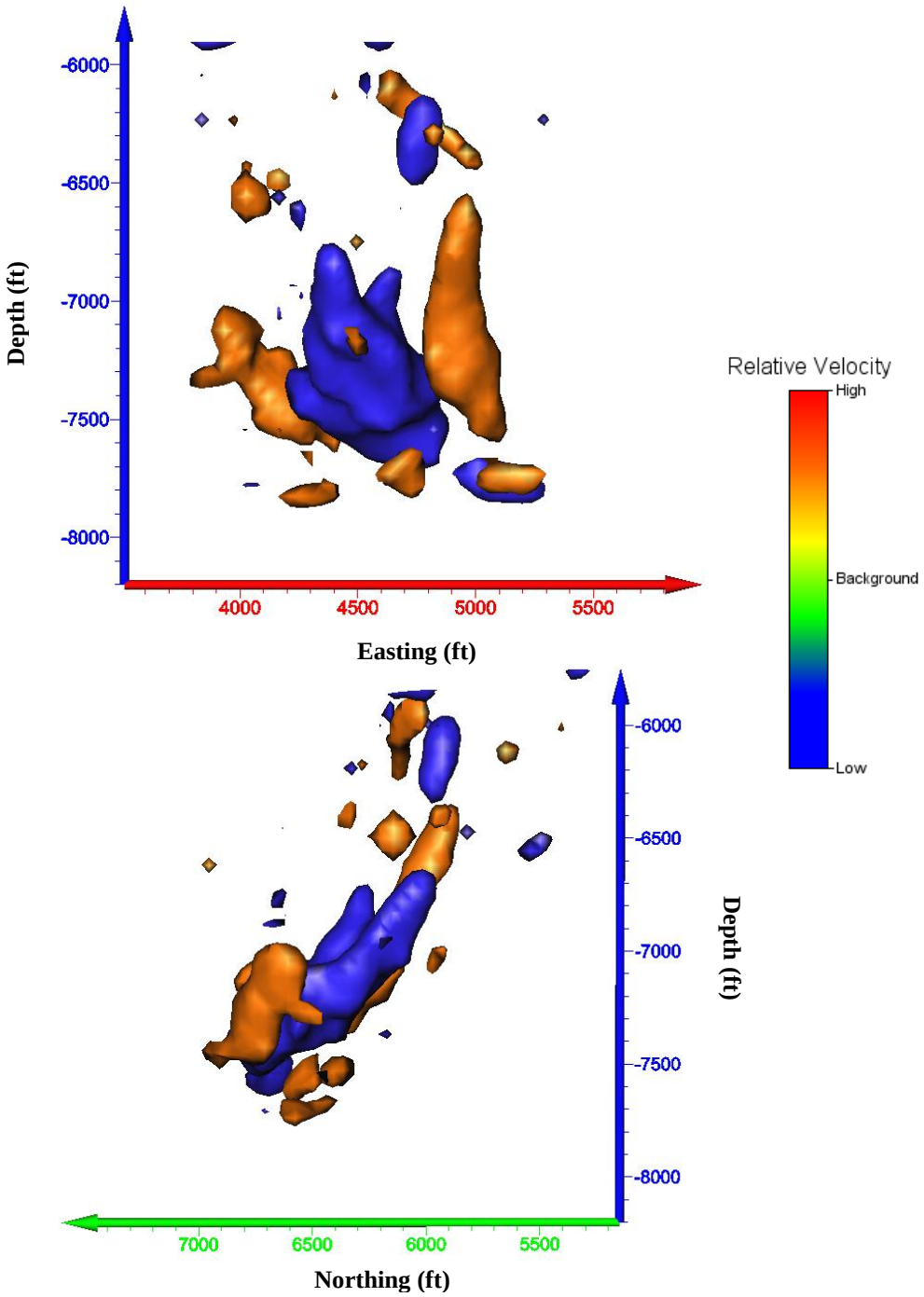

Figure 3.9: Mine scale imaging that shows a low velocity mass with high velocity lobes in relation to the easting, northing and depth. The top image is a XZ oriented isosurface image while the bottom image is an YZ oriented isosurface.

It is to be expected that the previously mined material would have a low velocity, as only weak, unconsolidated backfill material remains; this is demonstrated by the low velocity bulb. The low velocity bulb shown is located in the same orientation and progression through depth as

the orebodies at Creighton Mine. Various smaller low velocity zones shown from the four time periods are consistent with previously mined stopes outside of the main orebody.

The high velocity lobes located to the southeast and northwest of the low velocity zone is also to be expected at Creighton Mine. Previous numerical modeling conducted at Creighton Mine shows that the previously mined, low stressed, zone would be surrounded by higher stressed conditions in an increased microseismic zone. In addition, the high velocity lobes correlate well to the direction of the major principal stresses, which was previously recorded as running from east to west.

Aside from the low velocity bulb with high velocity lobes, observations from the mine scale imaging indicate that the deepest low velocity zone, located at approximately 7,700 feet of depth corresponds to Stope 5078. Stope 5078 is located within the bounds of the low velocity zone with a high velocity lobe above the stope. The high velocity above the stope is a unique occurrence at Creighton Mine, as most stopes have previous mining above. However, the mining sequence along Drift 7680 was altered due to a split in the orebody, placing Stope 5078 below an un-mined, higher stress zone. The low velocity zone representing Stope 5078 with the high velocity above the stope is shown in Figure 3.10.

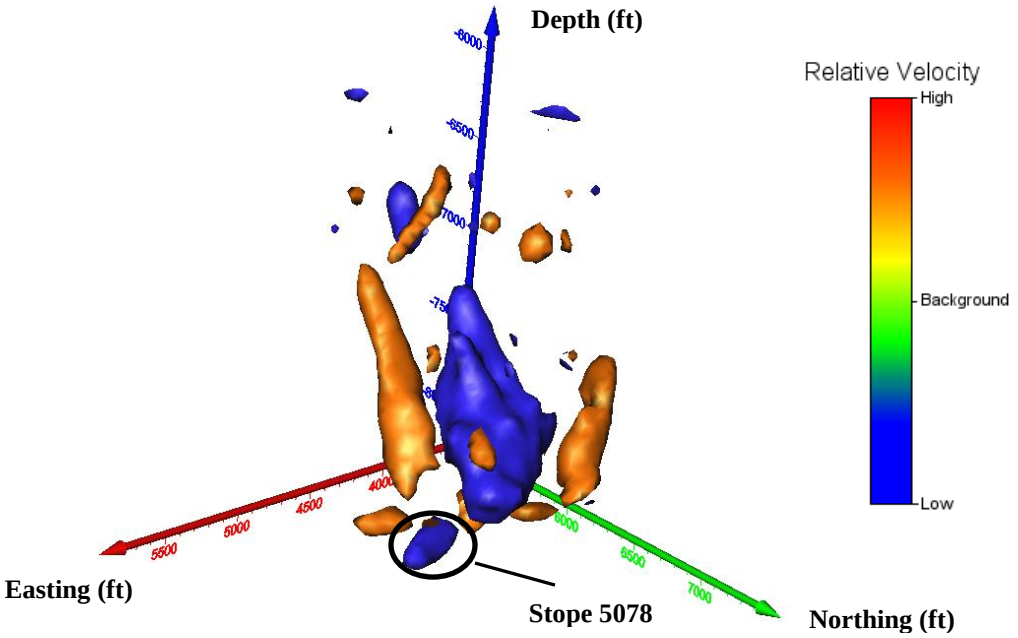

Figure 3.10: Low velocity zone for Stope 5078 with high velocity above. The image is an isosurface taken at an approximate negative 45 degree angle in the Z direction.

In comparison to the four time periods, the twenty time period tomograms are consistent with one another and show the previously mined low velocity zone. Unlike the four time periods

however, several of the twenty tomograms show the low velocity zone extending further above the 6,800 to 7,500 feet of depth zone. In addition, the high velocity lobes do not present themselves in the twenty time periods; various time periods show high velocity zones, but none can be correlated to the high velocity lobes.

While the same data set was used for both mine scale imaging scenarios, results were slightly different. These differences most likely occur due to significantly fewer events being used in each of the twenty time periods compared to the four time periods. Furthermore, the events included in the four time periods have the most number of source and receiver pairs of P wave arrival times whereas the twenty time periods utilize all P wave arrival times. The increased number of pairs utilized can lead to differing results due to the additional variety of ray paths to evaluate per node.

The two mine scale analyses conducted showed some similarities and some differences. The modeling of expected occurrences, such as the low velocity bulb with high velocity lobes and the isolated low velocity zone of Stope 5078, made the mine scale imaging a calibration tool for further analyses. Both the stope and event cluster imaging were accomplished using various input files for the tomographic inversion after the mine scale imaging showed expected results.

3.6.2 - Stope Scale Imaging

The small scale imaging of the stopes provided tomograms for a small, specific area of Creighton Mine. These specific areas cover an approximate 250 foot radius in the Easting, Northing, and Depth directions from the center of Stopes 5078 and 4448. Each stope analyzed used ten time periods, covering the two month data set provided.

Stope 5078 was the first of the two stopes imaged. Background velocity readings were observed from the tomograms for the majority of the ten time periods. All ten of the time periods had DWS coverage around the stope.

Though the majority of the tomograms were of background velocity, several time periods indicated low velocity readings located in the stope. Low to no velocity readings are to be expected in a stope during production as the material is unconsolidated and loose during production. The time periods that indicate low velocity readings inside the stope are typically time periods following blasts, as expected; blast events were not considered separately.

In addition to low velocity readings within the stope, the ten tomograms show a well-defined low velocity migration. This migration begins below Stope 5078 to the south and

advances through the stope and above the stope towards the north. Figure 3.11 is the first five of the ten time periods for Stope 5078, showing the low velocity readings in stope and the low velocity migration. Figure 3.12 is the final five time periods for Stope 5078. The time periods are arranged left to right, top to bottom with time period one being the first image in the series; all images are in the YZ plane. All images are taken at the Stope 5078 midpoint and show Stope 5078. Appendix D includes larger YZ plane images as well as XZ plane images for Stope 5078.

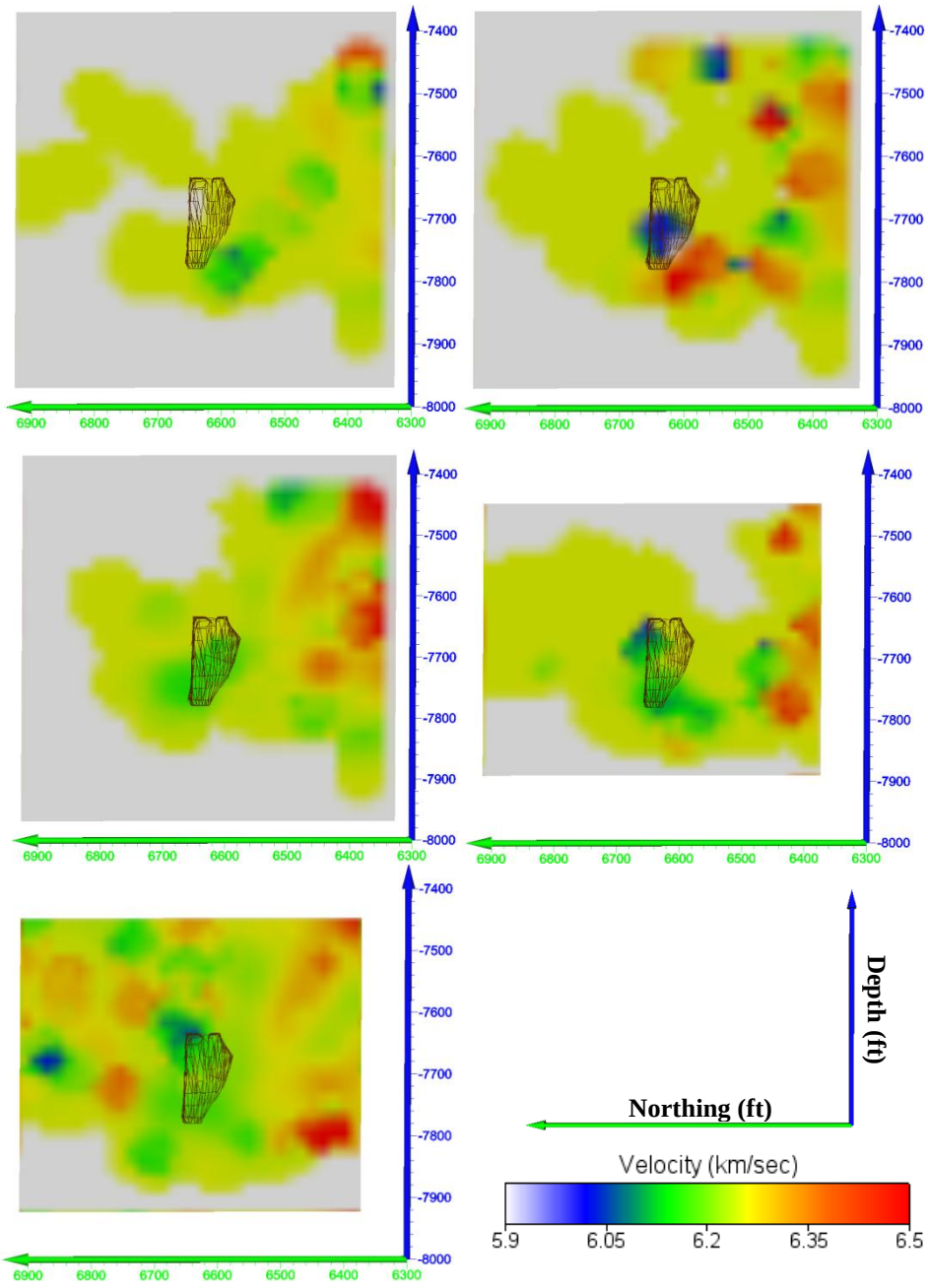

Figure 3.11: Tomograms of the first five time periods for Stope 5078. All tomograms are in the YZ plane located at mid-stope, approximately 5080 East.

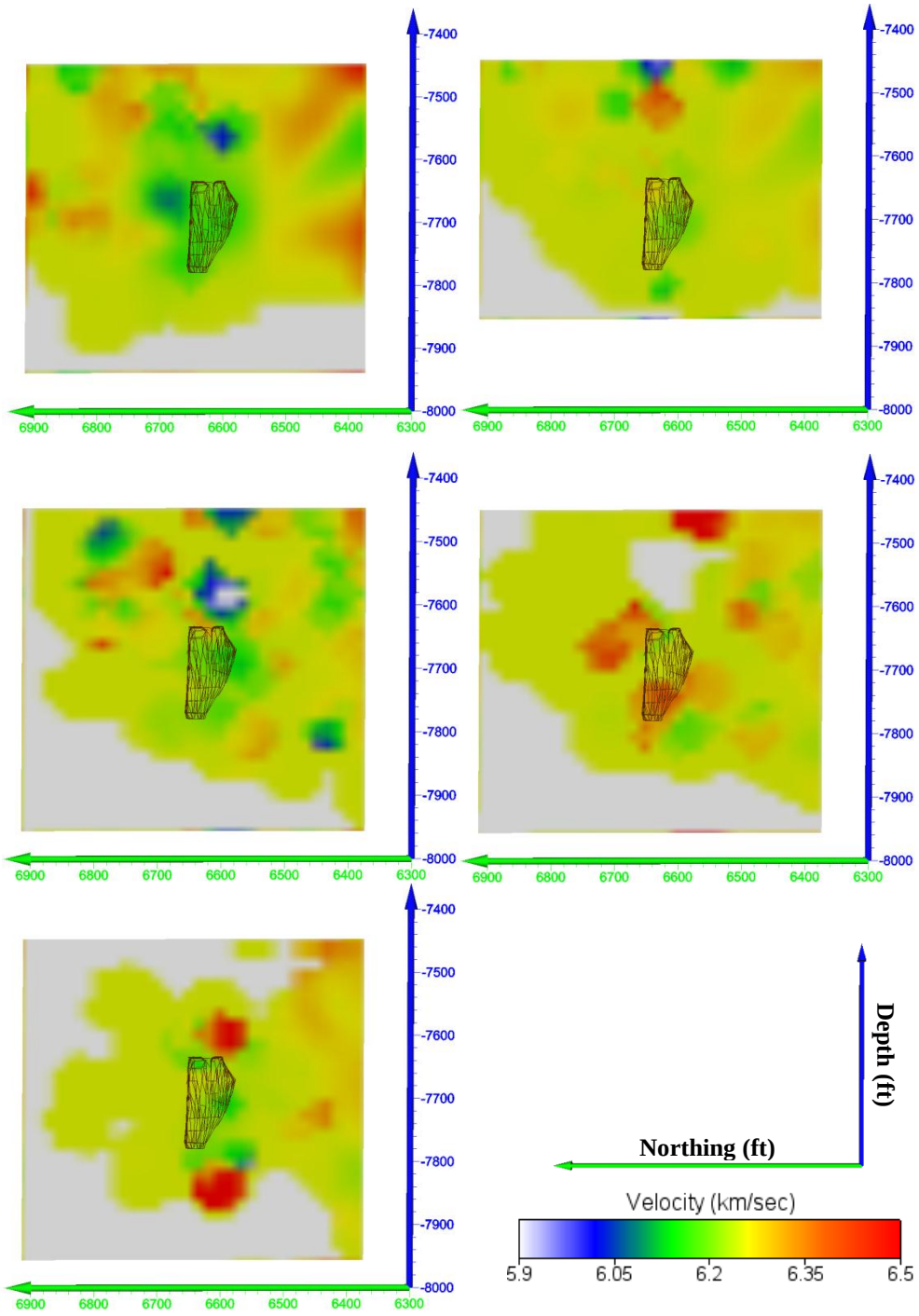

Figure 3.12: Tomograms of the final five time periods for Stope 5078. All tomograms are in the YZ plane located at mid-stope, approximately 5080 East.

During the sixth time period for Stope 5078, a large production blast of nearly 15,000 pounds, occurred. The tomogram of the sixth time period, shown in Figure 3.12, shows that, generally, there is lower velocity near the stope, with any high velocity readings occurring away from the stope. This can be expected at an underground metal mine, with the general area where

mining occurs to have stress relieved after mining, thus placing more stress at rock mass bounds. In conjunction, the seventh time period shows very little activity in regard to velocity change, which is expected; following a production blast at Creighton Mine, the area experiences elevated seismicity, but quickly diminishes to a lower amount due to the relaxed nature of the material and the rock mass returning to normal conditions.

The final time period observed related to Stope 5078 depicted areas of high velocity above and below the stope, with a small area of low velocity also below the stope. The higher velocity readings could be attributed to the increase in microseismic events near the viewing area. Approximately 80% of the events from the data set, per time period, were located more than 800 feet from Stope 5078, but the final time period had a higher amount of events located within 800 feet of the stope. Moreover, the low velocity with high velocity located below the stope is a common stress condition observed at Creighton Mine.

Beyond observations around mid-stope cross sections, another unique result observed was a common area of low velocity. During all but three of the time periods, areas of low velocity occur around the 7,810 foot level. These low velocity regions all correspond to Drift 7810, with the low velocity occurring both in and around the drift openings. While drifts have no material and could be considered locations for zero velocity readings, the size of a drift in relation to node spacing and coverage area would allow for a drift to be viewed as low velocity. Figure 3.13 shows the low velocity area in relation to Drift 7810.

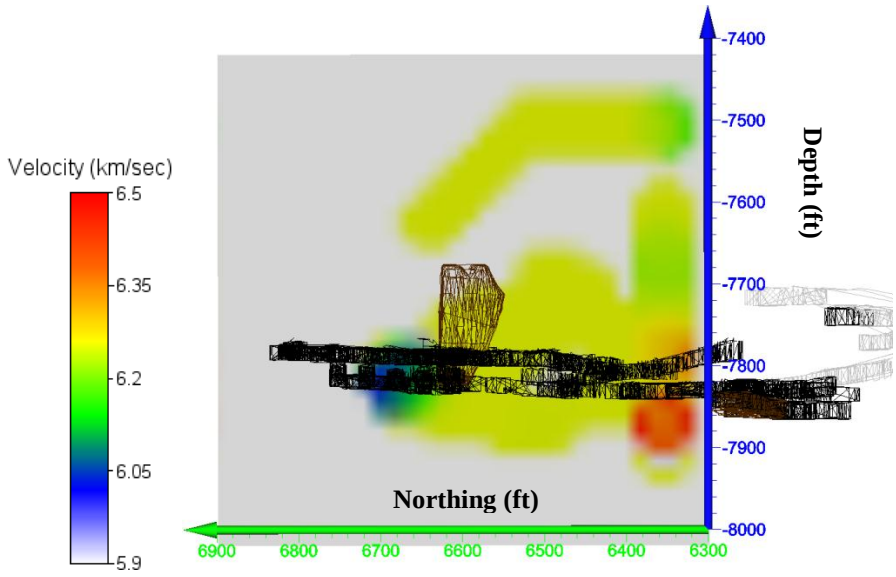

Figure 3.13: Low velocity in relation to Drift 7810 during the fifth time period. The tomogram is shown in the YZ plane, taken at approximately 5200 East.

To provide a comparison to the results observed at Stope 5078, Stope 4448 was analyzed. Stope 4448 had more coverage throughout the imaging zone than Stope 5078, however during three time periods the DWS coverage around the stope sporadically goes to zero. Similar to Stope 5078, the majority of the area shown by tomograms was of background velocity readings.

Mid stope tomograms of Stope 4448 are much more random than tomograms of Stope 5078. There are no location and velocity readings that are consistent through all ten time periods. However, west of the stope, the tomograms change during each of the first five time periods. The final five time periods also have numerous time period to time period changes, but it is not isolated to the western side of the viewing area. The drastic velocity changes occurring around Stope 4448 can be attributed to the high frequency of blasting during the first five time periods; 10 blasting events occurred from January 15 to February 14. All mid stope tomograms of the ten time periods, both XZ and YZ directions, of Stope 4448 are located in Appendix E.

Likewise, with the randomly changing velocities throughout the Stope 4448 imaging zone, most of the changes that occur are between the Drifts 7530 and 7680, or parallel to the stope. The changes that occur parallel to the stope occur more during the first six time periods while there is blasting occurring. While the velocity changes appear random, the increased presence of blasting can explain the amount of velocity changes throughout the zone. The rock mass undergoes various fluctuations due to blasting, and an increased number of blasts in a central location can lead to seemingly random velocity dispersions.

Similar to Stope 5078, a large production blast occurred during the sixth time period in Stope 4448. This production blast was 9,000 pounds. Following the 9,000 pound blast, numerous microseismic events were triggered within 500 feet of the stope. The close proximity of events to the viewing area, in addition to the amount of events, can lead to several areas of observable velocity change. Figure 3.14 shows the velocity changes during the sixth time period at mid stope in the YZ direction. The majority of velocity changes occur to the south of the stope in the footwall. Observing events in the footwall is a typical experience at Creighton Mine, thus rock mass changes could be observed through velocity changes during periods of elevated event frequency.

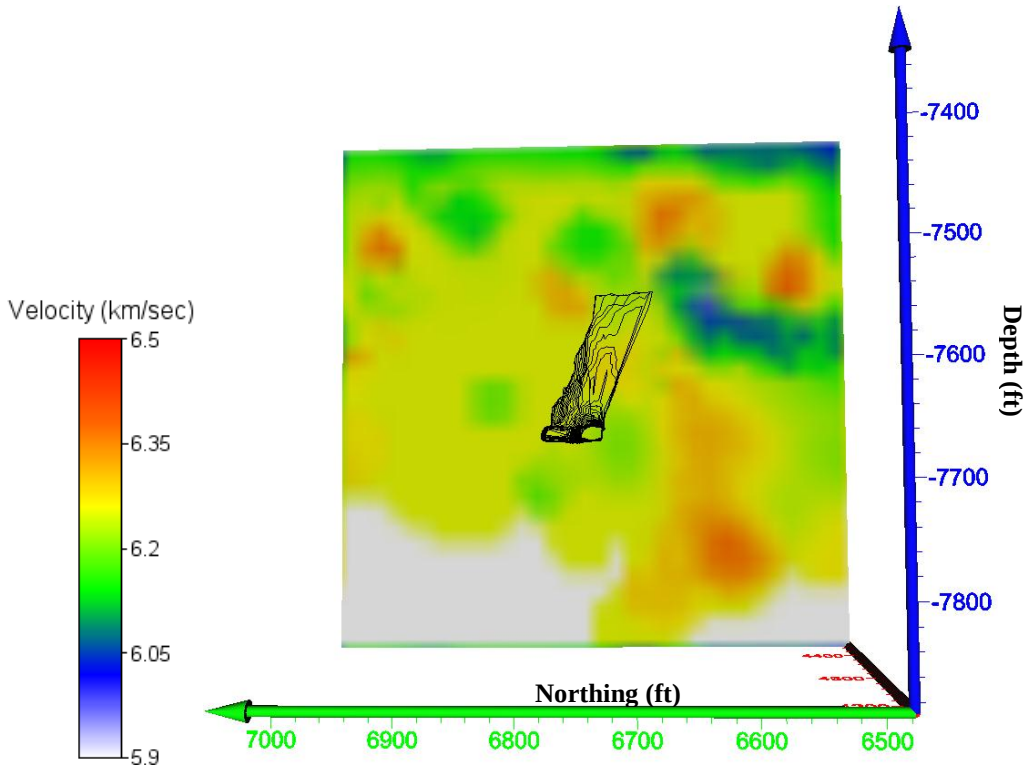

Figure 3.14: Numerous changes in the tomogram in the sixth time period of Stope 4448. The tomogram is shown in the YZ plane, taken at mid-stope, approximately 4450 East.

Comparable to the time period following the large blast in Stope 5078, Stope 4448 experienced a period of relaxation in the rock mass also. Other observations similar to those in Stope 5078 include two time periods that show low velocity in drifts and the stacked low velocity, high velocity below the stope. The comparable results yielded from both stopes are expected occurrences at Creighton Mine.

While the similar results obtained from the two stopes demonstrate the consistency of double-difference tomography, there were clear differences in the results. These variances are expected as the stopes are inherently different. Beyond the obvious differences, such as location and size of the stope, a significant difference that could affect change in tomograms is the location and clustering of events in relation to the stopes. The vast dissimilarities between the two stopes' results motivated further research into how event clusters can change tomograms.

3.6.3 - Stope Scale Imaging for an Event Cluster

With results and analysis from both the mine and stope tomograms for guidance, stope scale imaging for an event cluster was performed. Two groupings of above zero magnitude events were evaluated to determine their effects on a rock mass. Table 3.5, below, shows the

microseismic events used for each cluster; the table consists of a northing, easting, and depth coordinate as well as the moment magnitude and date of the event. These groupings include a before, during, and after the events time periods for each grouping set. The time period depicting the after conditions for grouping one also acts as the time period showing the before conditions for grouping two.

Table 3. 5: Coordinates and magnitudes for the above zero magnitude events used in clusters.

	Date	Northing	Easting	Depth	Magnitude
Cluster One	1/26/2009	6,729	4,361	-7,710	0.02
	1/27/2009	6,694	4,377	-7,695	0.05
	1/29/2009	6,710	4,352	-7,679	0.27
	1/31/2009	6,693	4,373	-7,604	0.03
Cluster Two	2/7/2009	6,724	4,333	-7,603	0.12
	2/11/2009	6,652	4,364	-7,668	0.1

The tomograms depicting the conditions prior to the cluster of events were the first time period and third time period. Both groupings of events show similar results from the tomograms. While the majority of the tomograms prior to the events show background velocity, the area surrounding the events has numerous high and low velocity regions, with the majority being of high velocity. A high velocity indication prior to an event is an anticipated occurrence, as it is common for seismic events to occur in a highly stressed zone.

However, a well-defined low velocity region exists between the future event locations in the east to west direction that would not be expected prior to large events. This low velocity region may have been formed due to prior seismic events that were precursors to the above zero magnitude events. Figure 3.15 is the tomograms for the time periods prior to the large events occurring that show the low velocity between events as well as the high velocity surrounding the event area in the YZ plane. In Figure 3.15, the tomograms are shown left to right, with the first grouping of events shown first. YZ and XZ images for before cluster of events are shown in Appendix F.

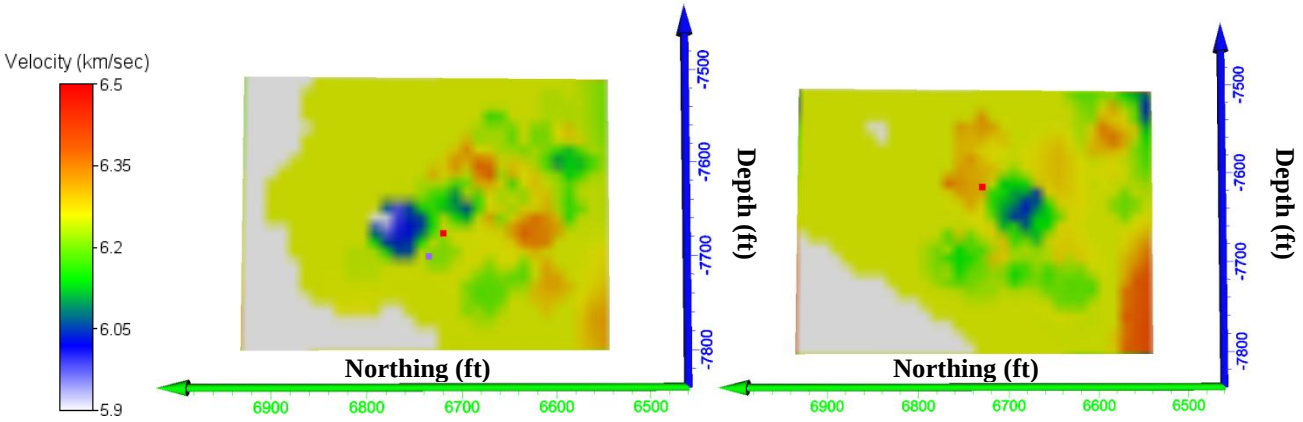

Figure 3.15: Tomograms of the time periods prior to seismic events. Grouping one is shown on the left and grouping two shown on the right. Both tomograms are in the YZ plane with grouping one at approximately 4360 East and grouping two at approximately 4340 East.

The tomograms depicting the conditions during the events were the second and fourth time periods. These tomograms were exceedingly similar to one another, and were consistent with expected results. Both tomograms were dominated by high velocity regions. The location of high velocity readings was also uniform, with both groupings of events showing high velocity concentrations below and to the south of the events in the footwall. In addition, in the XZ direction, high velocity is shown from above the events to the west, continuing through the events to below and east of the events. Figure 3.16 is the tomogram of the time period during the grouping one events in the XZ direction showing the high velocity band spanning the tomogram.

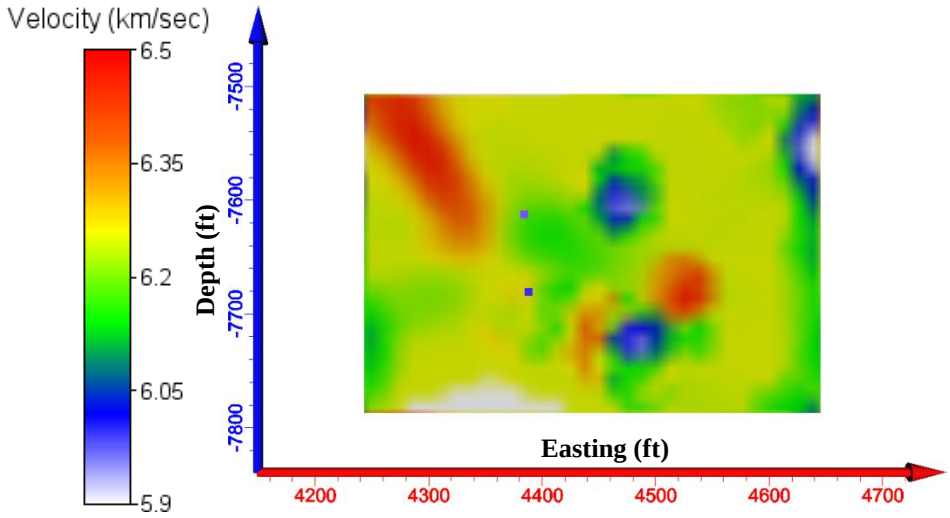

Figure 3.16: Tomogram of the time period during the grouping one events, depicting the high velocity that is present in both event groupings. Tomogram is in the XZ plane at approximately 6700 North.

As shown from Figure 3.6 in addition to the presence of high velocity, there are numerous low velocity regions. Both the high and low velocity regions are consistent with likely results. During periods of high seismic activity, local areas will become less stressed as the events occur due to rock mass relief, causing other locations to become more stressed. Locations for the high and low velocities will be different depending on local geology.

Figure 3.17 is the tomograms for the time periods during the large events that show the presence of both high and low velocities in the YZ plane. In Figure 3.17, the tomograms are shown left to right, with the first grouping of events shown first. YZ and XZ images during the events are shown in Appendix F.

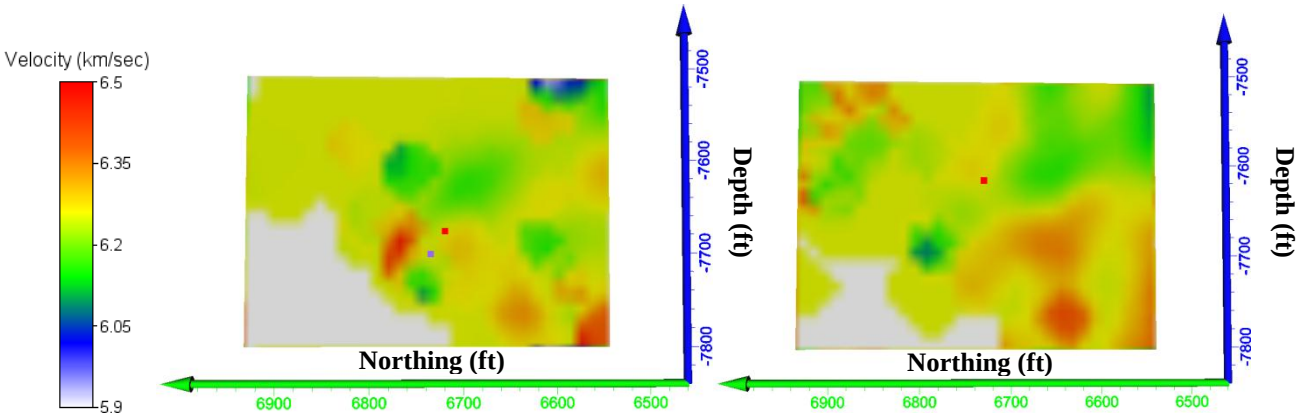

Figure 3.17: Tomograms of the time periods during the seismic events. Grouping one is shown on the left and grouping two shown on the right. Both tomograms are in the YZ plane with grouping one at approximately 4360 East and grouping two at approximately 4340 East.

The tomograms depicting the conditions after events with above zero magnitudes were from the third and fifth time periods. The third time period also acted as the time period prior to the group two events. Overall, the time periods have a random distribution of high and low velocity occurrences. However, some common occurrences between the two event groupings are the presence of non-background velocity around the event locations as well as high velocity zones appearing below and to the south of the events.

Typically seemingly random velocity distributions are not a promising observation, but after large events it can be expected that the rock mass is undergoing various changes. Knowledge of the site specific geology would assist a mine in determining the expected high and low velocity distribution. The high velocity zones to the south, like previous time periods, are likely results of the rock mass becoming more stressed due to the relaxation of the rock mass nearer the events.

Figure 3.18 shows the tomograms for the time periods after the large events that show the random distribution of high and low velocities, as well as the high velocity to the south of the events, in the YZ plane. In Figure 3.18, the tomograms are shown left to right, with the first grouping of events shown first. YZ and XZ images for after cluster of events are shown in Appendix F.

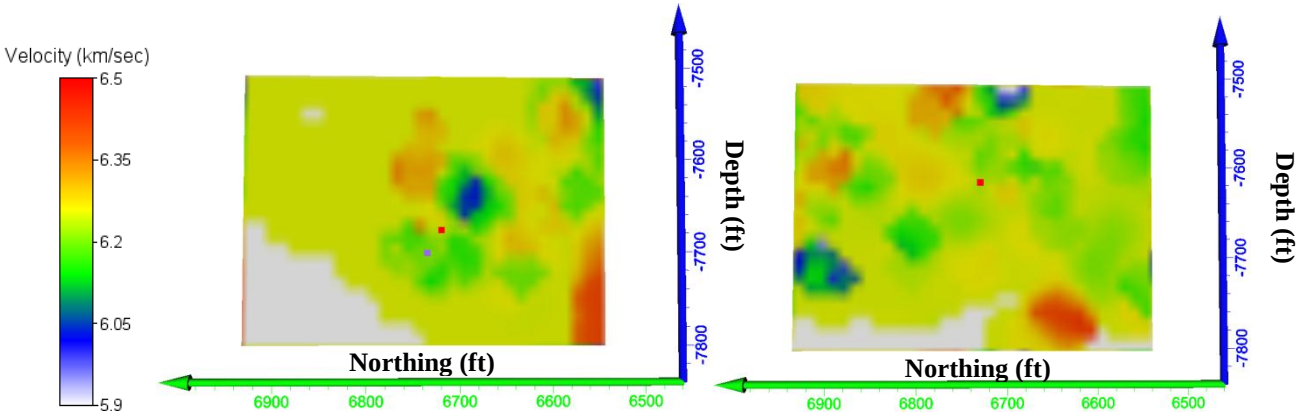

Figure 3.18: Tomograms of the time periods after the seismic events. Grouping one is shown on the left and grouping two shown on the right. Both tomograms are in the YZ plane with grouping one at approximately 4360 East and grouping two at approximately 4340 East.

With Figures 3.15 through 3.18 illustrating the similarities between the prior, during, and after event cluster tomograms, it is pertinent to visualize the progression of the event clusters in sequence to effectively utilize the event cluster tomograms. A distinct change in the rock mass is shown from the progression of the three tomograms. Initially, the rock mass shows higher velocities in the grouping region, with the rock mass undergoing changes to lower velocities in the grouping region following the events. The time period when the events occurred shows sporadic velocities in the grouping region.

The transition of the rock mass from high velocities to lower velocities following events is an expected occurrence as typically the rock mass becomes broken following events. Higher velocities on the bounds is expected following events also, as the broken rock mass is causing an increase in stiffness and stress away from the groupings. In addition, the sporadic velocities during the event cluster are also expected as typically large events cause a rock mass to change.

Figures 3.19 shows the progression of the first event grouping, beginning with time period one, ending with time period three. Figure 3.20 shows the progression of the second event grouping, beginning with time period three and ending with time period five. All images are shown in the YZ plane.

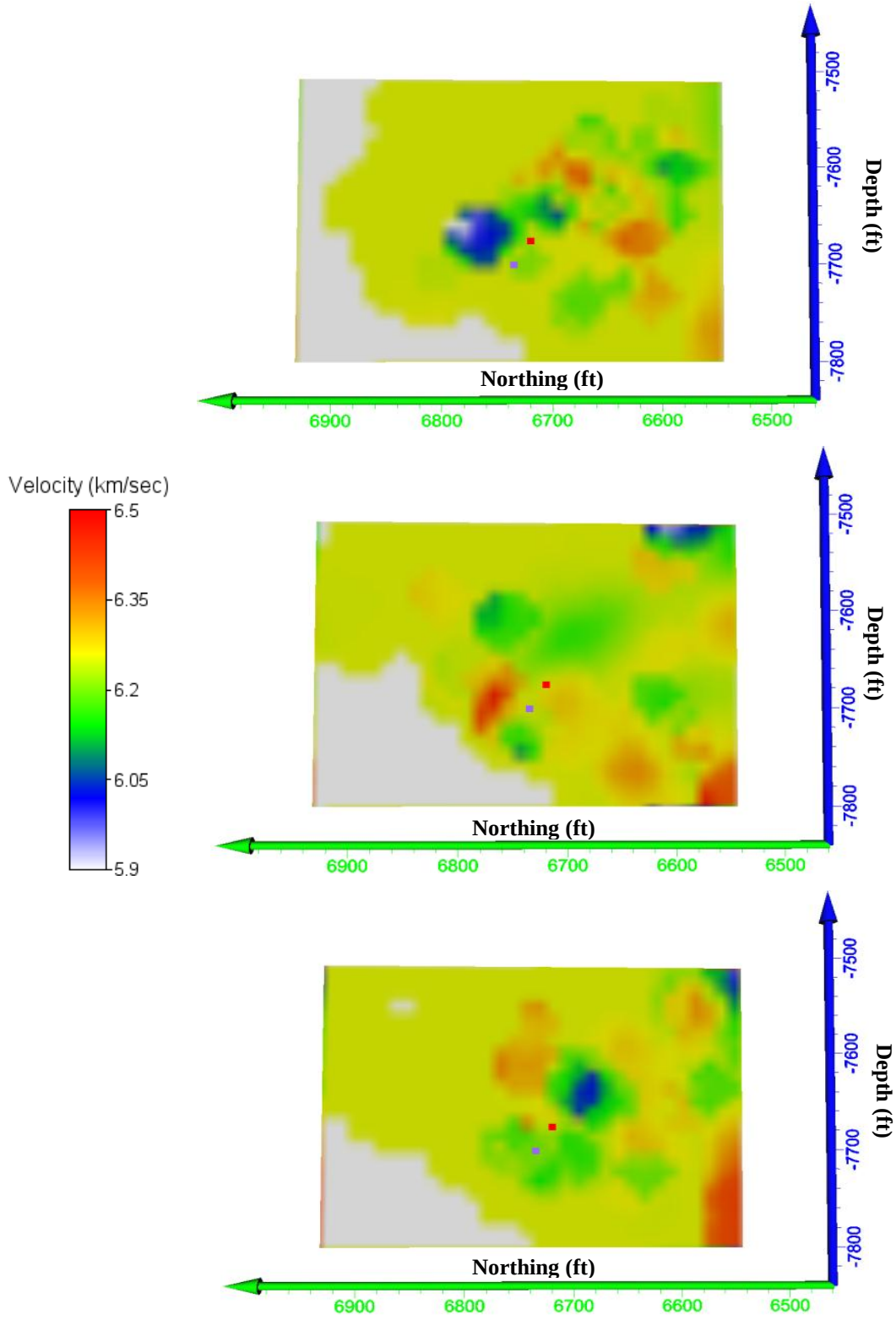

Figure 3.19: Tomograms for the first grouping of events. The top tomogram is of the first time period, the middle tomogram is of the second time period, and the bottom tomogram is of the third time period. All tomograms are in the YZ plane at approximately 4360 East.

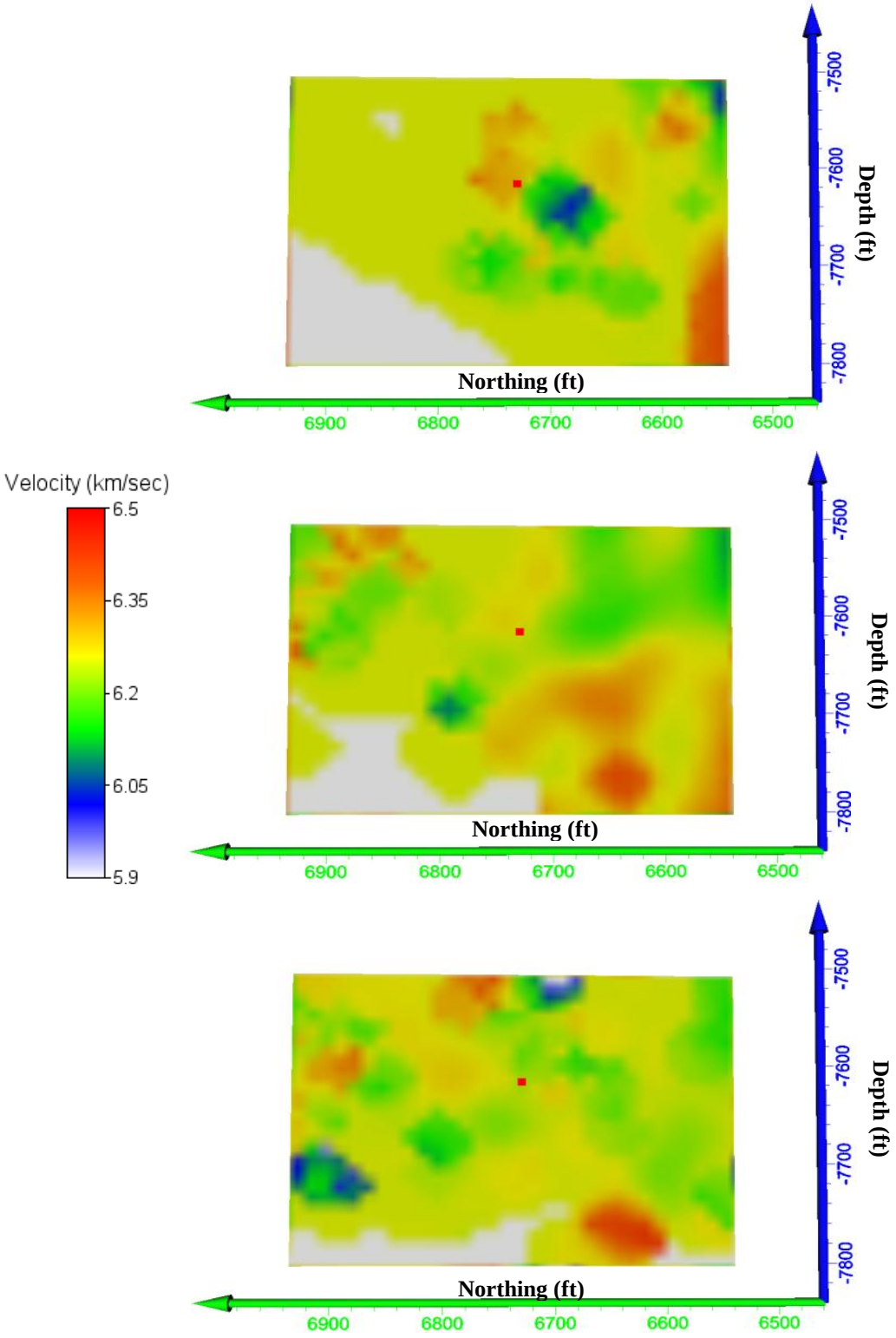

Figure 3.20: Tomograms for the second grouping of events. The top tomogram is of the third time period, the middle tomogram is of the fourth time period, and the bottom tomogram is of the fifth time period. All tomograms are in the YZ plane at approximately 4340 East.

To better visualize the changing velocities within the rock mass, Figures 3.21 and 3.22 show the differences of grouping one and two, respectively. Figures 3.21 and 3.22 are tomograms that show the difference of the rock mass after the groupings and prior to the groupings of events. These tomograms are shown as a relative change, with the scale indicating percent change in the velocity. Both images are shown in the YZ plane.

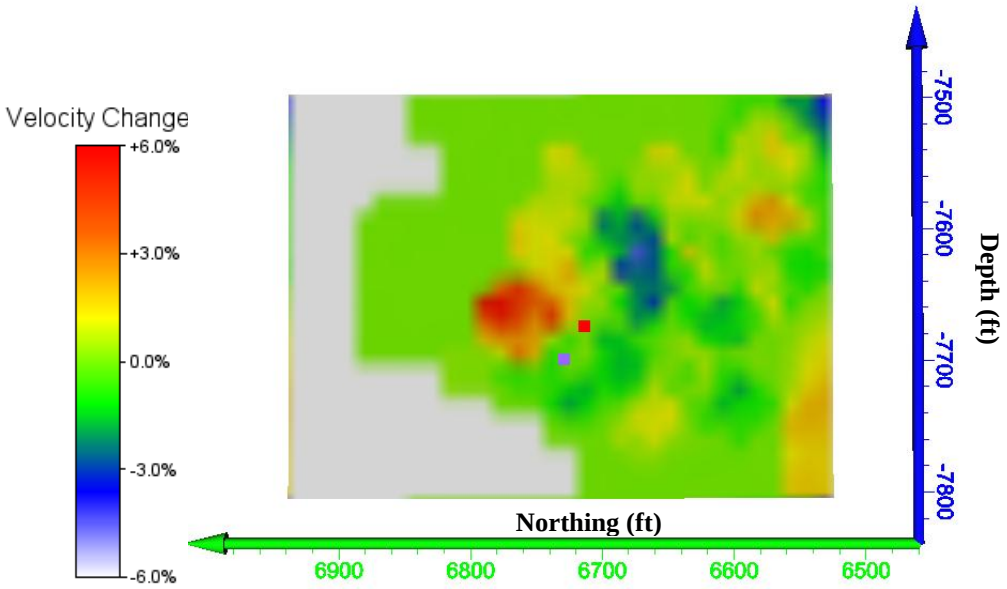

Figure 3.21: Differences in tomograms from the first grouping of events. Image was obtained by subtracting velocities of time period one from time period three. The tomogram is in the YZ plane at approximately 4360 East.

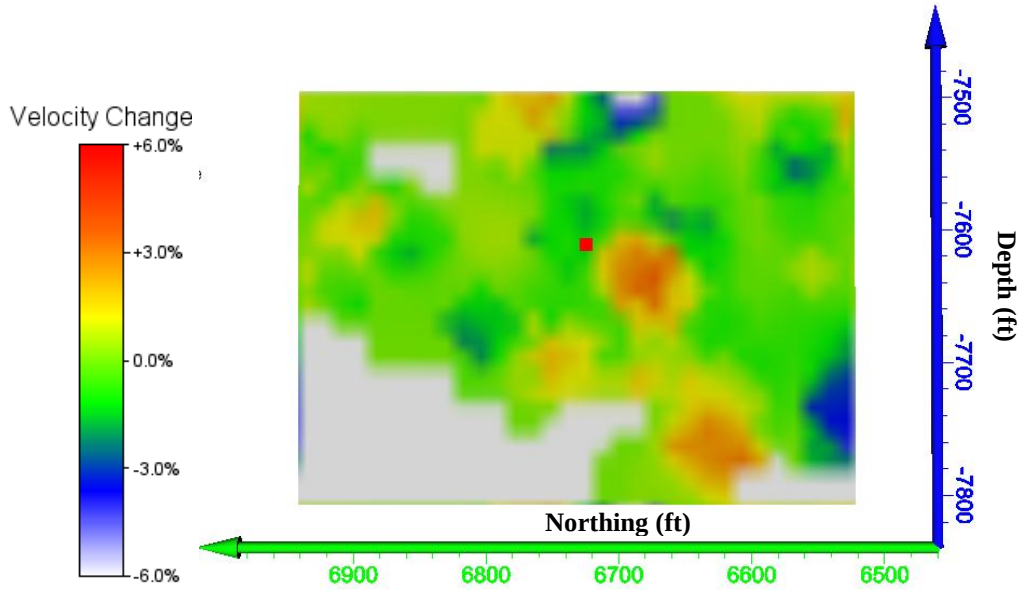

Figure 3.22: Differences in tomograms from the second grouping of events. Image was obtained by subtracting velocities of time period three from time period five. The tomogram is in the YZ plane at approximately 4360 East.

3.7 – Conclusions

The application of double-difference tomography was evaluated for uses in a deep metal mine. To evaluate the use of double-difference tomography three case studies were analyzed. In order to obtain an overall understanding of the mine site, and to calibrate the inversion process, tomograms for the entire mine below a depth of 5,000 feet were produced. With the inversion process calibrated, tomograms were produced over the scale of a single stope; Stope 5078 and Stope 4448 were the stopes used. Due to varying results from the tomograms of the two stopes, further stope scale tomograms were produced to determine the effect of groupings of events over a small area.

Many observed results obtained from the tomograms were compared to previous knowledge of mine conditions and expected stress redistribution at the mine site and found to be comparable. In addition, results were compared to widely known standard rock mass stress redistributions with similar results. Overall, the tomograms from the three different studies produced promising results in regards to the applicability of double-difference tomography in a deep metal mine.

In conclusion, data obtained from an in-place microseismic monitoring system can be used in a double-difference tomographic inversion for a deep hard rock mine. Double-difference

tomography produced consistent images along time periods, as well as correlating well to prior mine knowledge and common rock mass movements. It should be noted however, that not all results are necessarily due to changes in the rock mass; velocities shown in tomograms may have originated, and changed, due to geologic factors. Overall, results obtained from the studies at Creighton Mine are promising and provide a base evaluation for the applications of double-difference tomography in a deep hard rock mine.

3.8 – Future Work

With encouraging results from the three studies conducted with data from Creighton Mine demonstrating that there are prospective uses for double-difference tomography at a deep metal mine, the potential for future research exists. To further the understanding of uses of double-difference tomography for a deep metal mine, additional studies should be conducted on well-known mine geometries and geologies. In addition to known geometries and geologies, studies on accurately located, large magnitude events should be conducted to determine characteristics of an area prior to, and during, a single large event. With a baseline set of results for a mine site for well-known areas and events, further research should be conducted to determine the amount of events required to produce an accurate tomogram to determine the approximate time data required for an accurate tomogram. In addition to an approximate number of events and time needed to conduct a tomographic investigation, utilizing a time period of one day following a blasting event until the hour prior to the next blasting event of a stope could help determine effects on the rock mass from blasting events. All results from additional studies should be corroborated with personal observations either from the researcher or mine personnel.

For double-difference tomography to be of use for a deep metal mine, the goal for the method must be to implement it at the mine level. At the mine level, accurate tomograms generated with known local geology and mine geometry, could be used as hazard maps to show areas of seismic concern. While mine level hazard maps are applicable and will improve safety at the mine level, the long term goal for double-difference tomography is to be able to forecast future events at a mine site and thus provide a real time, or close to real time, warning system to alert miners of future dangers.

Chapter 3 References

Blum, P. (1997). P Wave Velocity. Physical Properties Handbook.

Caldwell, J. (2011). "Rock Burst." Retrieved September 7, 2011.

Caterpillar (2008). Vale Inco's Creighton Mine; Digging Deeper by the Day. Viewpoint: Perspectives on Modern Mining, Caterpillar Global Mining.

Got, J.-L., V. Monteiller, J. Virieux, S. Operto (2008). "Potential and Limits of Double Difference Tomographic Methods." Geophysical Prospecting 56: 477-491.

Gray, R. E. (1981). Accoustic Emissions in Geotechnical Engineering Practice, ASTM International.

Gutenberg, B., and C. F. Richter. "Frequency of Earthquakes in California." Bulletin of the Seismological Society of America 34 (1944): 185-88.

Malek, F., F.T. Surorineni, P. Vasak (2009). Geomechanics Strategies for Rockburst Management at Vale Inco Creighton Mine. 3rd CANUS Rock Mechanics Symposium. Toronto, Ontario, Canada.

Mark, C., A.T. Iannacchione (2010). Ground Control Issues for Safety Professionals. Pittsburgh, PA, NIOSH.

Moos, D., M.D. Zoback (1983). "In Situ Studies of Velocity in Fractured Crystalline Rocks." Journal of Geophysical Research 88(B3): 2345-2358.

Rawlinson, N., S. Pozgay, and S. Fishwick (2010). "Seismic Tomography: A Window into Deep Earth." Phys. Earth Planet. Int 178(3-4): 101-135.

Snelling, P. (2009). The Influences of Stress and Structure on Mining-Induced Seismicity in Creighton Mine, Sudbury, Canada. Department of Geological Sciences and Geological Engineering. Kingston, Ontario, Canada, Queen's University. Master of Science.

Song, L., H. Liu, S. Chun, Z. Song, S. Zhang (1998). "Mapping an Underground Rock Mass by Anisotropic Acoustical Transmission Tomography." Ultrasonics 36: 1009-1012.

Stoddard, E. (2011). Depth for South Africa's Gold Mines. Reuters. Carletonville, South Africa.

Trifu, C.I., F.T. Sourineni (2009). Use of Microseismic Monitoring for Rockburst Management at Vale Inco Mines. Sudbury, Ontario, Canada, Engineering Seismology Group: 12.

Urbancic, T., C. Trifu (2000). "Recent advances in seismic monitoring technology at Canadian mines." Journal of Applied Geophysics 45: 225-237.

Watanabe, T., K. Sassa (1996). "Seismic Attenuation Tomography and its Application to Rock Mass Evaluation." International Journal of Rock Mechanics, Mining Sciences, and Geomechanics 33(5): 467-477.

Westman, E. (2004). "Use of Tomography for Inference of Stress Redistribution in Rock." IEEE Transactions on Industry Applications 40(5): 1413-1418.

Wiles, T., P. MacDonald (1988). "Correlation of Stress Analysis Results with Visual and Microseismic Monitoring at Creighton Mine." Computers and Geotechnics 5: 105-121.

Zhang, H. (2003). Double-Difference Seismic Tomography Method and its Applications. Geophysics. Madison, WI, University of Wisconsin. Ph.D.

Zhang, H., C. Thurber (2006). "Development and Applications of Double-difference Seismic Tomography." Pure and Applied Geophysics 163: 373-403.

Zhang, H., C.H. Thurber (2003). "Double-Difference Tomography: The Method and Its Application to the Hayward Fault, California." Bulletin of the Seismological Society of America 93(5): 1875-1889.

Zhang, H., S. Sarkar, M.N. Toksoz, H.S. Kuleli, F. Al-kindy (2009). "Passive Seismic Tomography Using Induced Seismicity at a Petroleum Field in Oman." Geophysics 74(6): 57-69.

Chapter 4 – Summary of Results and Conclusions

4.1 – Summary of Work, Results, and Conclusions

The application of double-difference tomography was evaluated for its' use for a deep hard rock mine; reasonable tomograms, or tomograms that were consistent throughout time periods in addition to following expected patterns, were produced for the mine. The deep metal mine, Creighton Mine, located in Sudbury, Ontario, Canada, is currently operating at a depth of 7,800 feet. Over two months of microseismic data analyzed, Creighton Mine averaged approximately 150 events per day, as recorded by the Hyperion and Paladin microseismic monitoring systems from ESG. A total of 9,270 microseismic events occurred.

All events recorded were located below a depth of 5,000 feet and over a range of 3,500 feet in both the Easting and Northing directions. The majority of the microseismic events occurred in the footwall. Due to the relatively close proximity of all the events, all 9,270 events were used in determining a background velocity for Creighton Mine. The background velocity was determined to be 6.25 kilometers per second from a distance versus time plot.

To evaluate the use of double-difference tomography three case studies were analyzed. In order to obtain an overall understanding of the mine site, and to calibrate the inversion process, tomograms for the entire mine below a depth of 5,000 feet were produced; two event breakdowns were used for the mine scale tomograms, four time period and twenty time periods. With the inversion process calibrated, tomograms were produced over the scale of a single stope; Stope 5078 and Stope 4448 were the stopes used. Due to varying results from the tomograms of the two stopes, further stope scale tomograms were produced to determine the effect of groupings of events over a small area. The tomograms for both the stopes and event cluster were optimized through a process to determine the optimum weighting and damping values for the tomographic inversion, as well as the optimum number of iterations in the inversion.

Many observed results obtained from the tomograms were compared to previous knowledge of mine conditions and expected stress redistribution at the mine site, and were found to be comparable. In addition, results were compared to widely known stress redistributions in a rock mass with similar results. Results obtained from the mine scale tomograms that were comparable to previous knowledge include:

- The presence of a low velocity bulb with adjacent high velocity lobes to the southeast and northwest that represent the mined out ore bodies with adjacent seismically active zone.
- The high velocity zone located above Stope 5078 indicating the area above Stope 5078 is not mined out, which is a unique occurrence as this was a deviation from traditional mining sequence.
- Consistency between the four time periods and twenty time periods tomograms, both showing the mined out ore bodies.

Results obtained from the stope scale tomograms of Stopes 5078 and 4448 that were comparable to previous knowledge include:

- Low velocity located in the stopes, typically following blasting events from the stope.
- Lower than background velocity after blasting events indicate stress relief from the blasting.
- A return to background velocity across the majority of the tomograms following large production blasts of 15,000 and 9,000 pounds indicating the settling of the rock mass.
- Low velocity zones located in various parts of the drifts used to access stopes.

Results obtained from the stope scale tomograms of a cluster of events comparable to previous knowledge include:

- Prior to events occurring, elevated velocity (above background velocity) was observed in the locations of the future events.
- The time period that the events occurred shows the combination of lower velocity zones in the event locations, indicating a broken rock mass, with high velocity zones surrounding the low velocity, indicating the transfer of stress from the relaxed zone.
- The various locations of velocity differences from the previous time periods observed in the periods following the events indicates that the rock mass was undergoing various changes due to redistribution.

In conclusion, data obtained from an in-place microseismic monitoring system can be used in a double-difference tomographic inversion for a deep hard rock mine. Double-difference tomography produced consistent tomograms along time periods, as well as tomograms that correlated well to prior mine knowledge and common rock mass movements. It should be noted however, that not all results are necessarily due to changes in the rock mass; velocities shown in tomograms may have originated, and changed, due to geologic factors. Overall, the results

obtained from the studies at Creighton Mine are promising and provide a base evaluation for the applications of double-difference tomography in a deep hard rock mine.

4.2 – Future Work

With encouraging results from the three studies conducted with data from Creighton Mine demonstrating that there are prospective uses for double-difference tomography at a deep metal mine, the potential for future research exists. To further the understanding of uses of double-difference tomography for a deep metal mine, additional studies should be conducted on well-known mine geometries and geologies. In addition to known geometries and geologies, studies on accurately located, large magnitude events should be conducted to determine characteristics of an area prior to, and during, a single large event. With a baseline set of results for a mine site for well-known areas and events, further research should be conducted to determine the amount of events required to produce an accurate tomogram to determine the approximate time data required for an accurate tomogram. In addition to an approximate number of events and time needed to conduct a tomographic investigation, utilizing a time period of one day following a blasting event until the hour prior to the next blasting event of a stope could help determine effects on the rock mass from blasting events. All results from additional studies should be corroborated with personal observations either from the researcher or mine personnel.

For double-difference tomography to be of use for a deep metal mine, the goal for the method must be to implement it at the mine level. At the mine level, accurate tomograms generated with known local geology and mine geometry, could be used as hazard maps to show areas of seismic concern. While mine level hazard maps are applicable and will improve safety at the mine level, the long term goal for double-difference tomography is to be able to forecast future events at a mine site and thus provide a real time, or close to real time, warning system to alert miners of future dangers.

Appendix A – Stope 5078 Methods

Appendix A will include pertinent information used to create the resulting tomograms of the stope scale study for Stope 5078. The breakdown of the ten time periods will be illustrated initially, followed by plots to determine weighting (illustrated as smoothing) and damping, number of iterations, and the top 75% DWS cutoff value; the breakdown of the ten time periods is applicable to Stope 4448 also. All plots for a given time period will be introduced together, beginning with weighting and damping, followed by number of iterations, and ending with top 75% DWS cutoff value. On the top 75% DWS cutoff value plots, the histogram utilizes the primary Y axis while the cumulative percent line chart is plotted on the secondary Y axis.

Table A.1: Time period details for Stope 5078 and Stope 4448.

	Time Period Details – Stope 5078			
Period	**Start**	**End**	**Number of Days**	**Number of Events**
1	1/14/2009	1/17/2009	4	302
2	1/18/2009	1/24/2009	7	529
3	1/25/2009	1/31/2009	7	505
4	2/1/2009	2/7/2009	7	446
5	2/8/2009	2/14/2009	7	1245
6	2/15/2009	2/17.5/2009	2.5	1195
7	2/17.5/2009	2/21/2009	4.5	845
8	2/22/2009	2/28/2009	7	654
9	3/1/2009	3/7/2009	7	543
10	3/8/2009	3/13/2009	6	580

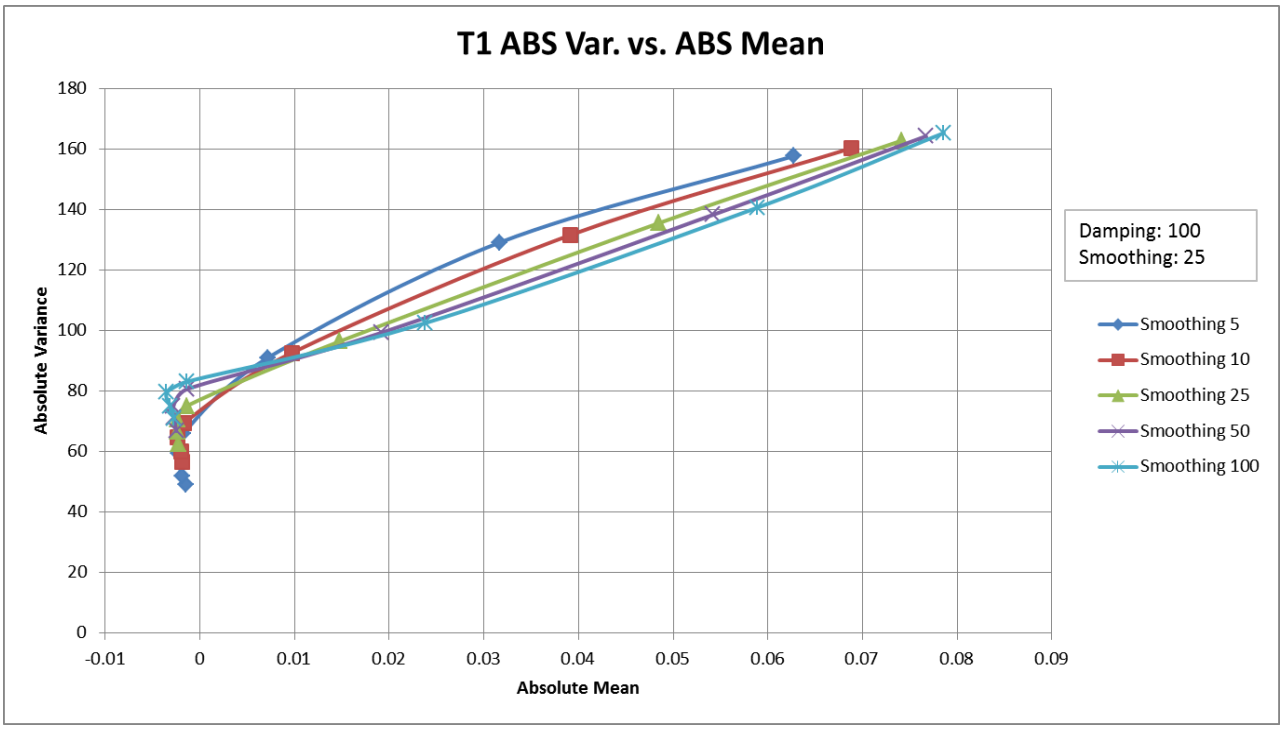

Figure A.1: Absolute variance versus absolute mean plot for Stope 5078's first time period.

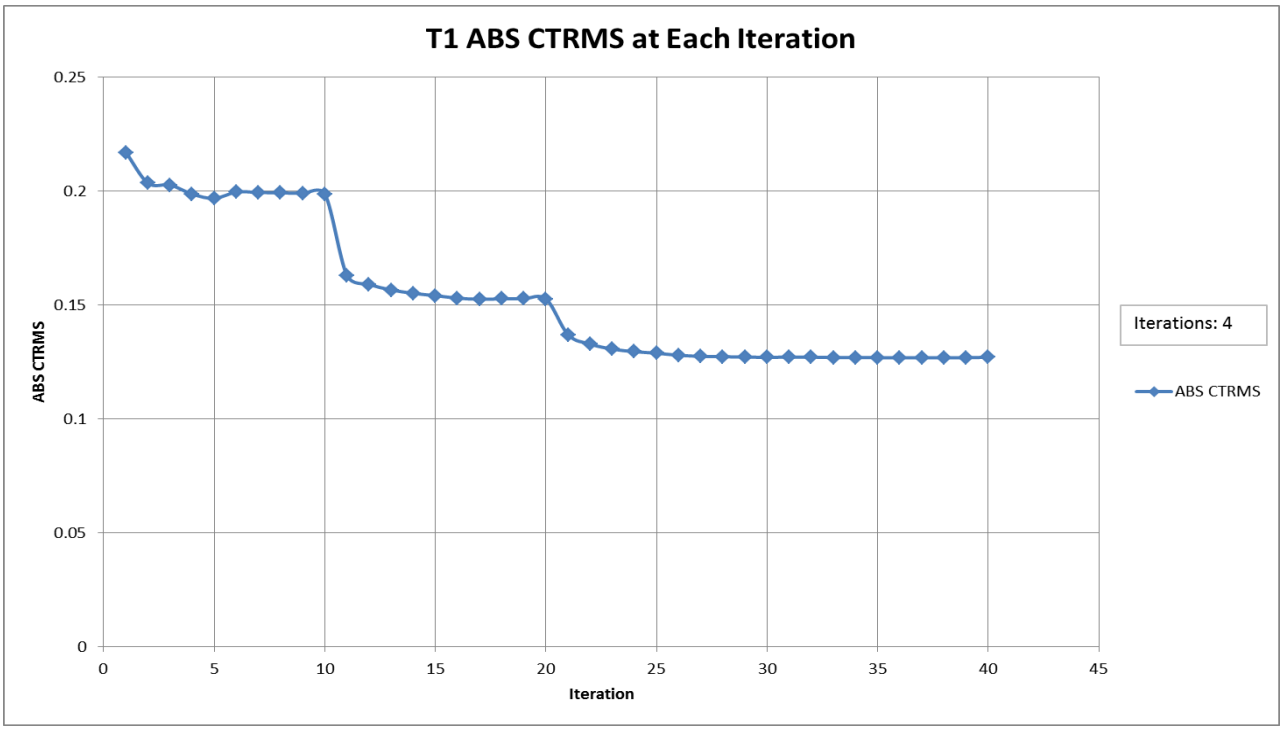

Figure A.2: Absolute CTRMS value for each iteration for Stope 5078's first time period.

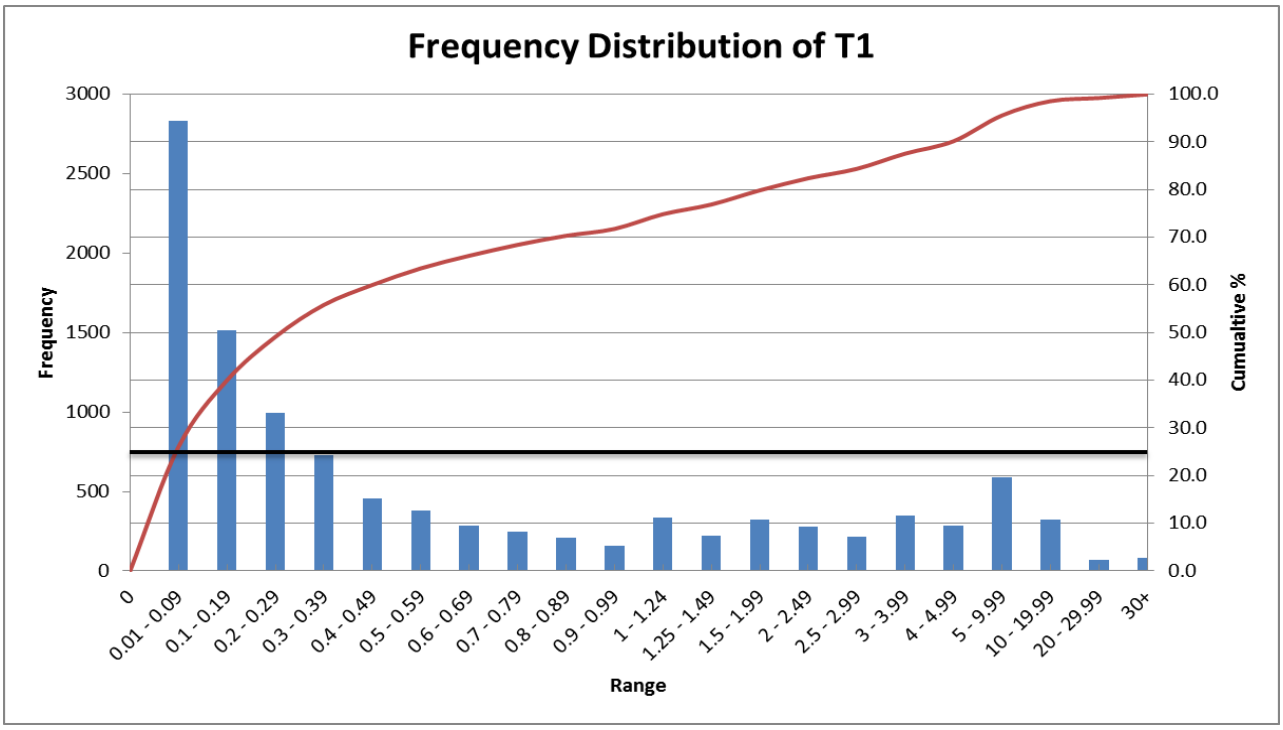

Figure A.3: Top 75% DWS cutoff value determination for Stope 5078's first time period.

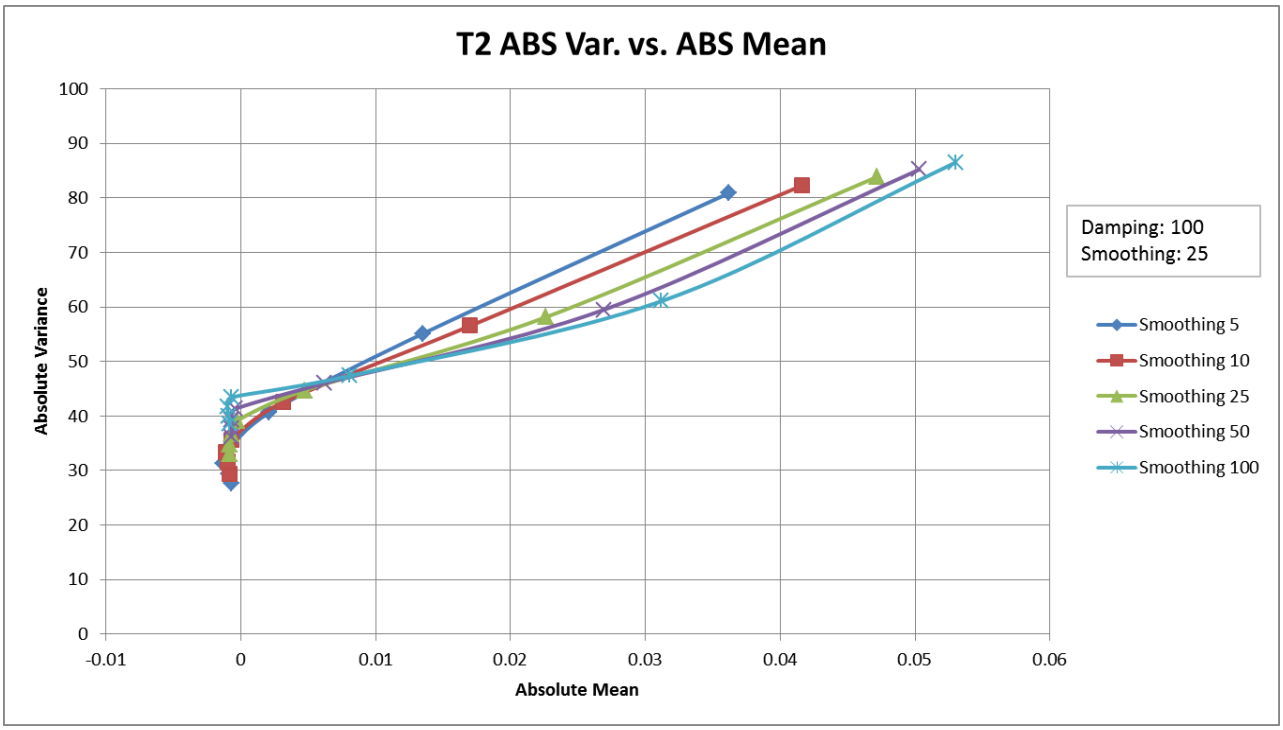

Figure A.4: Absolute variance versus absolute mean plot for Stope 5078's second time period.

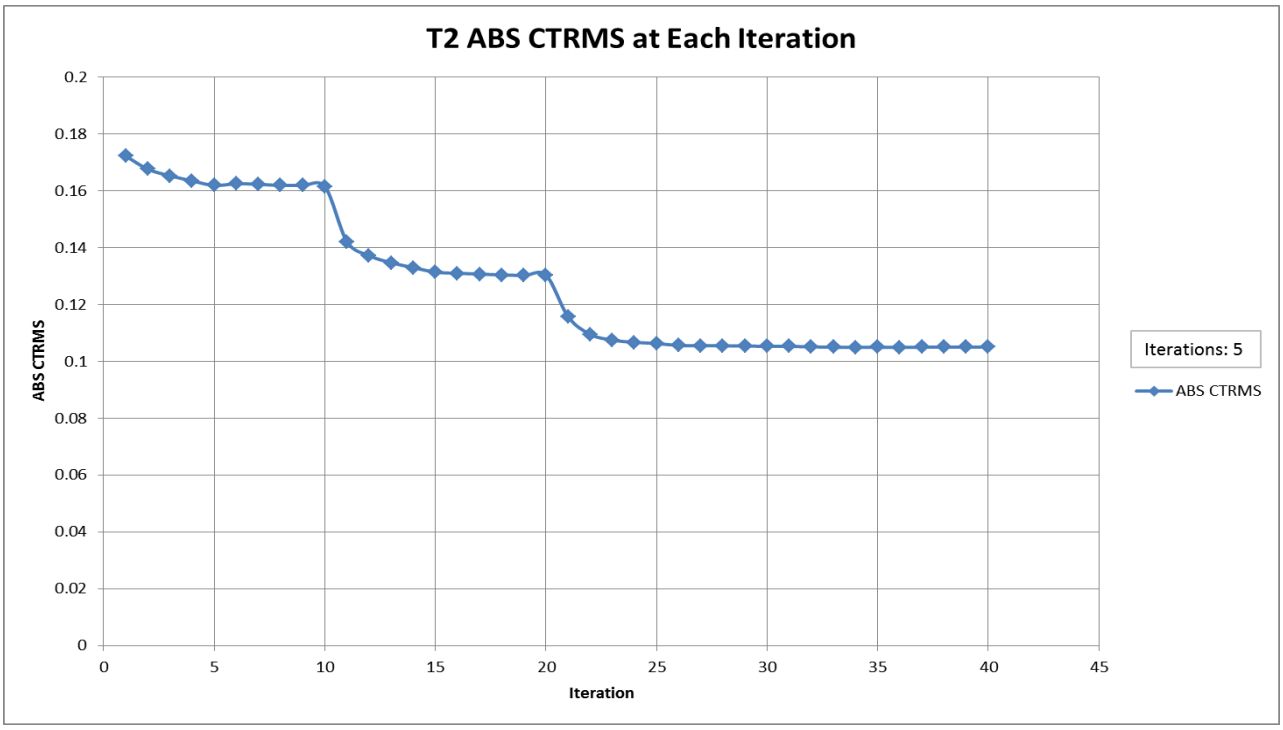

Figure A.5: Absolute CTRMS value for each iteration for Stope 5078's second time period.

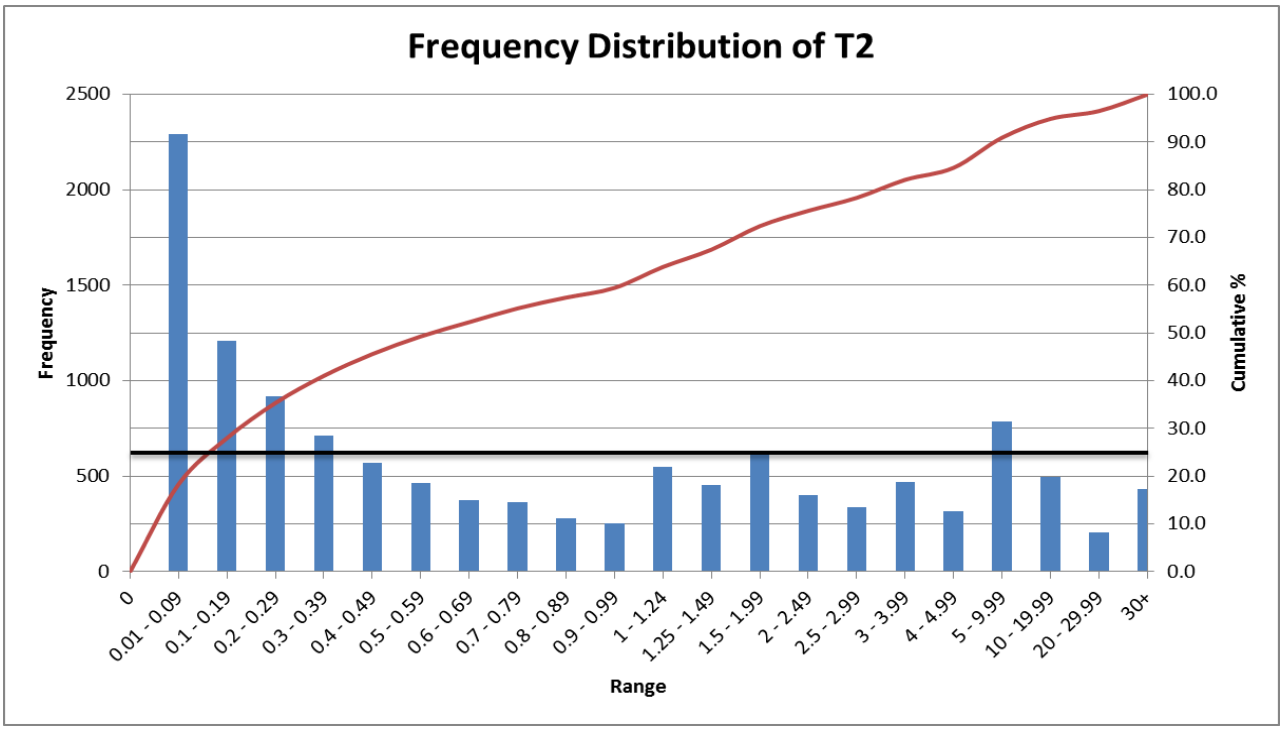

Figure A.6: Top 75% DWS cutoff value determination for Stope 5078's second time period.

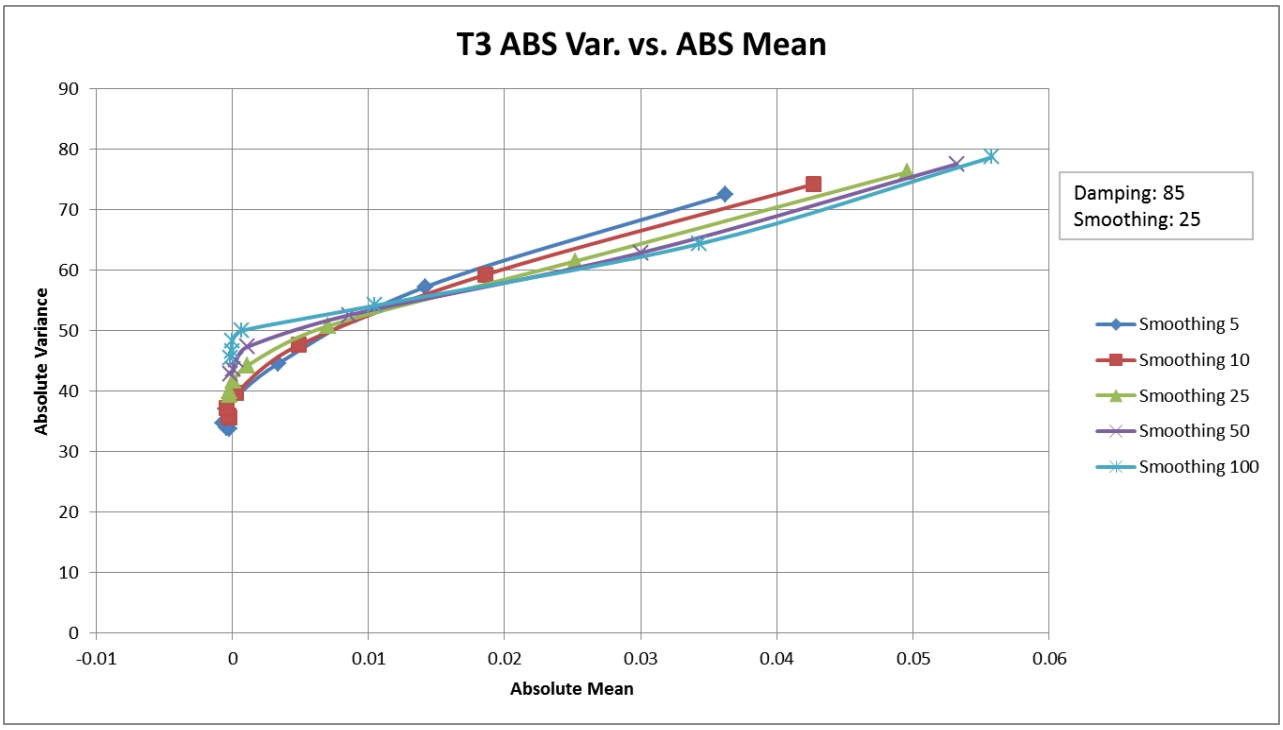

Figure A.7: Absolute variance versus absolute mean plot for Stope 5078's third time period.

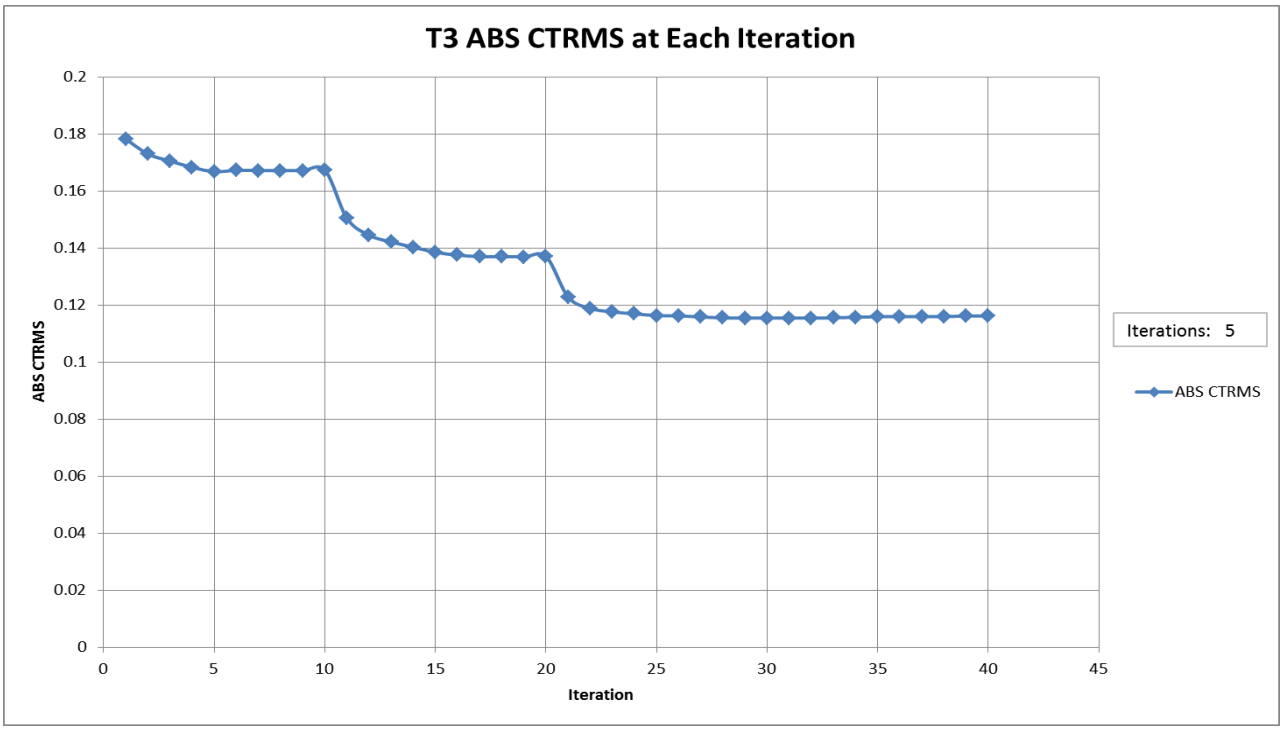

Figure A.8: Absolute CTRMS value for each iteration for Stope 5078's third time period.

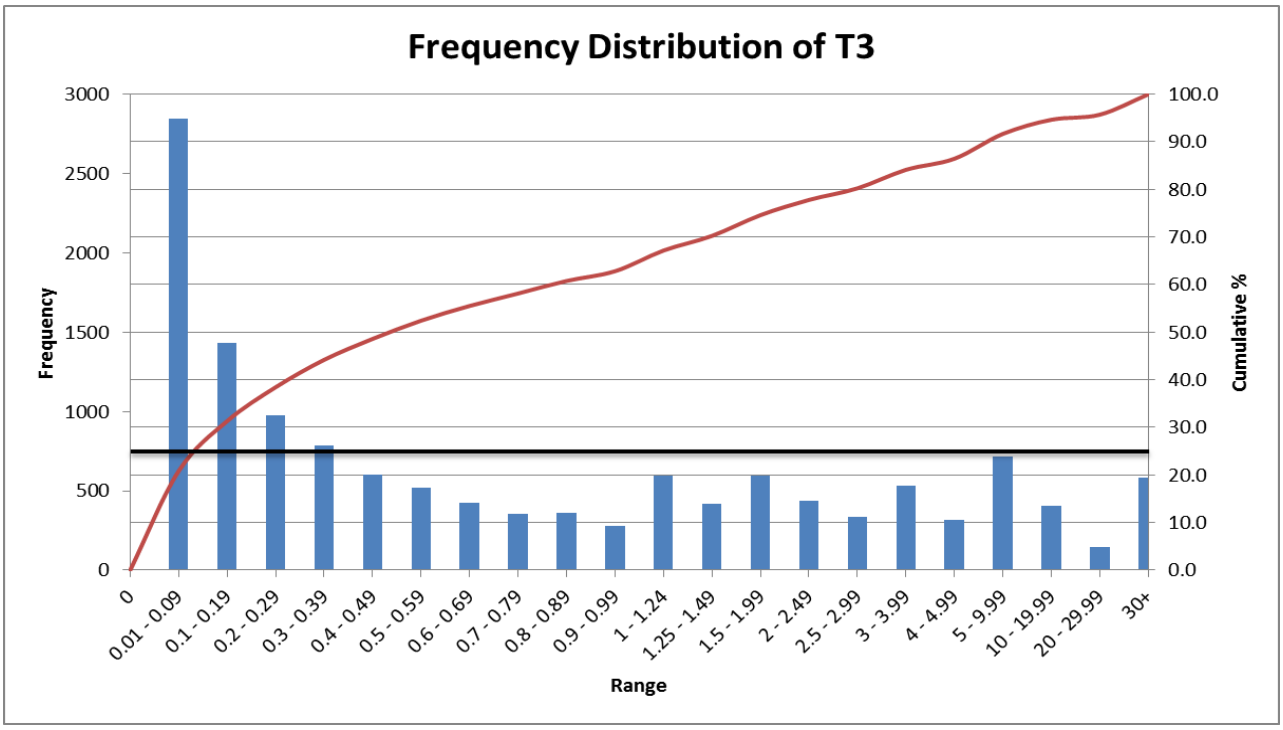

Figure A.9: Top 75% DWS cutoff value determination for Stope 5078's third time period.

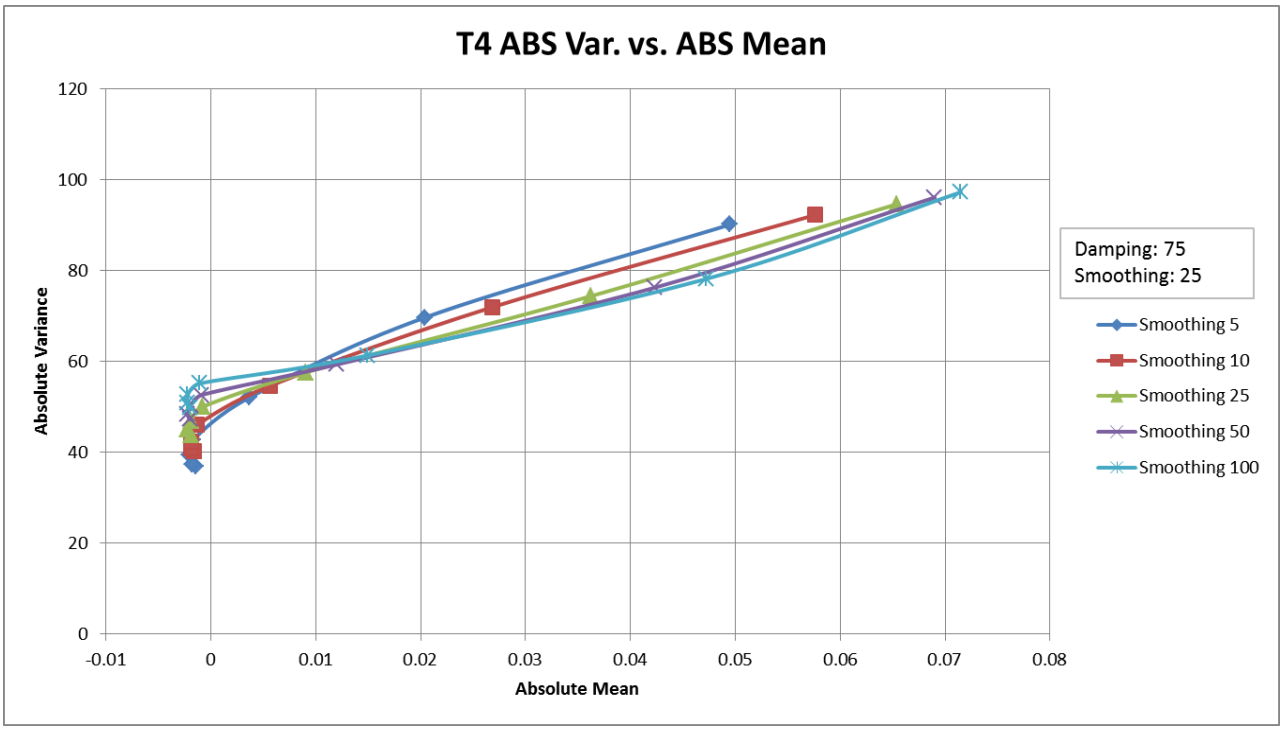

Figure A.10: Absolute variance versus absolute mean plot for Stope 5078's fourth time period.

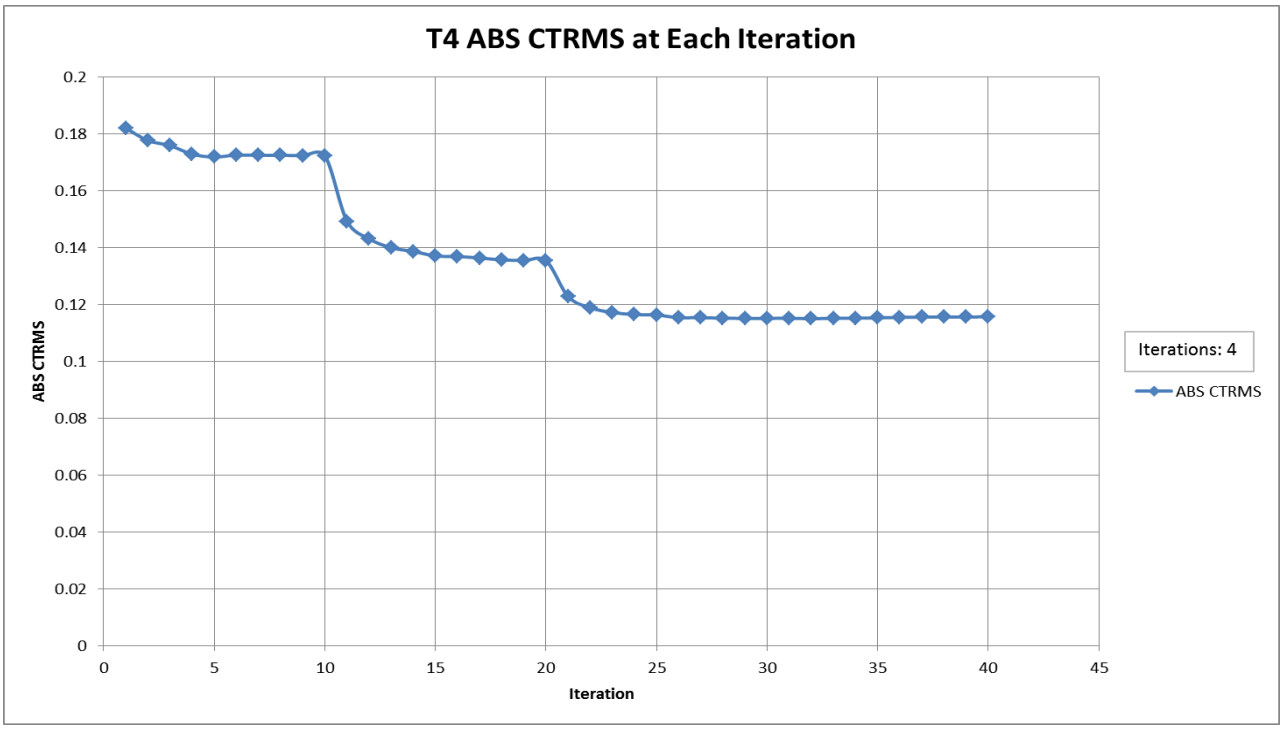

Figure A.11: Absolute CTRMS value for each iteration for Stope 5078's fourth time period.

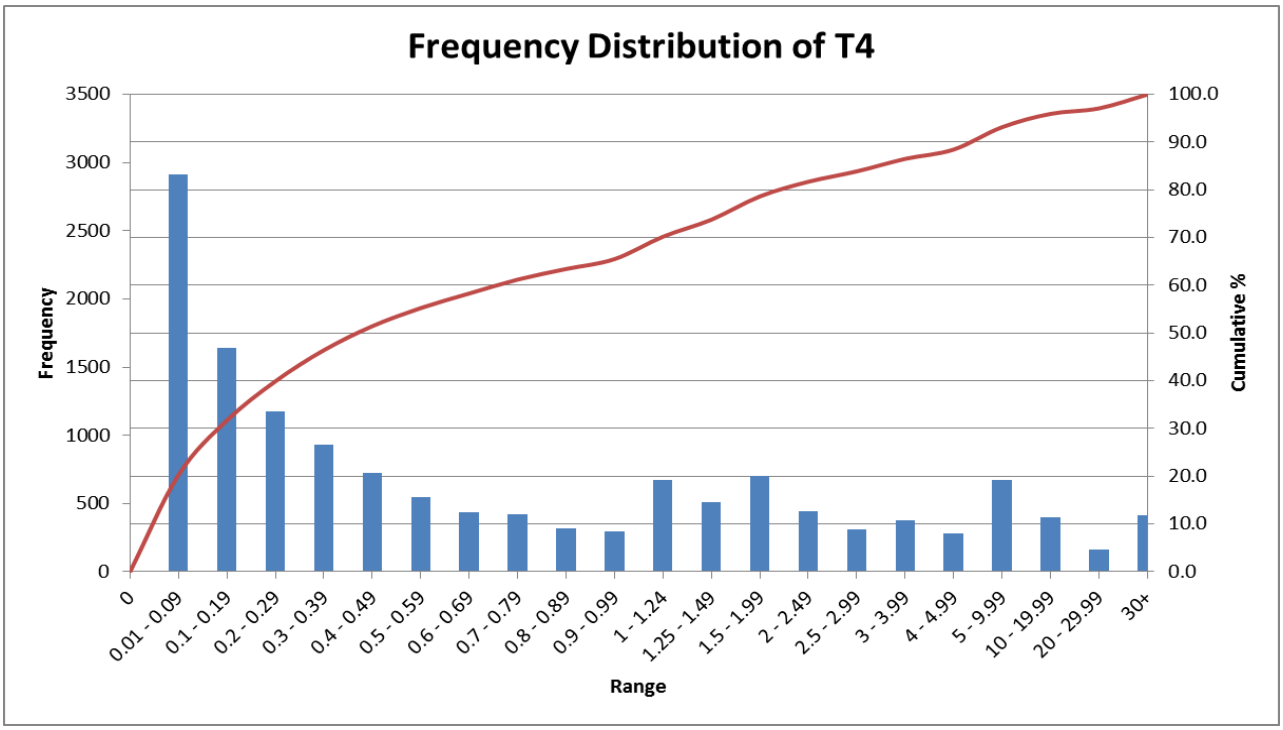

Figure A.12: Top 75% DWS cutoff value determination for Stope 5078's fourth time period.

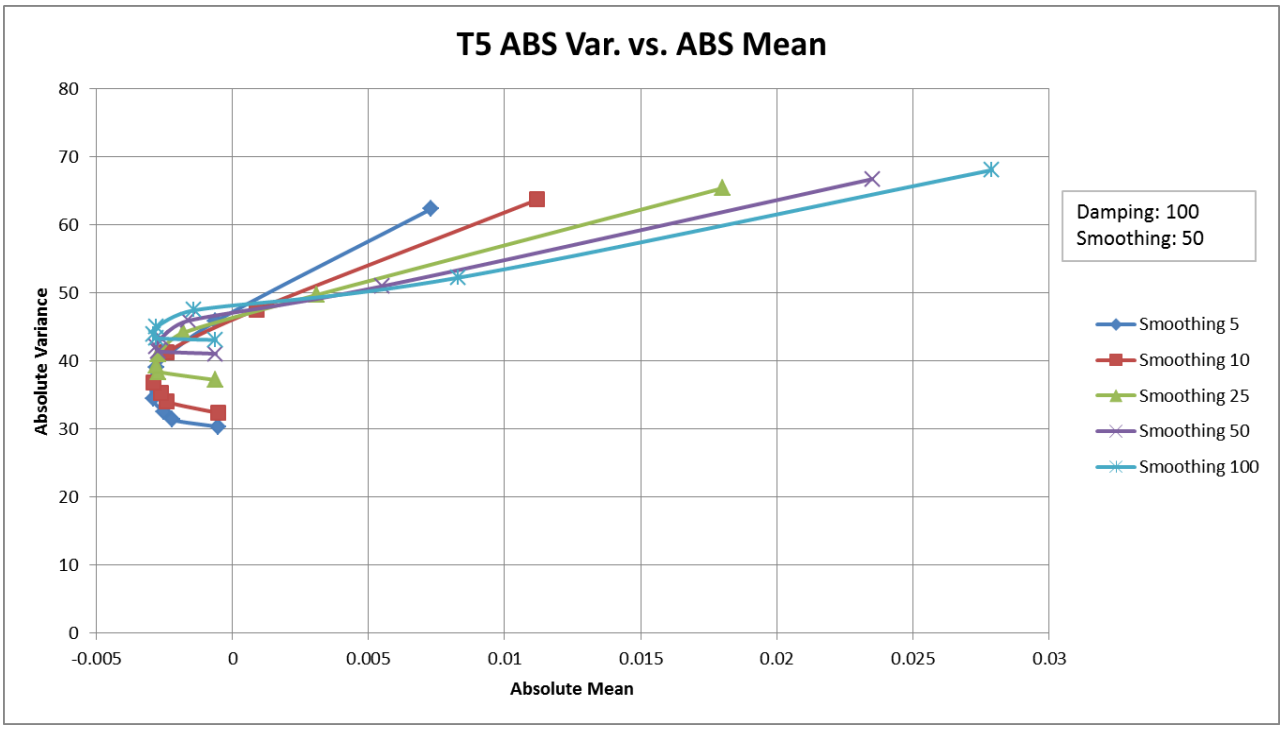

Figure A.13: Absolute variance versus absolute mean plot for Stope 5078's fifth time period.

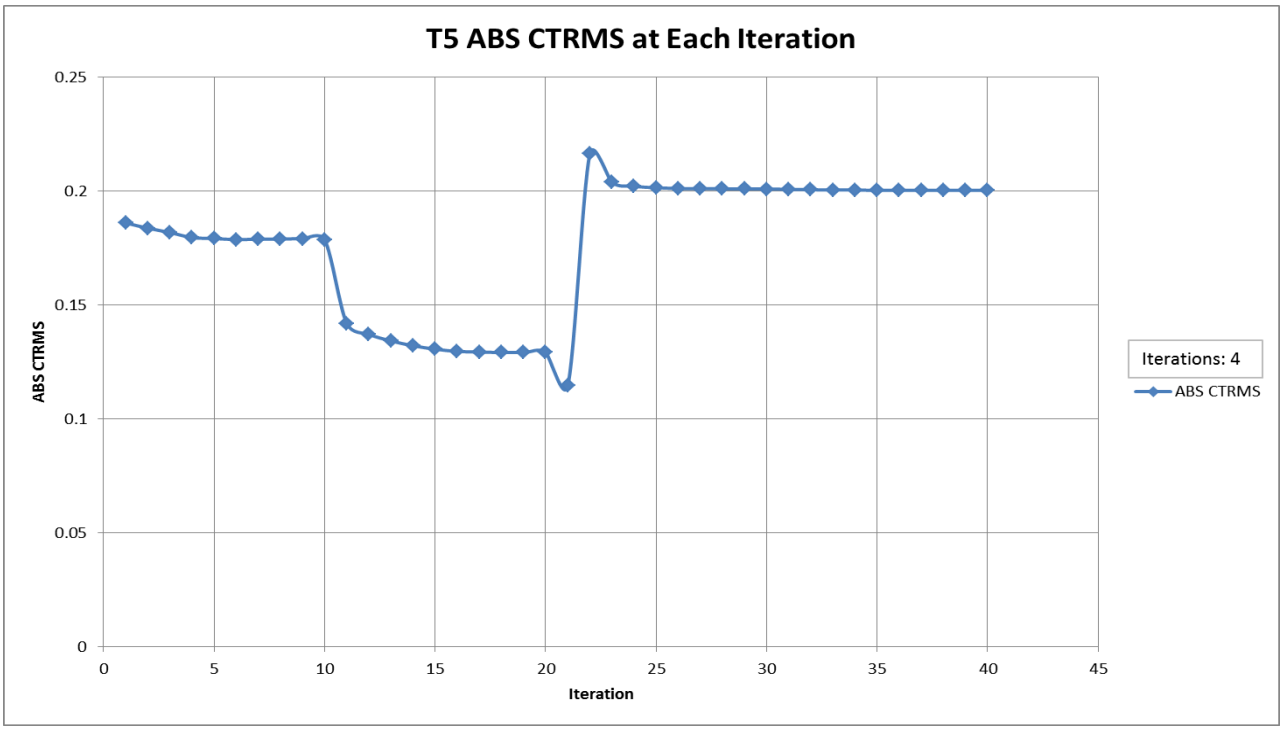

Figure A.14: Absolute CTRMS value for each iteration for Stope 5078's fifth time period.

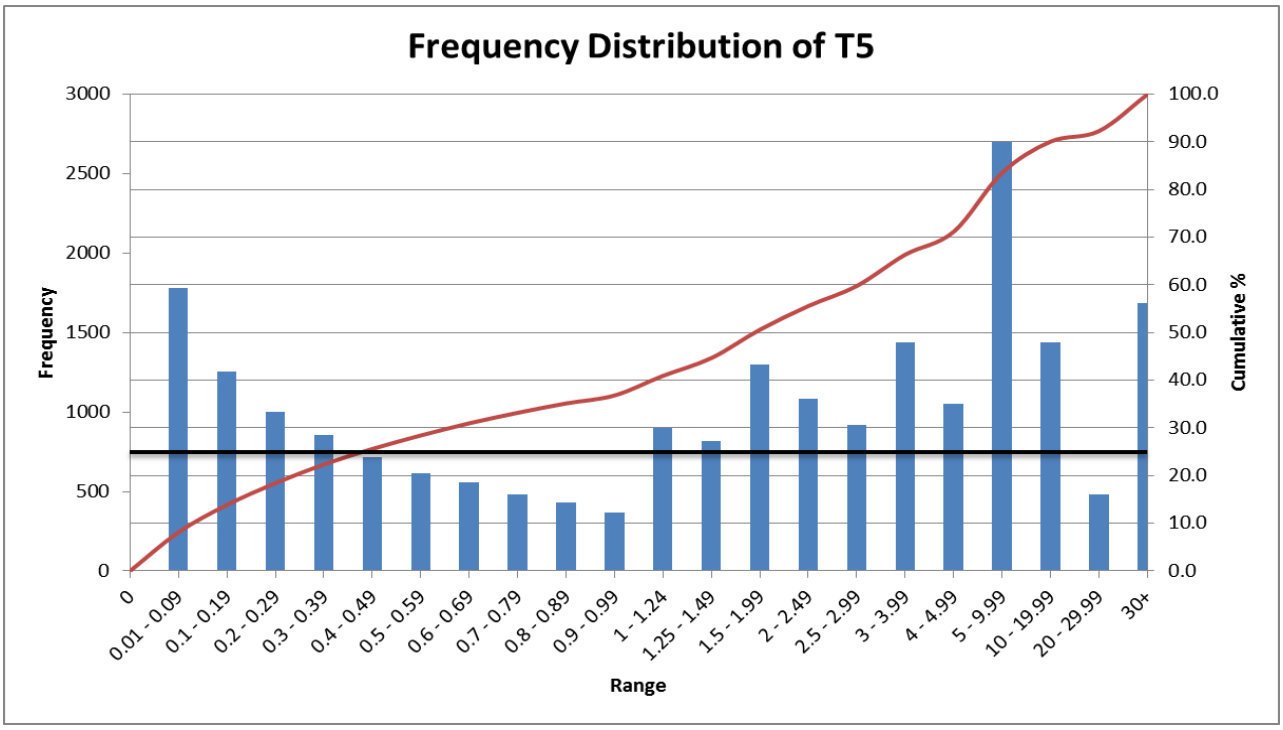

Figure A.15: Top 75% DWS cutoff value determination for Stope 5078's fifth time period.

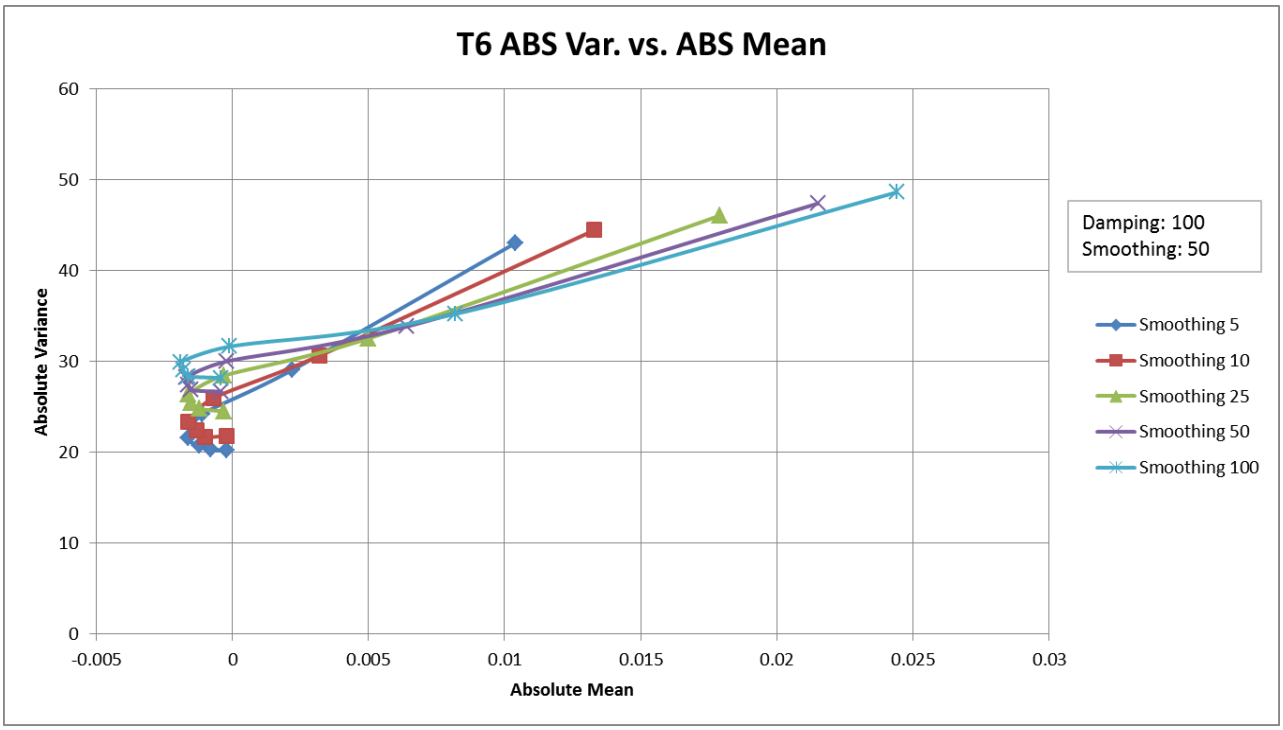

Figure A.16: Absolute variance versus absolute mean plot for Stope 5078's sixth time period.

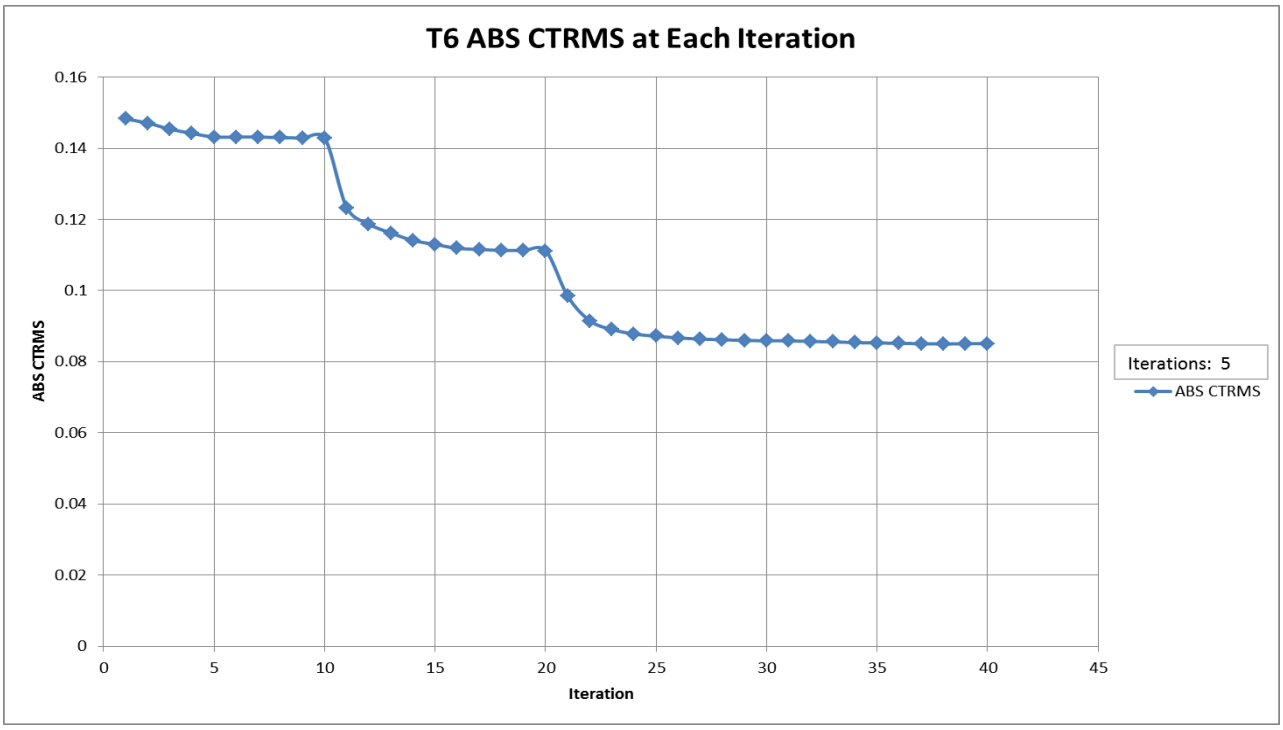

Figure A.17: Absolute CTRMS value for each iteration for Stope 5078's sixth time period.

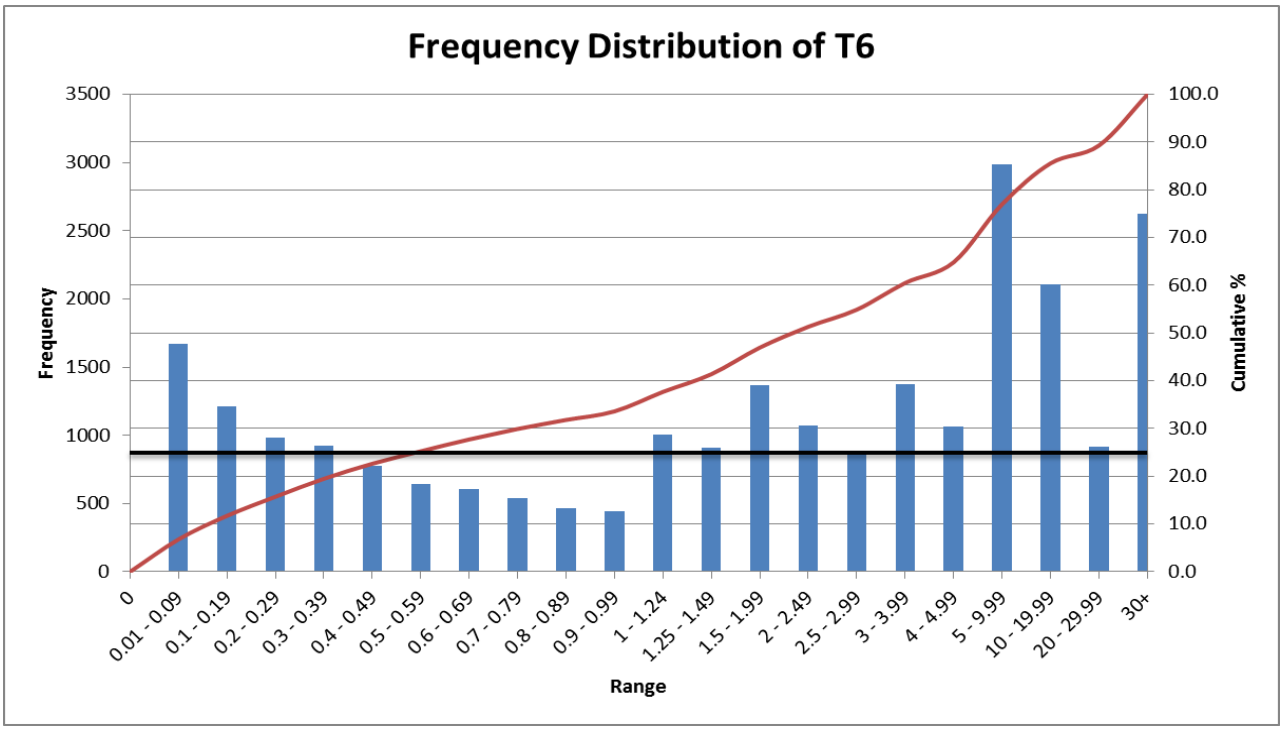

Figure A.18: Top 75% DWS cutoff value determination for Stope 5078's sixth time period.

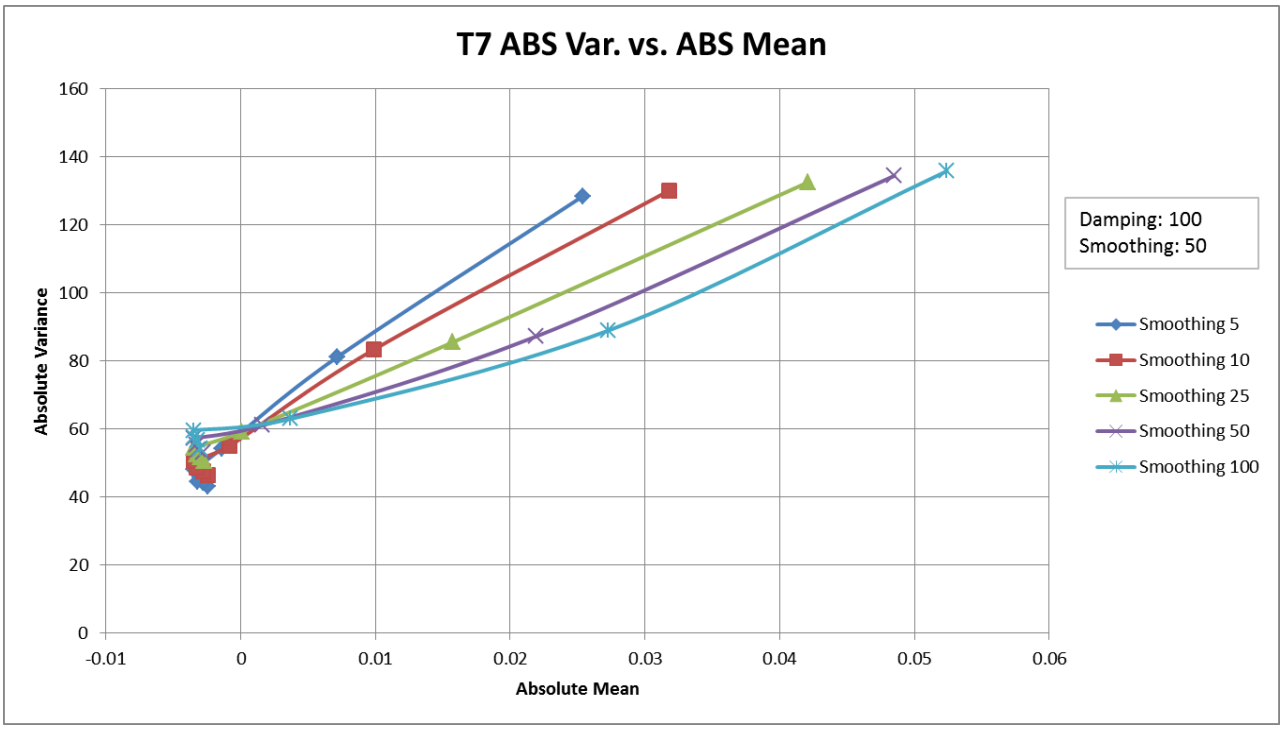

Figure A.19: Absolute variance versus absolute mean plot for Stope 5078's seventh time period.

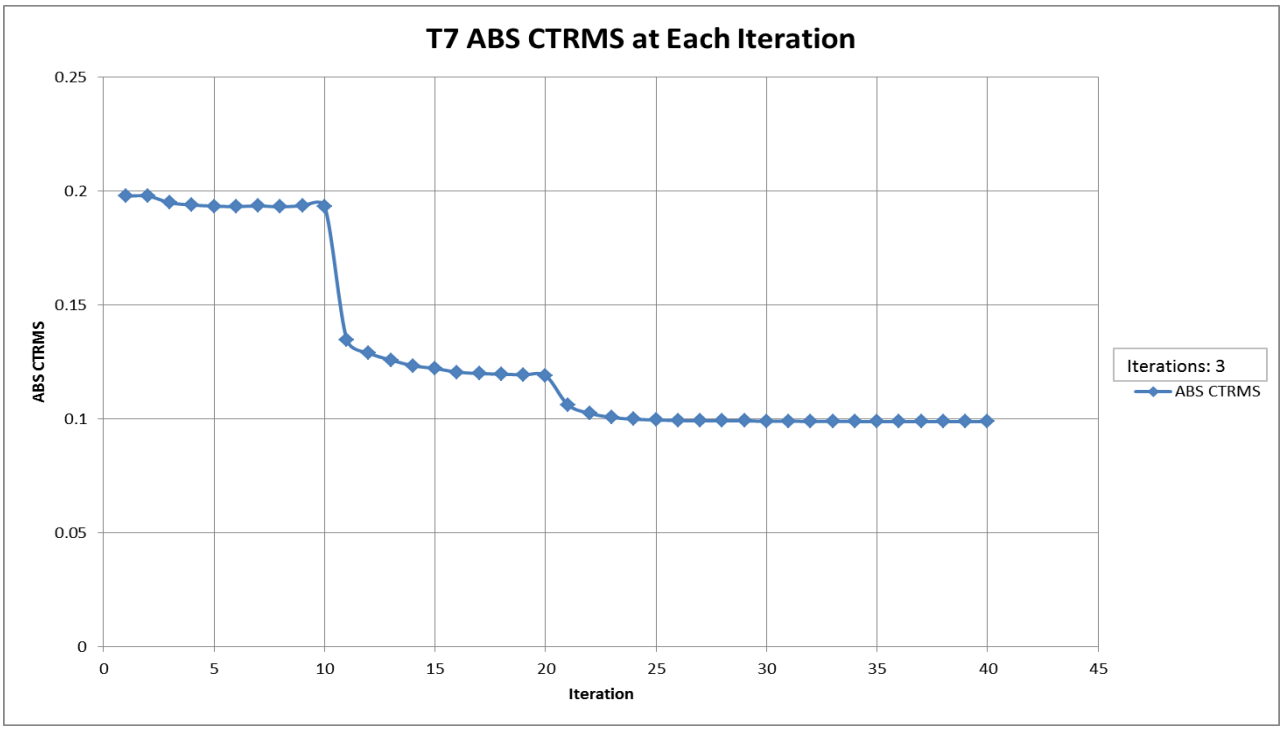

Figure A.20: Absolute CTRMS value for each iteration for Stope 5078's seventh time period.

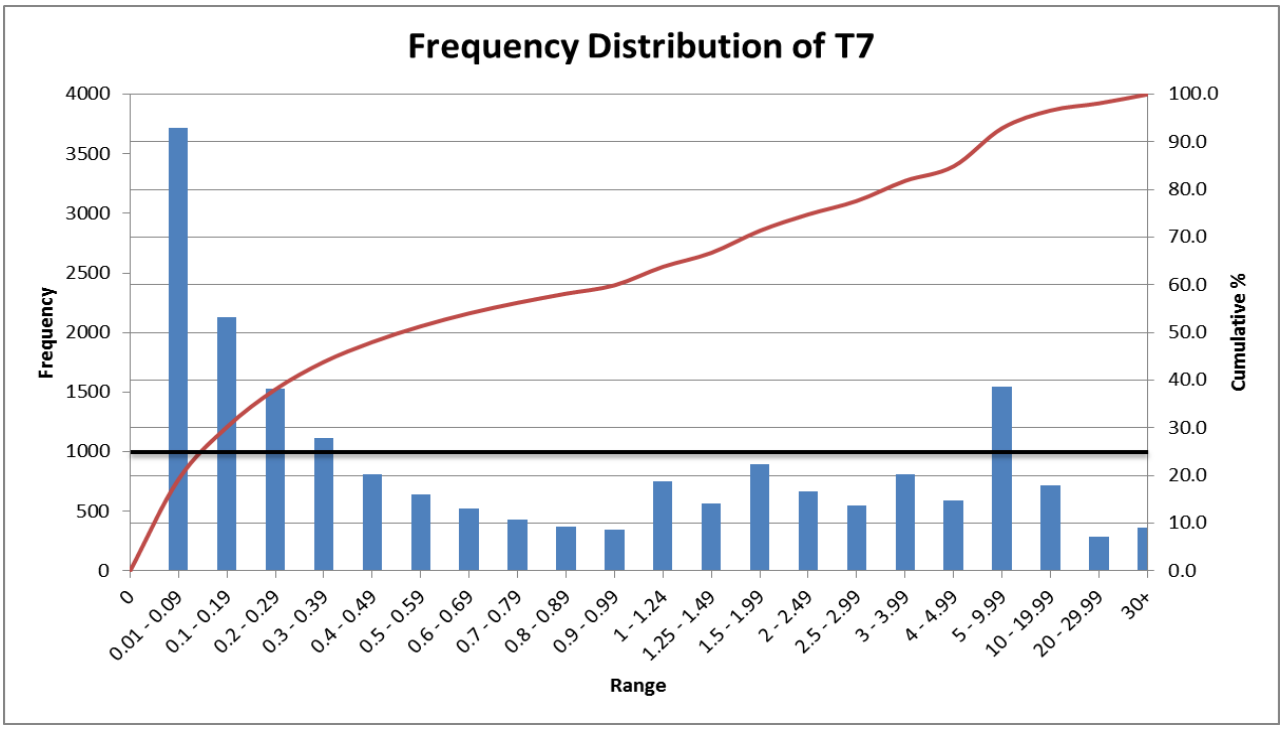

Figure A.21: Top 75% DWS cutoff value determination for Stope 5078's seventh time period.

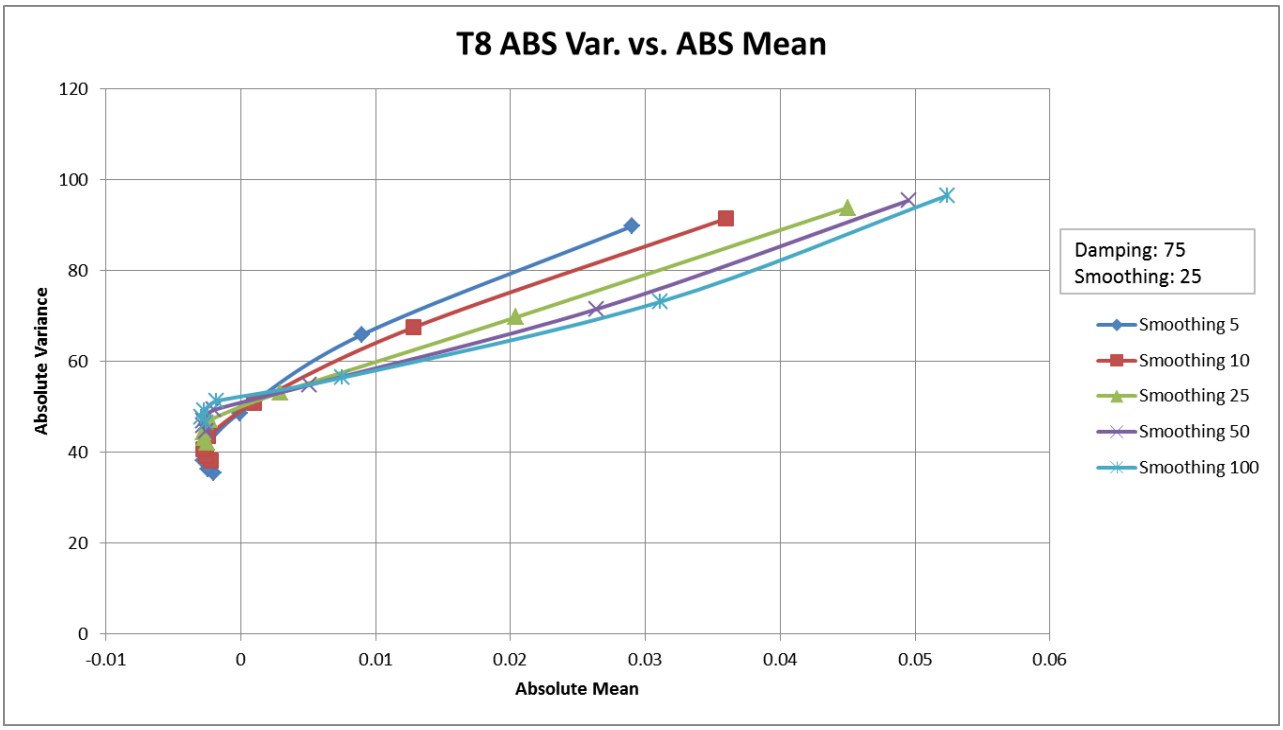

Figure A.22: Absolute variance versus absolute mean plot for Stope 5078's eighth time period.

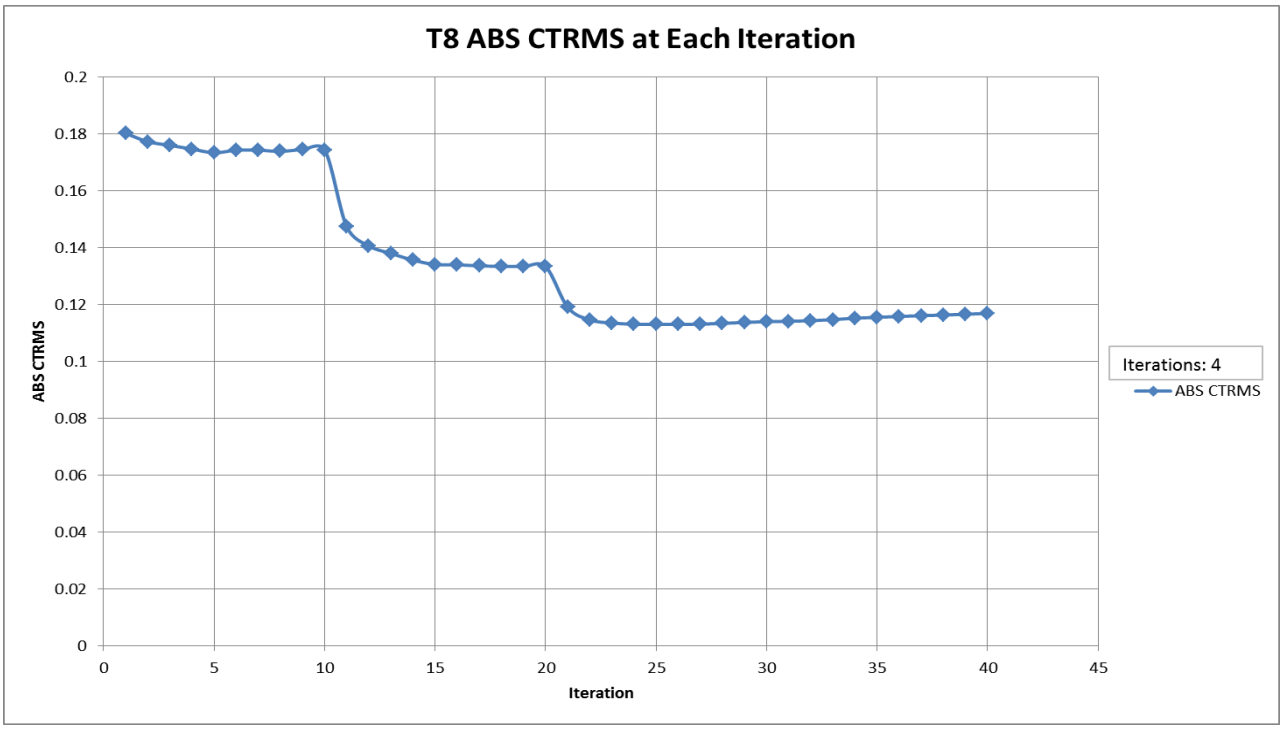

Figure A.23: Absolute CTRMS value for each iteration for Stope 5078's eighth time period.

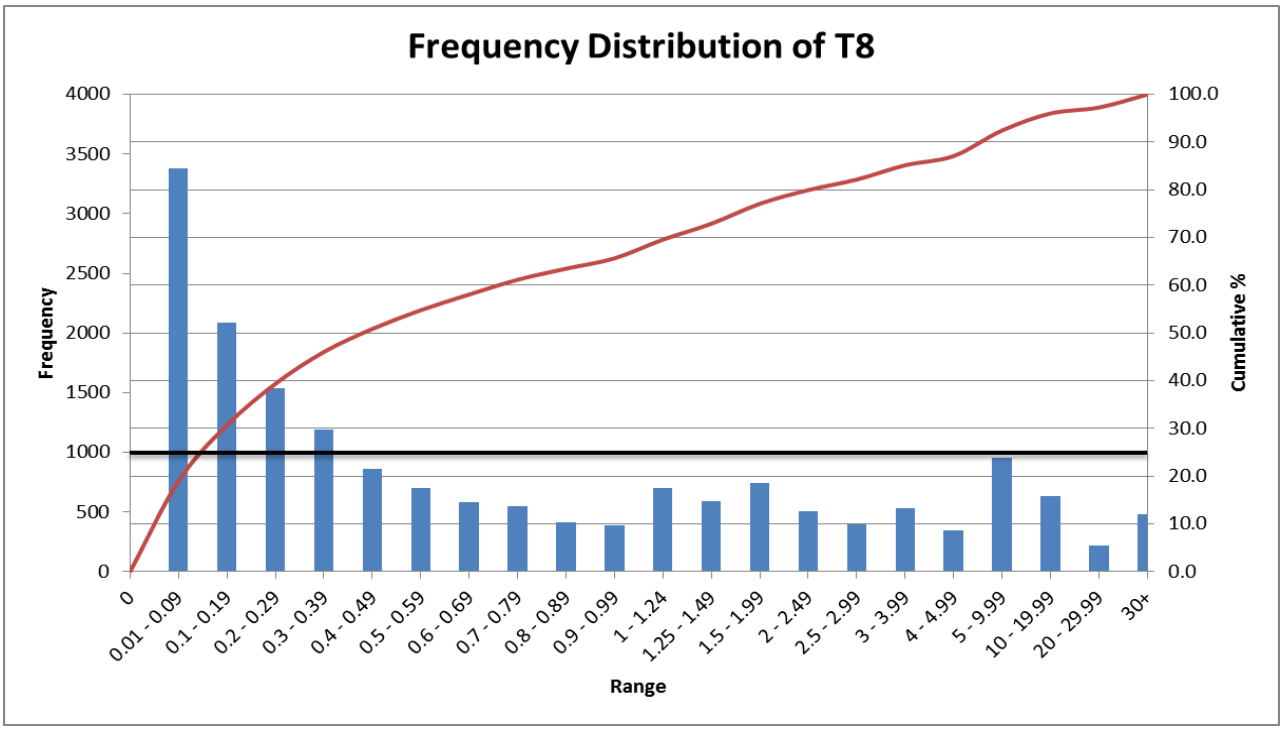

Figure A.24: Top 75% DWS cutoff value determination for Stope 5078's eighth time period.

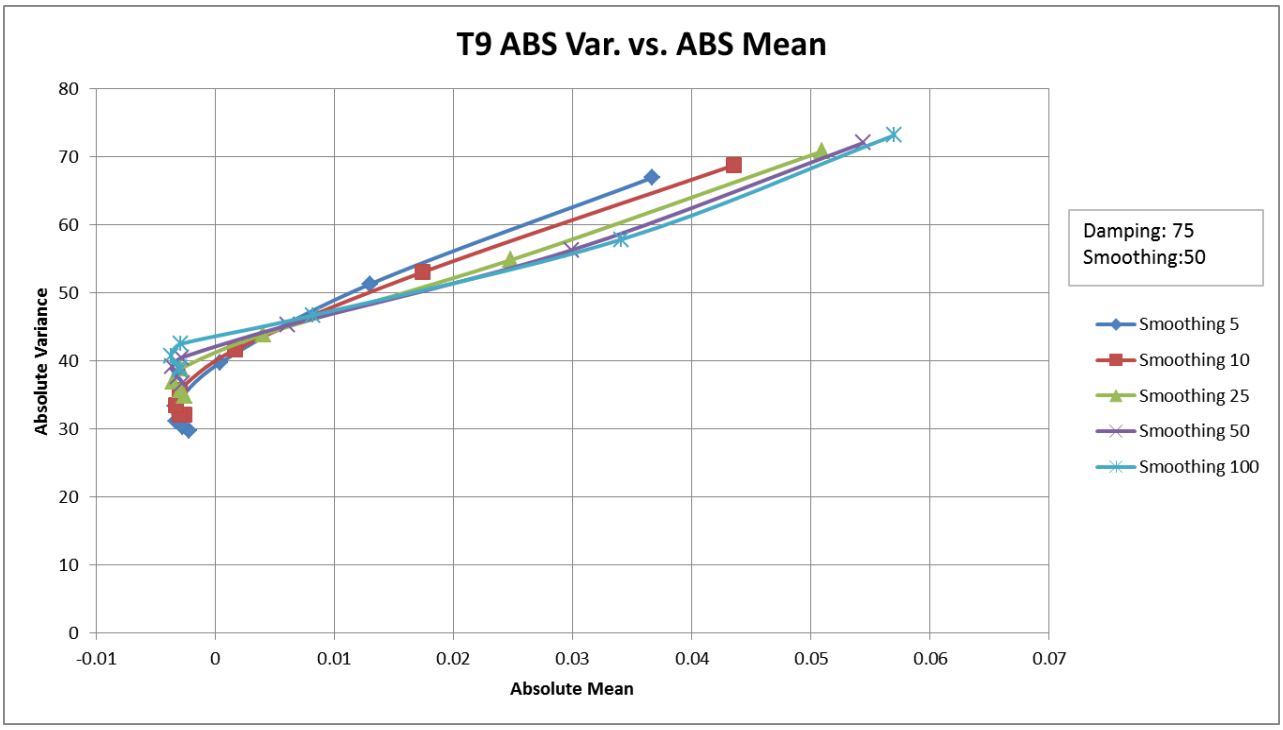

Figure A.25: Absolute variance versus absolute mean plot for Stope 5078's ninth time period.

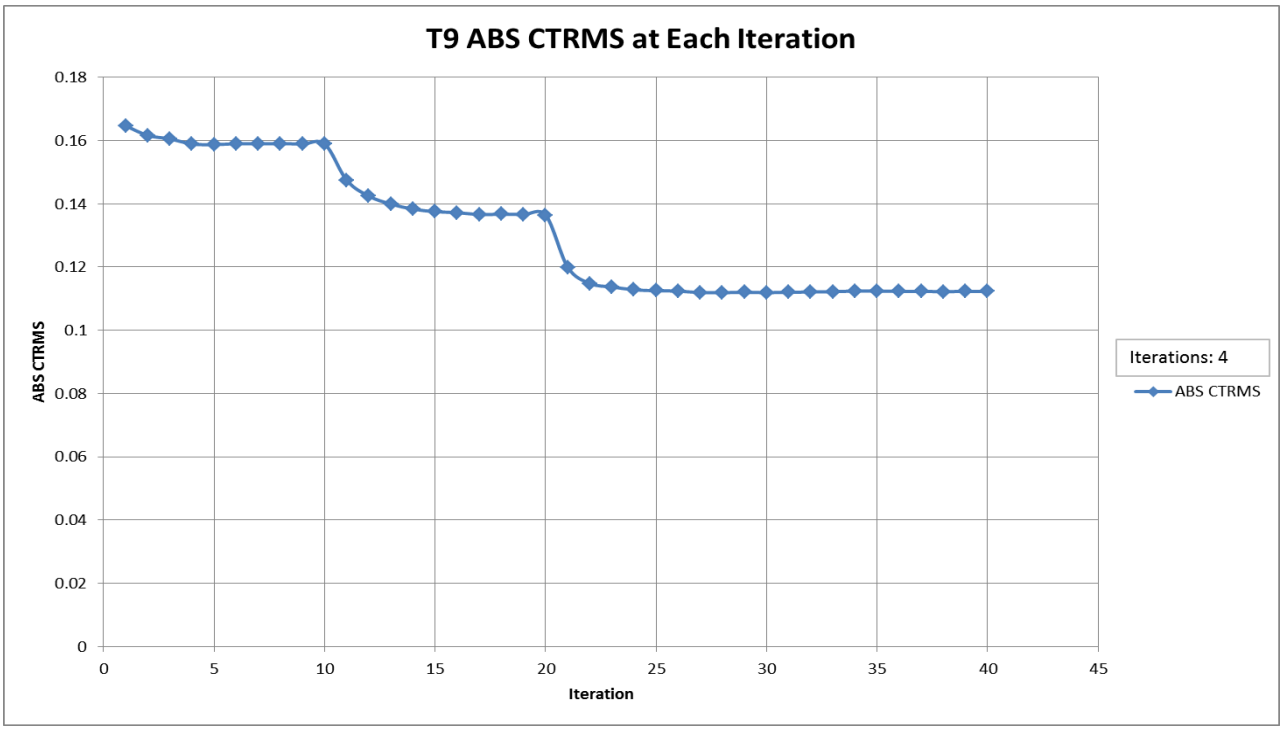

Figure A.26: Absolute CTRMS value for each iteration for Stope 5078's ninth time period.

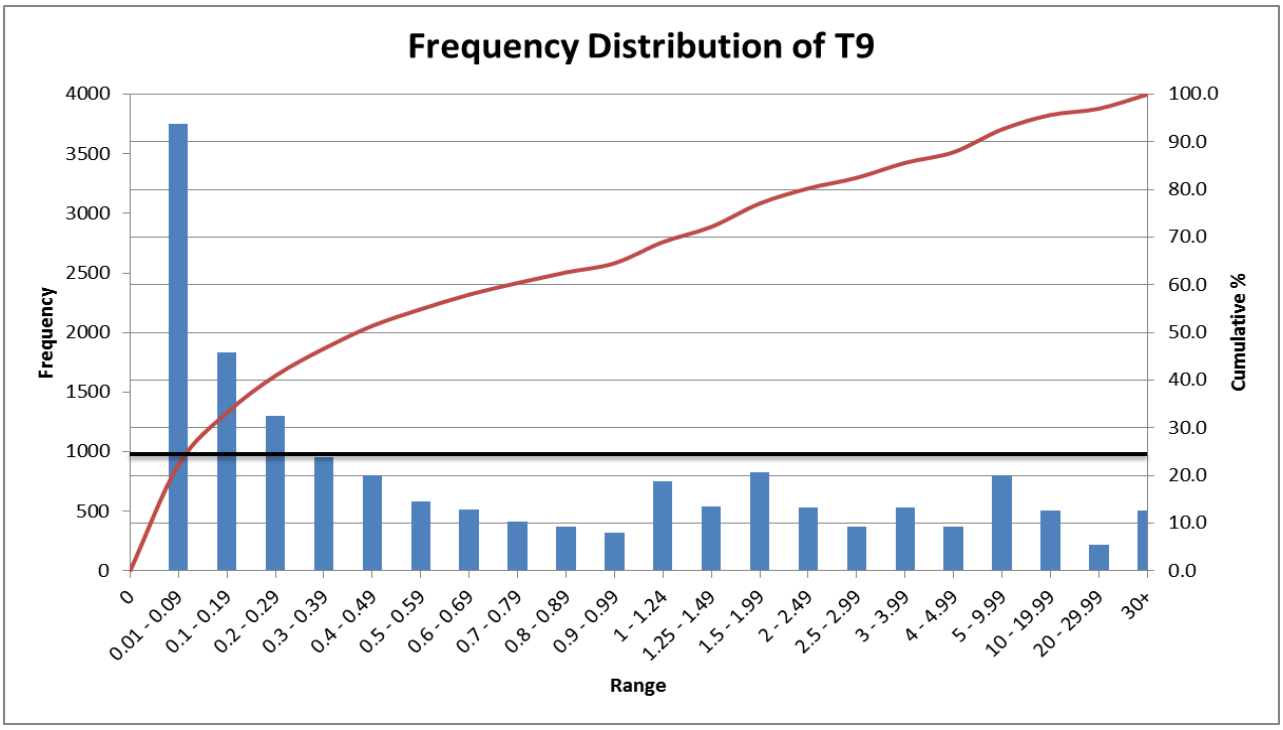

Figure A.27: Top 75% DWS cutoff value determination for Stope 5078's ninth time period.

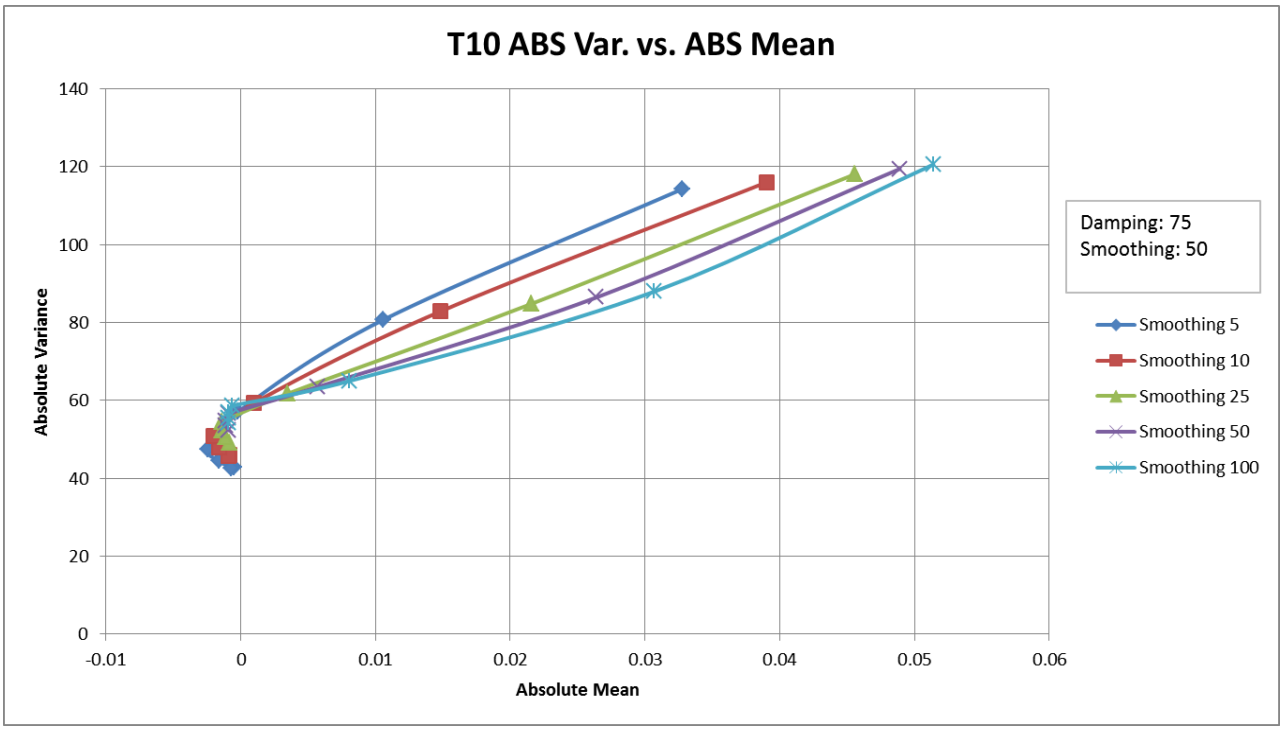

Figure A.28: Absolute variance versus absolute mean plot for Stope 5078's tenth time period.

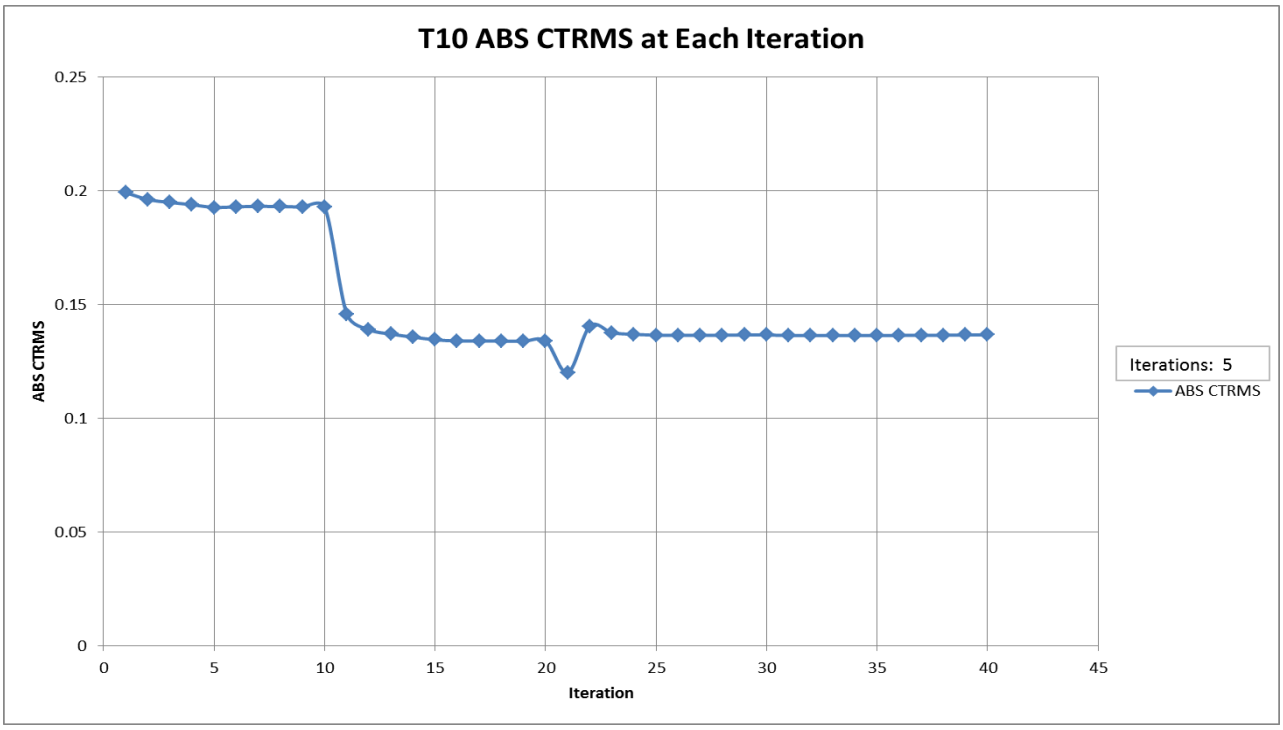

Figure A.29: Absolute CTRMS value for each iteration for Stope 5078's tenth time period.

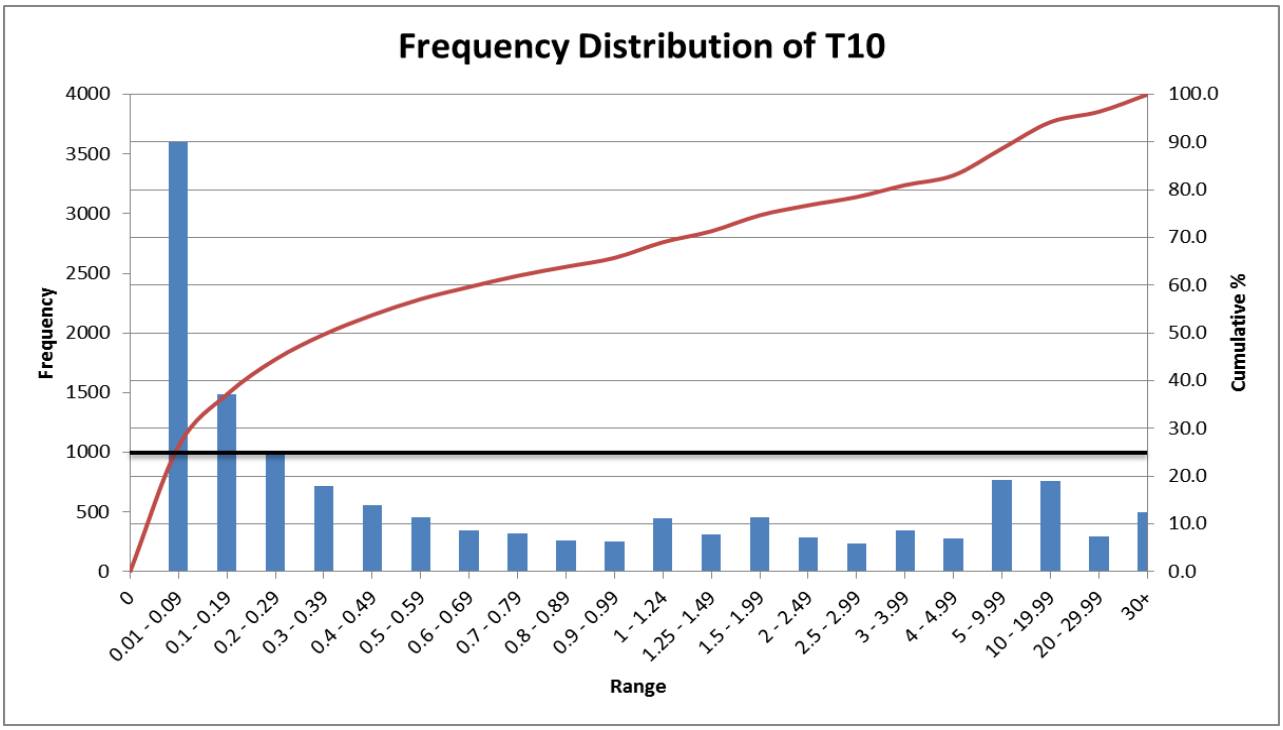

Figure A.30: Top 75% DWS cutoff value determination for Stope 5078's tenth time period.

Appendix B – Stope 4448 Methods

Appendix B will include pertinent information used to create the resulting tomograms of the stope scale study for Stope 4448. Plots to determine weighting (illustrated as smoothing) and damping, number of iterations, and the top 75% DWS cutoff value will be presented. All plots for a given time period will be introduced together, beginning with weighting and damping, followed by number of iterations, and ending with top 75% DWS cutoff value. On the top 75% DWS cutoff value plots, the histogram utilizes the primary Y axis while the cumulative percent line chart is plotted on the secondary Y axis.

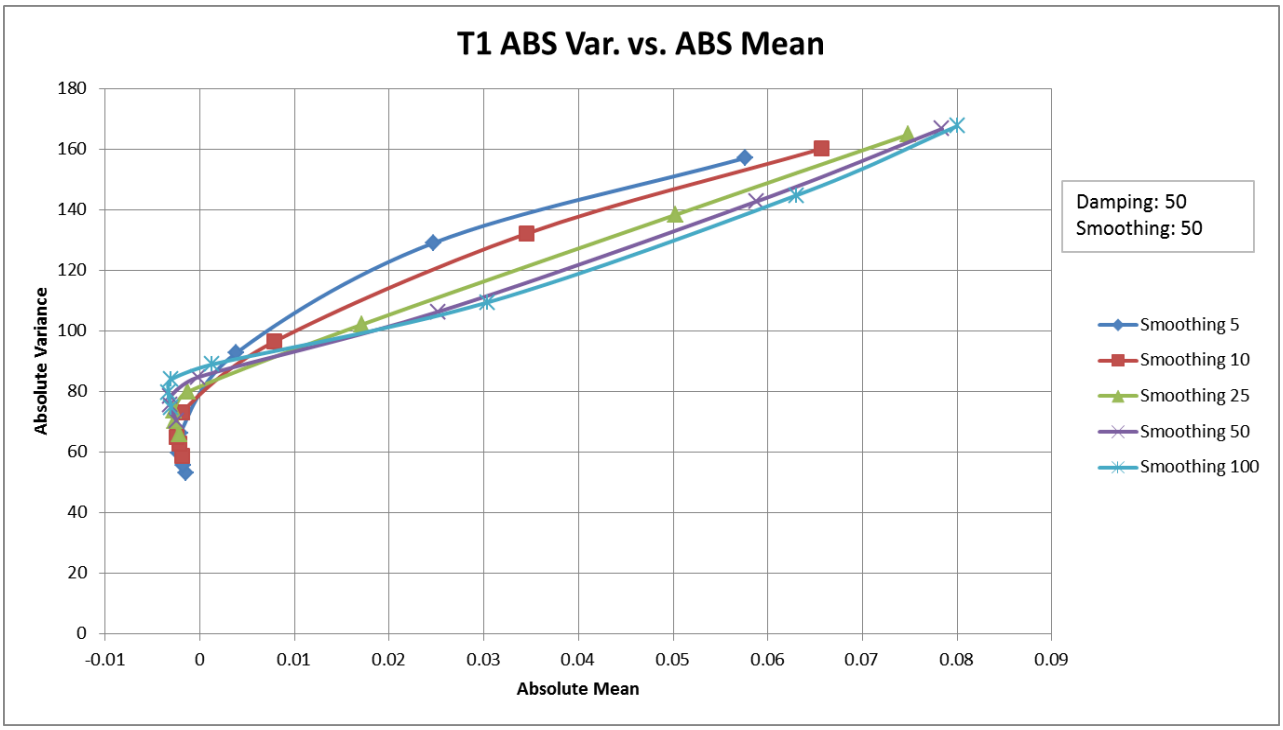

Figure B.1: Absolute variance versus absolute mean plot for Stope 4448's first time period.

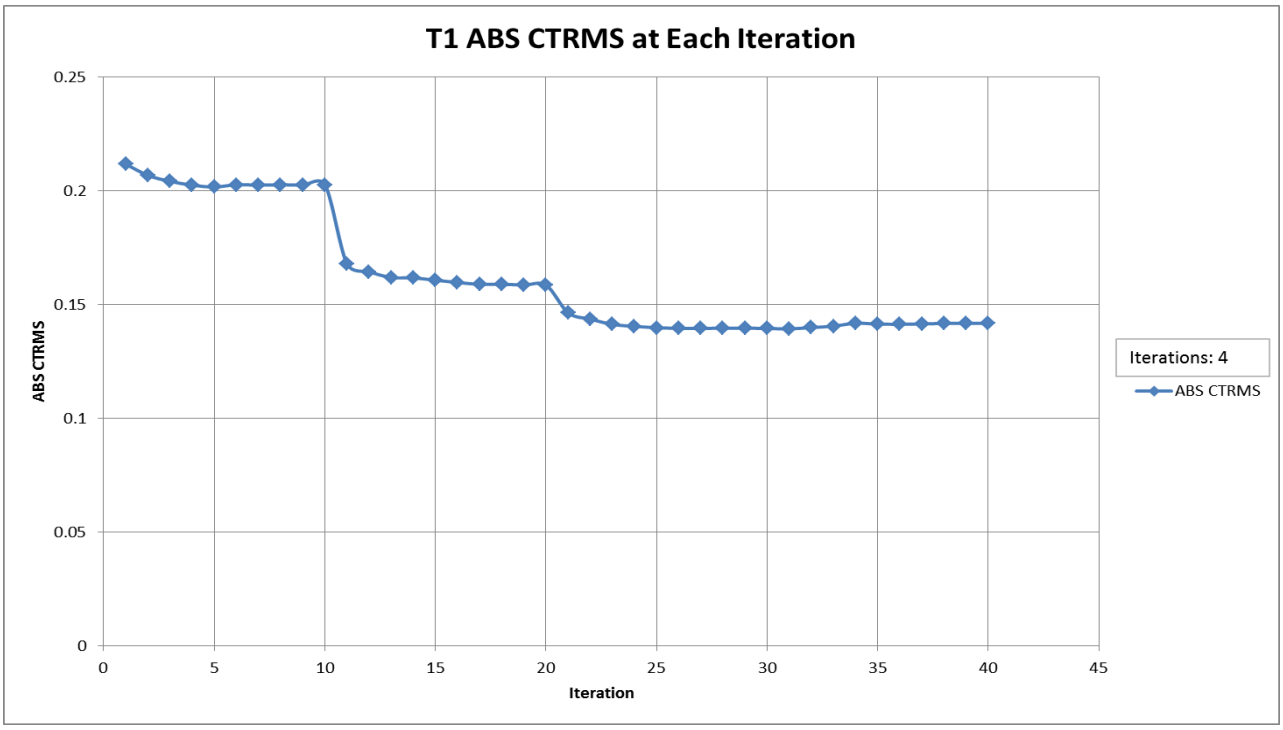

Figure B.2: Absolute CTRMS value for each iteration for Stope 4448's first time period.

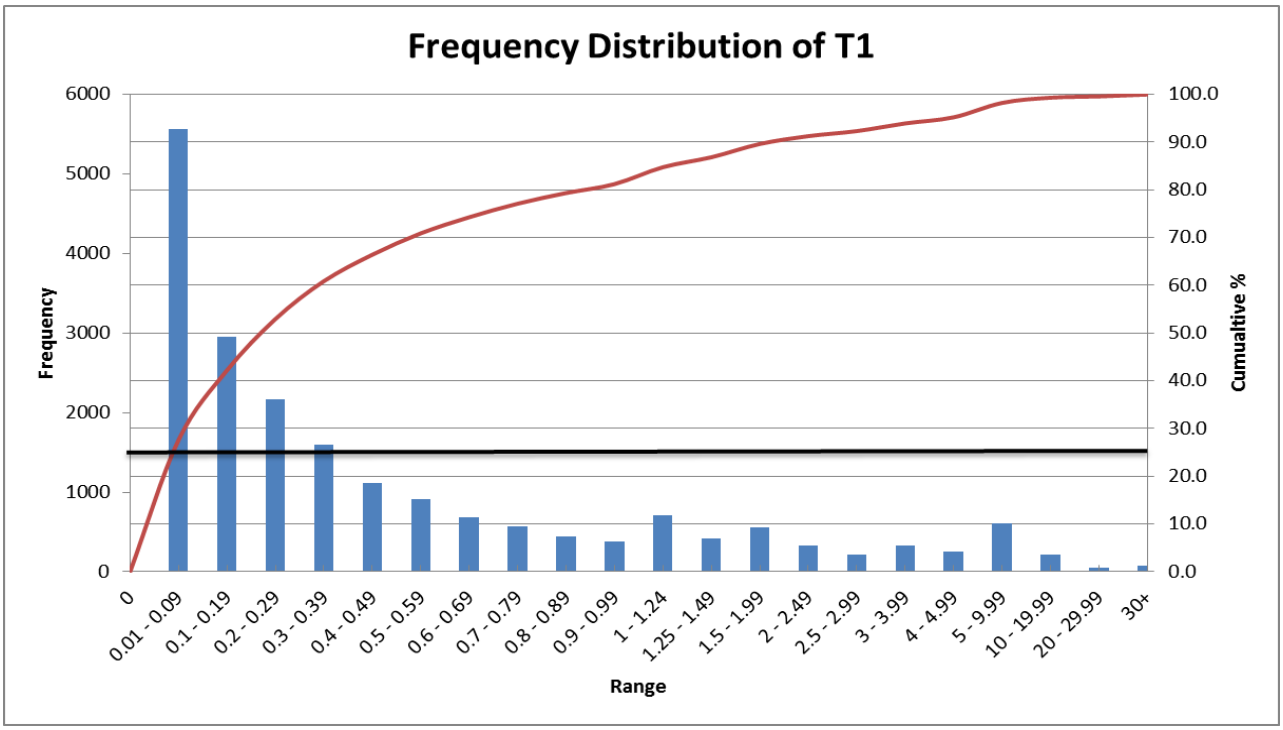

Figure B.3: Top 75% DWS cutoff value determination for Stope 4448's first time period.

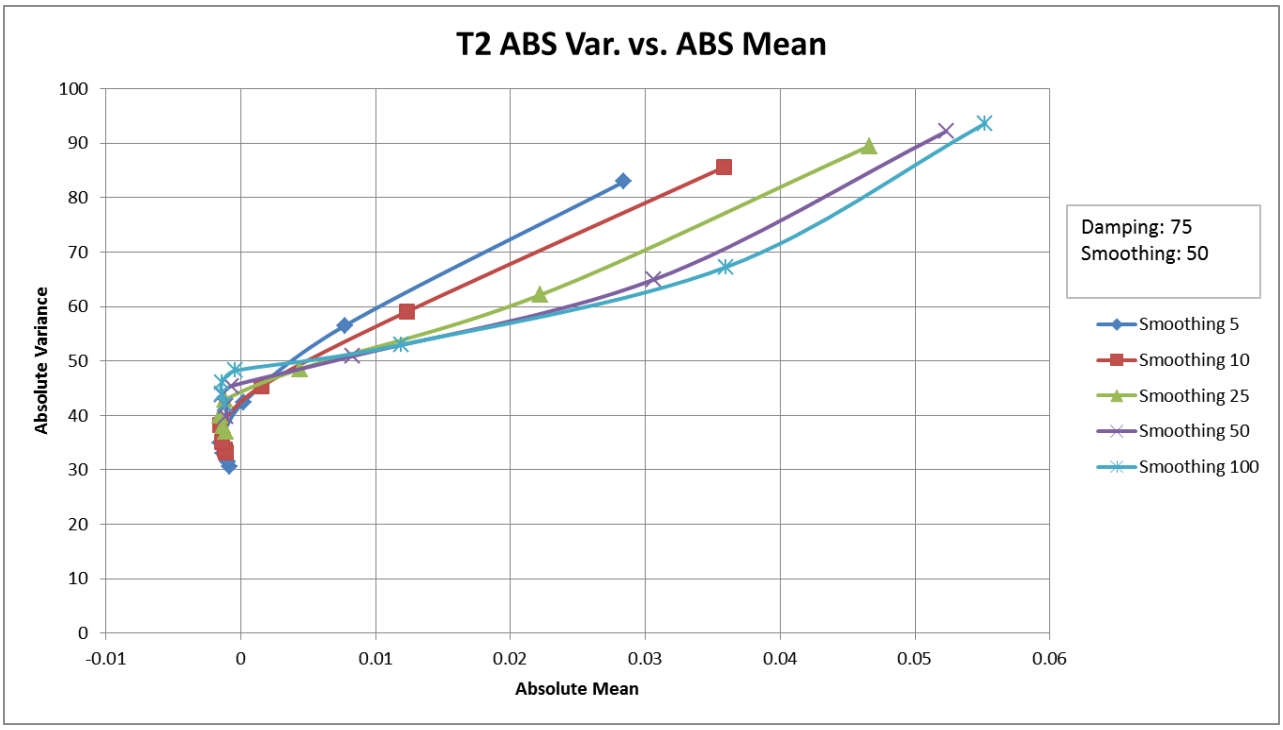

Figure B.4: Absolute variance versus absolute mean plot for Stope 4448's second time period.

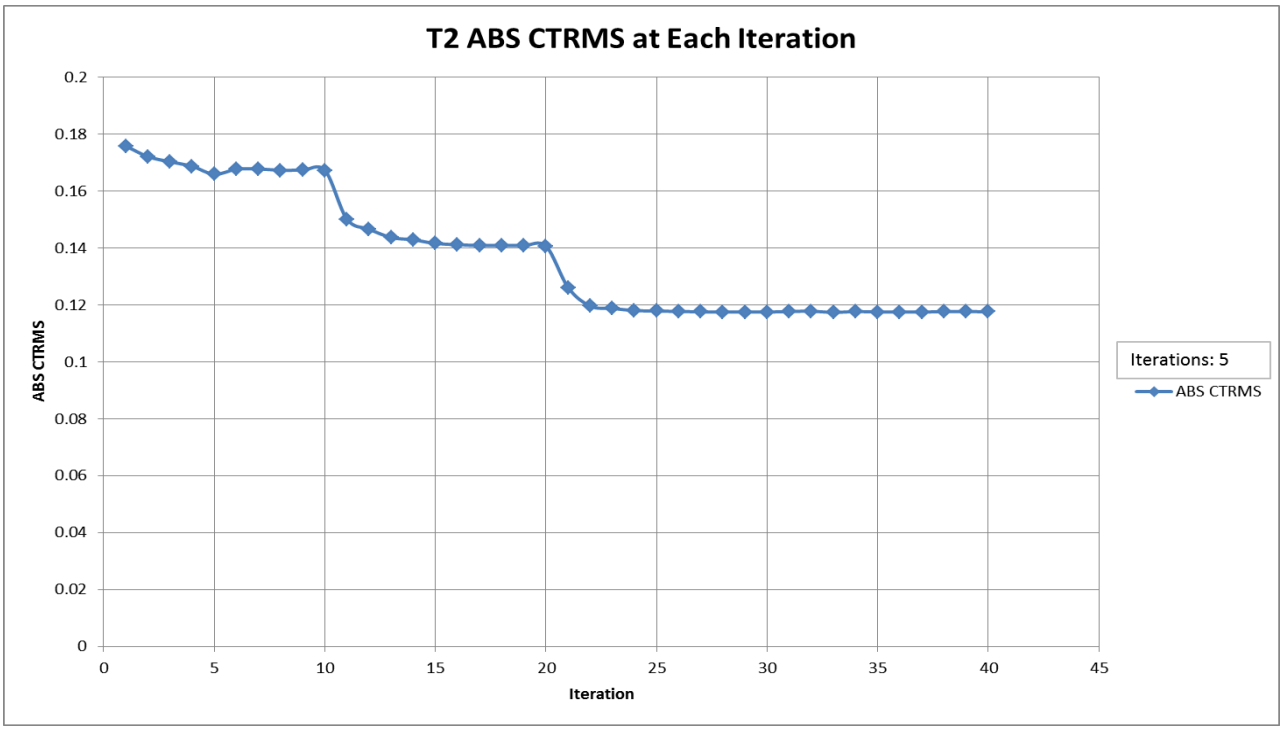

Figure B.5: Absolute CTRMS value for each iteration for Stope 4448's second time period.

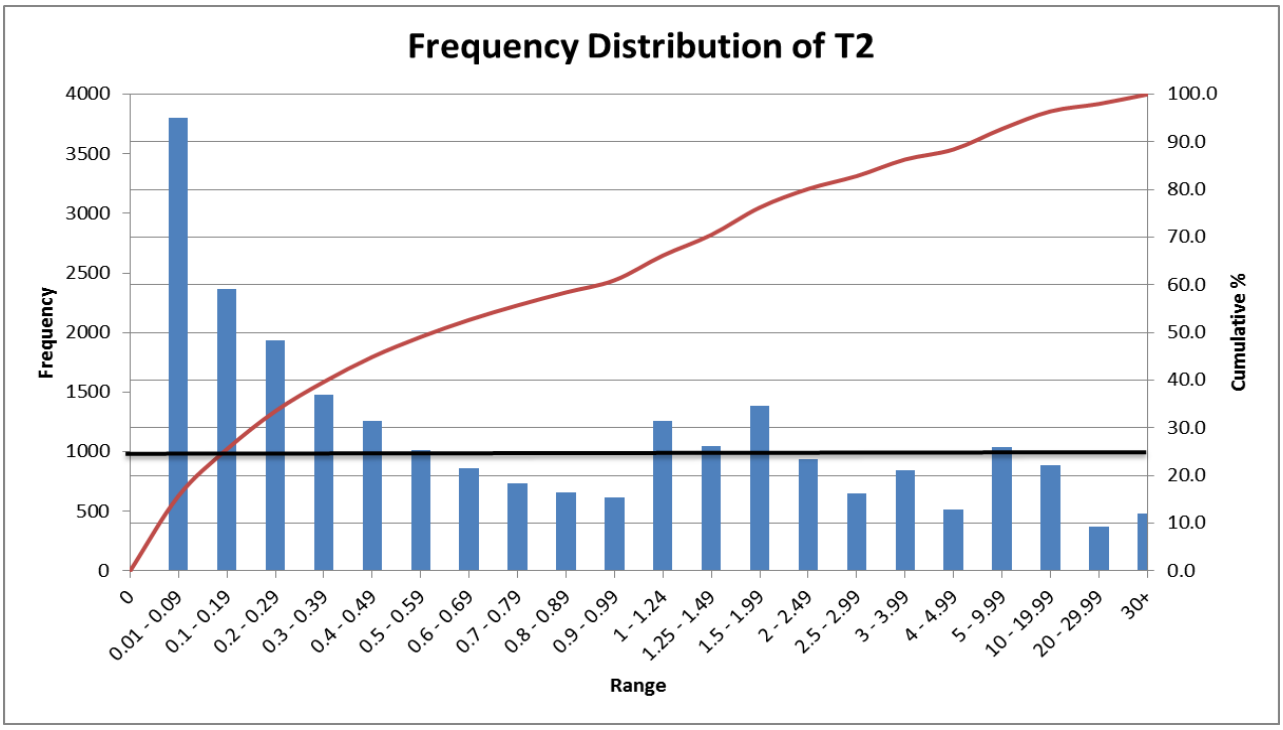

Figure B.6: Top 75% DWS cutoff value determination for Stope 4448's second time period.

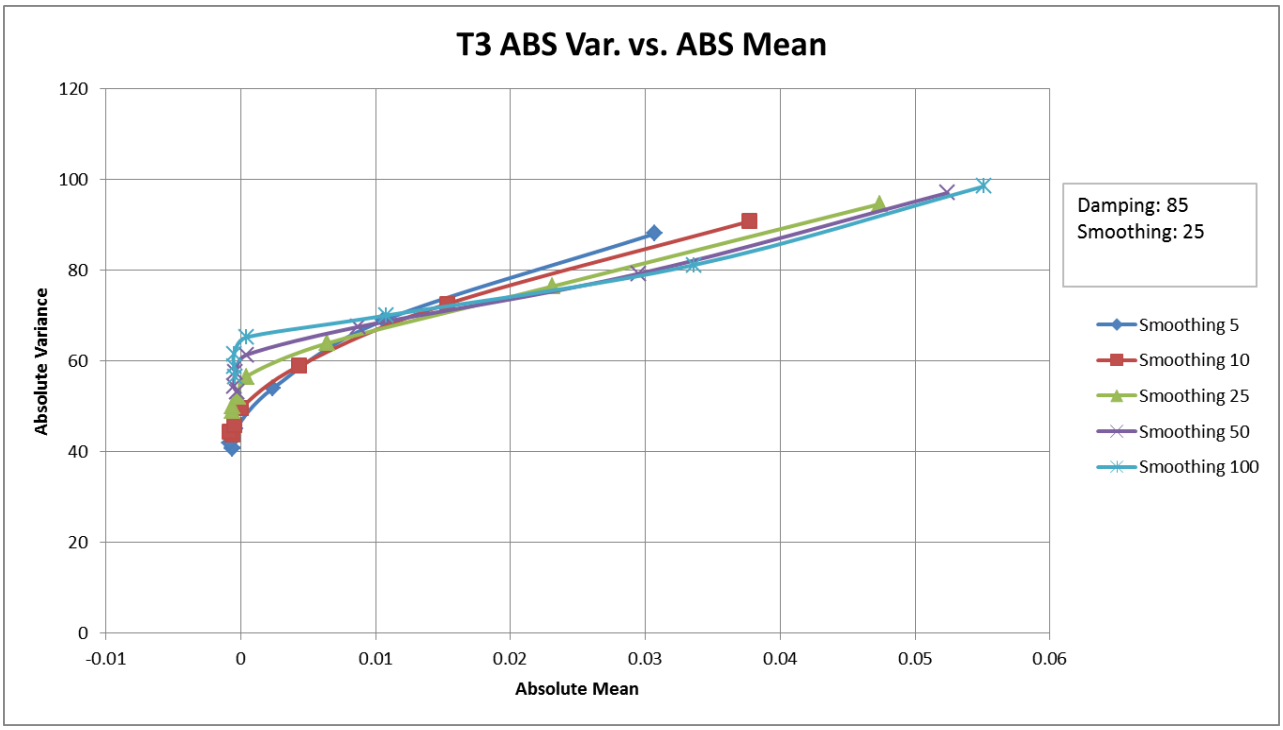

Figure B.7: Absolute variance versus absolute mean plot for Stope 4448's third time period.

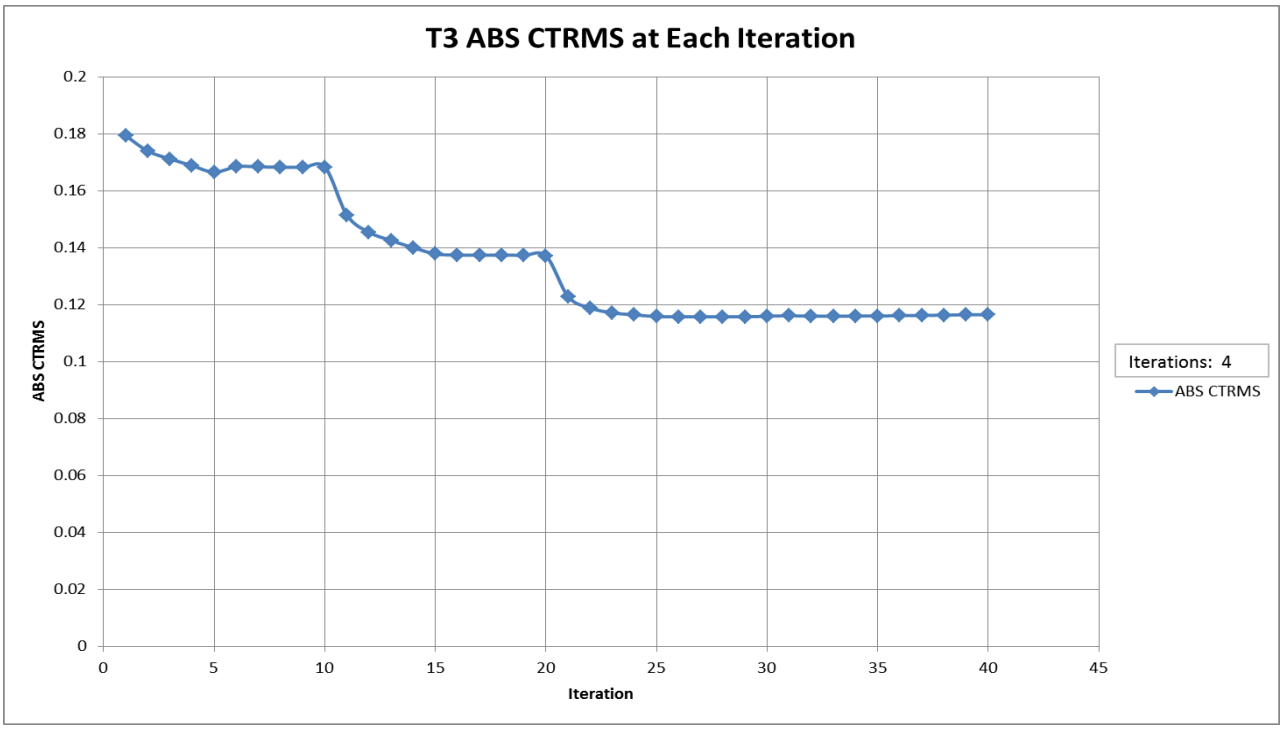

Figure B.8: Absolute CTRMS value for each iteration for Stope 4448's third time period.

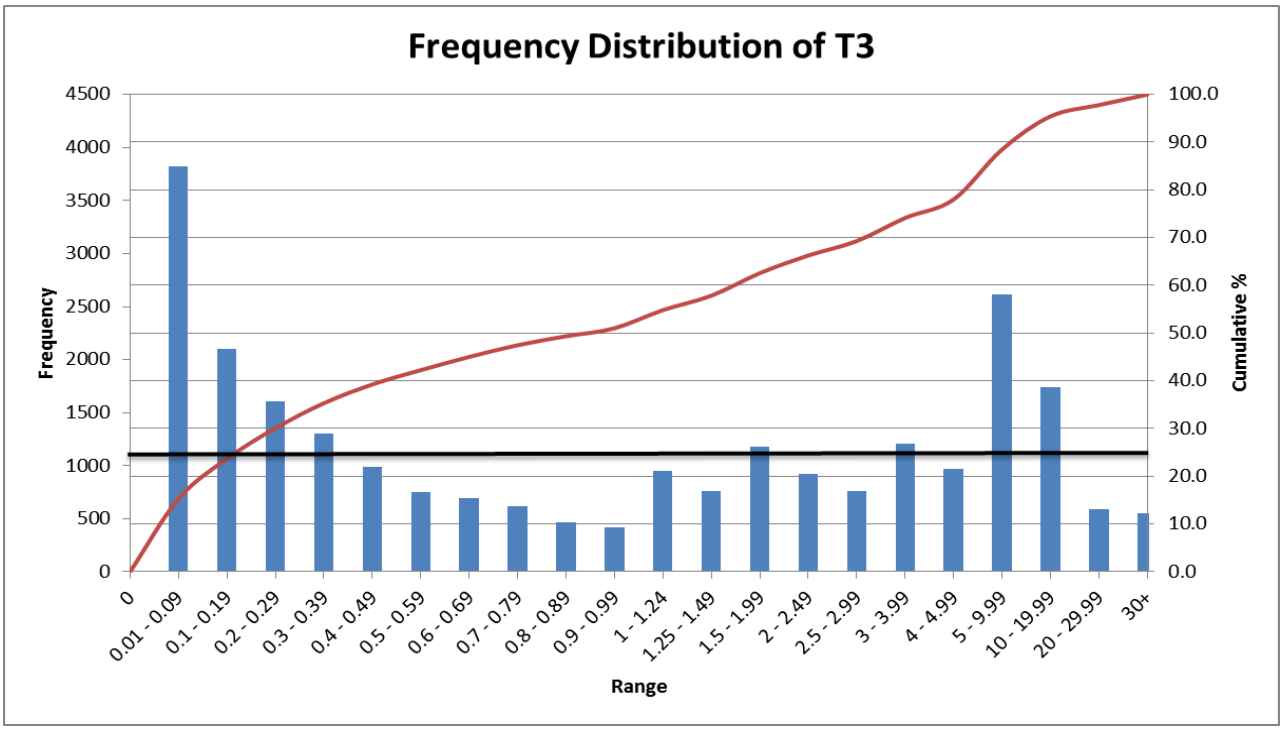

Figure B.9: Top 75% DWS cutoff value determination for Stope 4448's third time period.

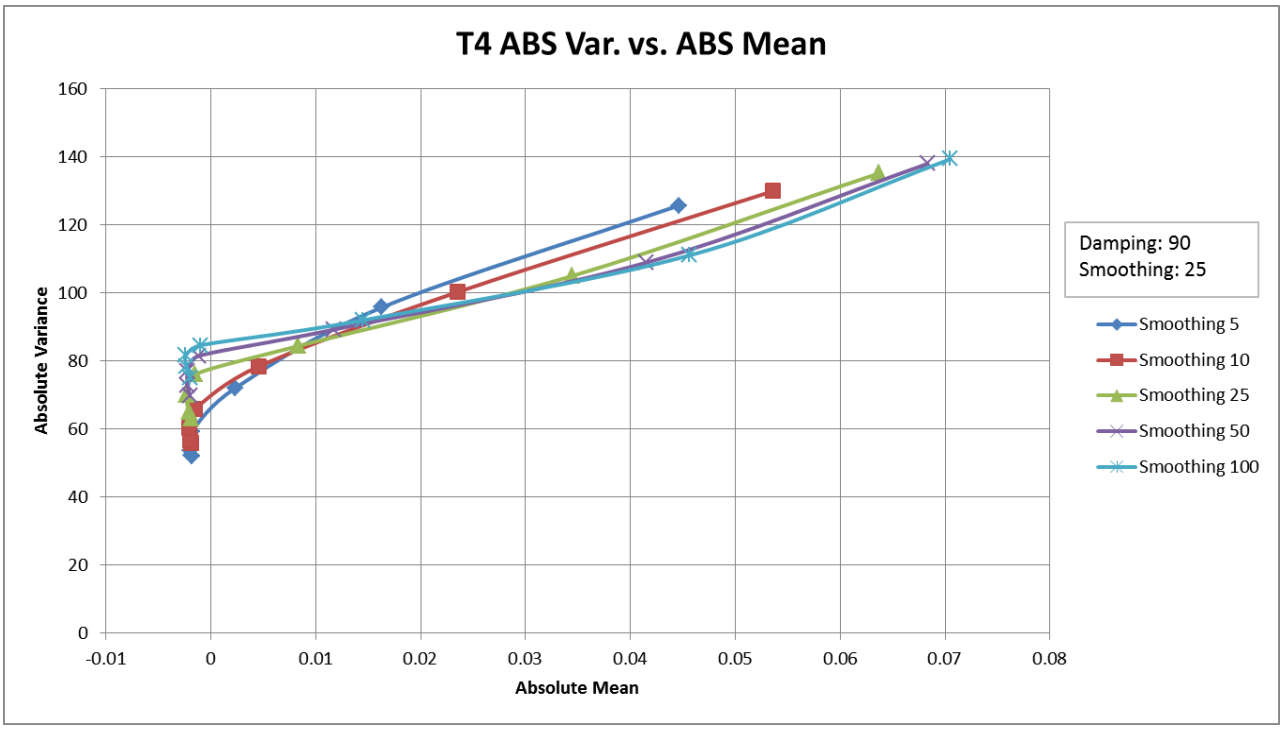

Figure B.10: Absolute variance versus absolute mean plot for Stope 4448's fourth time period.

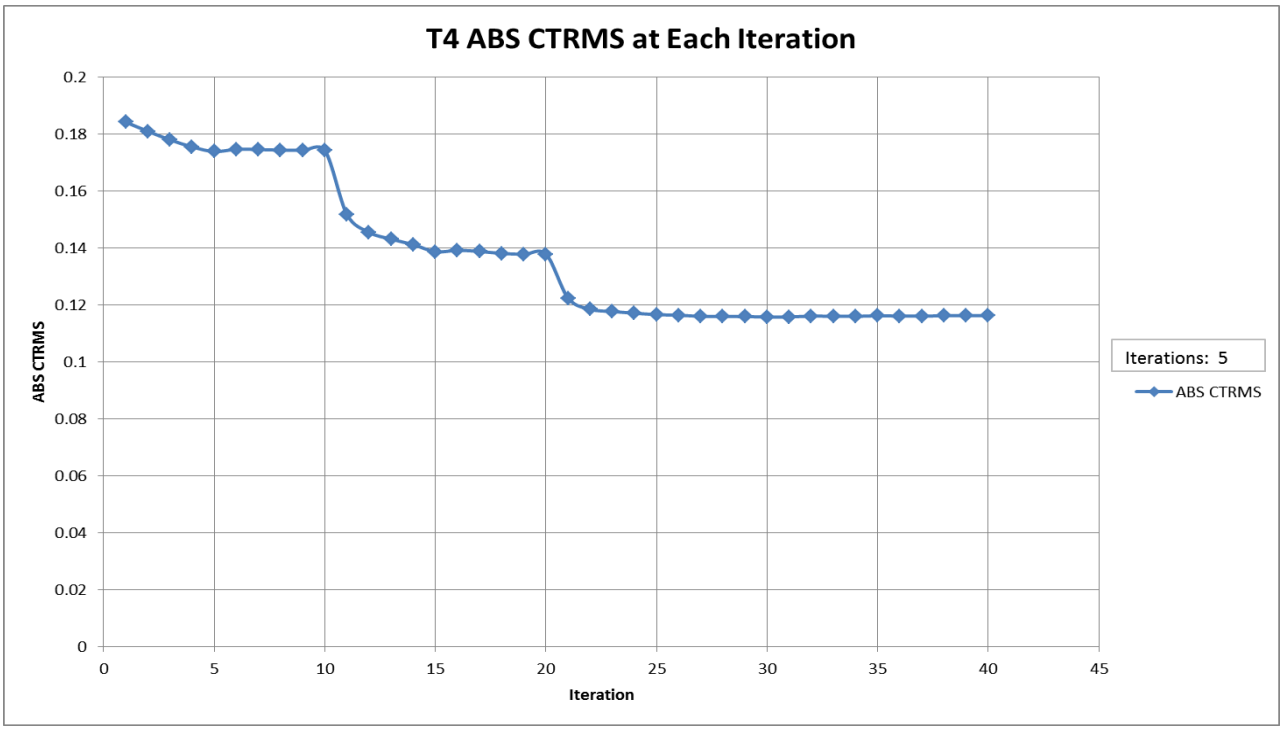

Figure B.11: Absolute CTRMS value for each iteration for Stope 4448's fourth time period.

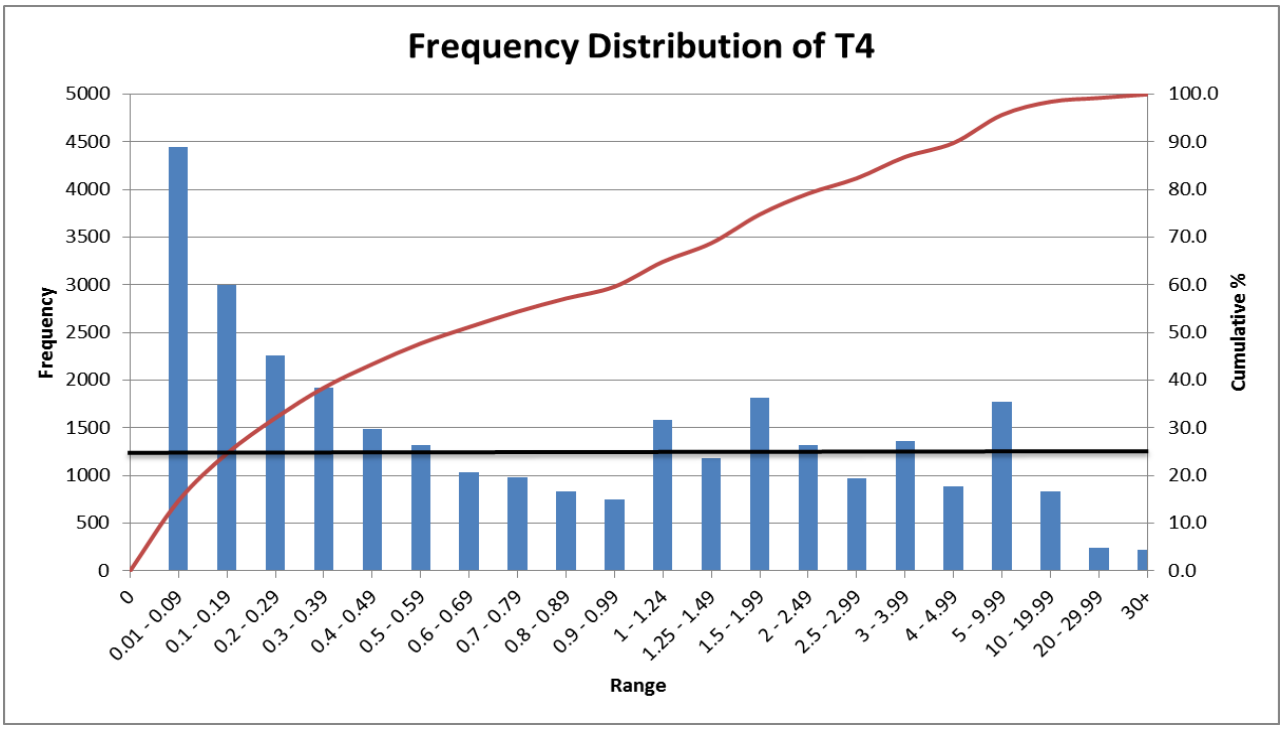

Figure B.12: Top 75% DWS cutoff value determination for Stope 4448's fourth time period.

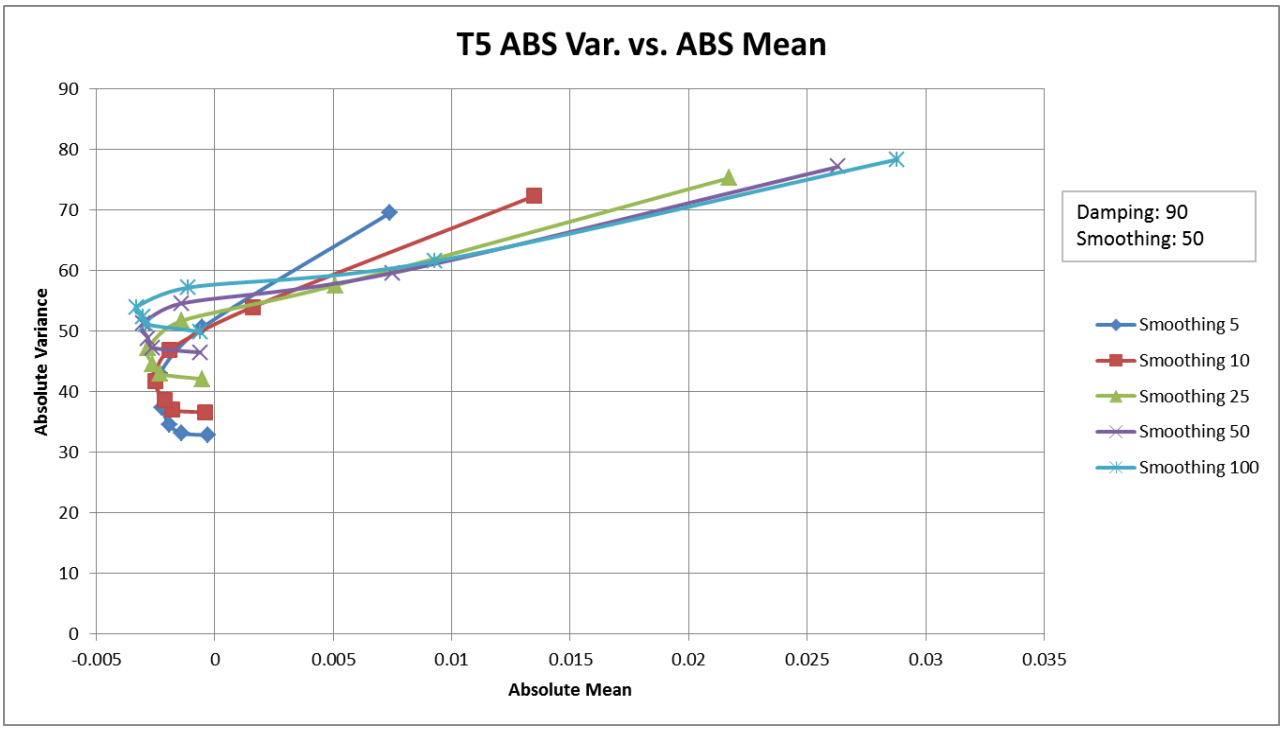

Figure B.13: Absolute variance versus absolute mean plot for Stope 4448's fifth time period.

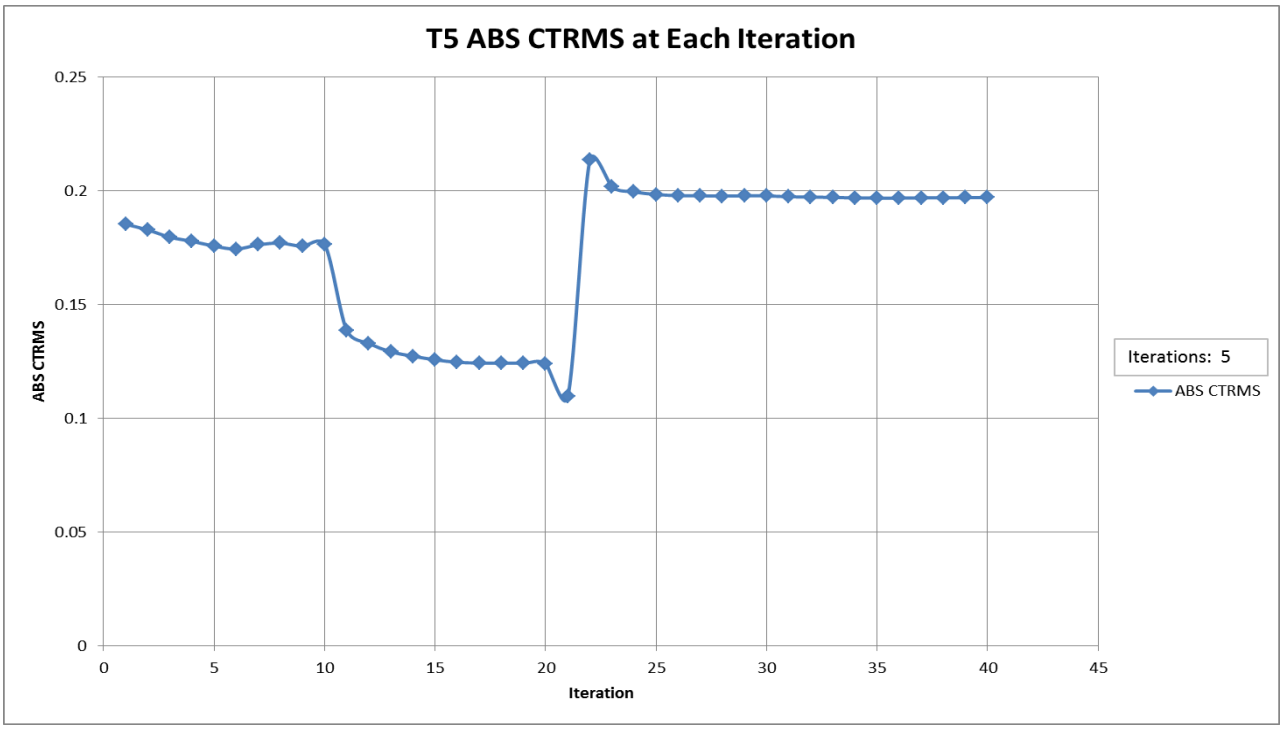

Figure B.14: Absolute CTRMS value for each iteration for Stope 4448's fifth time period.

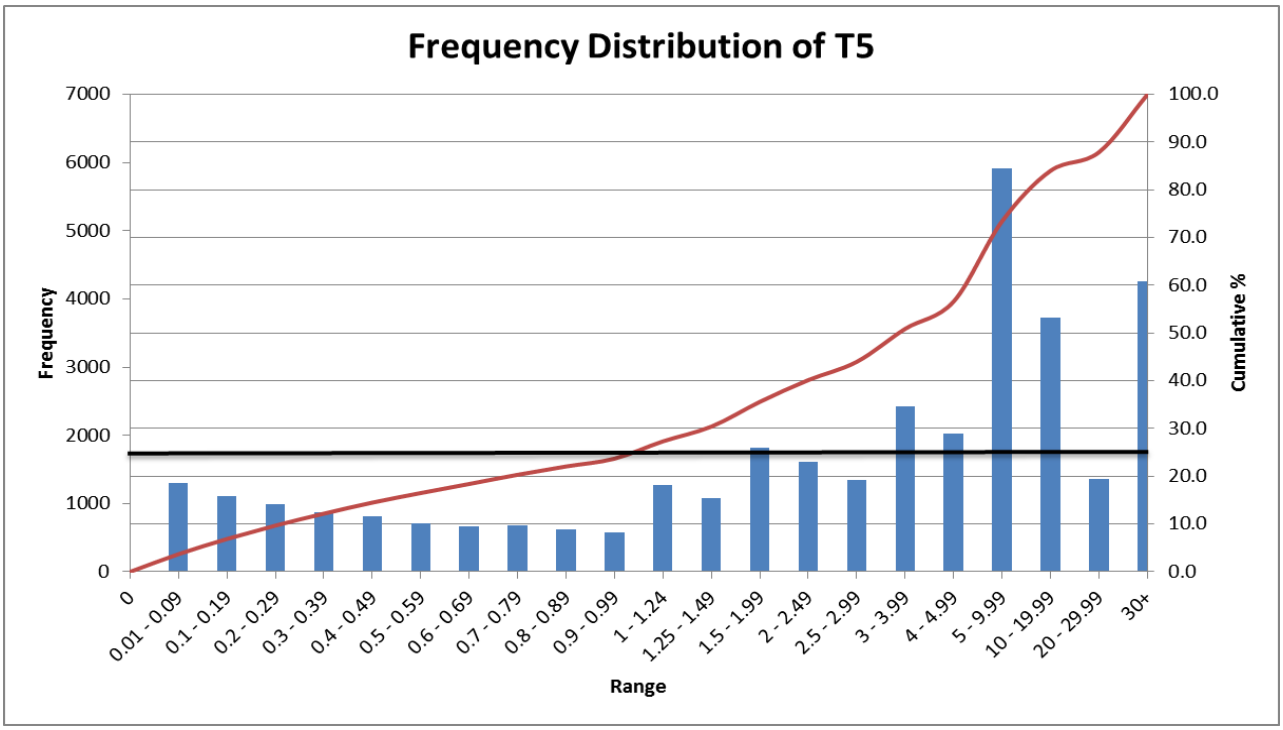

Figure B.15: Top 75% DWS cutoff value determination for Stope 4448's fifth time period.

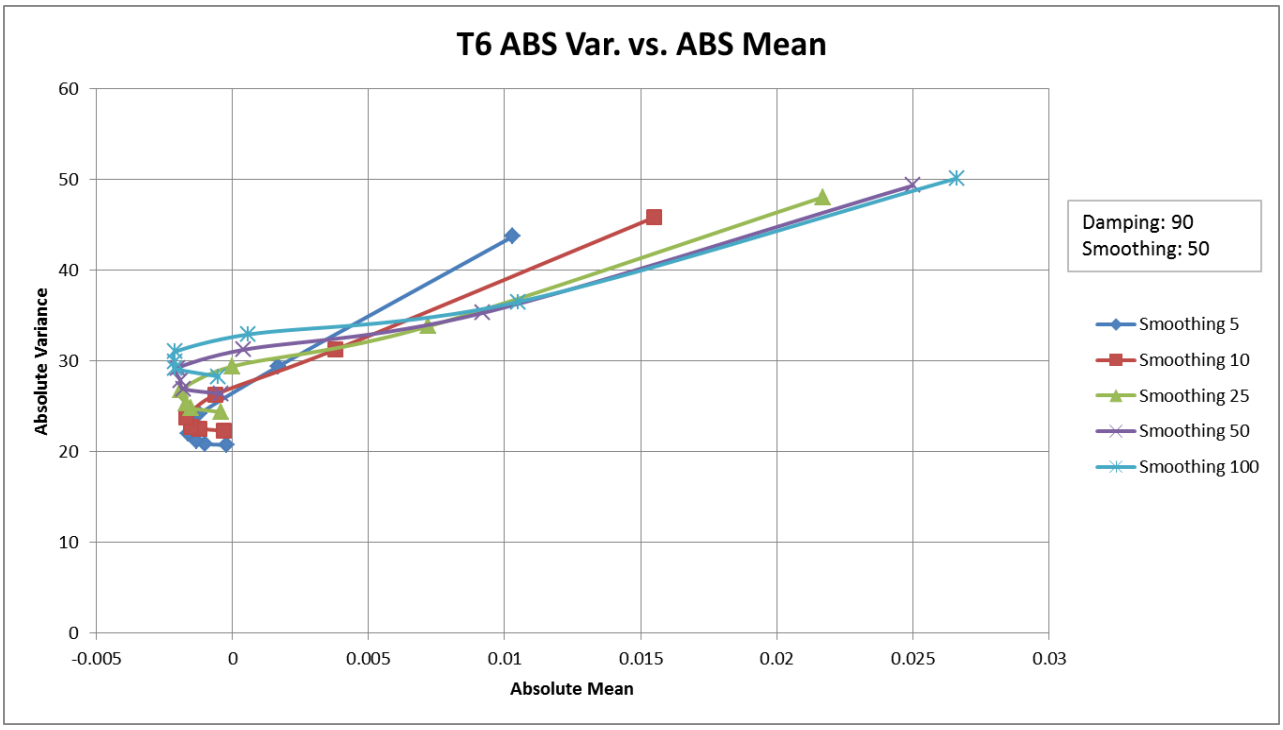

Figure B.16: Absolute variance versus absolute mean plot for Stope 4448's sixth time period.

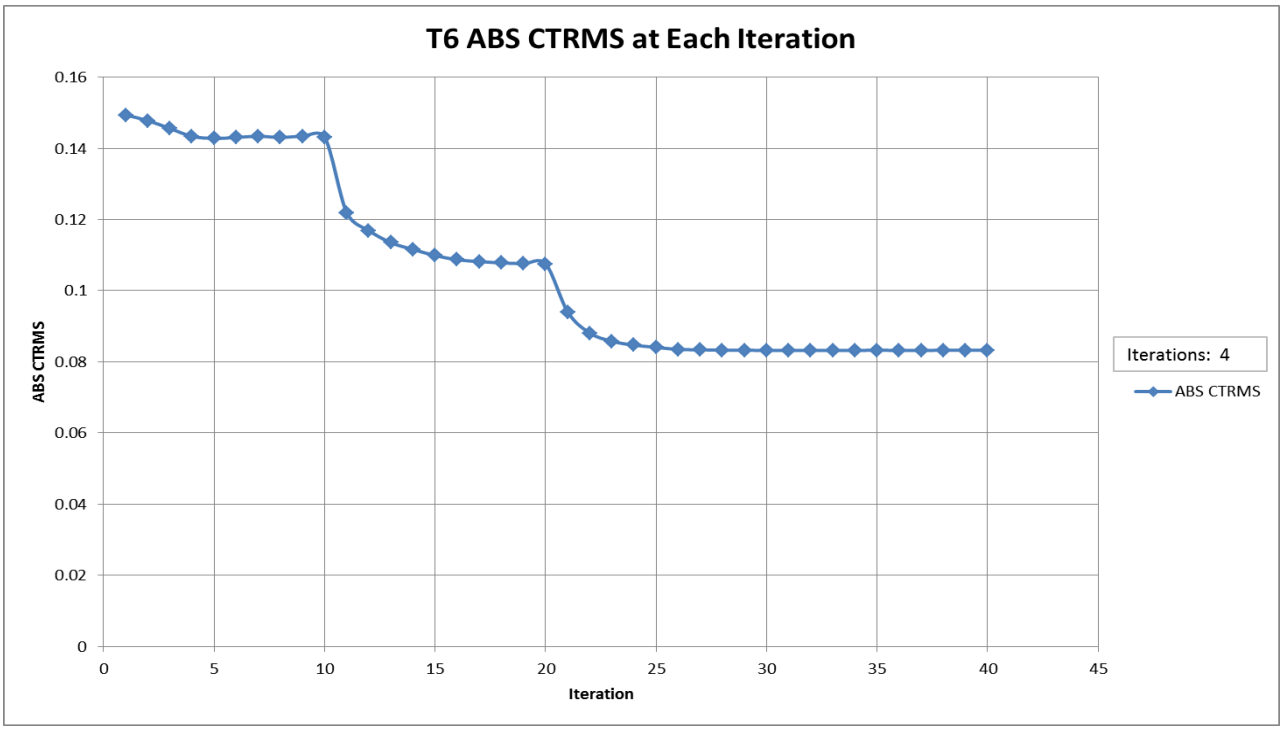

Figure B.17: Absolute CTRMS value for each iteration for Stope 4448's sixth time period.

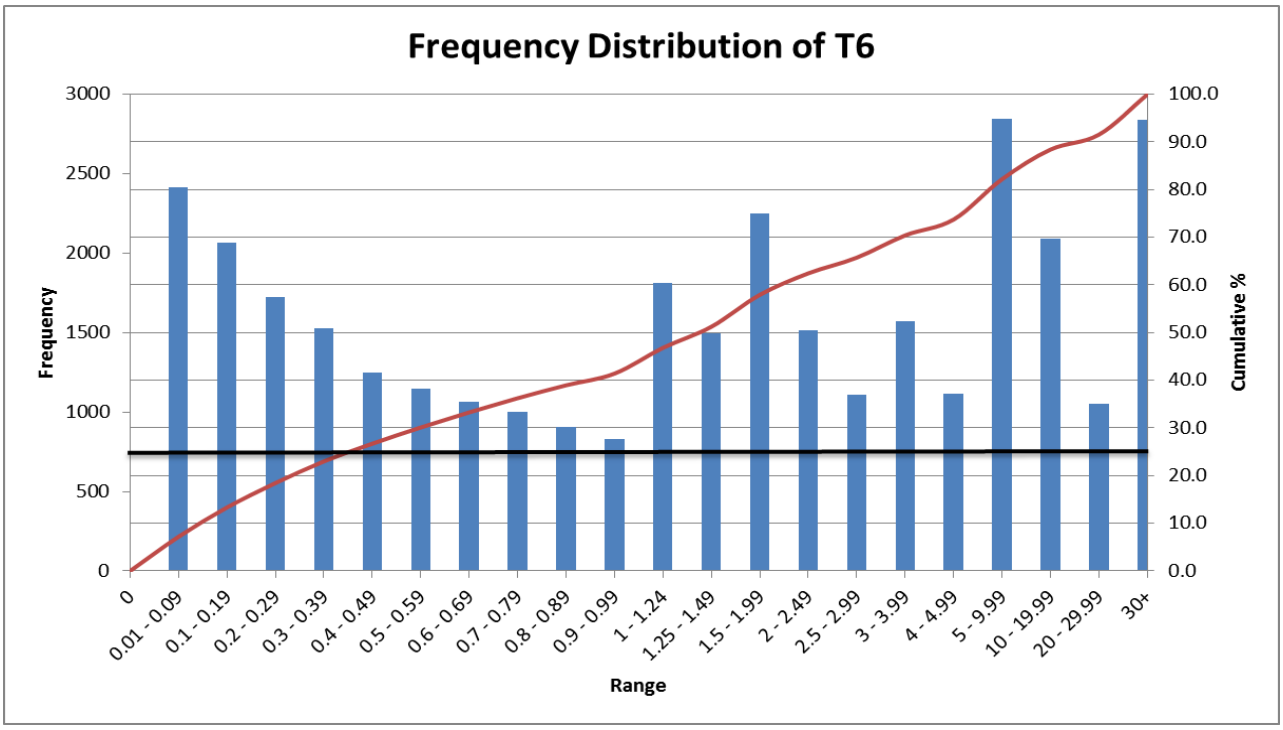

Figure B.18: Top 75% DWS cutoff value determination for Stope 4448's sixth time period.

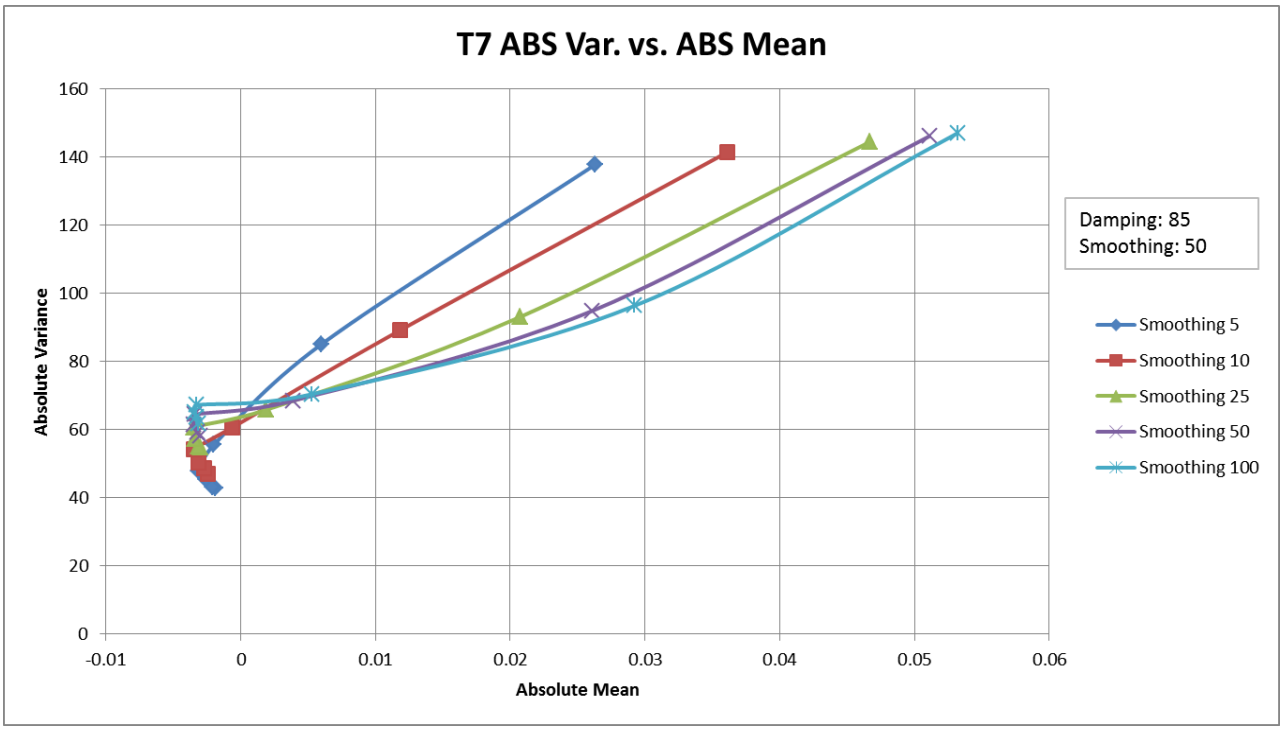

Figure B.19: Absolute variance versus absolute mean plot for Stope 4448's seventh time period.

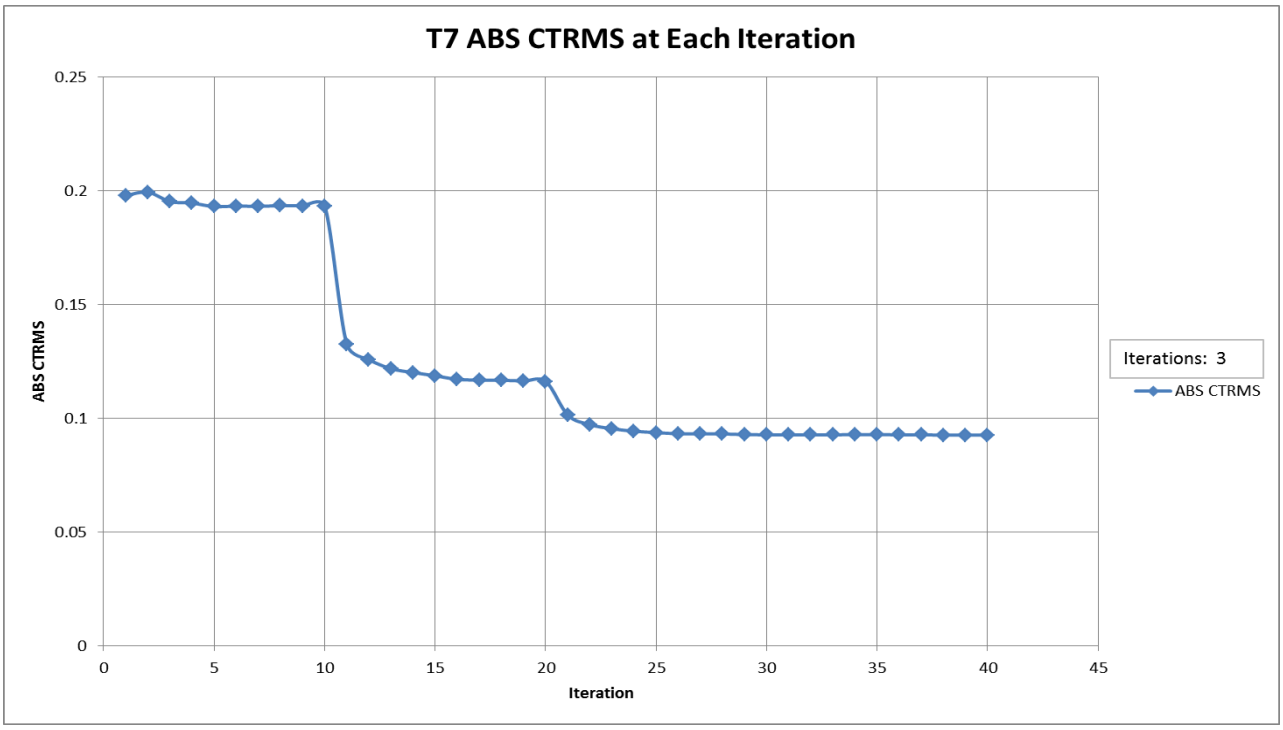

Figure B.20: Absolute CTRMS value for each iteration for Stope 4448's seventh time period.

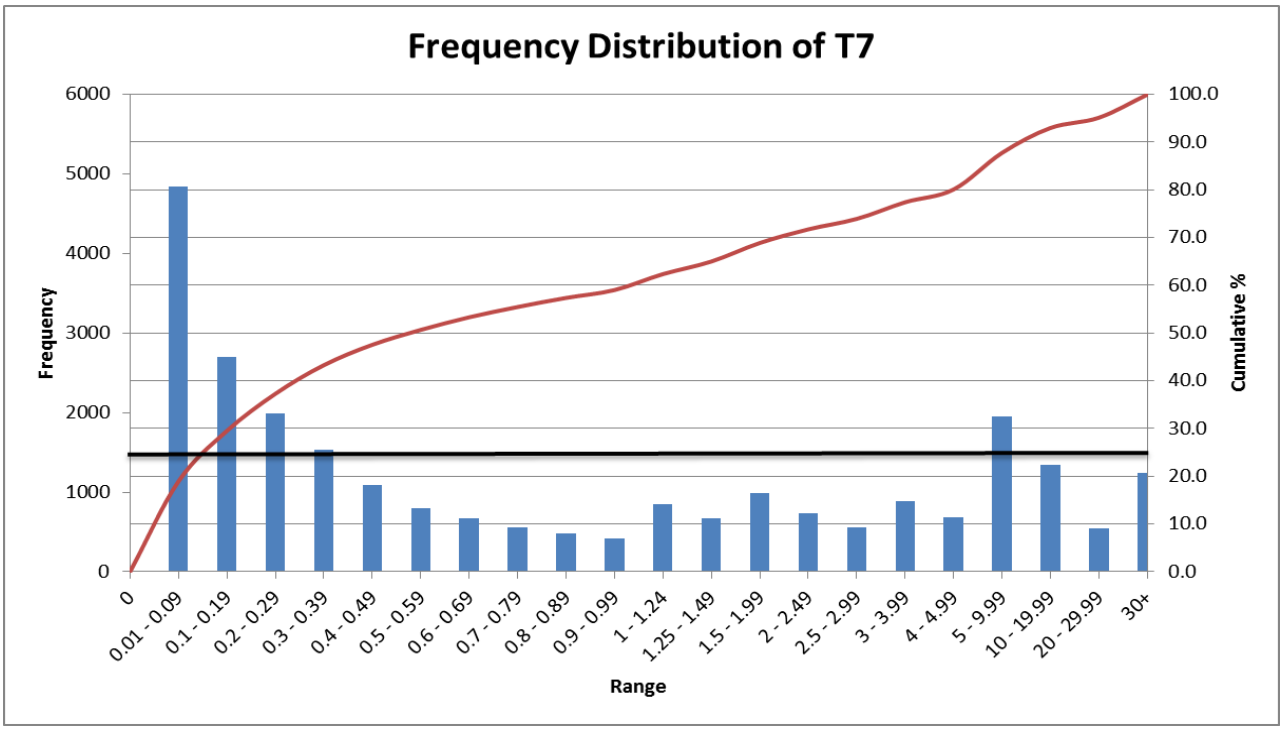

Figure B.21: Top 75% DWS cutoff value determination for Stope 4448's seventh time period.

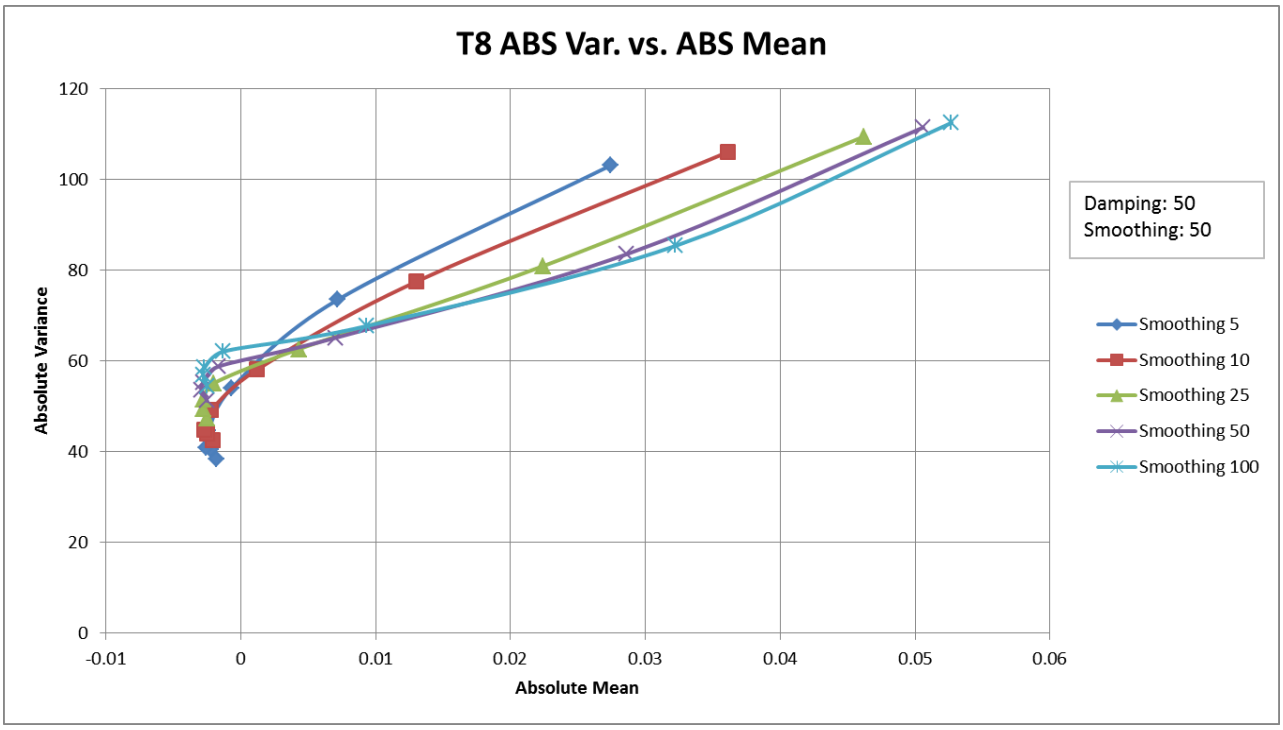

Figure B.22: Absolute variance versus absolute mean plot for Stope 4448's eighth time period.

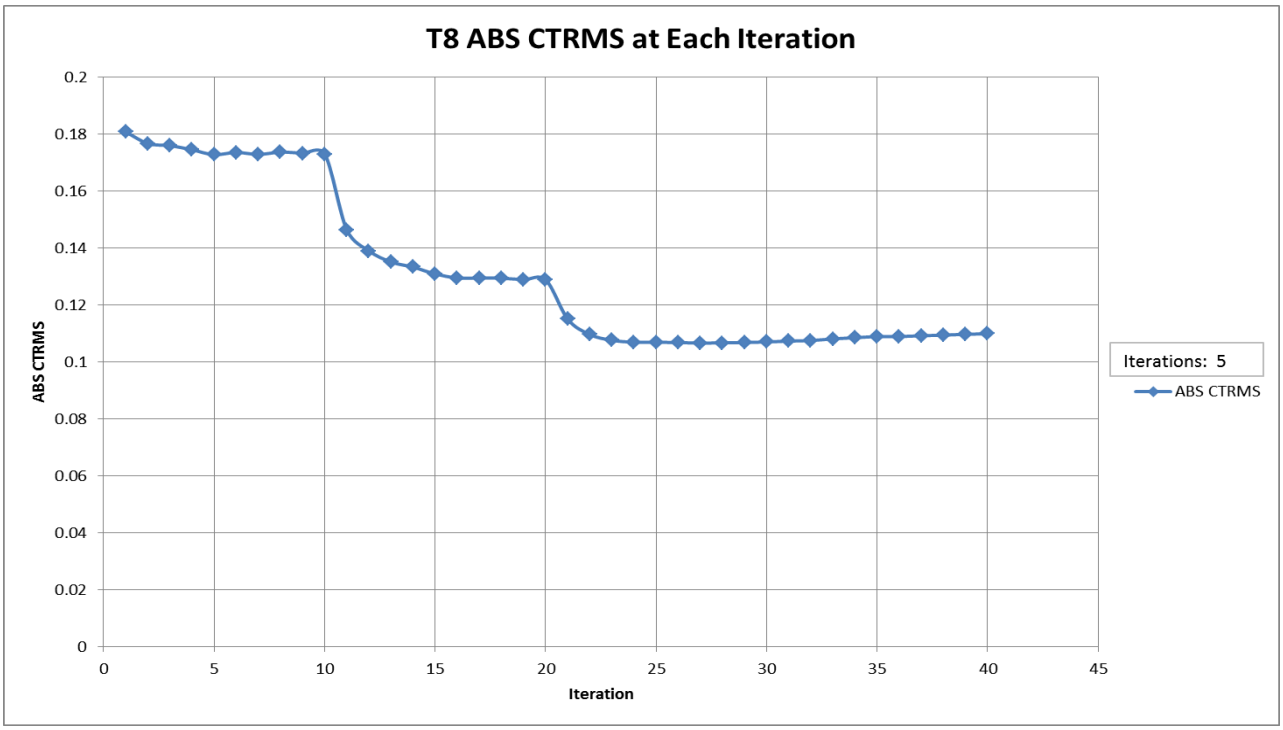

Figure B.23: Absolute CTRMS value for each iteration for Stope 4448's eighth time period.

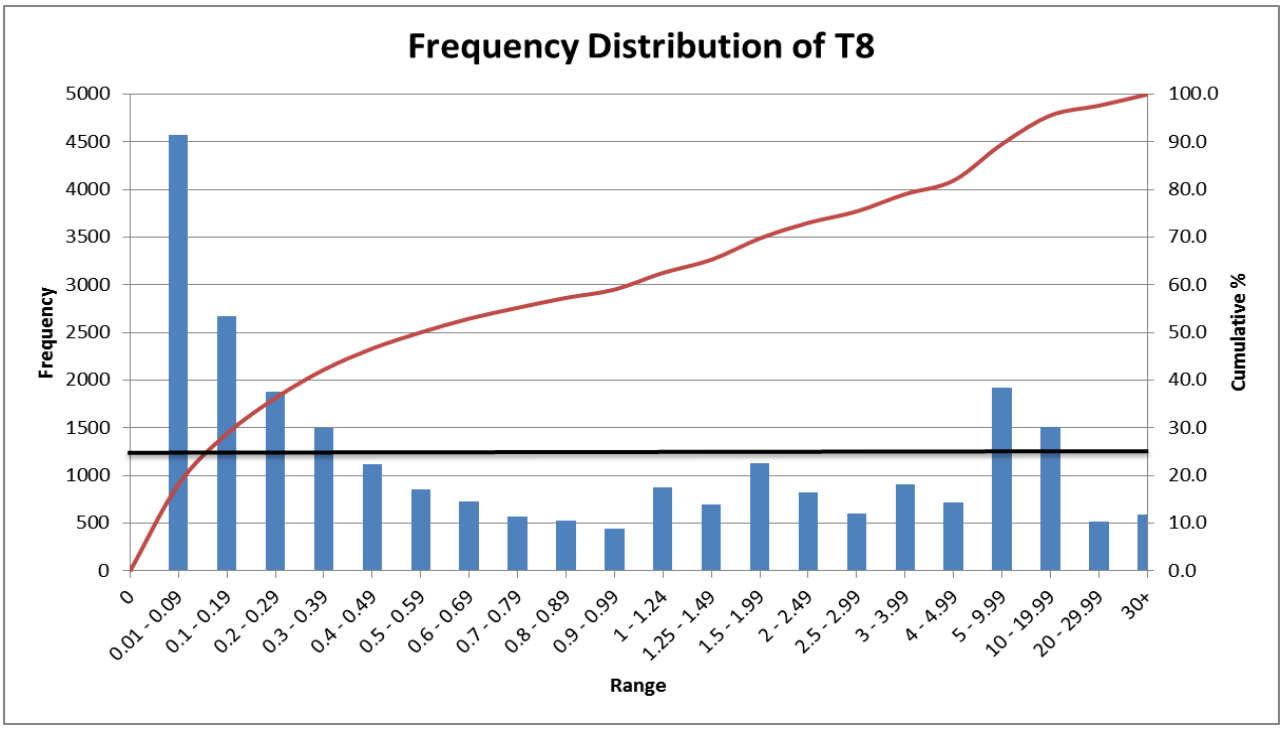

Figure B.24: Top 75% DWS cutoff value determination for Stope 4448's eighth time period.

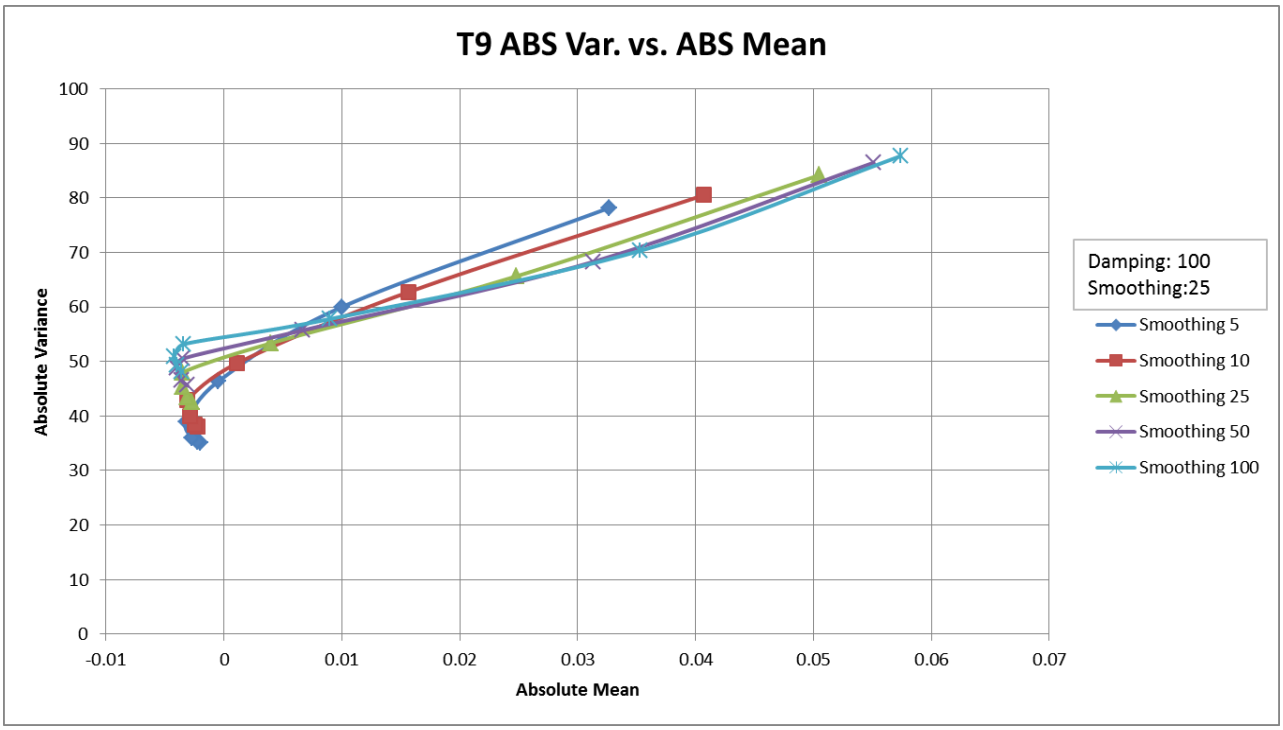

Figure B.25: Absolute variance versus absolute mean plot for Stope 4448's ninth time period.

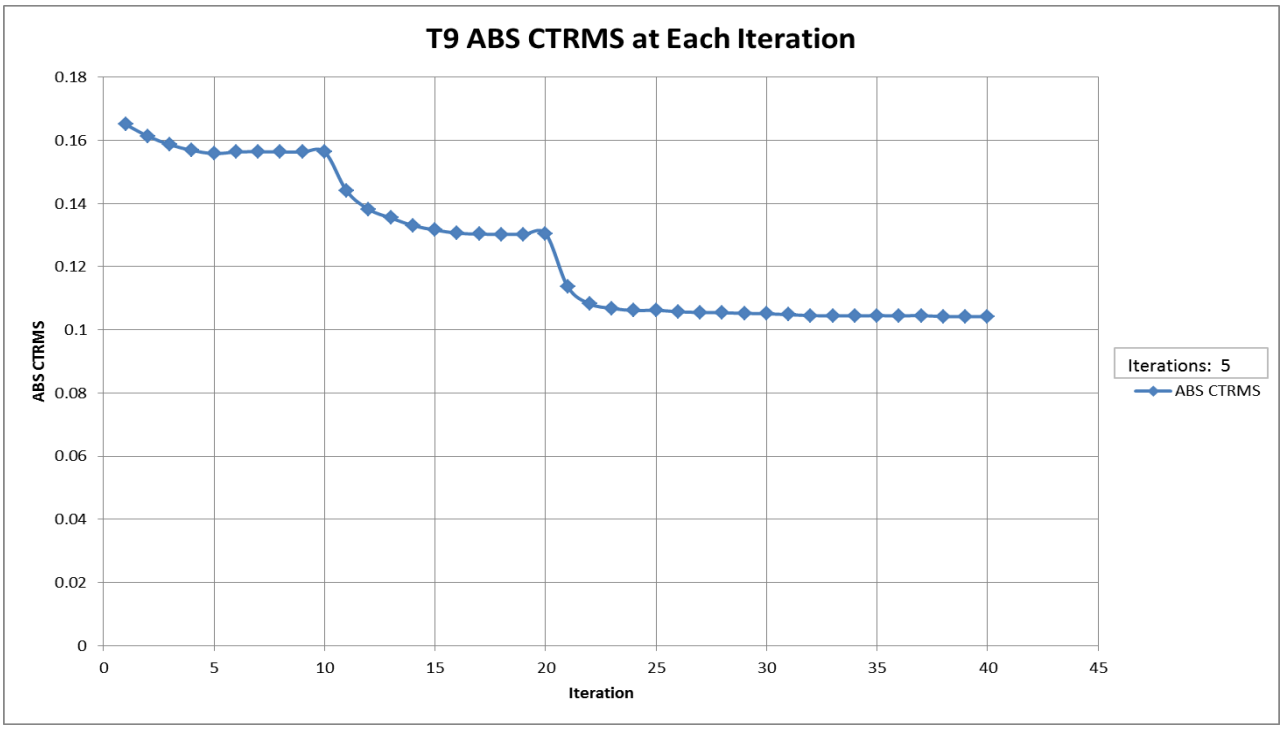

Figure B.26: Absolute CTRMS value for each iteration for Stope 4448's ninth time period.

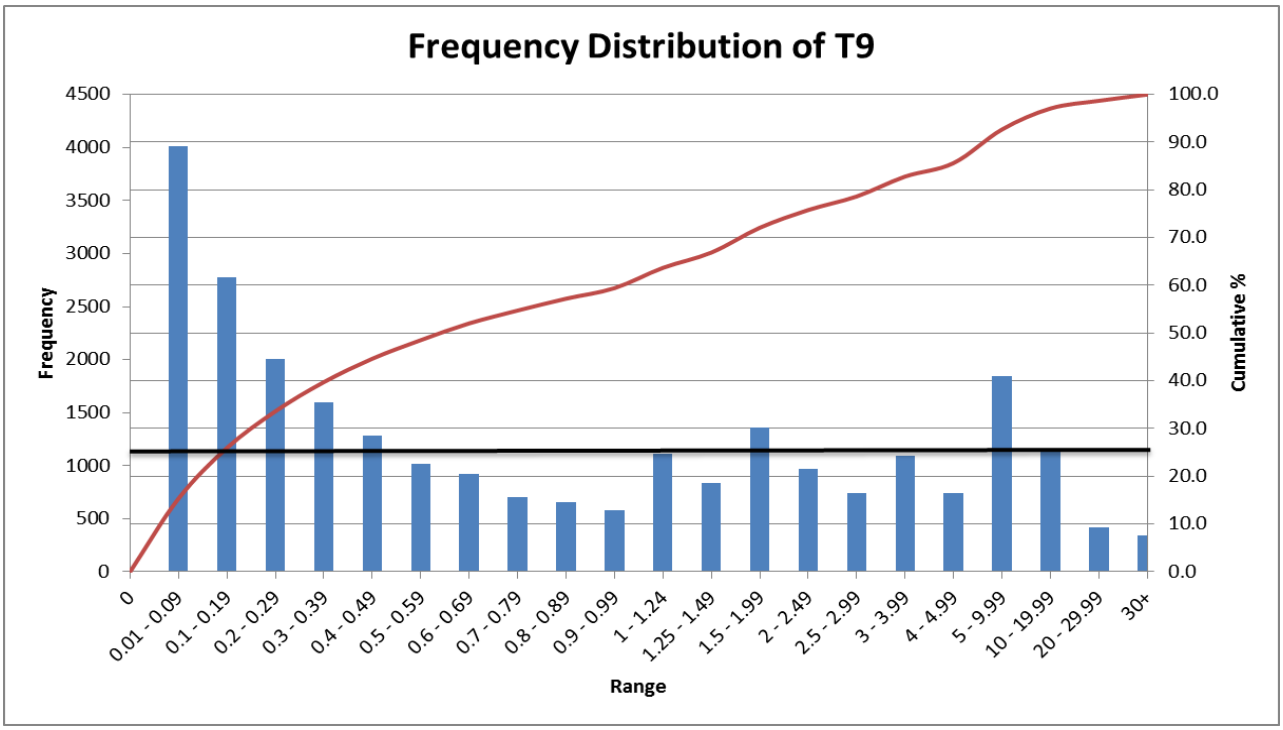

Figure B.27: Top 75% DWS cutoff value determination for Stope 4448's ninth time period.

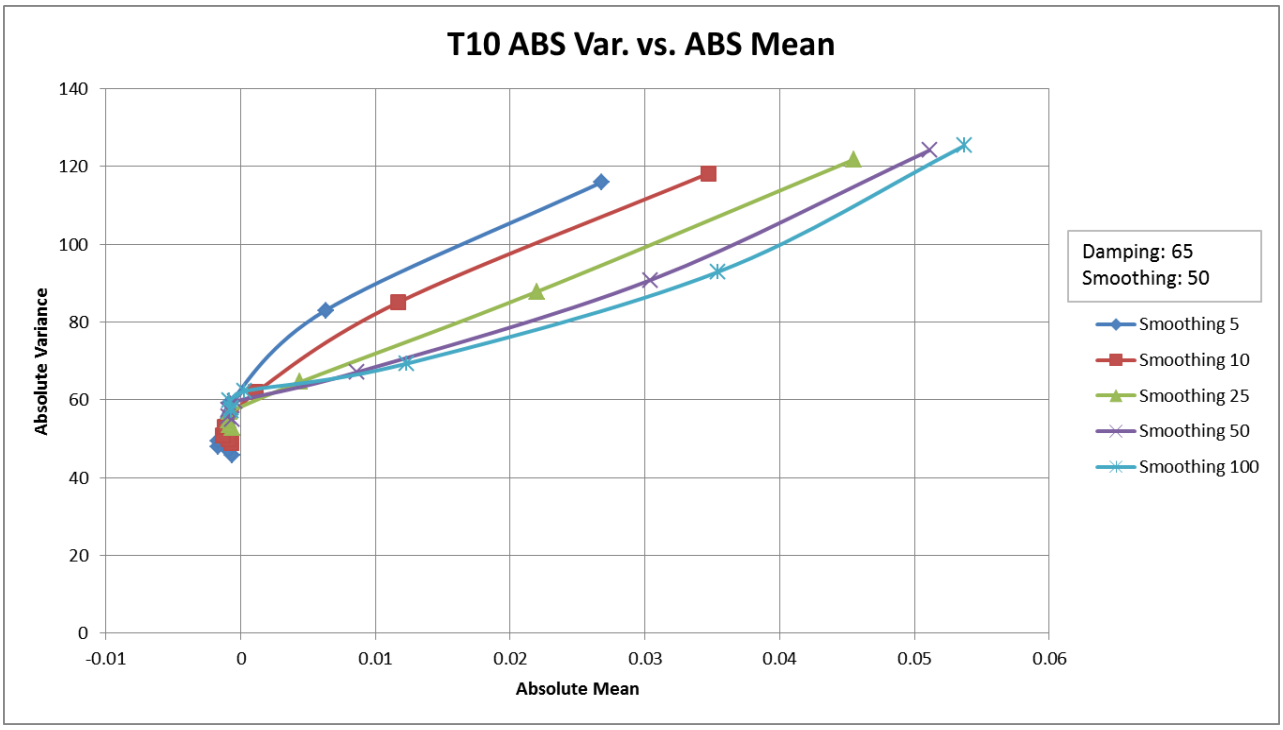

Figure B.28: Absolute variance versus absolute mean plot for Stope 4448's tenth time period.

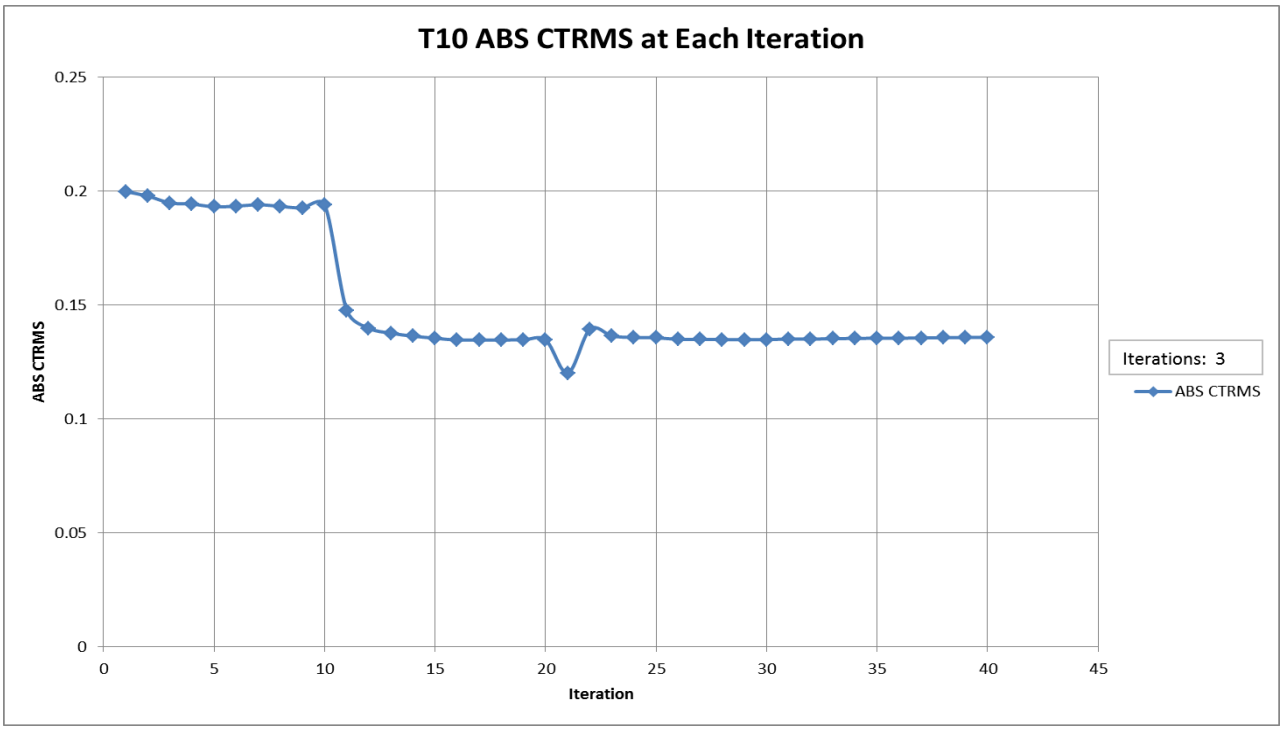

Figure B.29: Absolute CTRMS value for each iteration for Stope 4448's tenth time period.

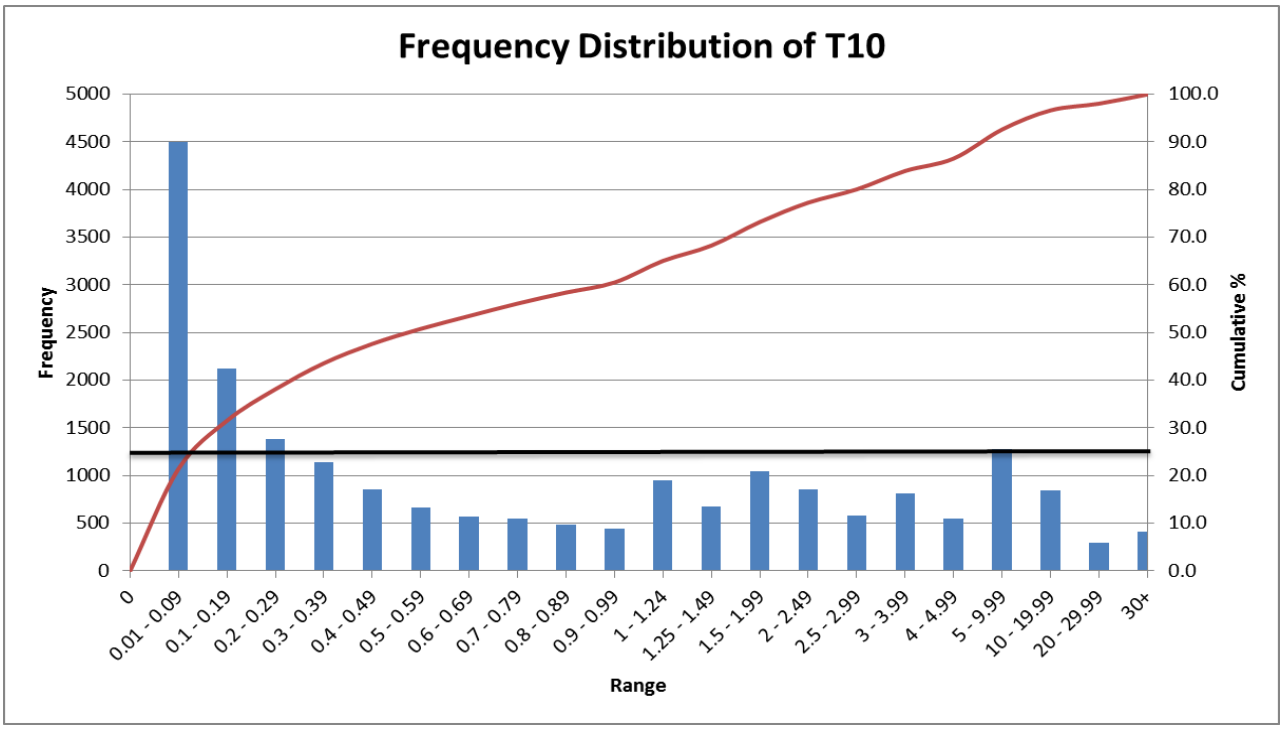

Figure B.30: Top 75% DWS cutoff value determination for Stope 4448's tenth time period.

Appendix C – Event Cluster Methods

Appendix C will include pertinent information used to create the resulting tomograms of the stope scale study for the cluster of events. The breakdown of the five time periods will be illustrated initially, followed by plots to determine weighting (illustrated as smoothing) and damping, number of iterations, and the top 75% DWS cutoff value; time periods one through three indicate grouping one of events for the cluster, with three through five being for grouping two of the events in the cluster. All plots for a given time period will be introduced together, beginning with weighting and damping, followed by number of iterations, and ending with top 75% DWS cutoff value. On the top 75% DWS cutoff value plots, the histogram utilizes the primary Y axis while the cumulative percent line chart is plotted on the secondary Y axis.

Table C.1: Time period details for the event cluster.

Period	Date Beg	Date End	Number of Days	Number of Events
1	1/18/2009	1/24/2009	7	529
2	1/25/2009	1/31/2009	7	505
3	2/1/2009	2/6/2009	6	333
4	2/7/2009	2/13/2009	7	801
5	2/14/2009	2/16.25/2009	2.25	1197

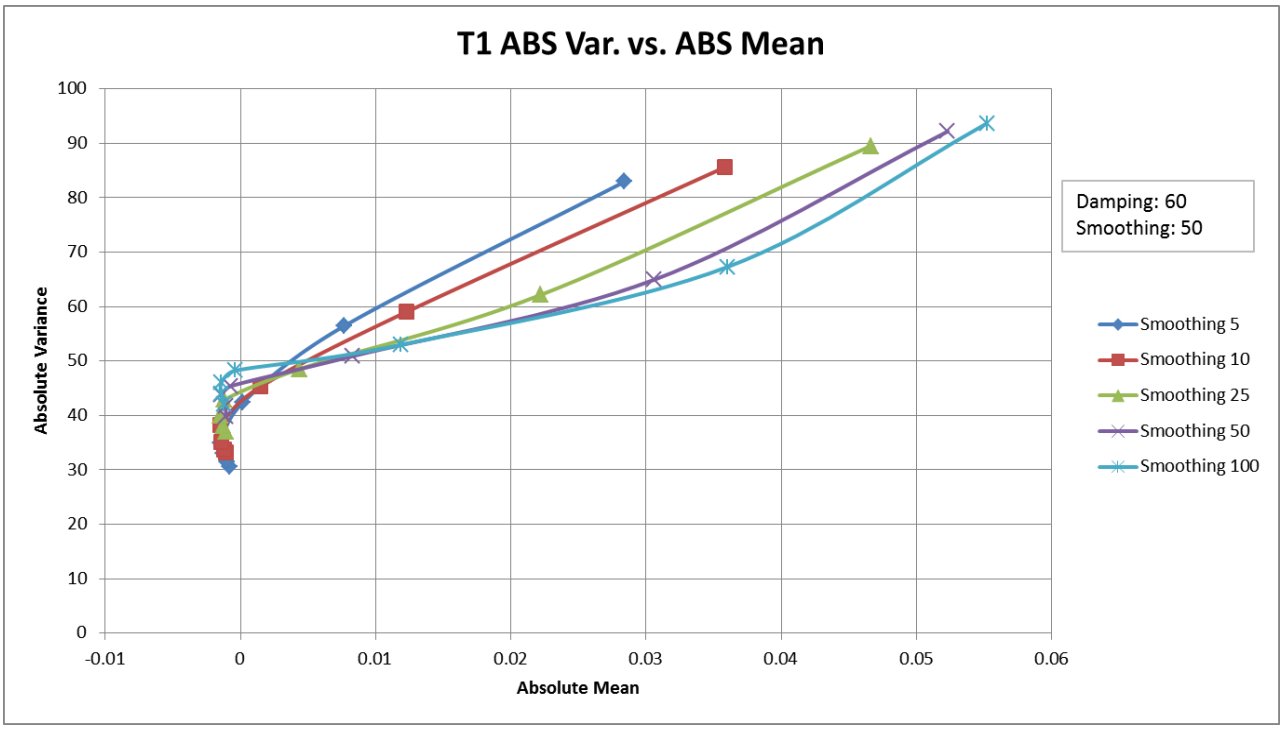

Figure C.1: Absolute variance versus absolute mean plot for the event cluster's first time period.

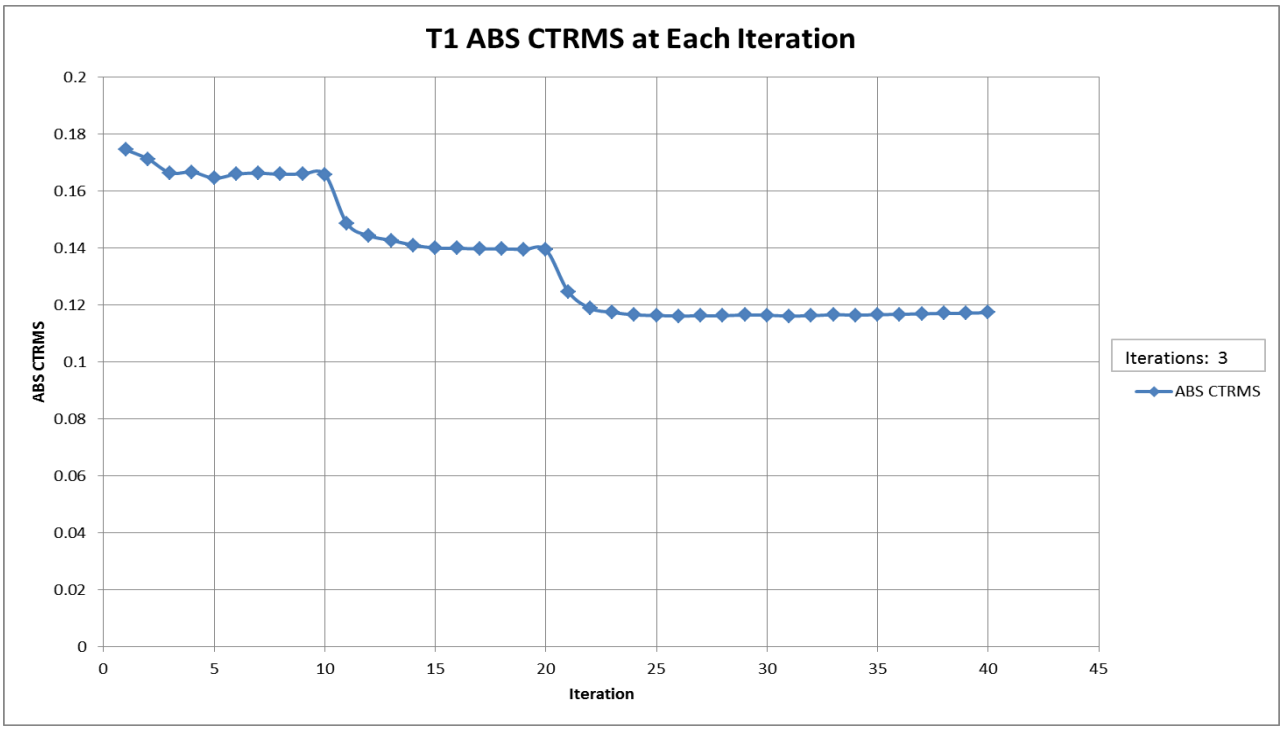

Figure C.2: Absolute CTRMS value for each iteration for the event cluster's first time period.

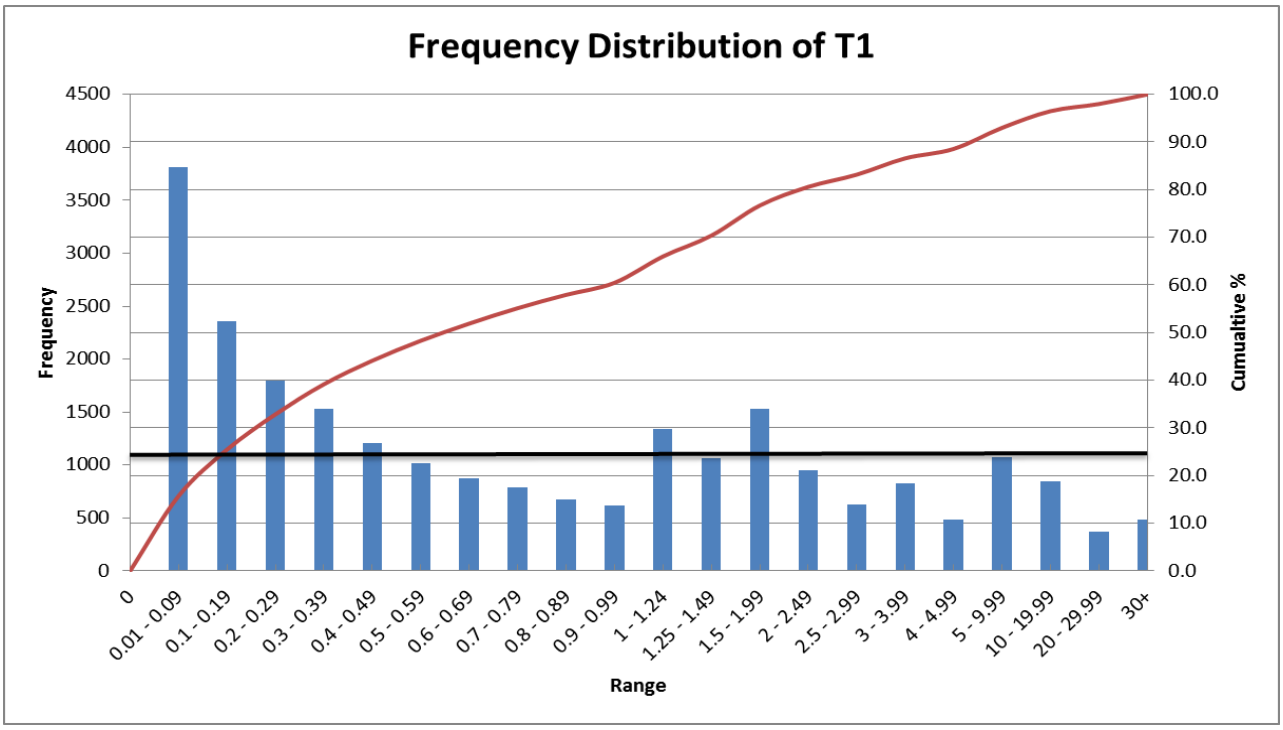

Figure C.3: Top 75% DWS cutoff value determination for the event cluster's first time period.

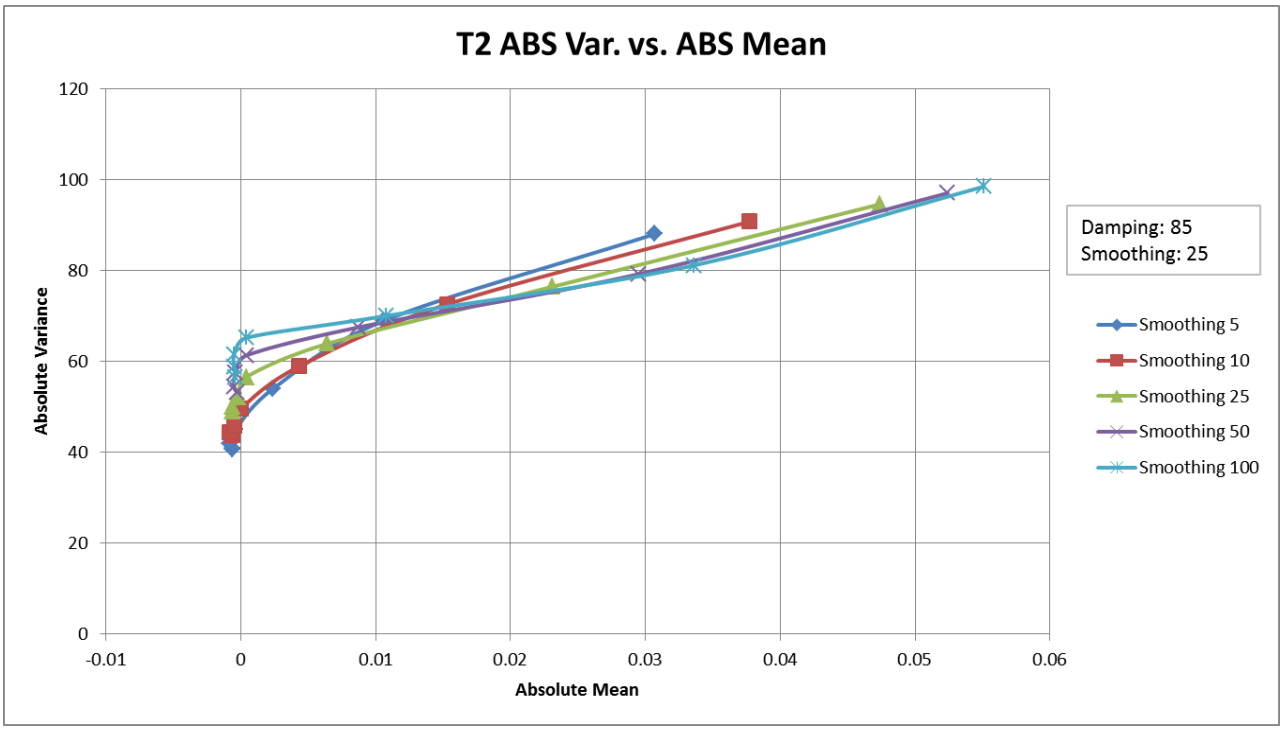

Figure C.4: Absolute variance versus absolute mean plot for the event cluster's second time period.

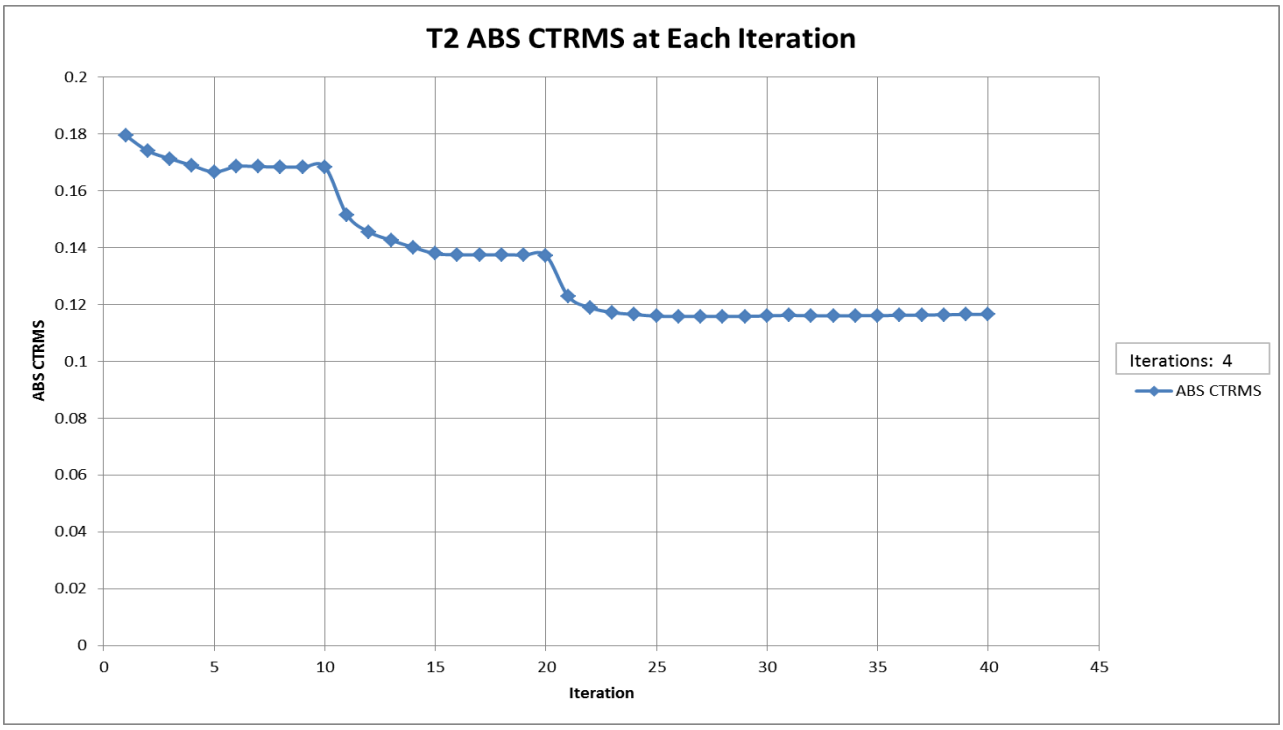

Figure C.5: Absolute CTRMS value for each iteration for the event cluster's second time period.

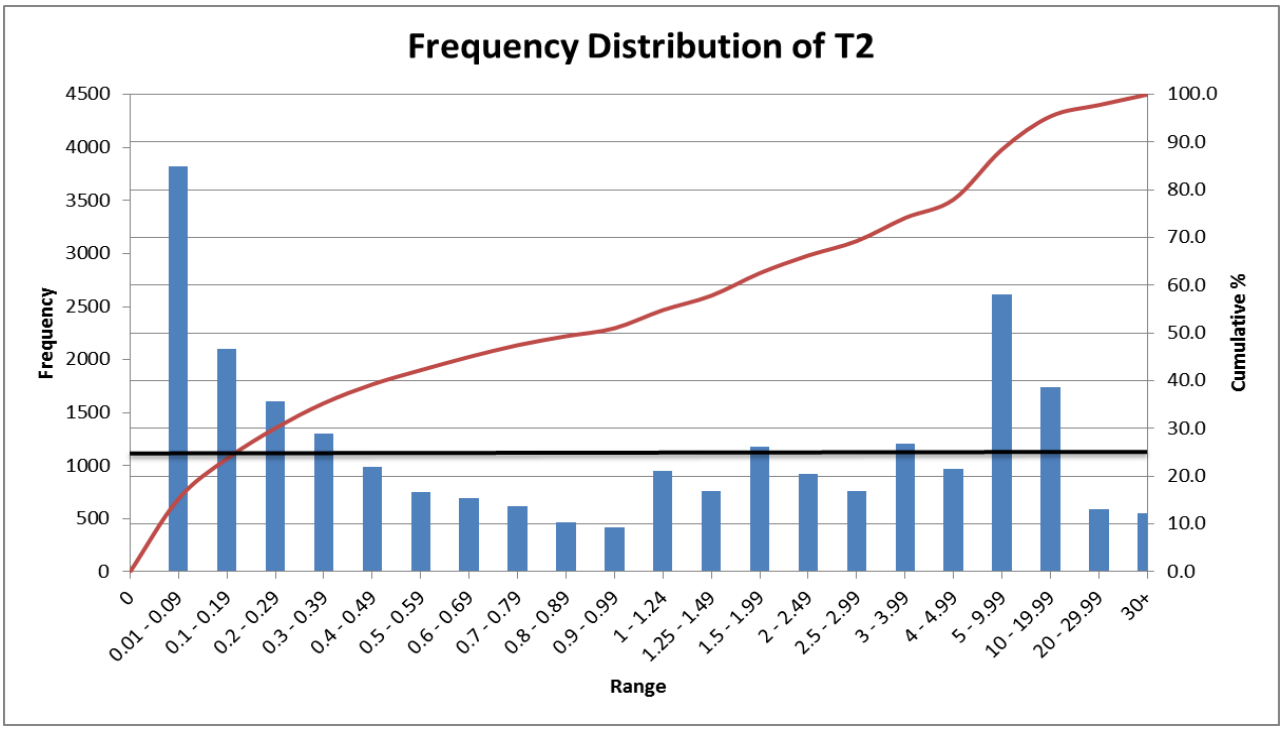

Figure C.6: Top 75% DWS cutoff value determination for the event cluster's second time period.

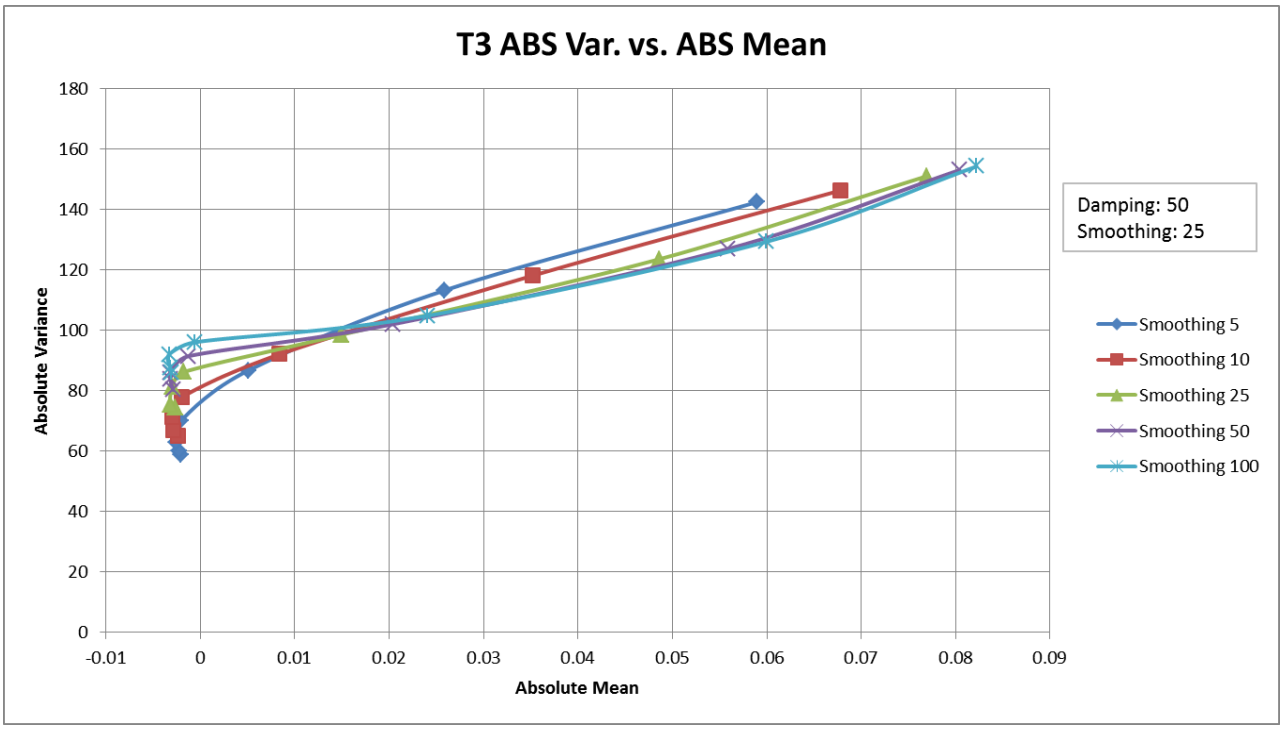

Figure C.7: Absolute variance versus absolute mean plot for the event cluster's third time period.

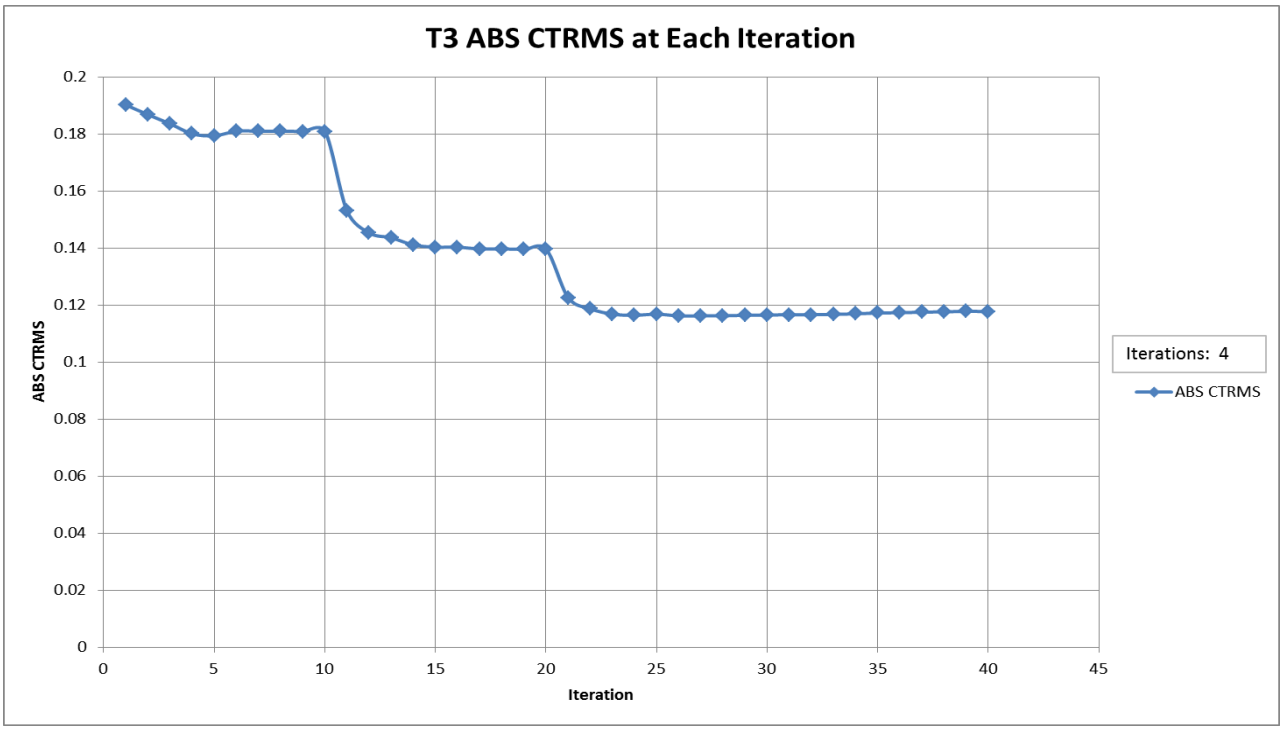

Figure C.8: Absolute CTRMS value for each iteration for the event cluster's third time period.

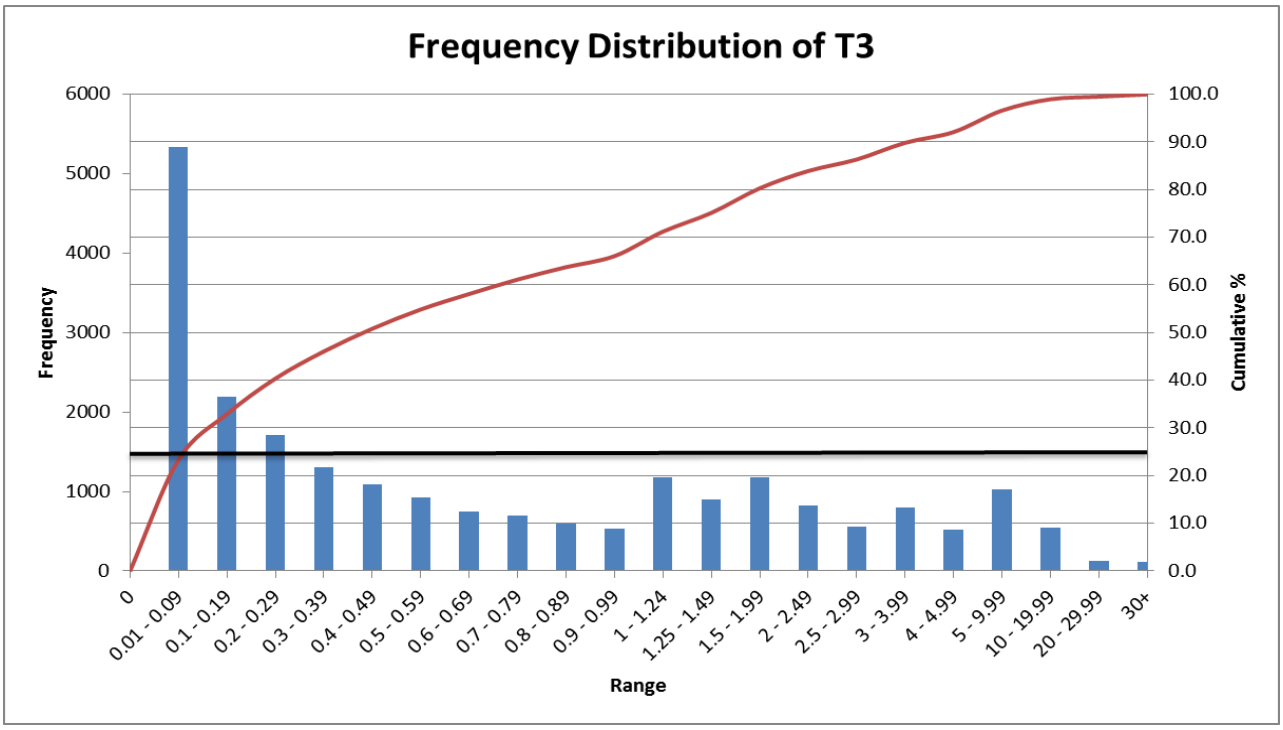

Figure C.9: Top 75% DWS cutoff value determination for the event cluster's third time period.

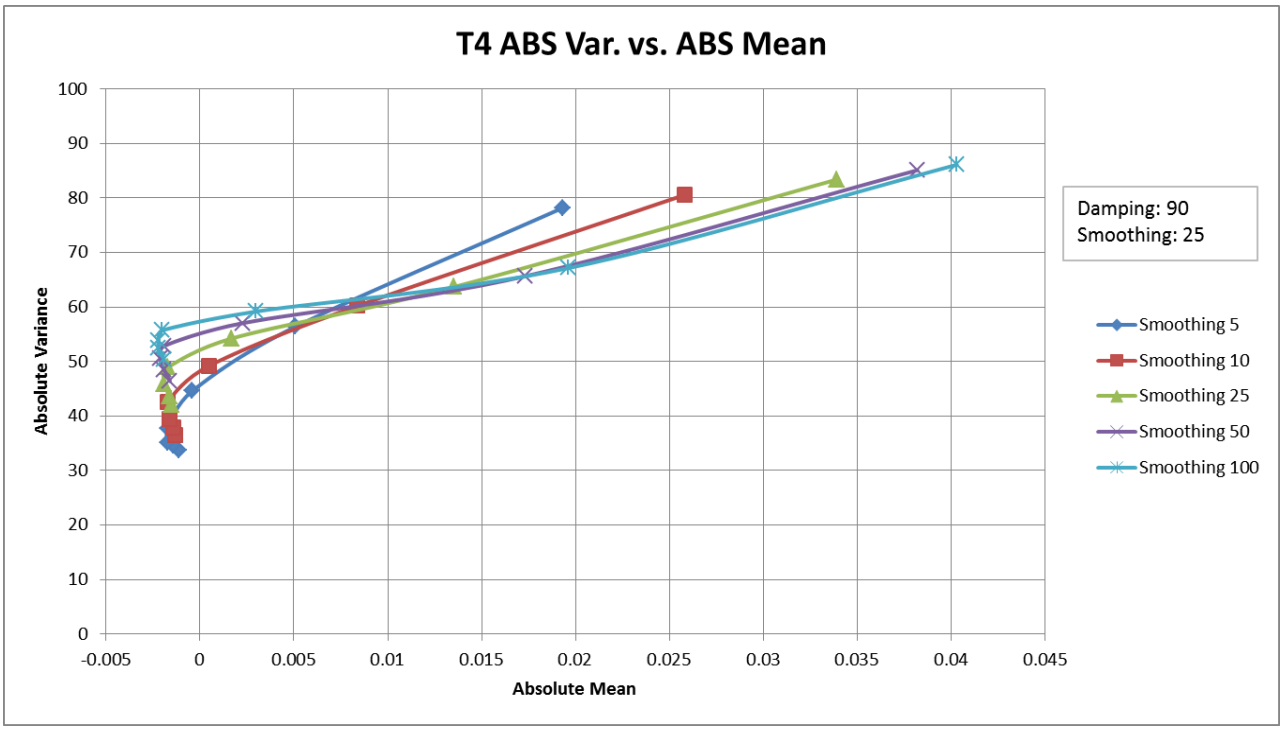

Figure C.10: Absolute variance versus absolute mean plot for the event cluster's fourth time period.

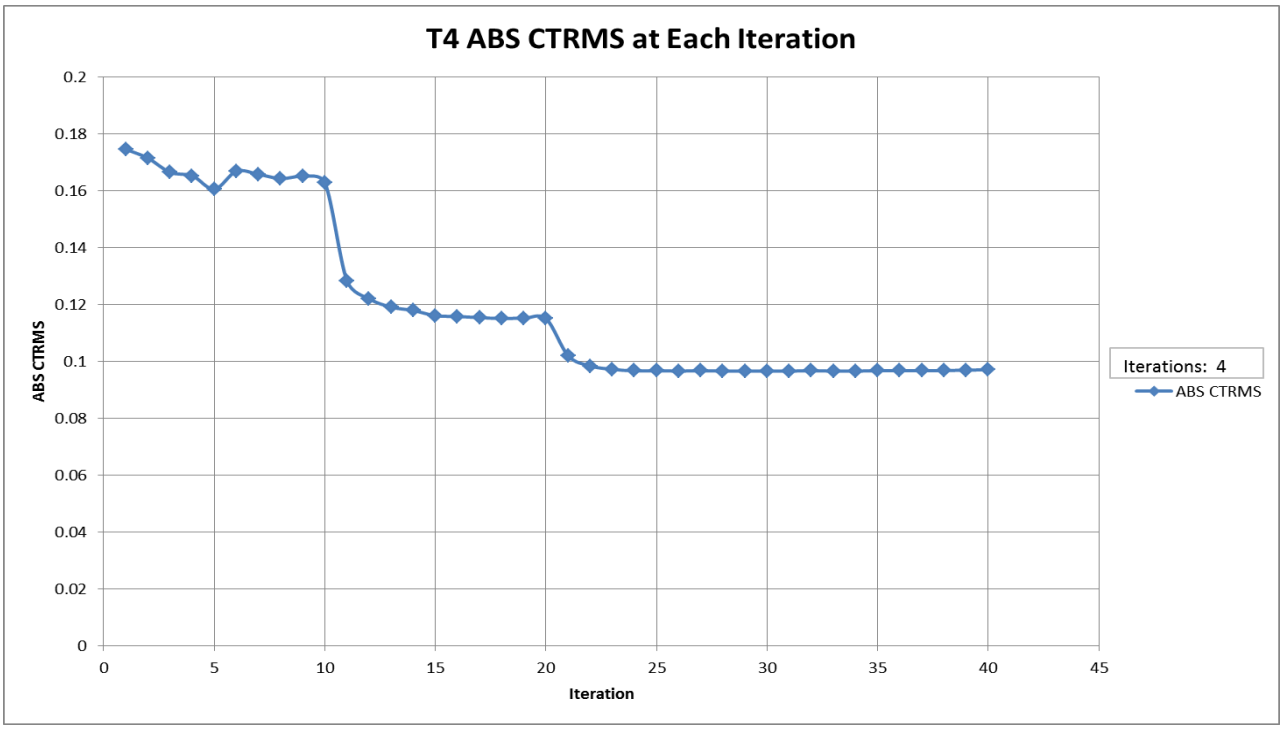

Figure C.11: Absolute CTRMS value for each iteration for the event cluster's fourth time period.

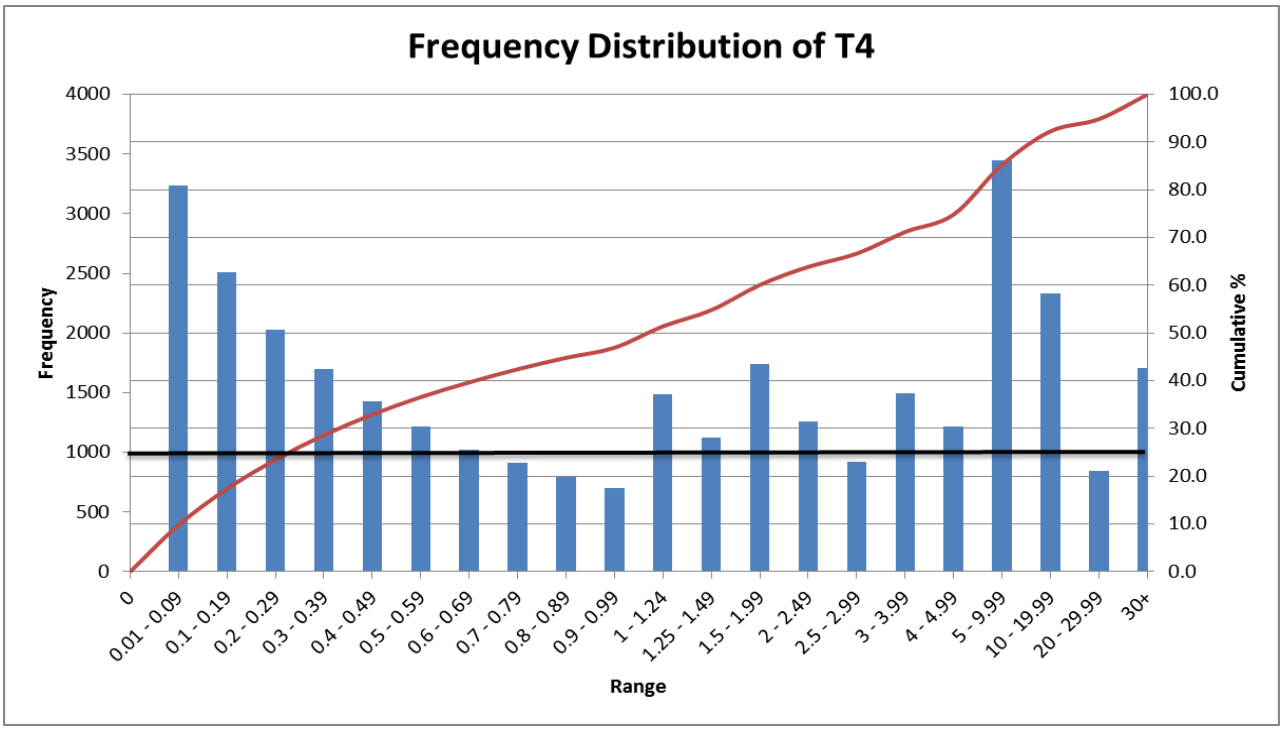

Figure C.12: Top 75% DWS cutoff value determination for the event cluster's fourth time period.

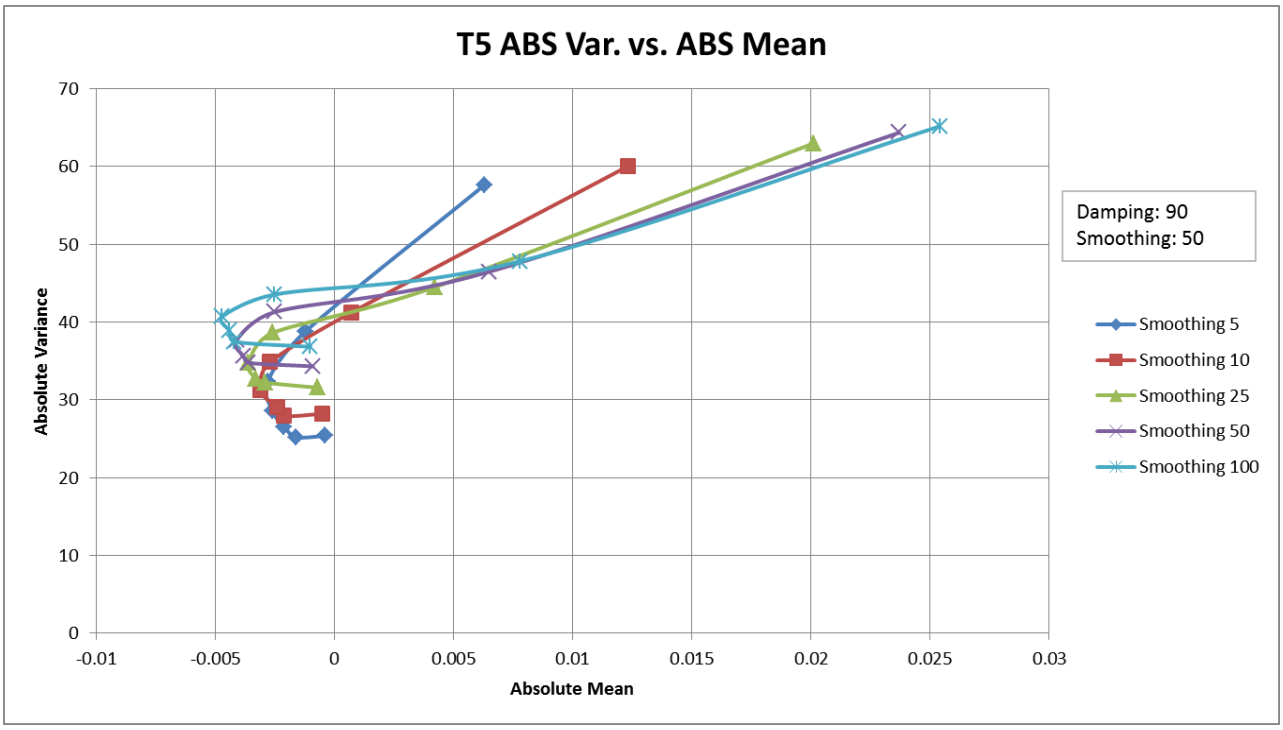

Figure C.13: Absolute variance versus absolute mean plot for the event cluster's fifth time period.

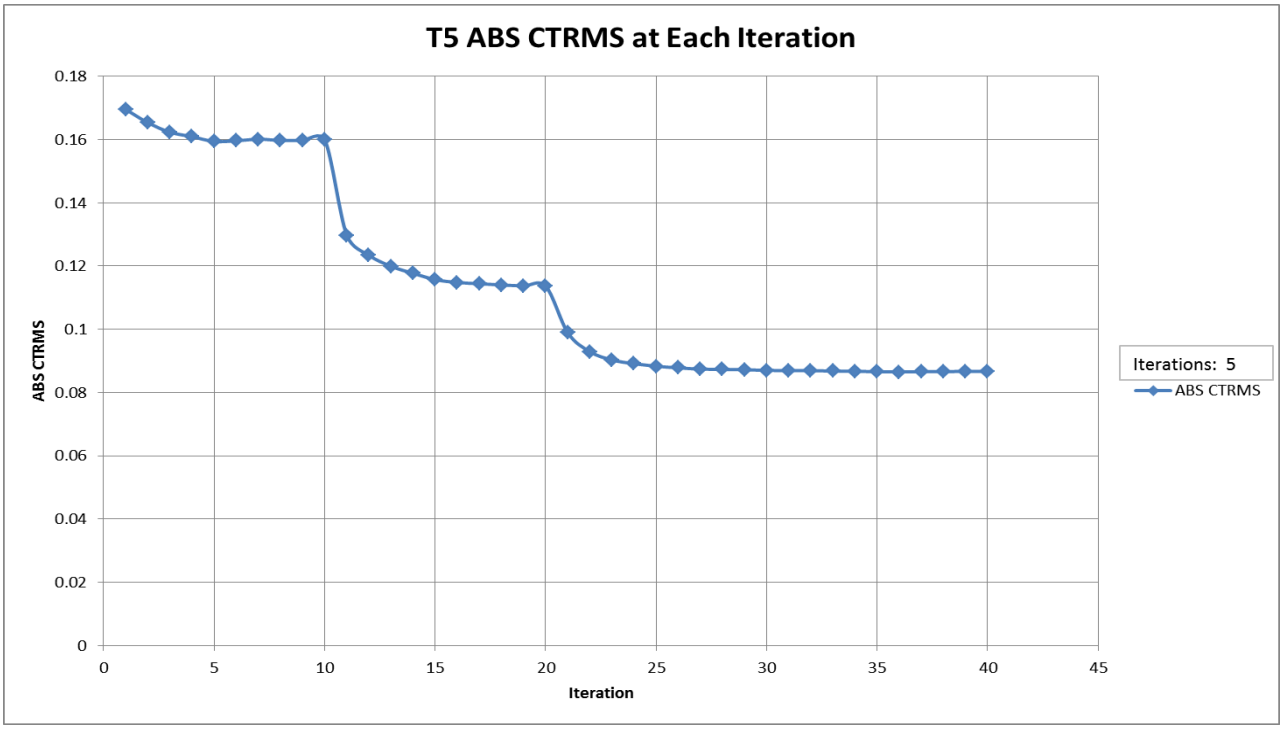

Figure C.14: Absolute CTRMS value for each iteration for the event cluster's fifth time period.

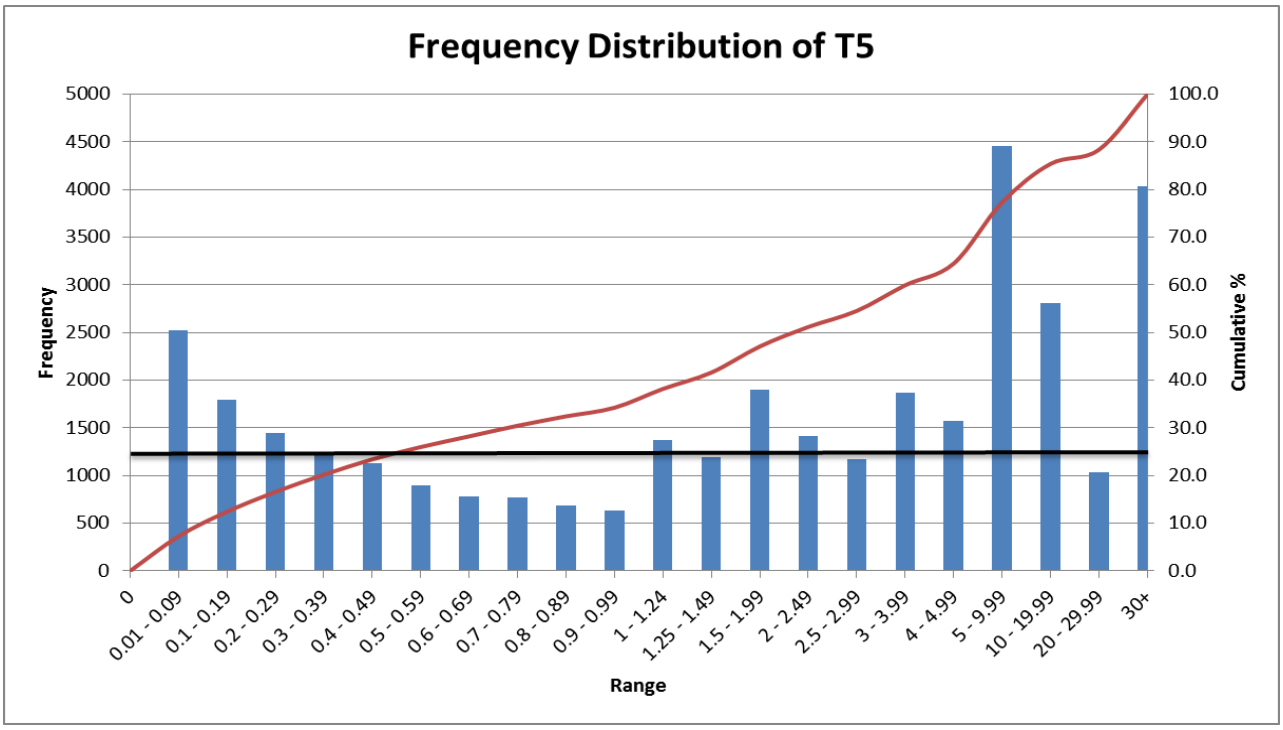

Figure C.15: Top 75% DWS cutoff value determination for the event cluster's fifth time period.

Appendix D – Stope 5078 Results

Appendix D will include mid stope tomograms for Stope 5078. Tomograms will be shown in time period order with two tomograms per time period, the XZ plane and the YZ plane. XZ plane tomograms are displayed with respect to the Easting and depth of the stope, while the YZ plane tomograms are displayed with respect to the Northing and depth of the stope.

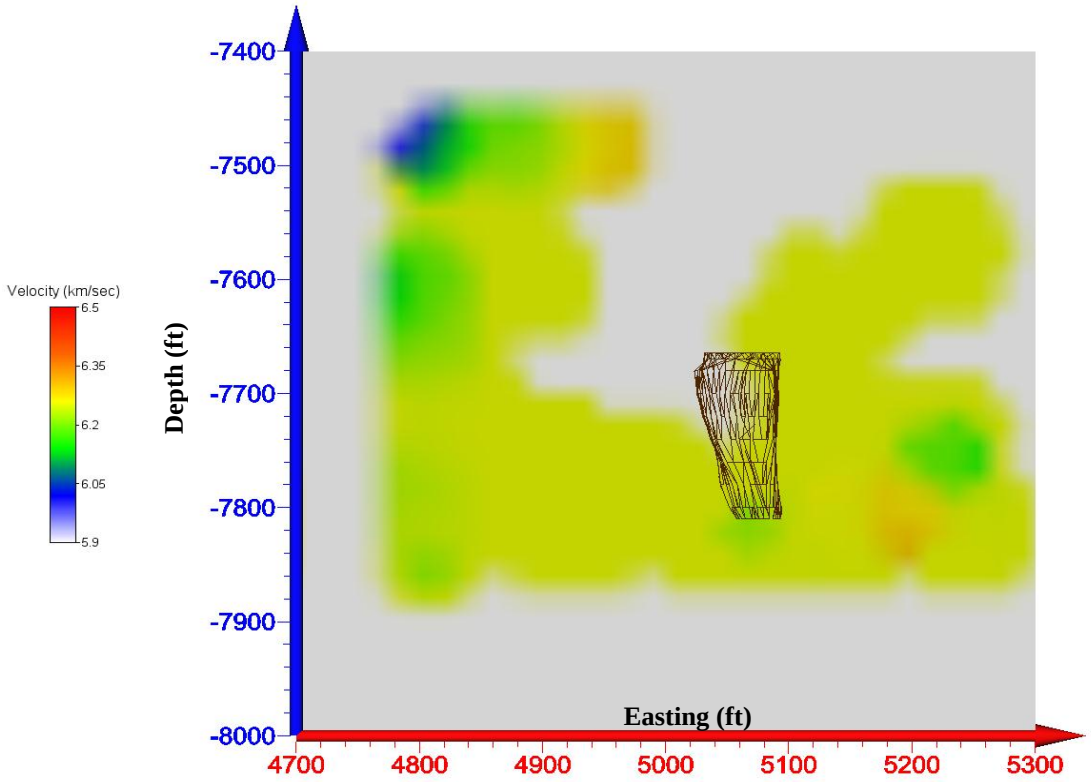

Figure D.1: XZ tomogram at the mid-stope level of Stope 5078 during the first time period.

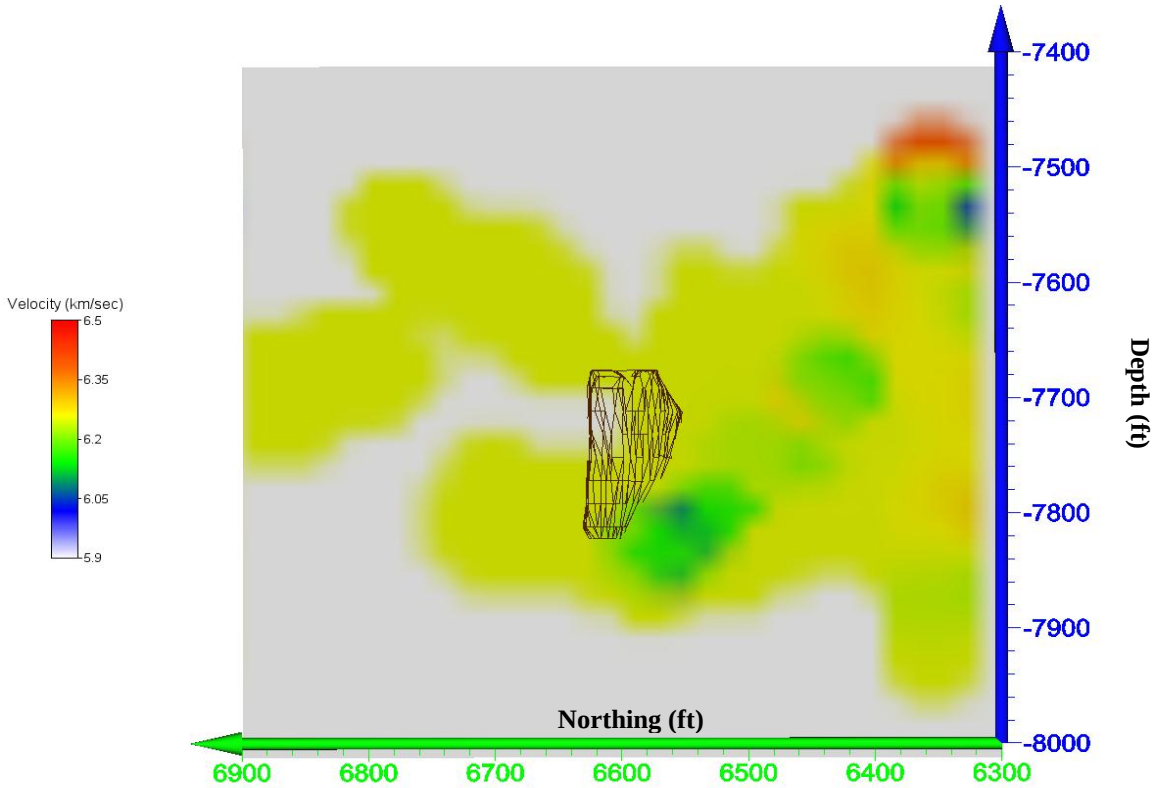

Figure D.2: YZ tomogram at the mid-stope level of Stope 5078 during the first time period.

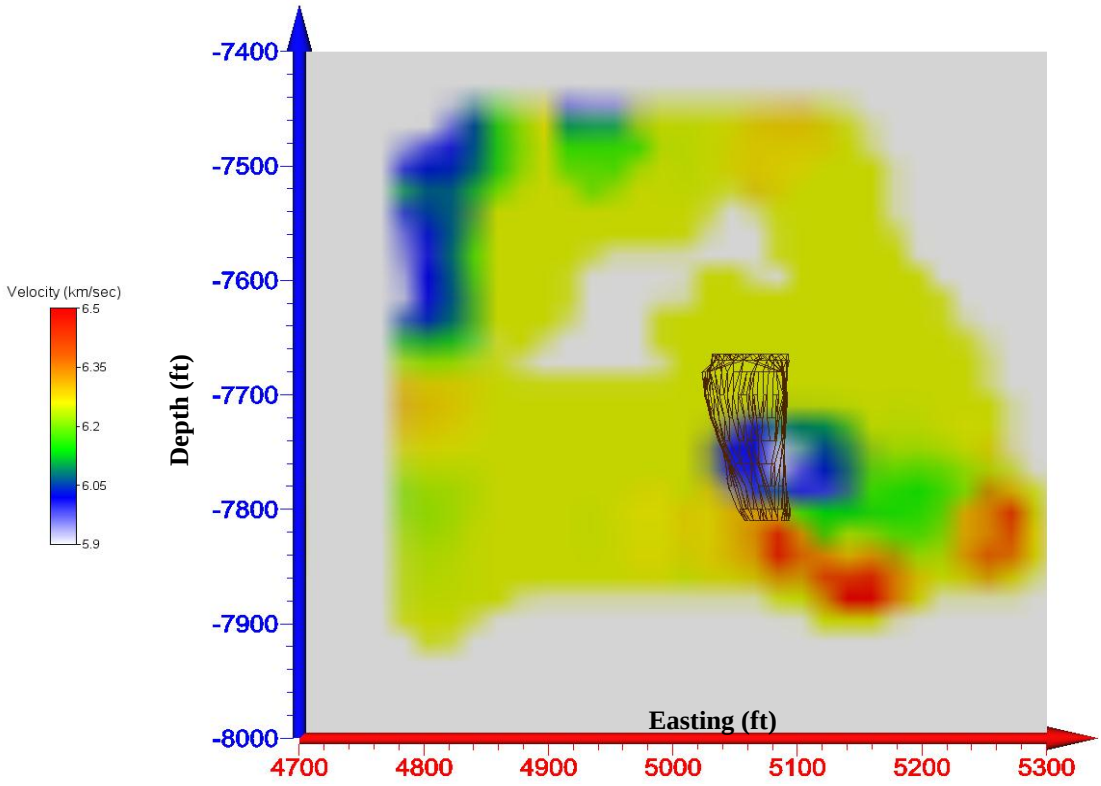

Figure D.3: XZ tomogram at the mid-stope level of Stope 5078 during the second time period.

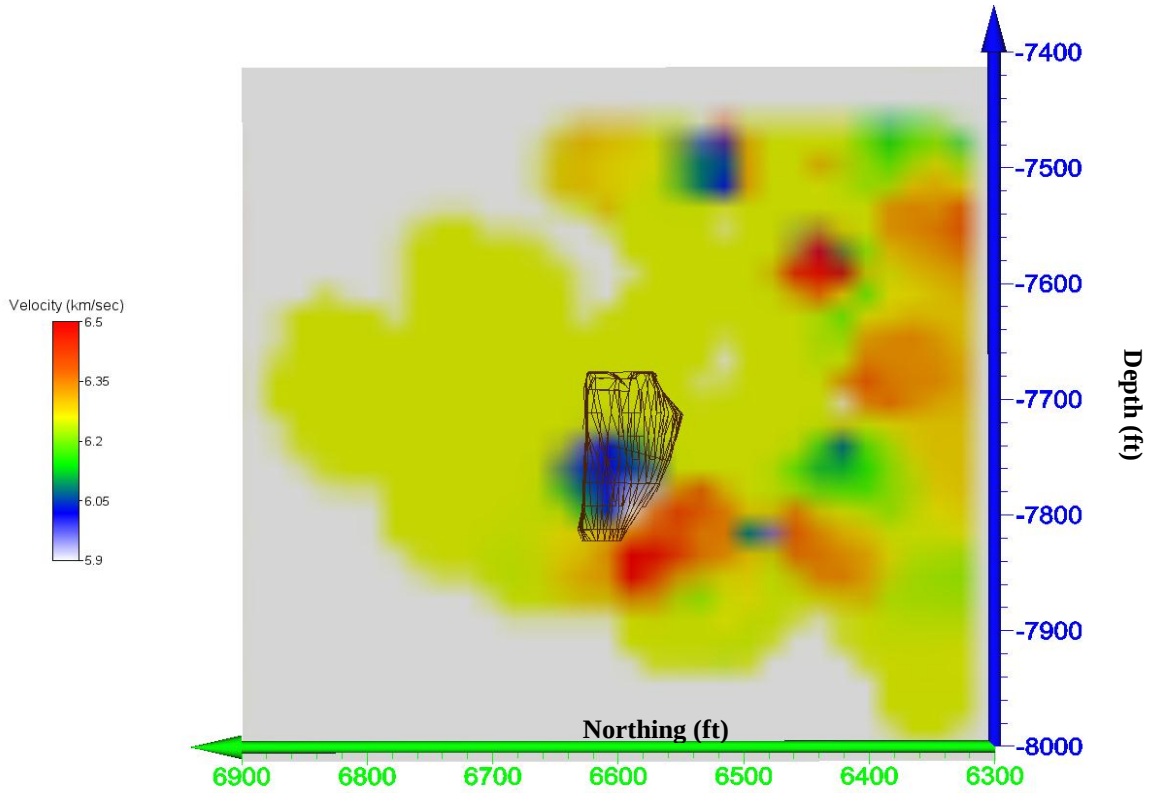

Figure D.4: YZ tomogram at the mid-stope level of Stope 5078 during the second time period.

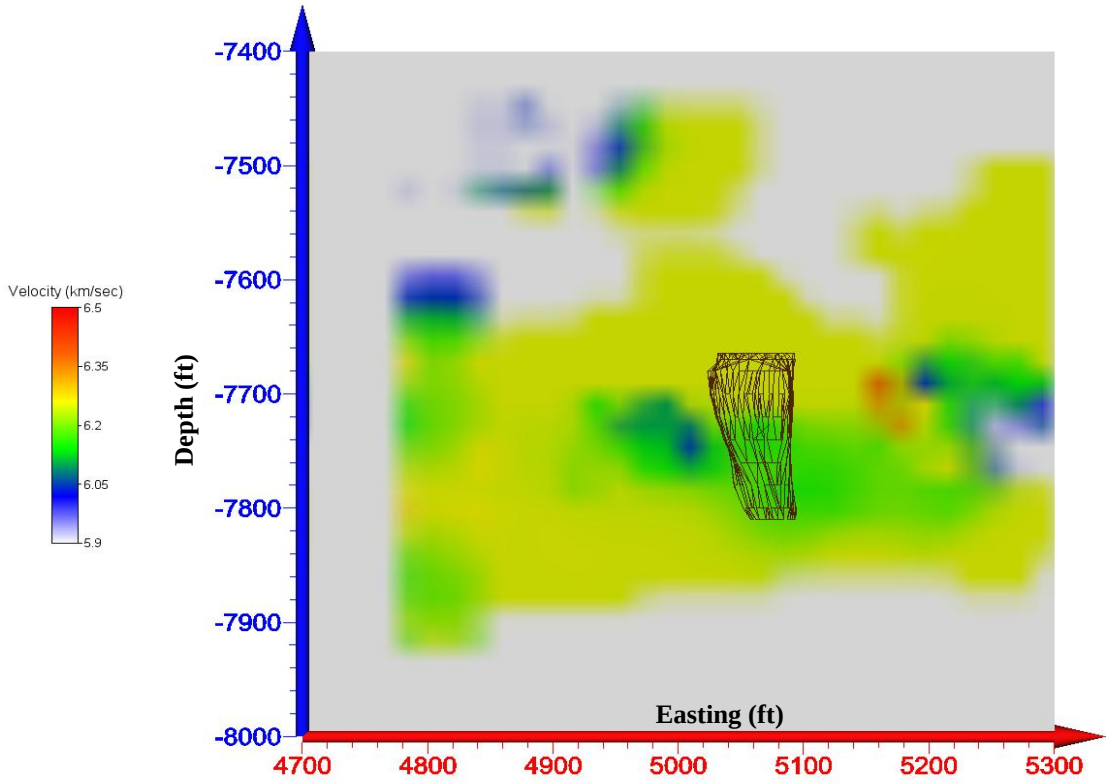

Figure D.5: XZ tomogram at the mid-stope level of Stope 5078 during the third time period.

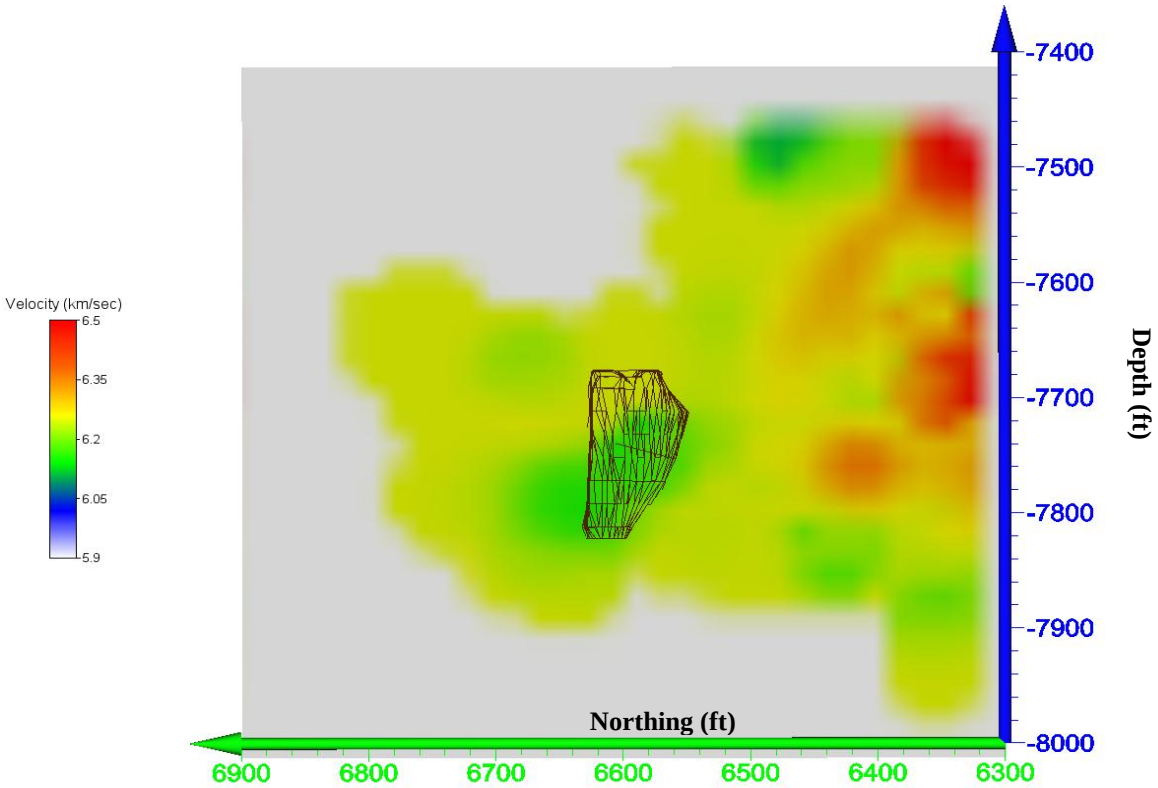

Figure D.6: YZ tomogram at the mid-stope level of Stope 5078 during the third time period.

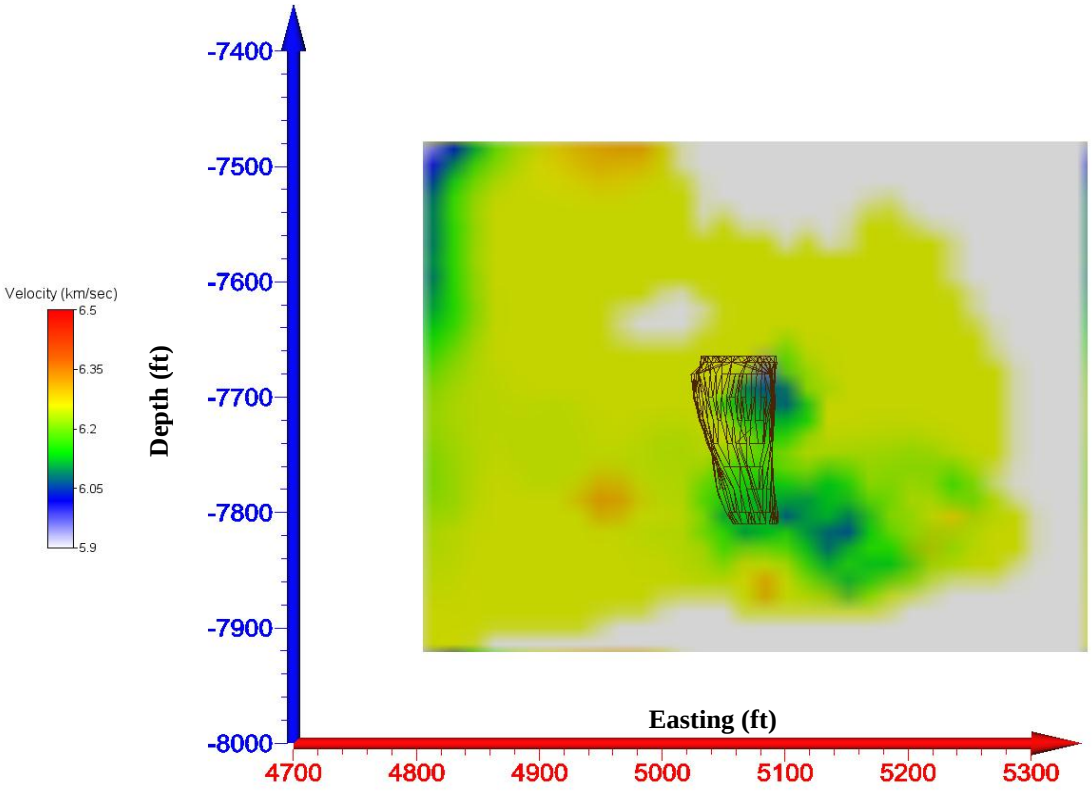

Figure D.7: XZ tomogram at the mid-stope level of Stope 5078 during the fourth time period.

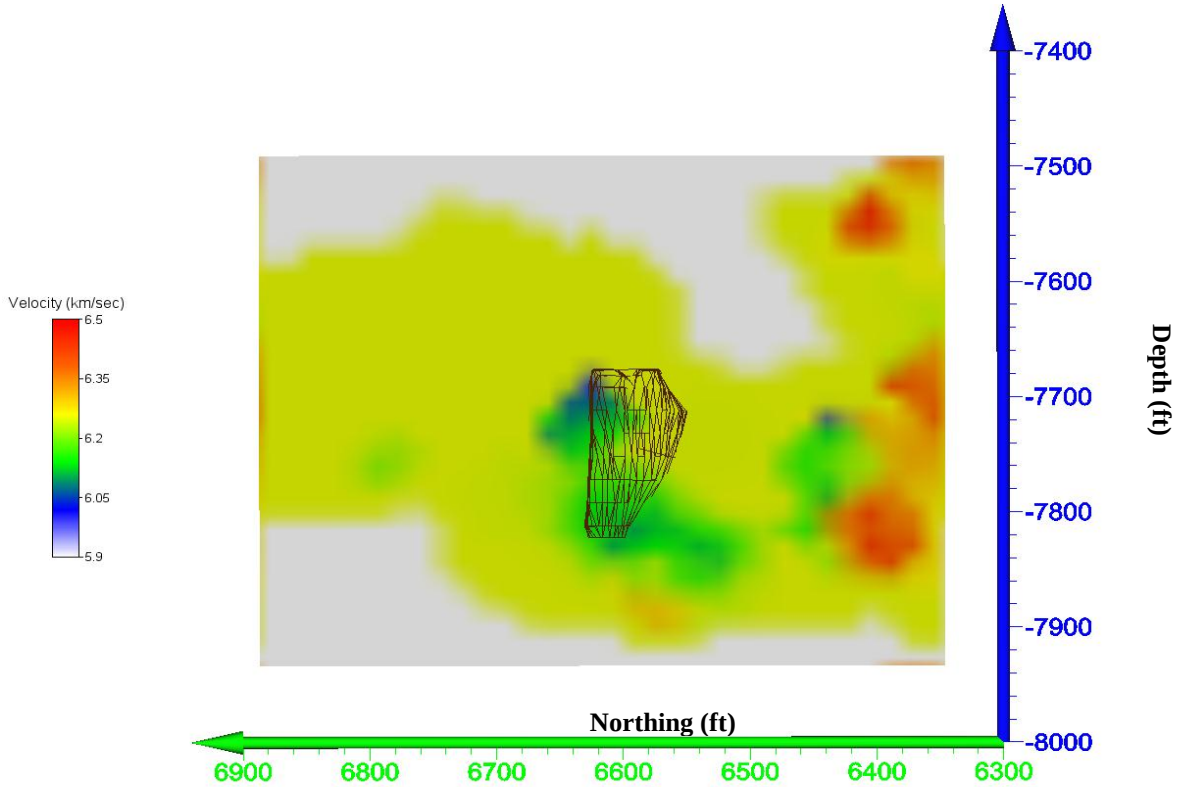

Figure D.8: YZ tomogram at the mid-stope level of Stope 5078 during the fourth time period.

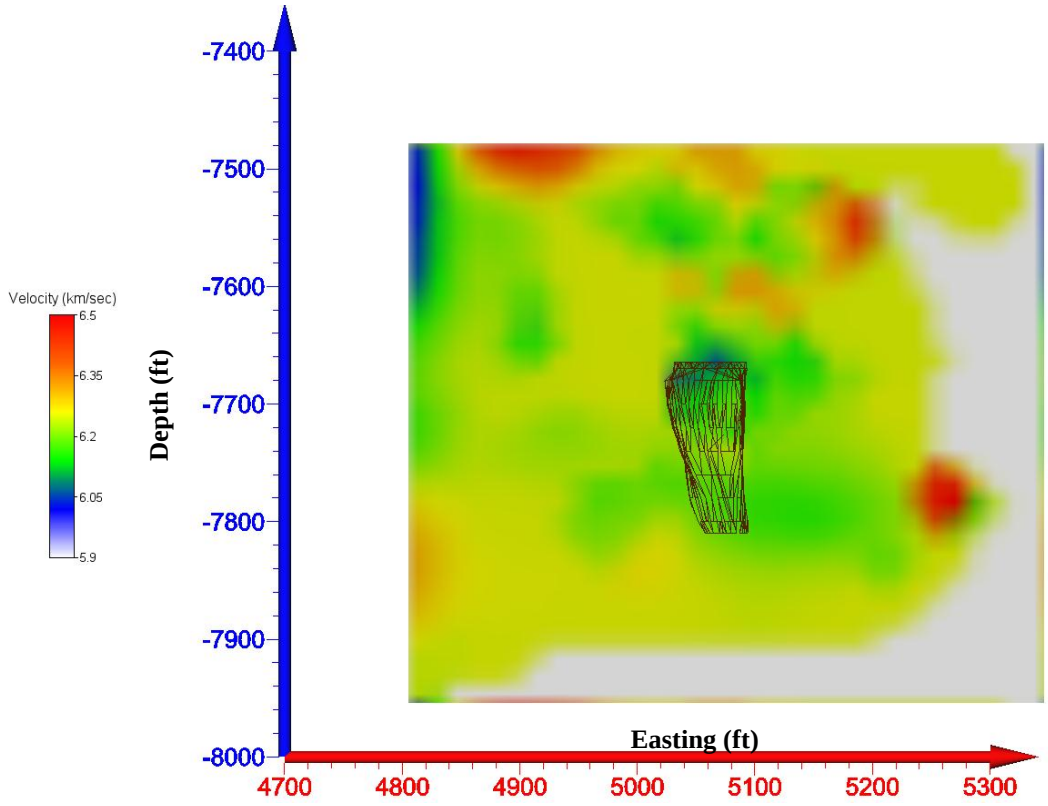

Figure D.9: XZ tomogram at the mid-stope level of Stope 5078 during the fifth time period.

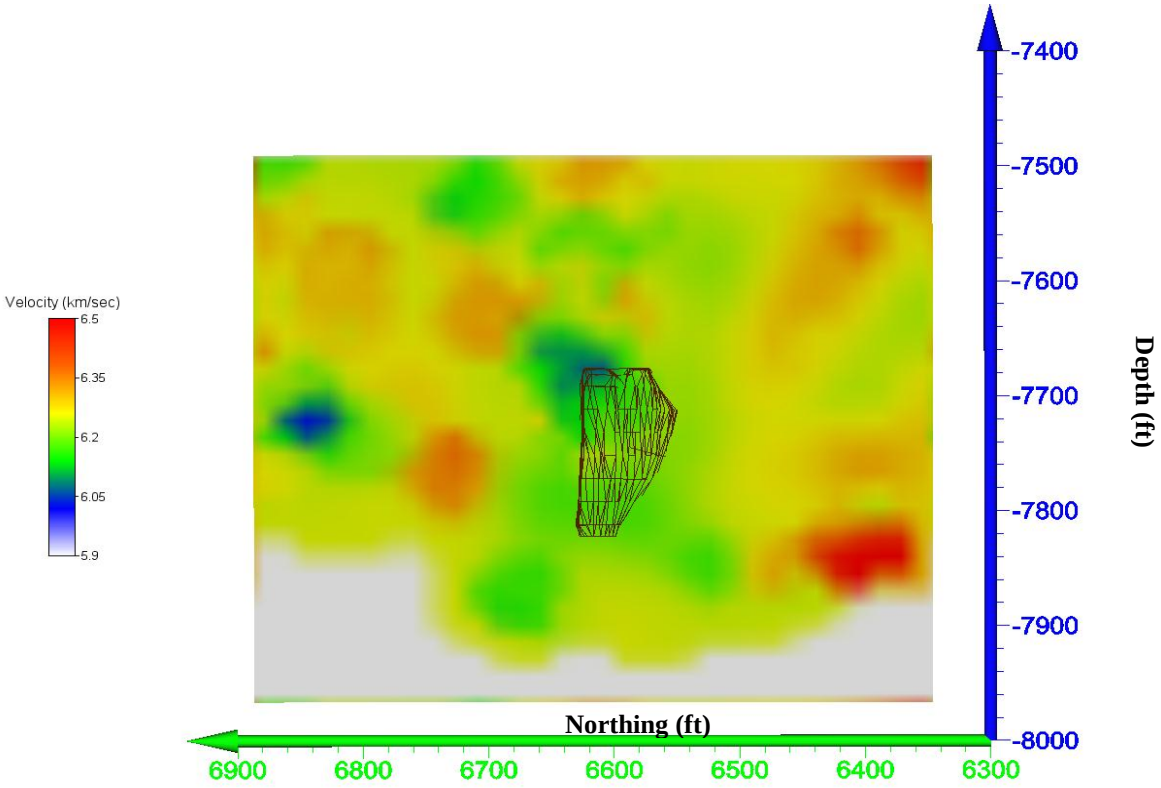

Figure D.10: YZ tomogram at the mid-stope level of Stope 5078 during the fifth time period.

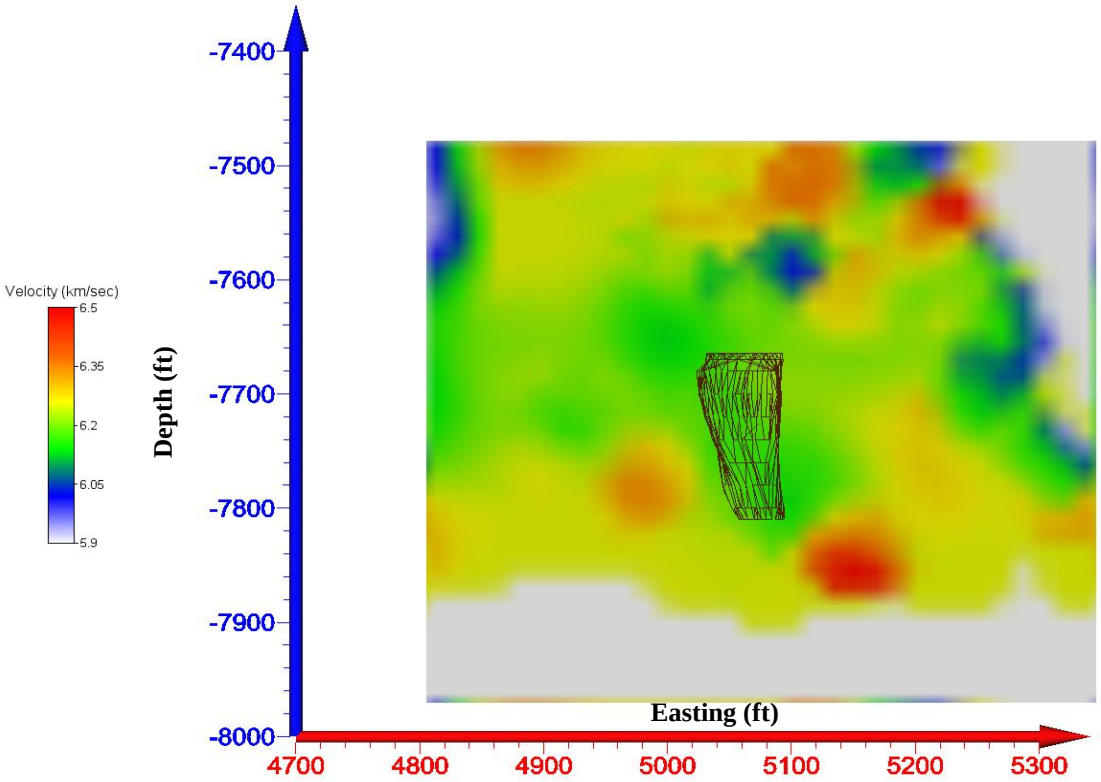

Figure D.11: XZ tomogram at the mid-stope level of Stope 5078 during the sixth time period.

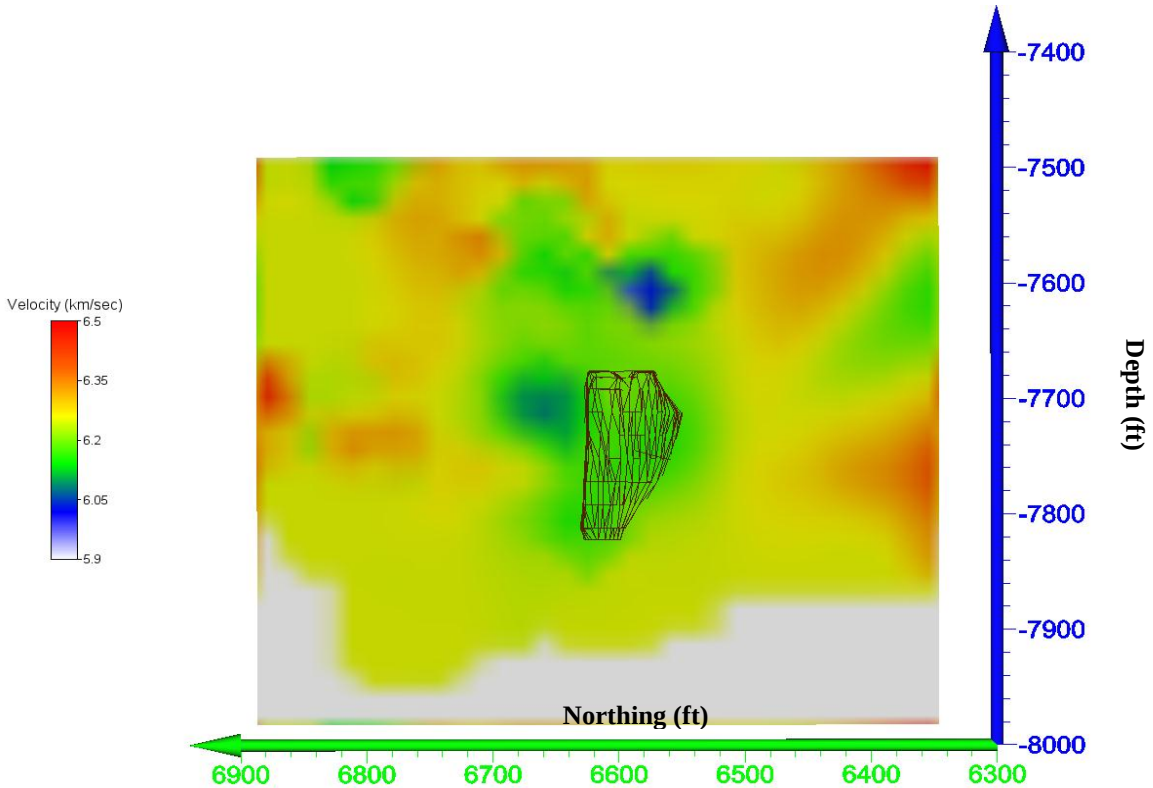

Figure D.12: YZ tomogram at the mid-stope level of Stope 5078 during the sixth time period.

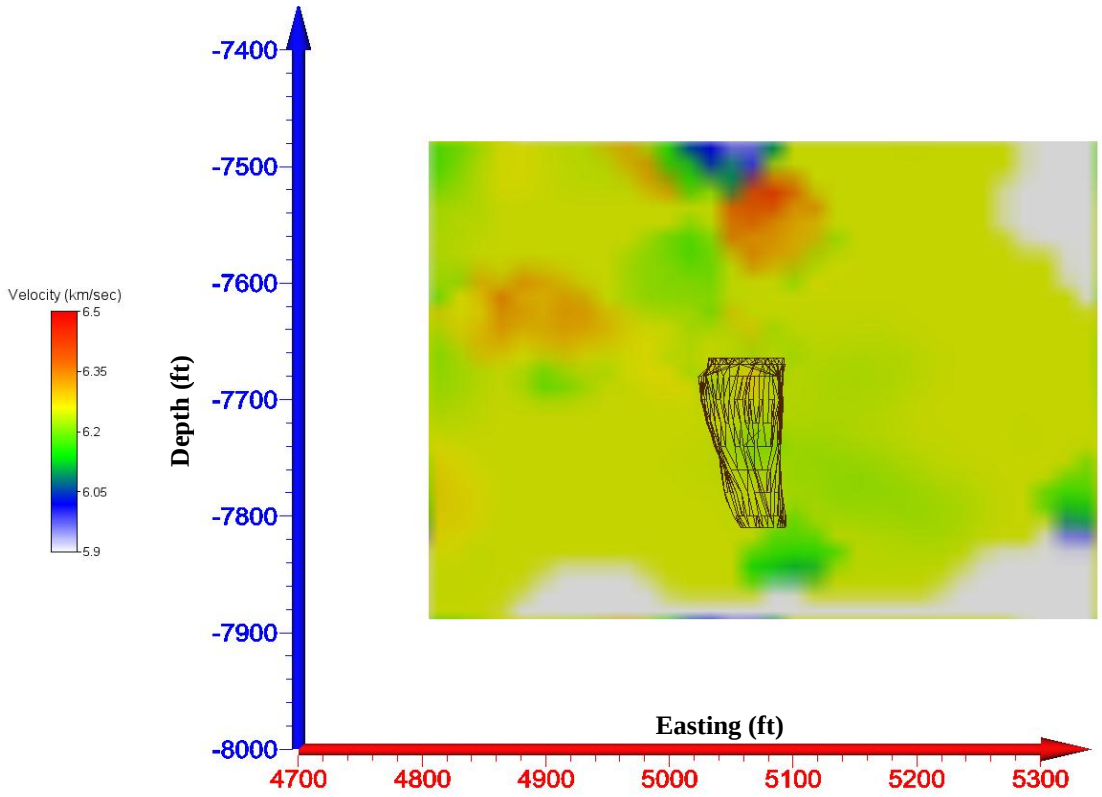

Figure D.13: XZ tomogram at the mid-stope level of Stope 5078 during the seventh time period.

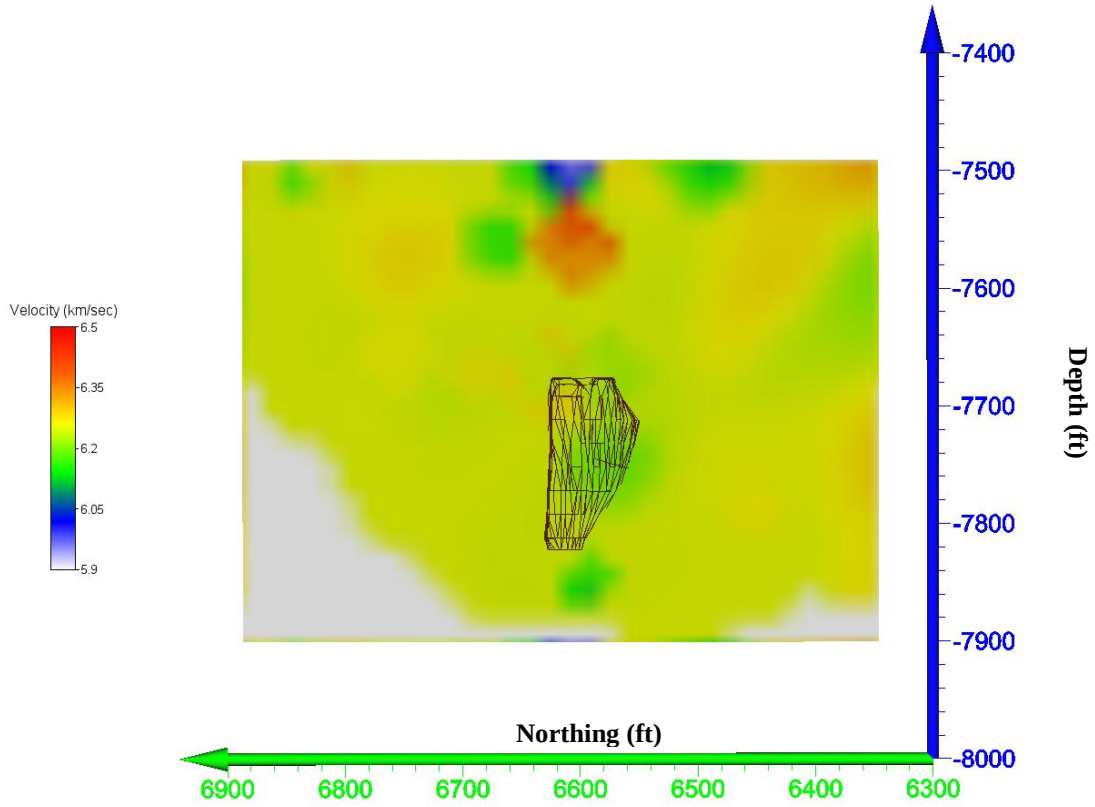

Figure D.14: YZ tomogram at the mid-stope level of Stope 5078 during the seventh time period.

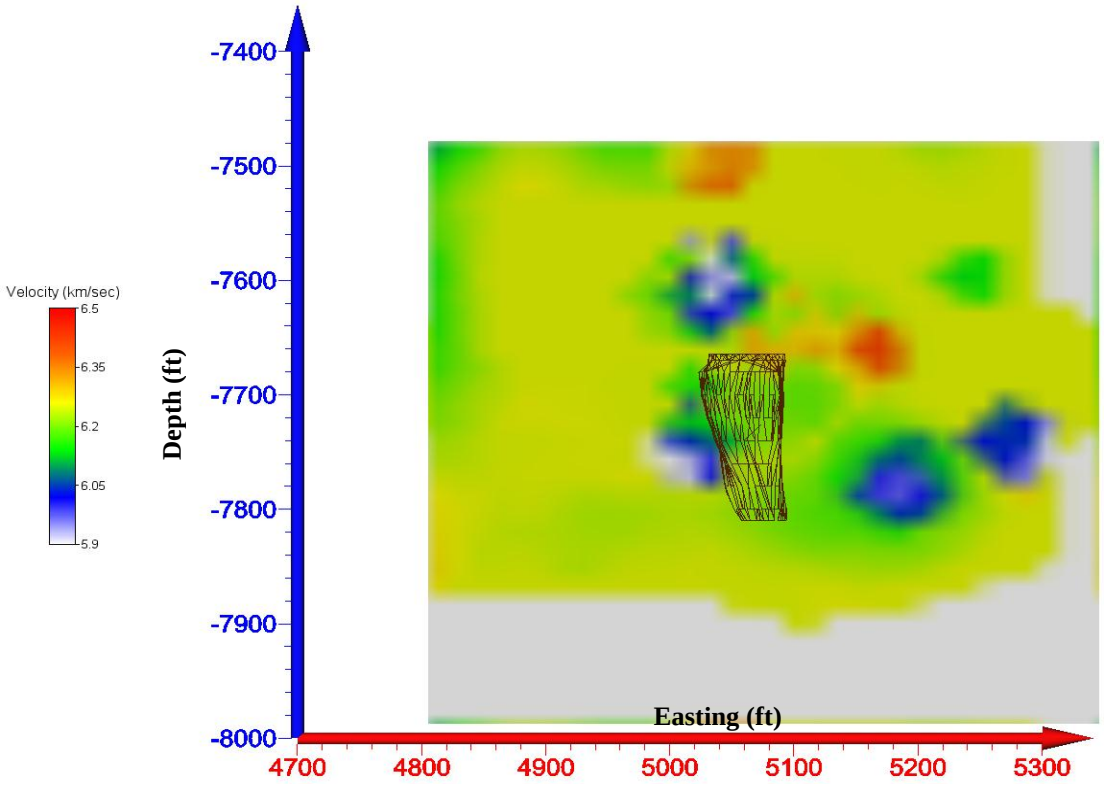

Figure D.15: XZ tomogram at the mid-stope level of Stope 5078 during the eighth time period.

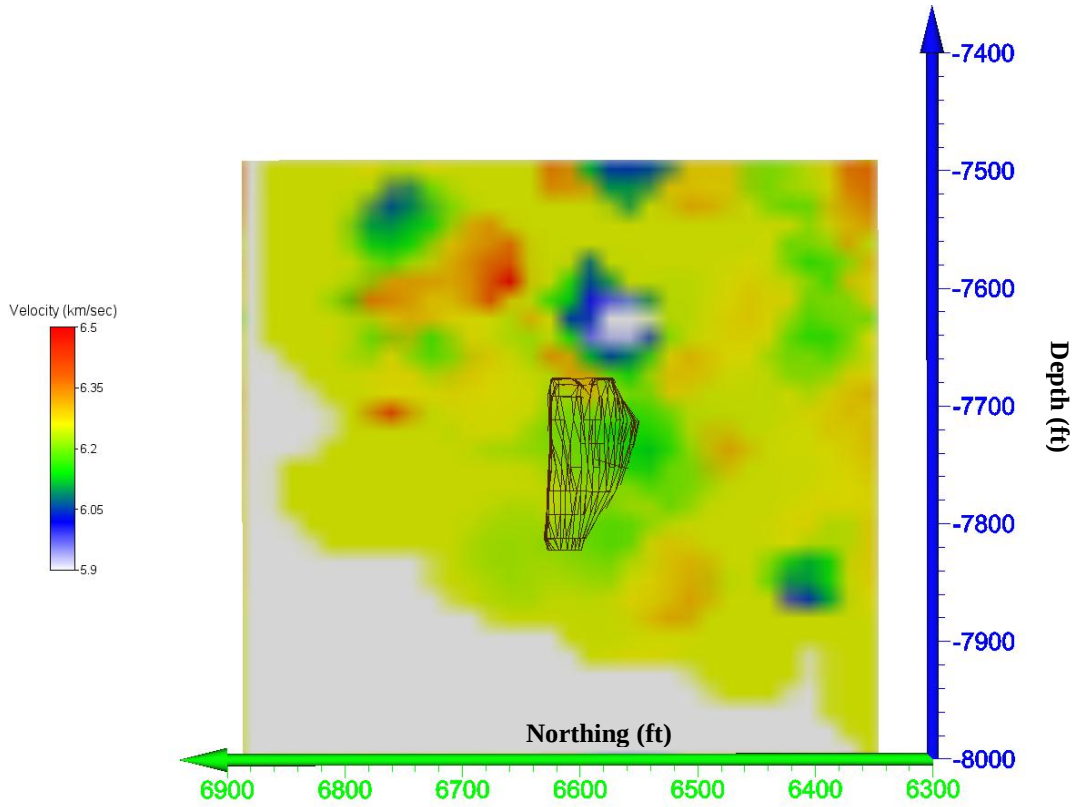

Figure D.16: YZ tomogram at the mid-stope level of Stope 5078 during the eighth time period.

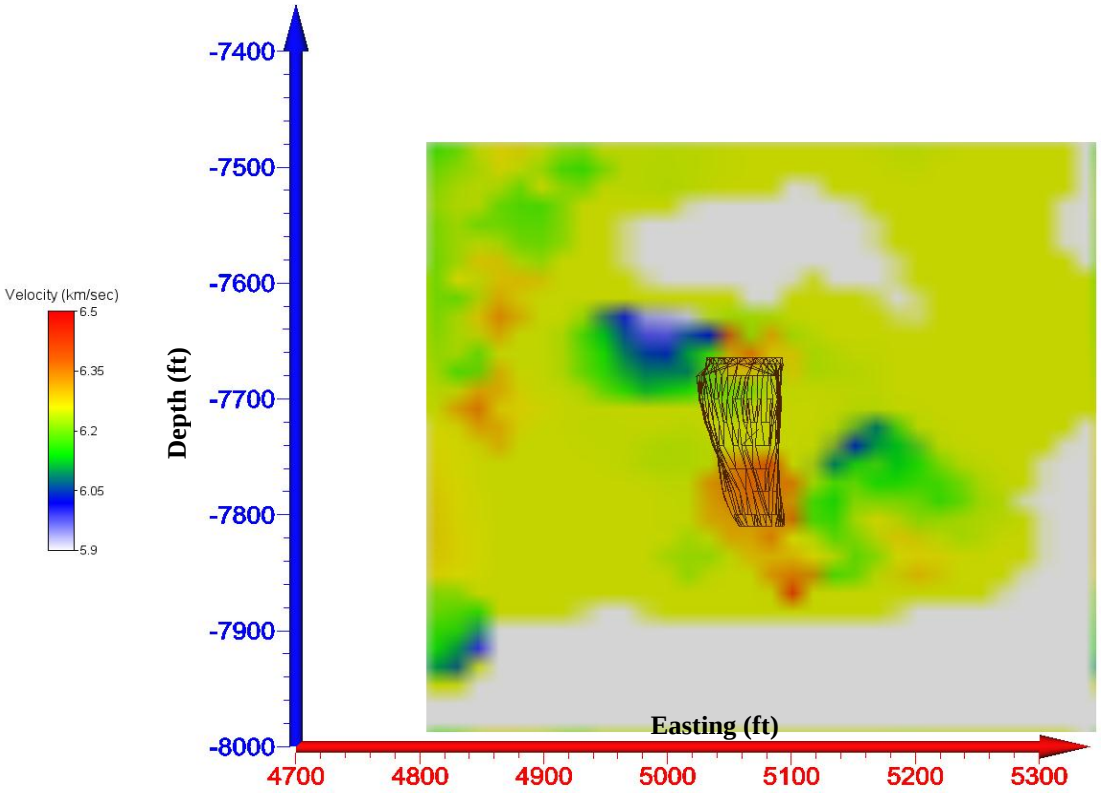

Figure D.17: XZ tomogram at the mid-stope level of Stope 5078 during the ninth time period.

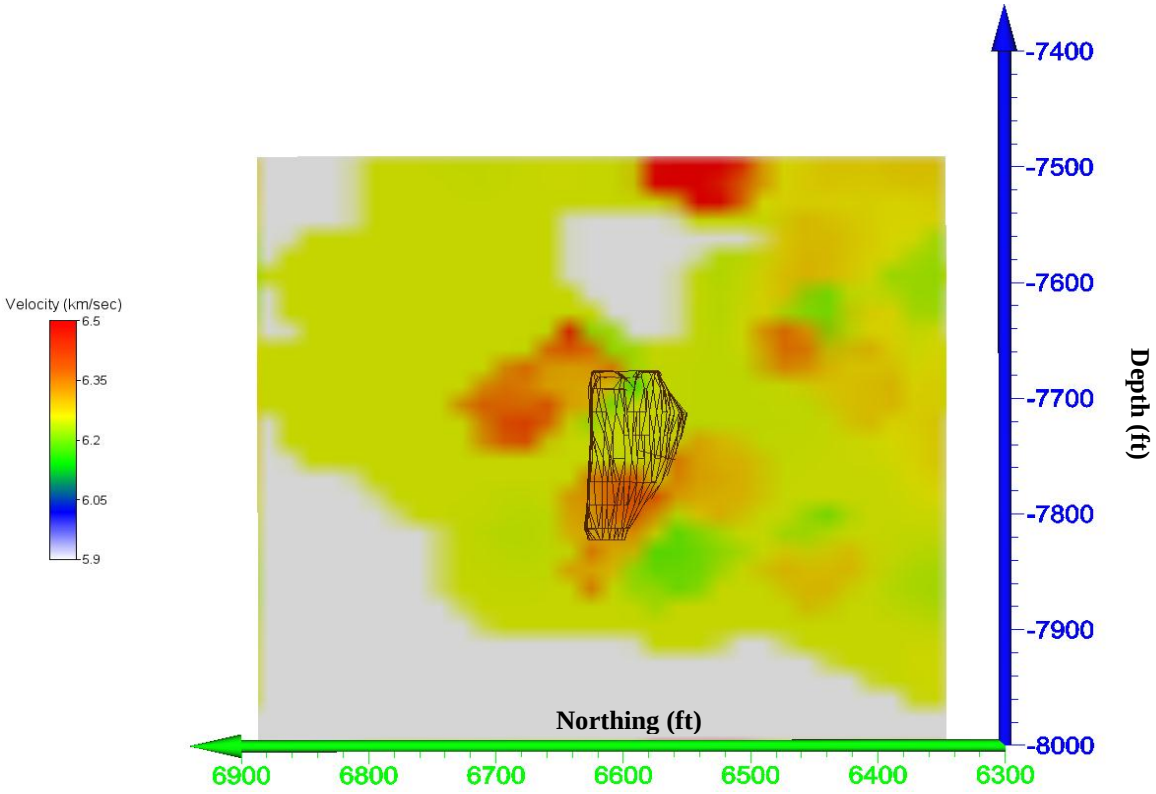

Figure D.18: YZ tomogram at the mid-stope level of Stope 5078 during the ninth time period.

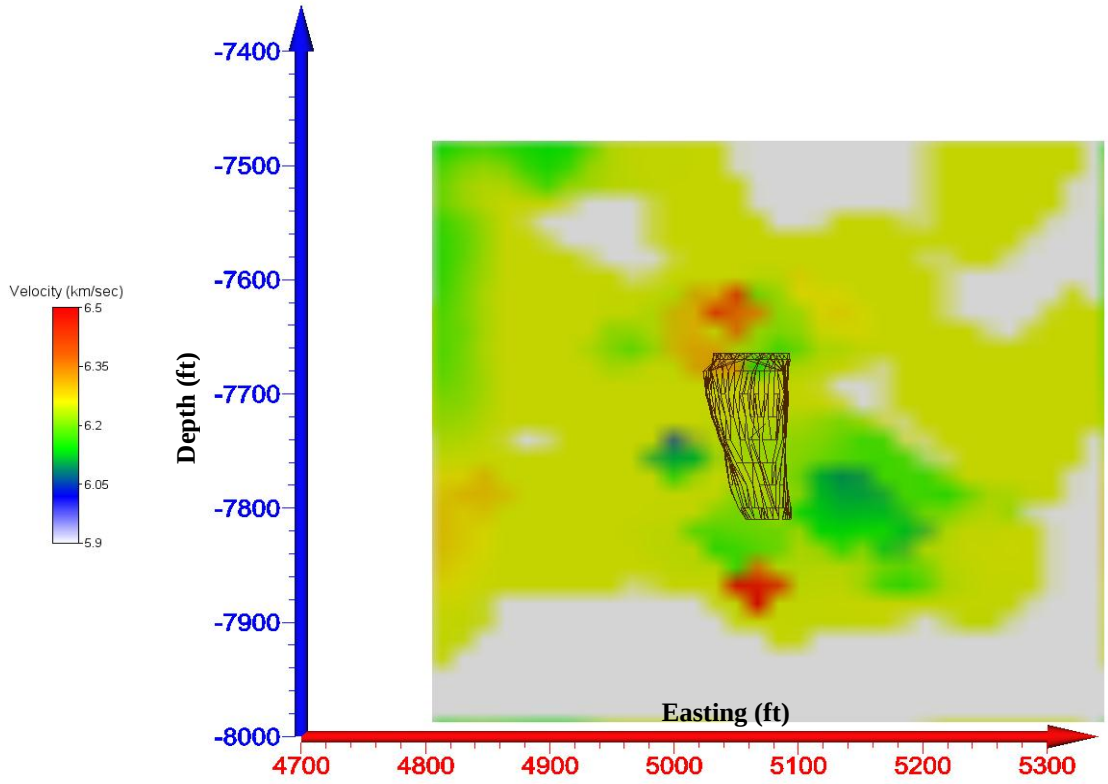

Figure D.19: XZ tomogram at the mid-stope level of Stope 5078 during the tenth time period.

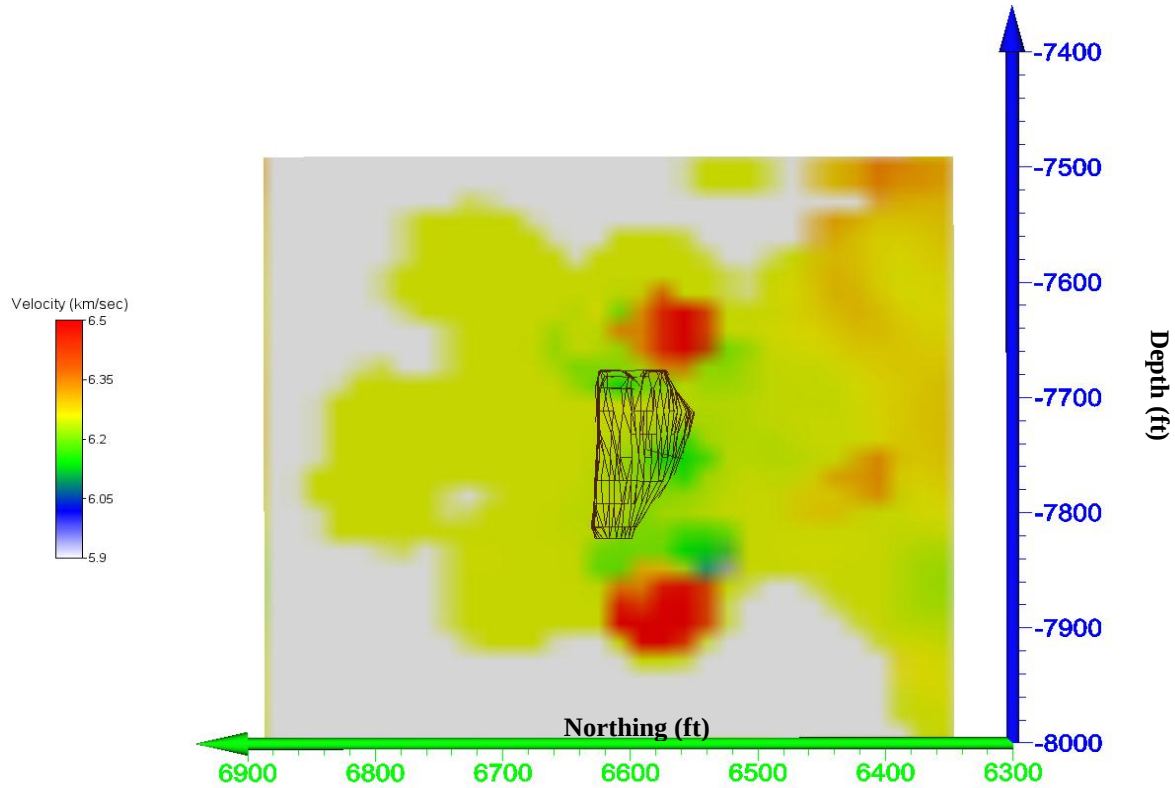

Figure D.20: YZ tomogram at the mid-stope level of Stope 5078 during the tenth time period.

Appendix E – Stope 4448 Results

Appendix E will include mid stope tomograms for Stope 4448. Tomograms will be shown in time period order with two tomograms per time period, the XZ plane and the YZ plane. XZ plane tomograms are displayed with respect to the Easting and depth of the stope, while the YZ plane tomograms are displayed with respect to the Northing and depth of the stope.

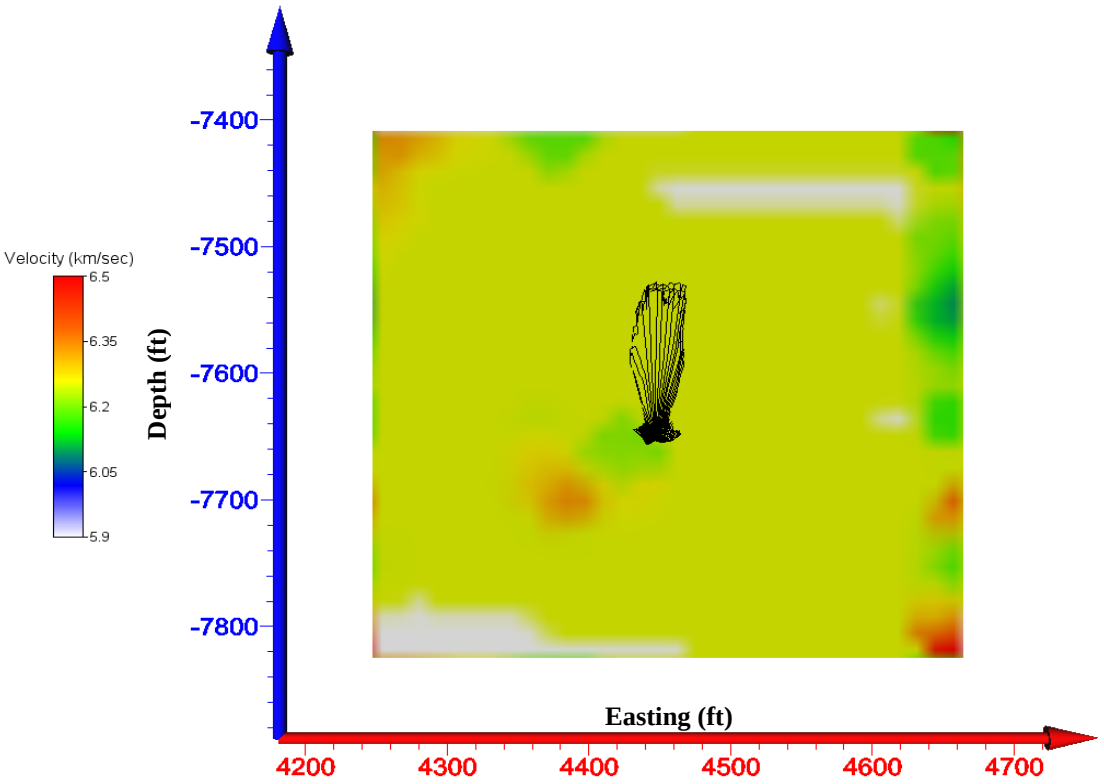

Figure E.1: XZ tomogram at the mid-stope level of Stope 4448 during the first time period.

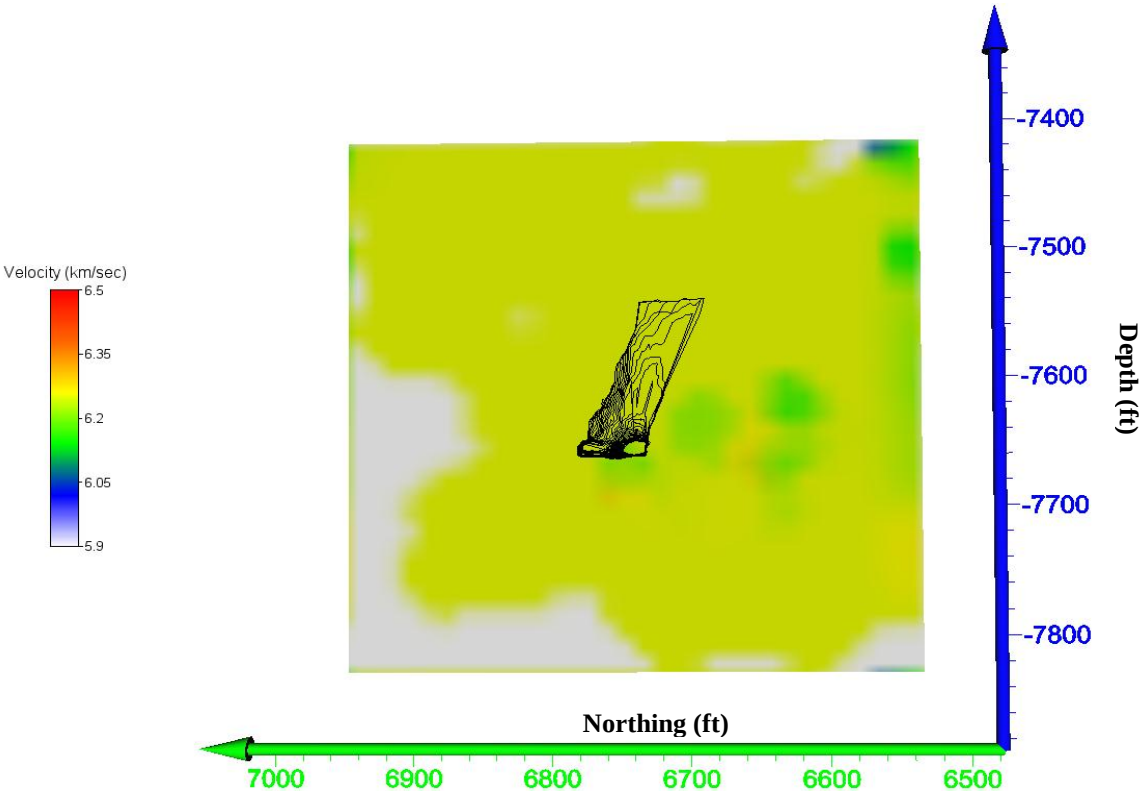

Figure E.2: YZ tomogram at the mid-stope level of Stope 4448 during the first time period.

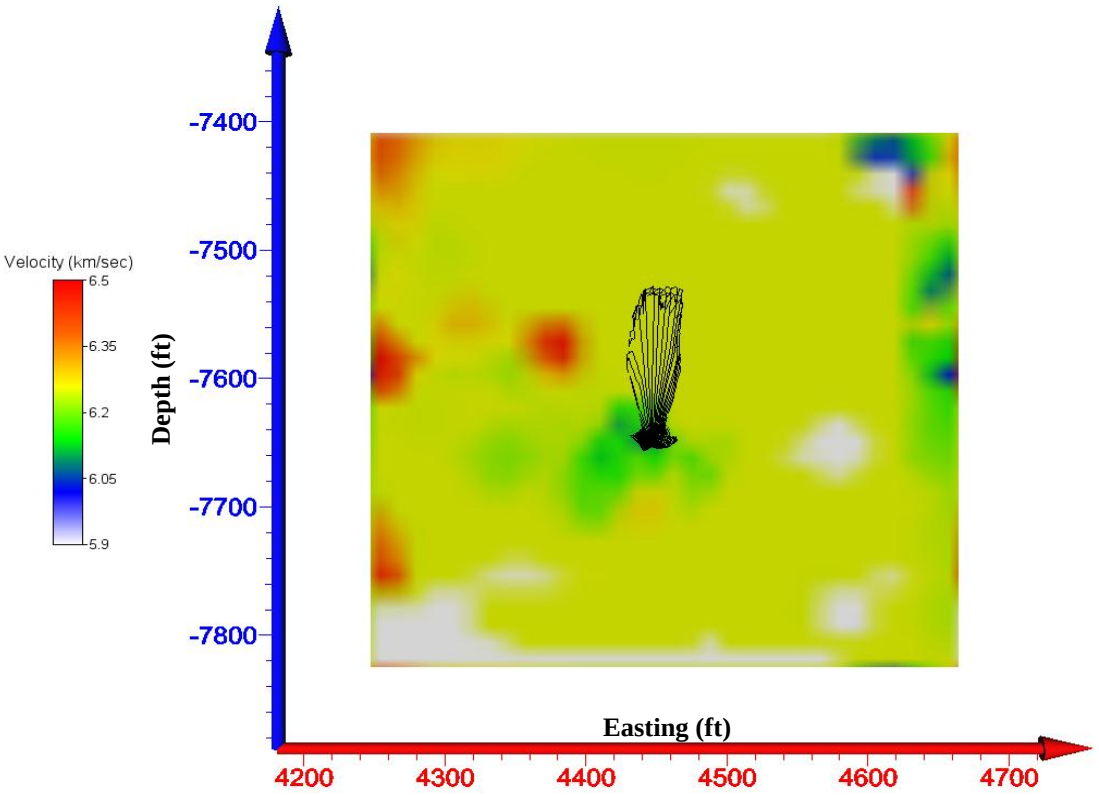

Figure E.3: XZ tomogram at the mid-stope level of Stope 4448 during the second time period.

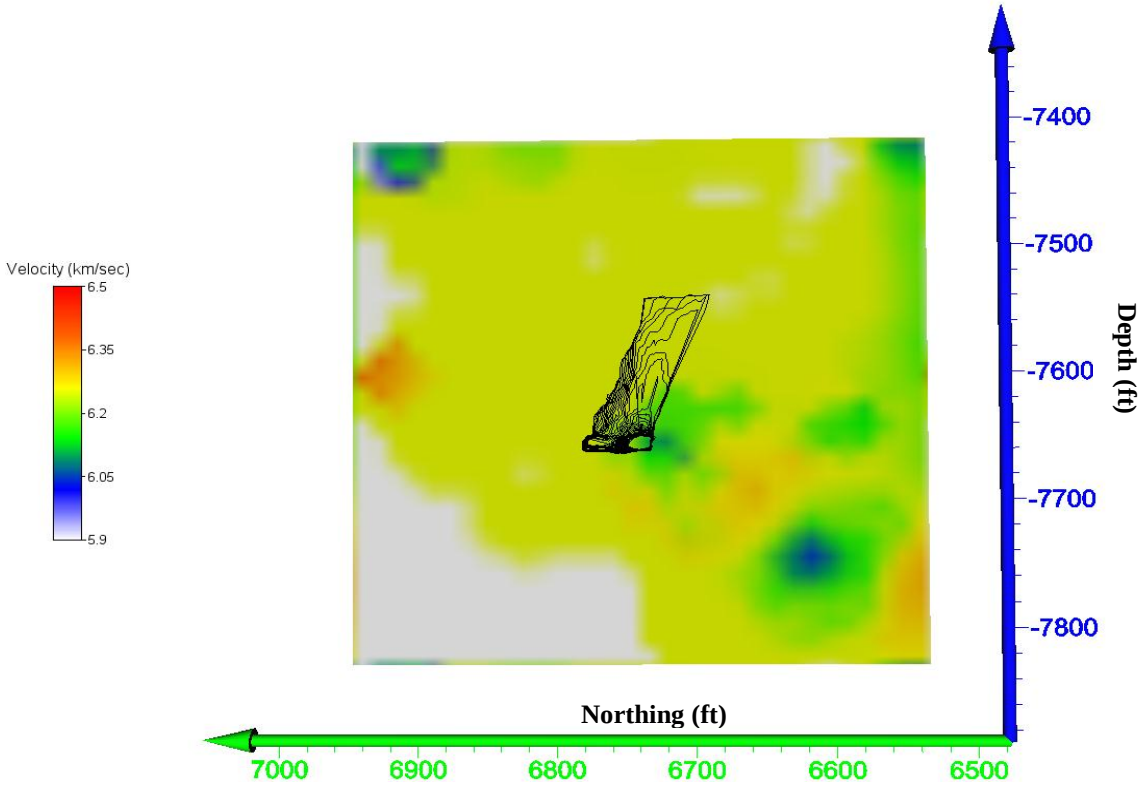

Figure E.4: YZ tomogram at the mid-stope level of Stope 4448 during the second time period.

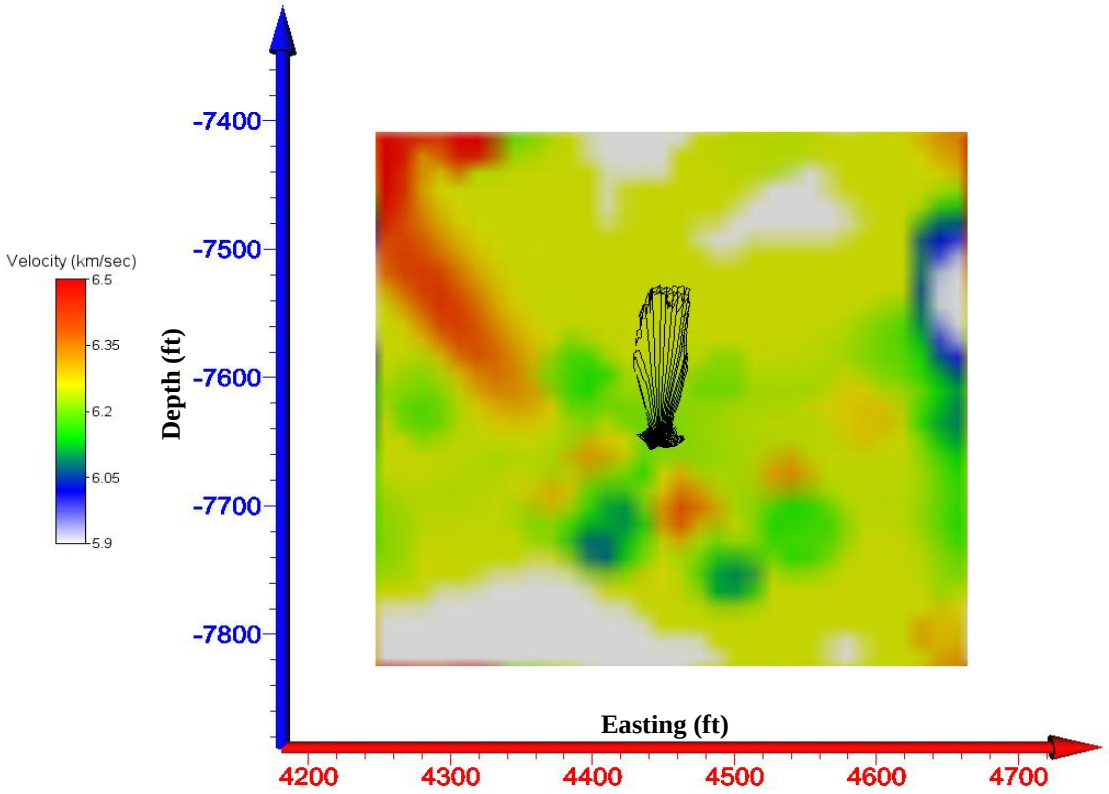

Figure E.5: XZ tomogram at the mid-stope level of Stope 4448 during the third time period.

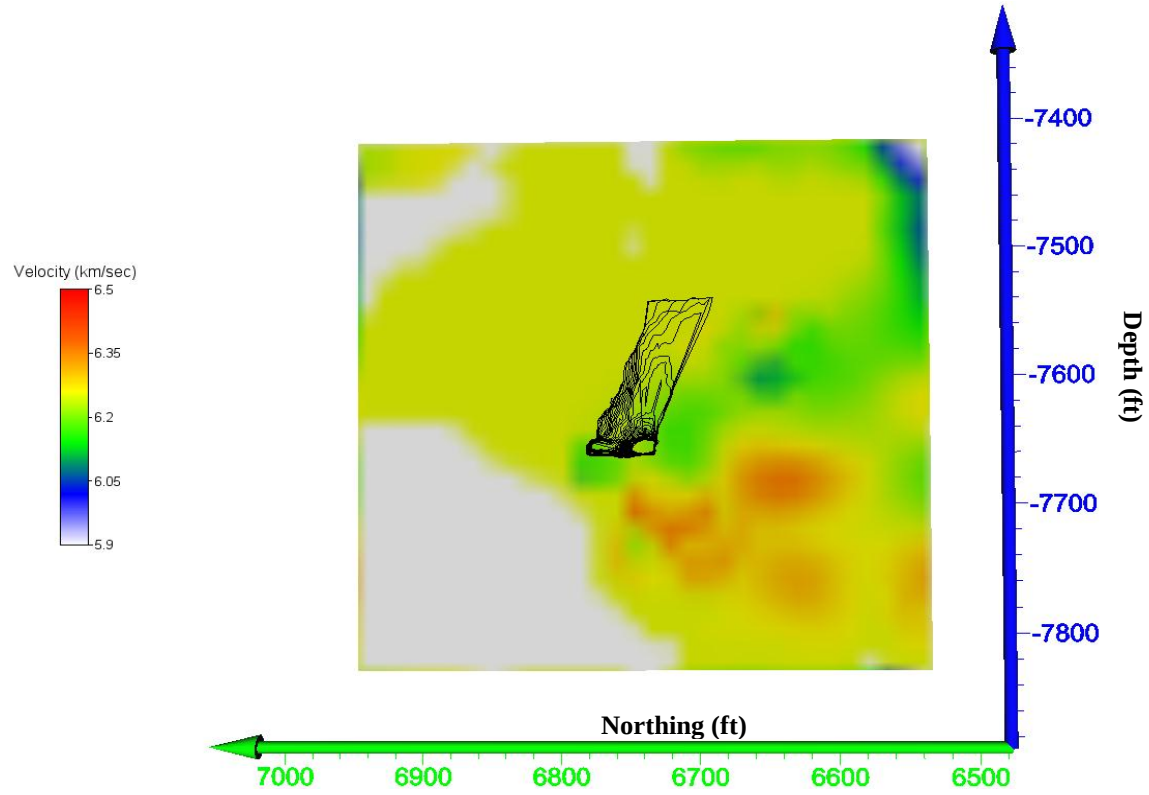

Figure E.6: YZ tomogram at the mid-stope level of Stope 4448 during the third time period.

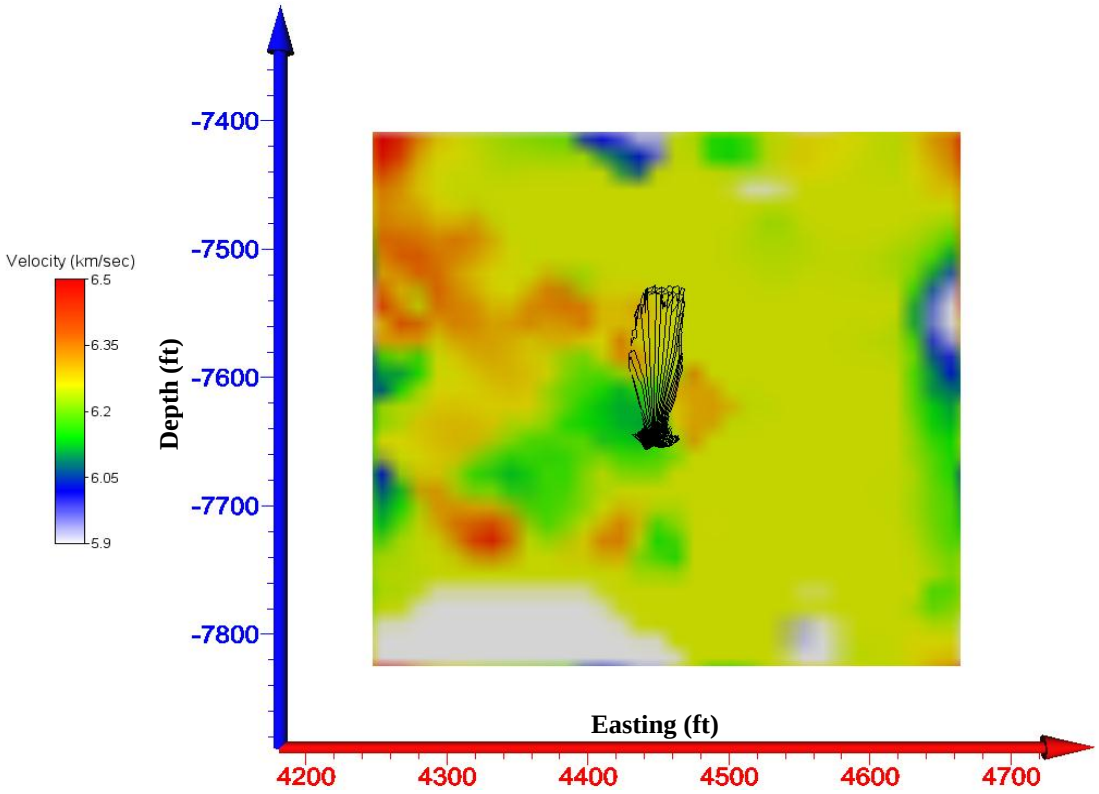

Figure E.7: XZ tomogram at the mid-stope level of Stope 4448 during the fourth time period.

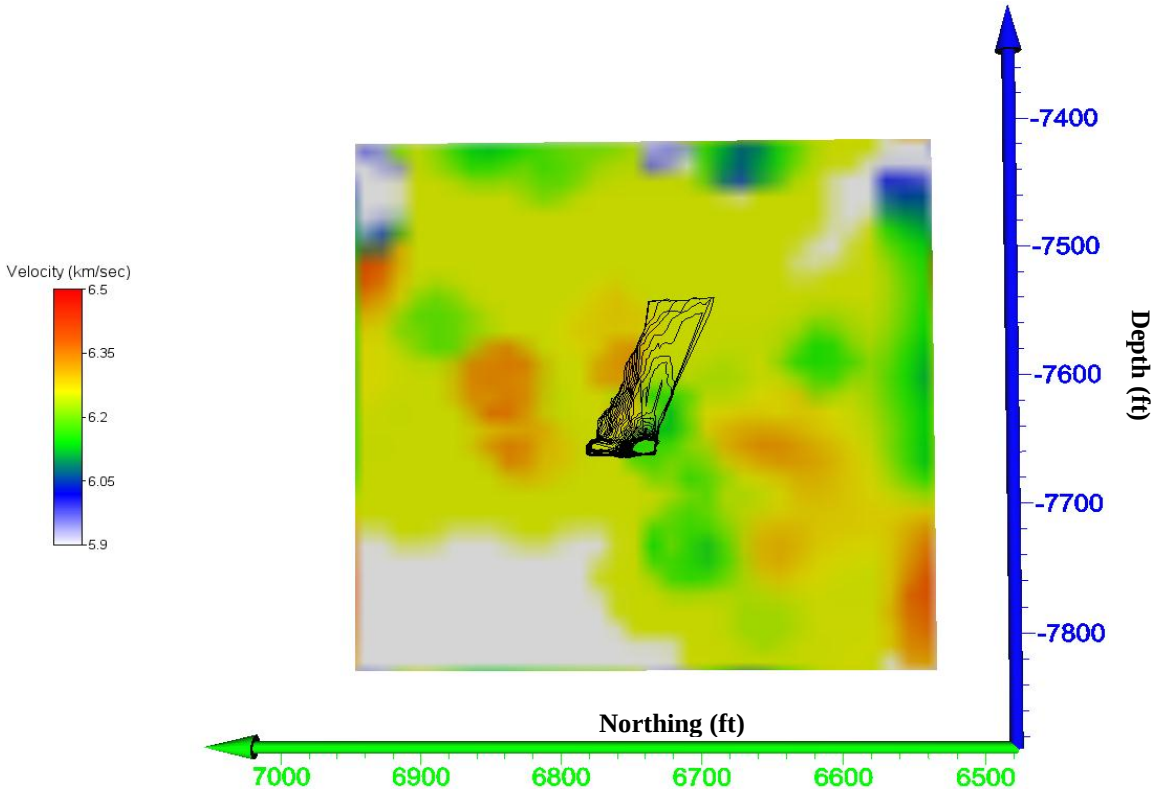

Figure E.8: YZ tomogram at the mid-stope level of Stope 4448 during the fourth time period.

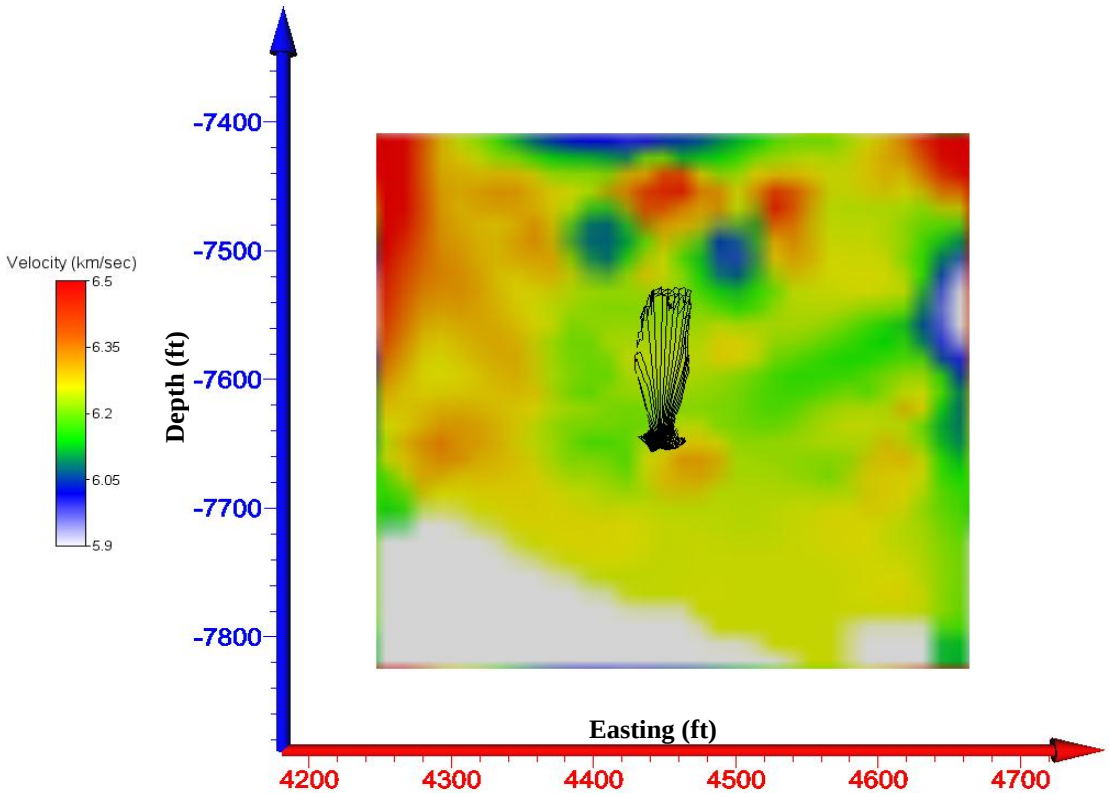

Figure E.9: XZ tomogram at the mid-stope level of Stope 4448 during the fifth time period.

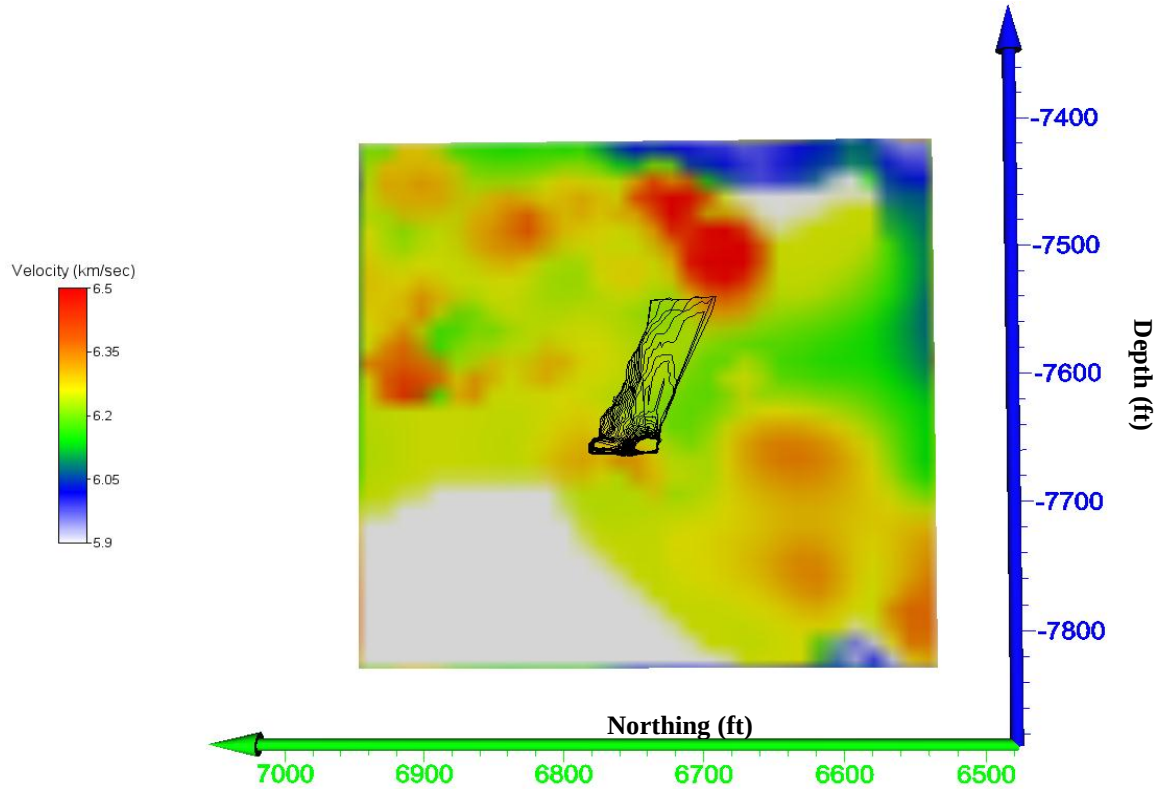

Figure E.10: YZ tomogram at the mid-stope level of Stope 4448 during the fifth time period.

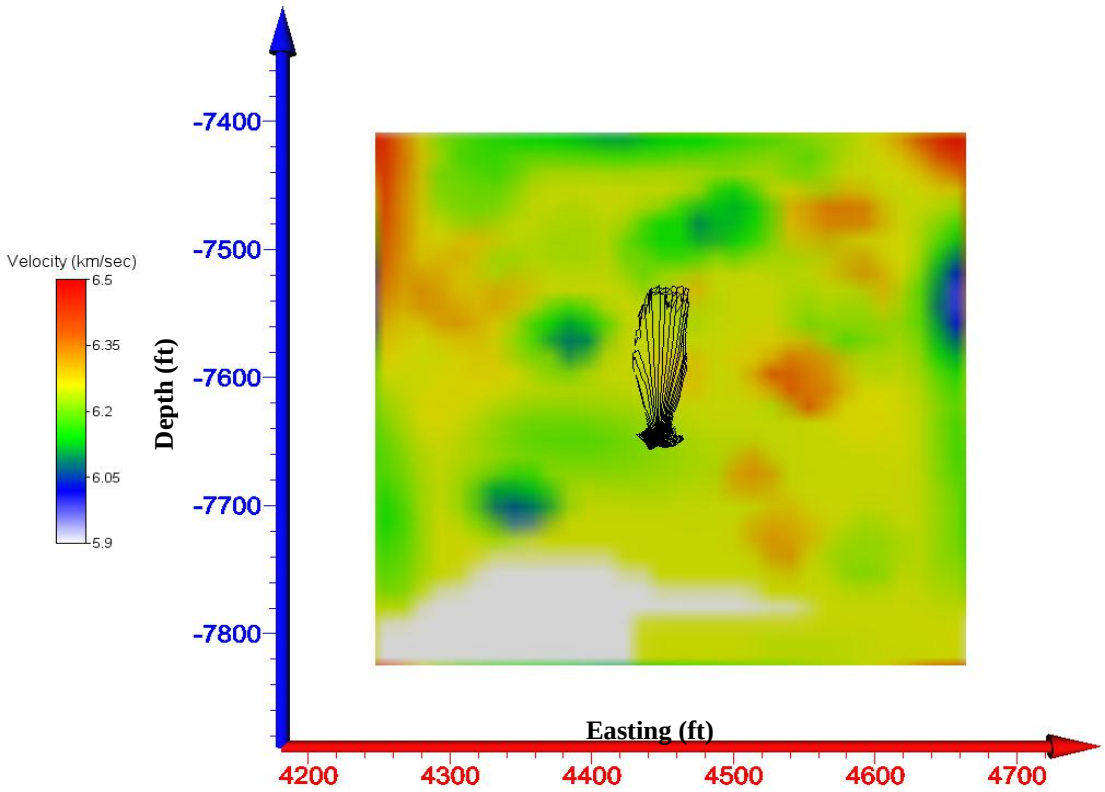

Figure E.11: XZ tomogram at the mid-stope level of Stope 4448 during the sixth time period.

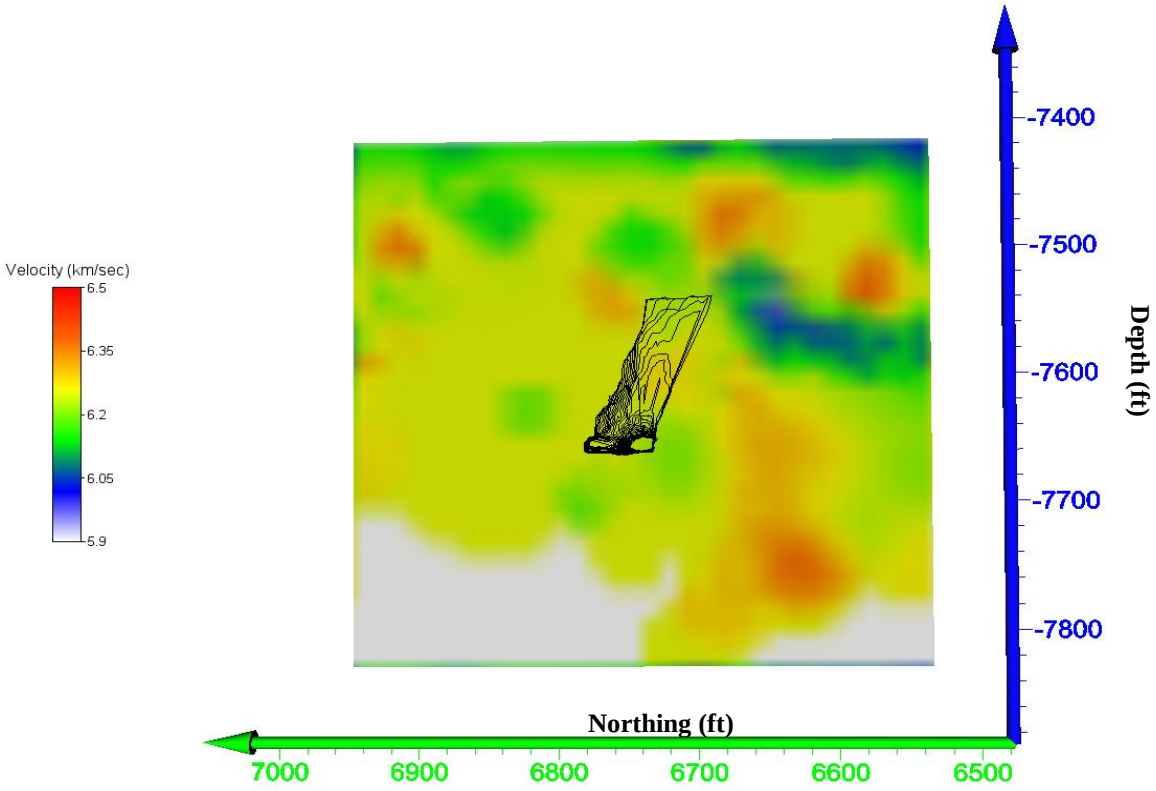

Figure E.12: YZ tomogram at the mid-stope level of Stope 4448 during the sixth time period.

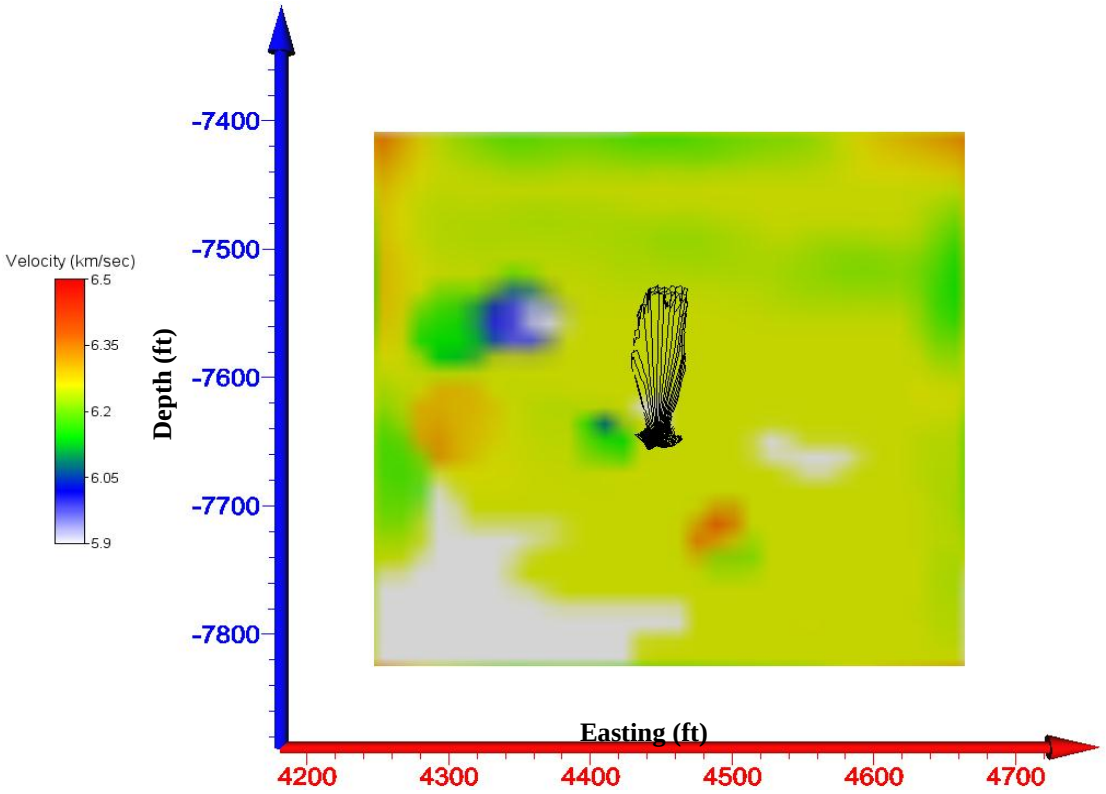

Figure E.13: XZ tomogram at the mid-stope level of Stope 4448 during the seventh time period.

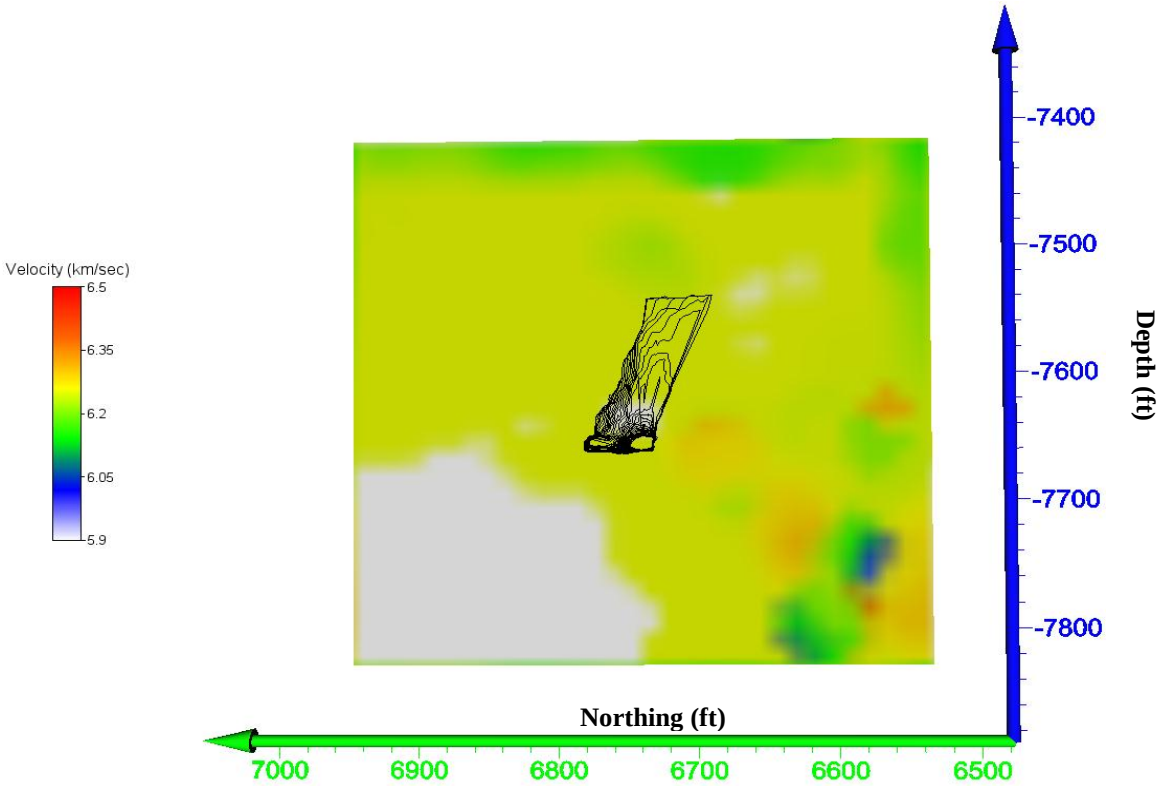

Figure E.14: YZ tomogram at the mid-stope level of Stope 4448 during the seventh time period.

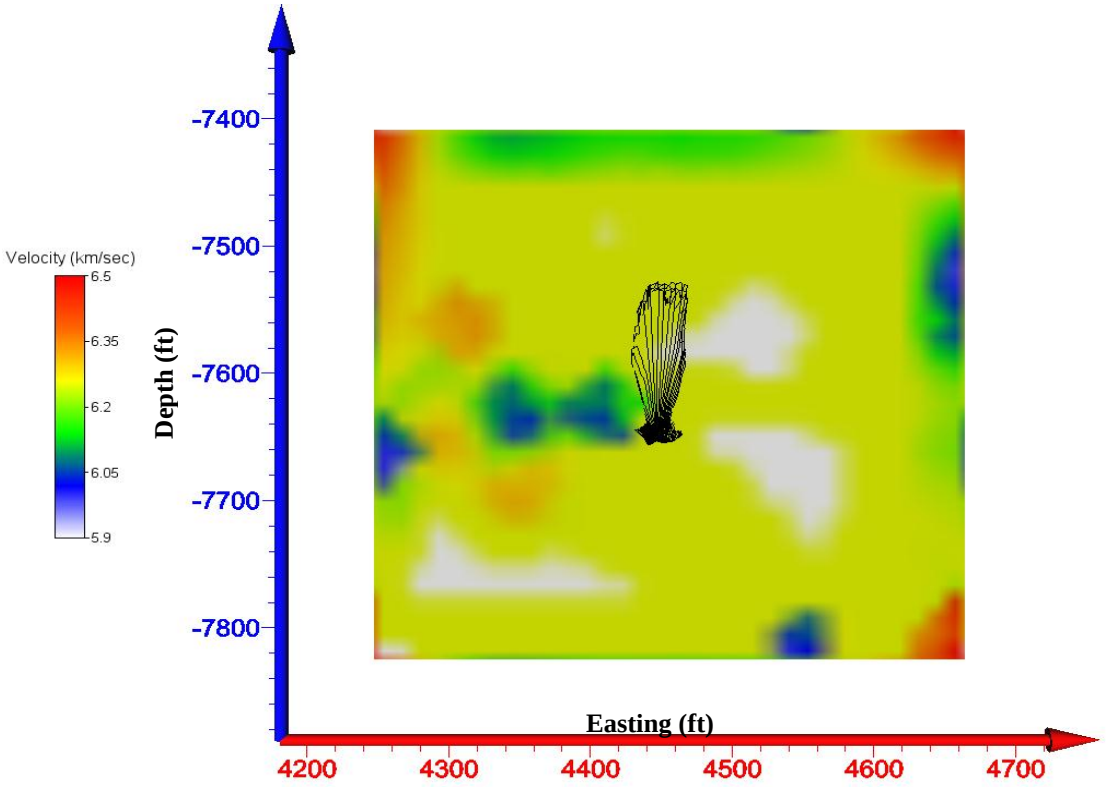

Figure E.15: XZ tomogram at the mid-stope level of Stope 4448 during the eighth time period.

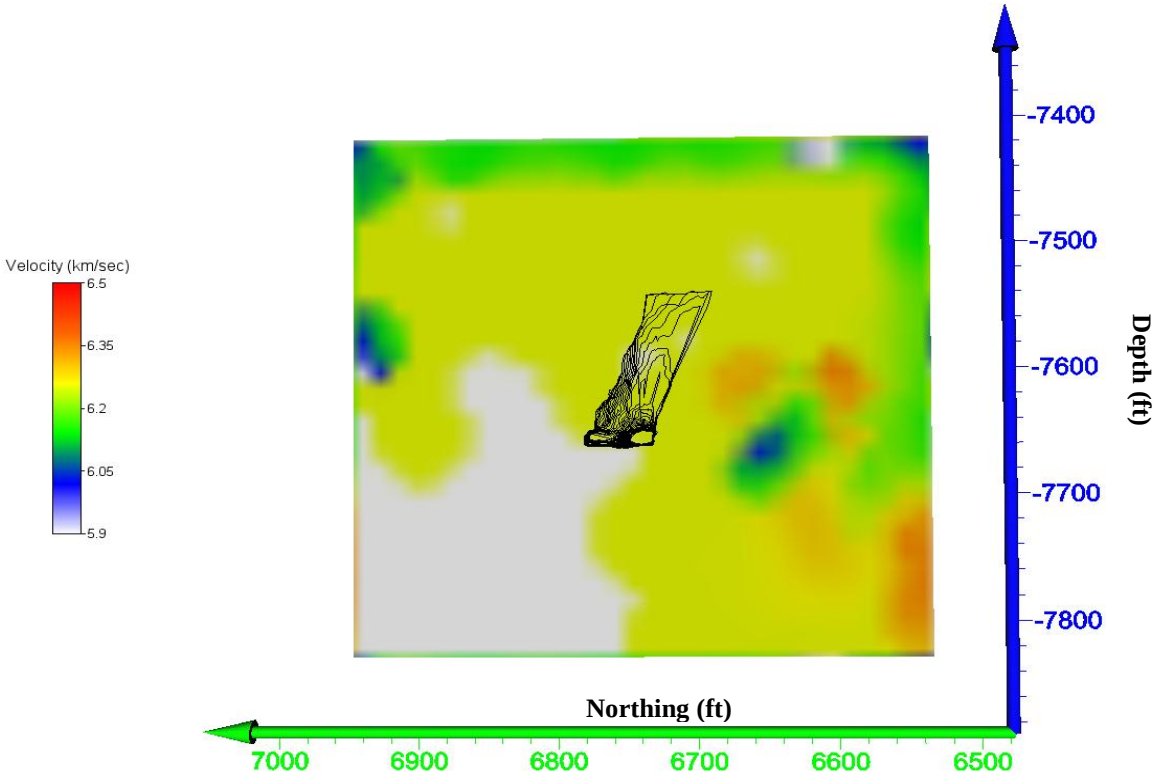

Figure E.16: YZ tomogram at the mid-stope level of Stope 4448 during the eighth time period.

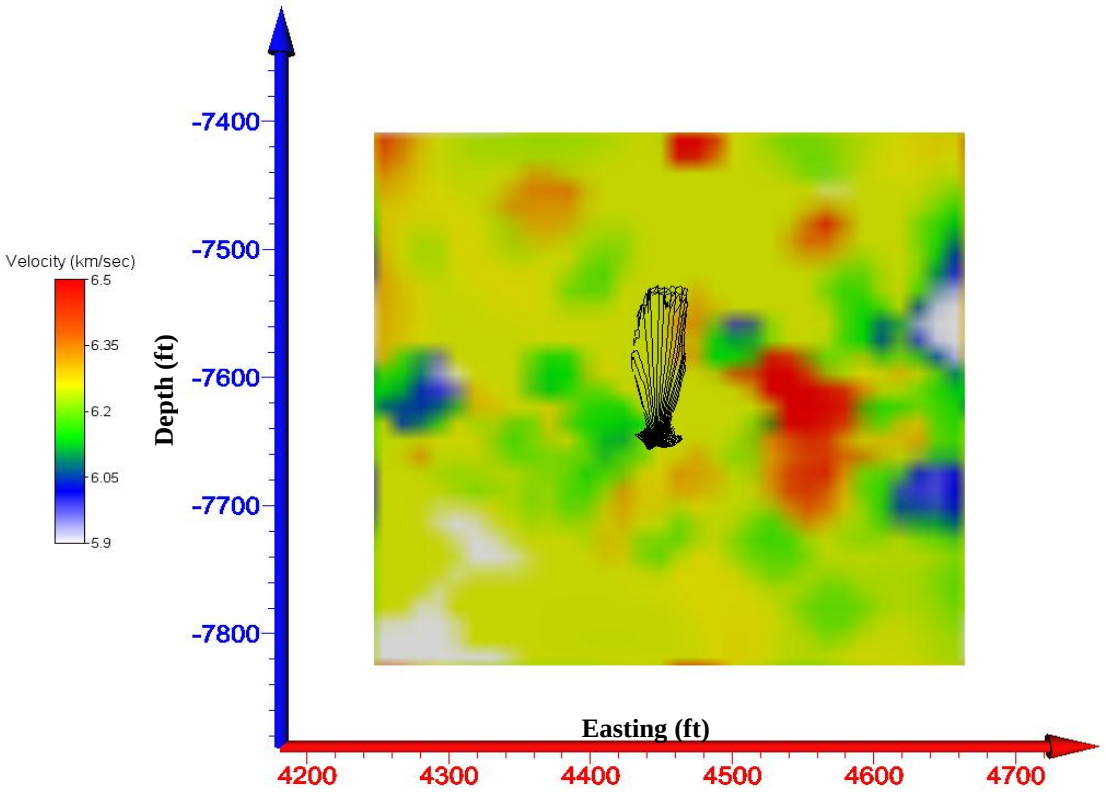

Figure E.17: XZ tomogram at the mid-stope level of Stope 4448 during the ninth time period.

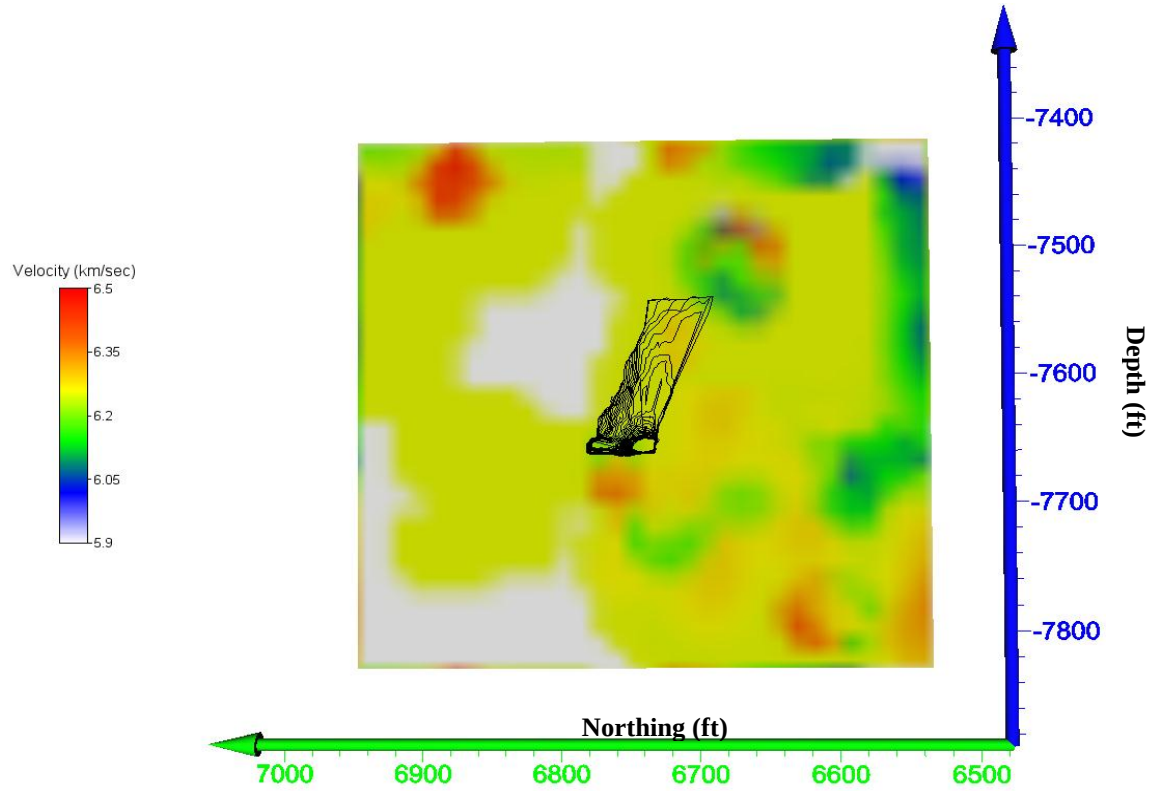

Figure E.18: YZ tomogram at the mid-stope level of Stope 4448 during the ninth time period.

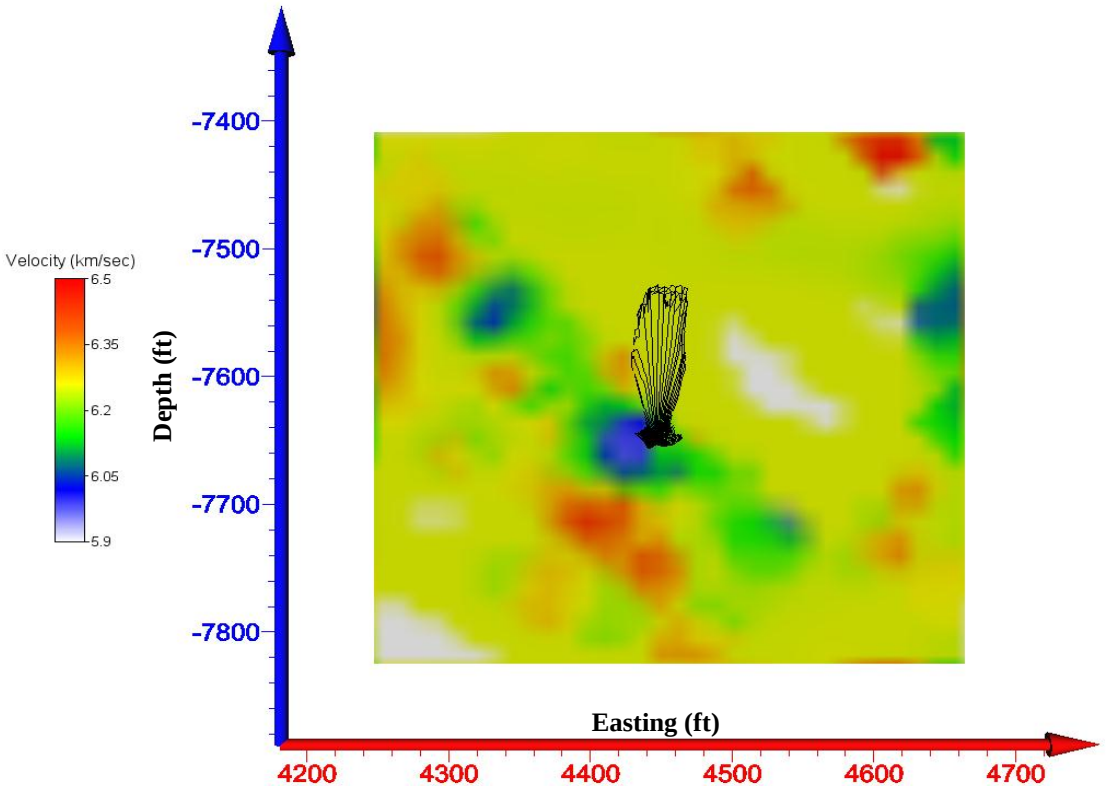

Figure E.19: XZ tomogram at the mid-stope level of Stope 4448 during the tenth time period.

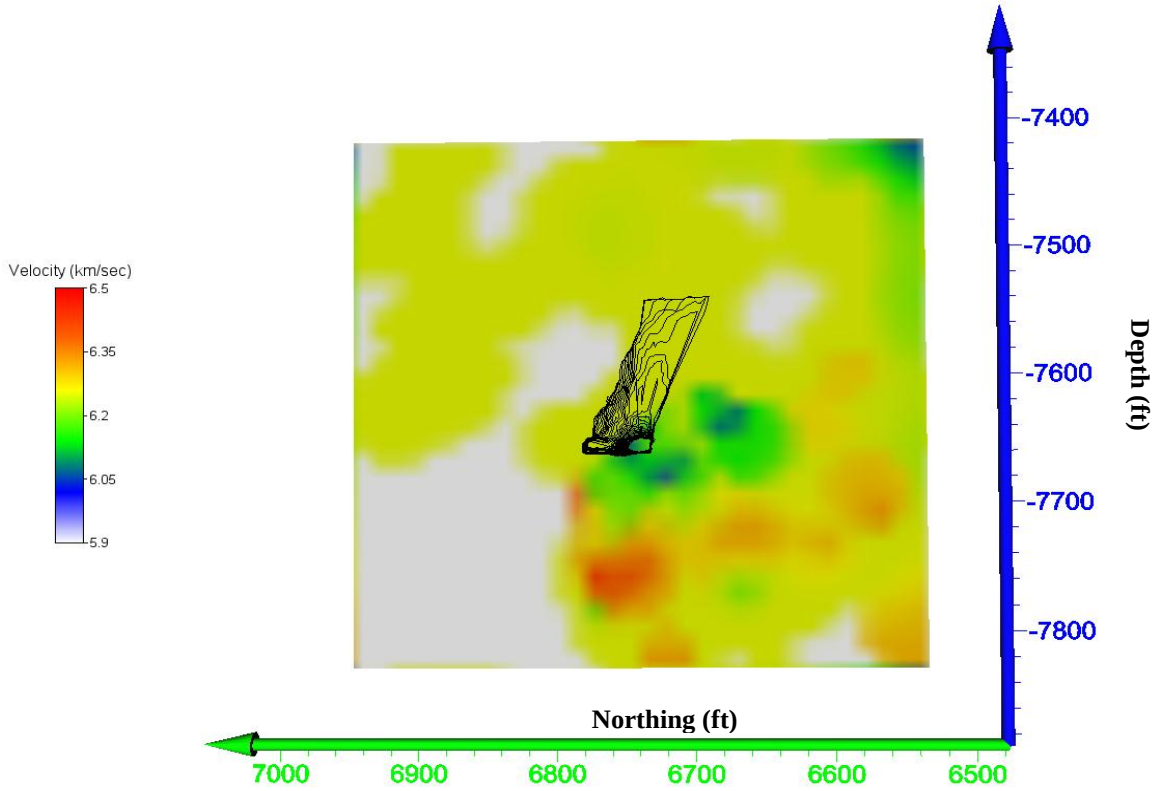

Figure E.20: YZ tomogram at the mid-stope level of Stope 4448 during the tenth time period.

Appendix F – Event Cluster Results

Appendix F will include tomograms of cross sections located between half of the events in the cluster of events. Tomograms will be shown in time period order with two tomograms per time period except for the third time period. The third time period will have four tomograms including two tomograms to represent after the first grouping of events and two tomograms to represent prior to the second grouping of events. Tomograms will be shown in the XZ and the YZ planes. XZ plane tomograms are displayed with respect to the Easting and depth of the stope, while the YZ plane tomograms are displayed with respect to the Northing and depth of the stope.

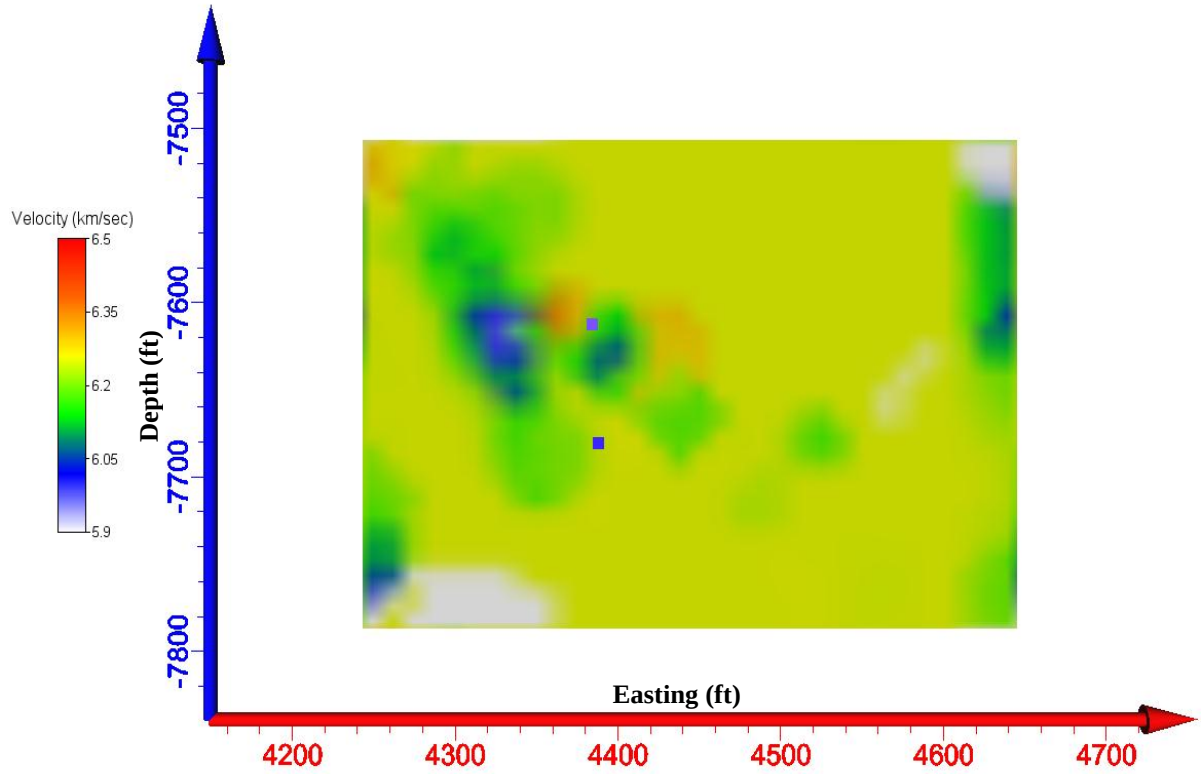

Figure F.1: XZ tomogram of the first grouping of events in the cluster prior to the events.

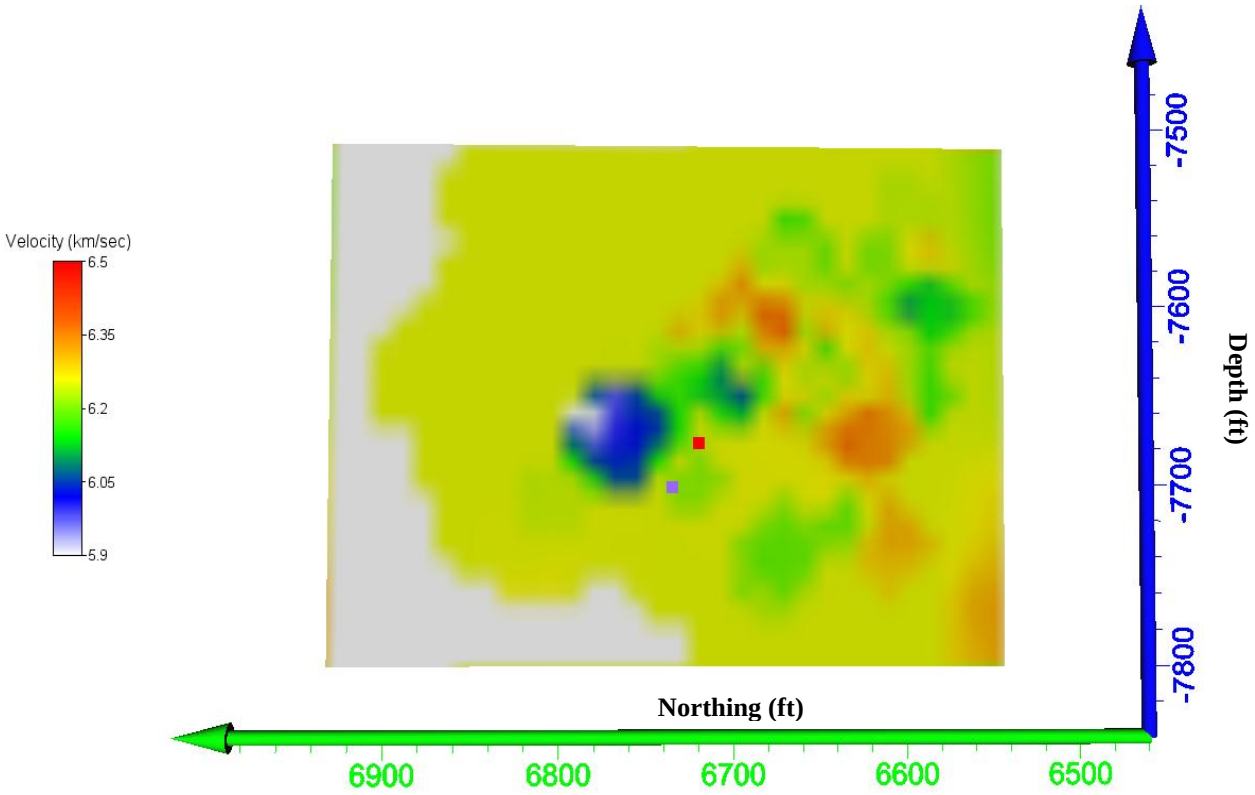

Figure F.2: YZ tomogram of the first grouping of events in the cluster prior to the events.

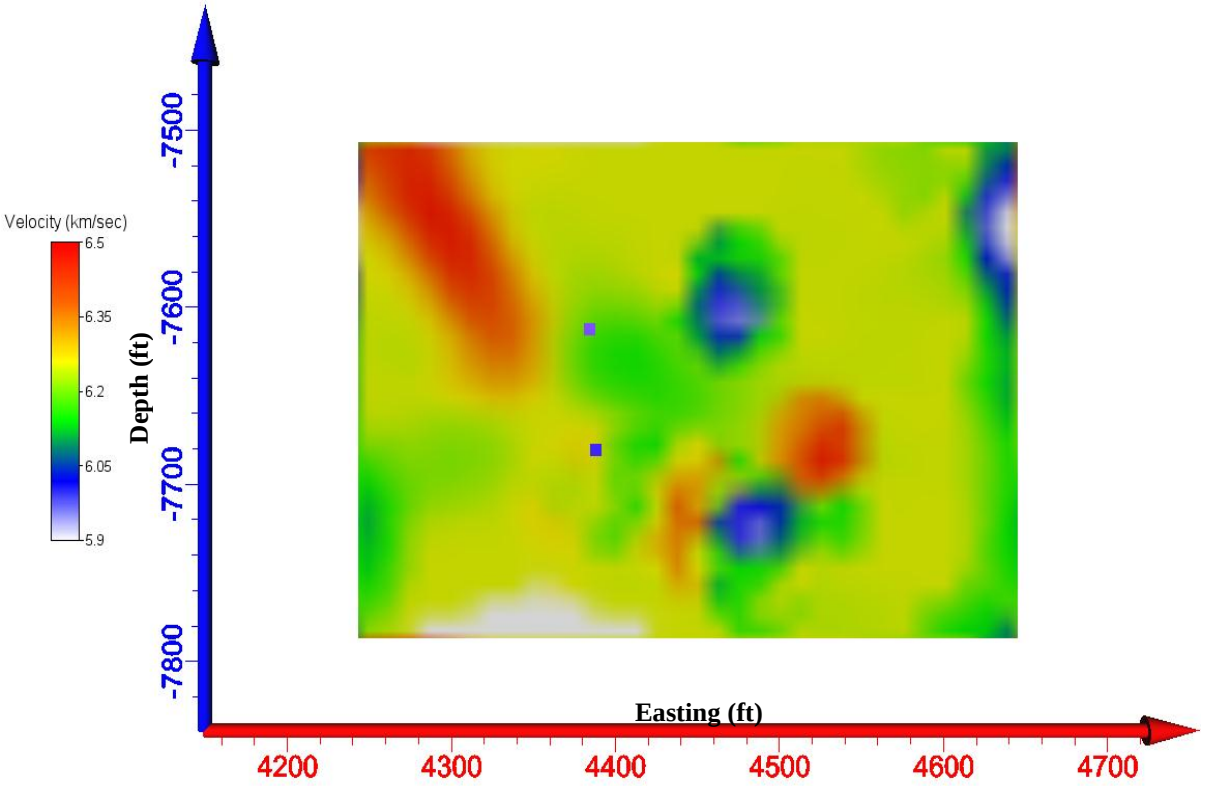

Figure F.3: XZ tomogram of the first grouping of events in the cluster during the events.

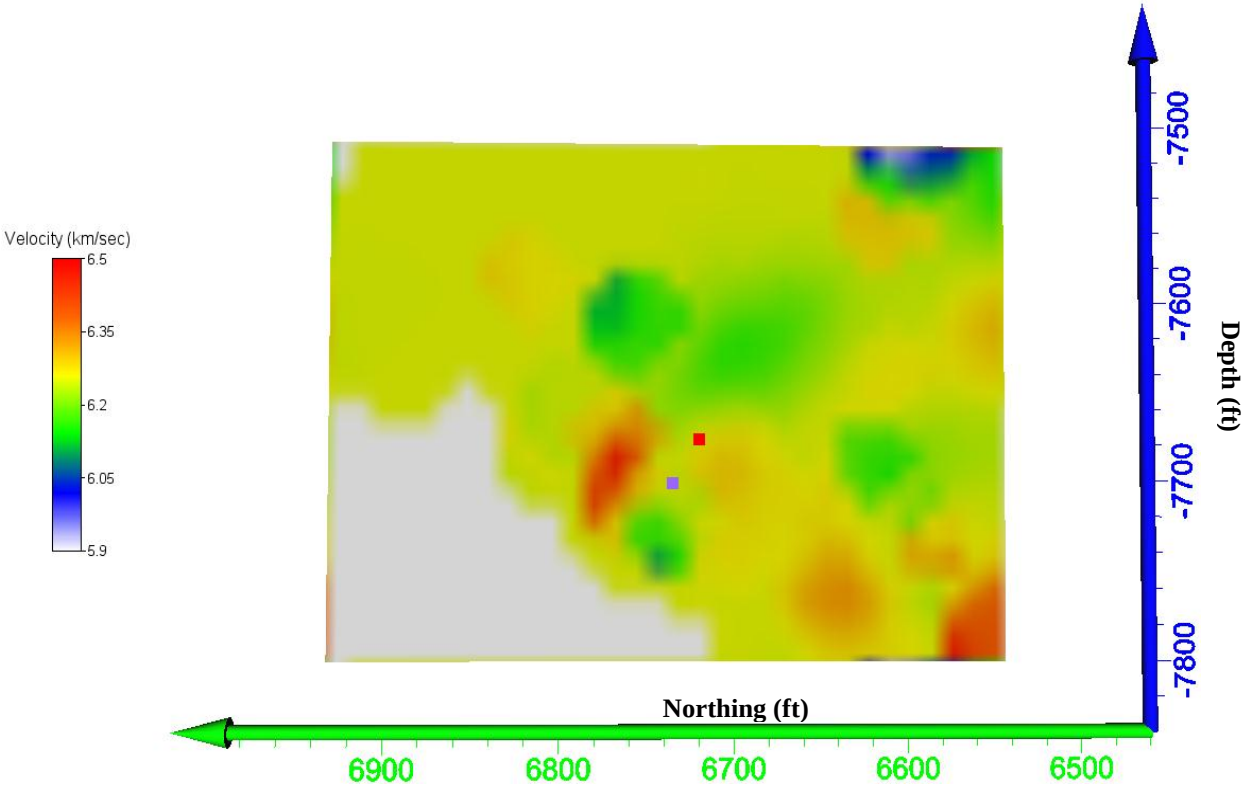

Figure F.4: YZ tomogram of the first grouping of events in the cluster during the events.

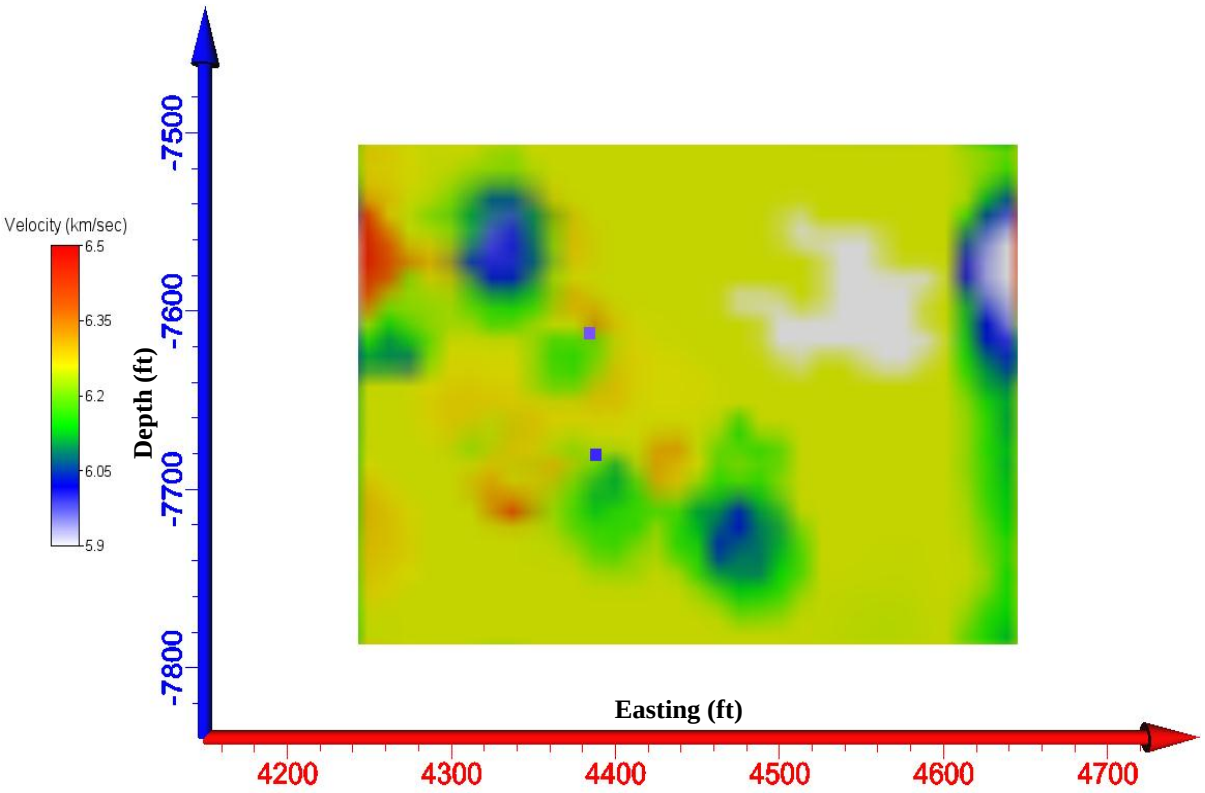

Figure F.5: XZ tomogram of the first grouping of events in the cluster after the events.

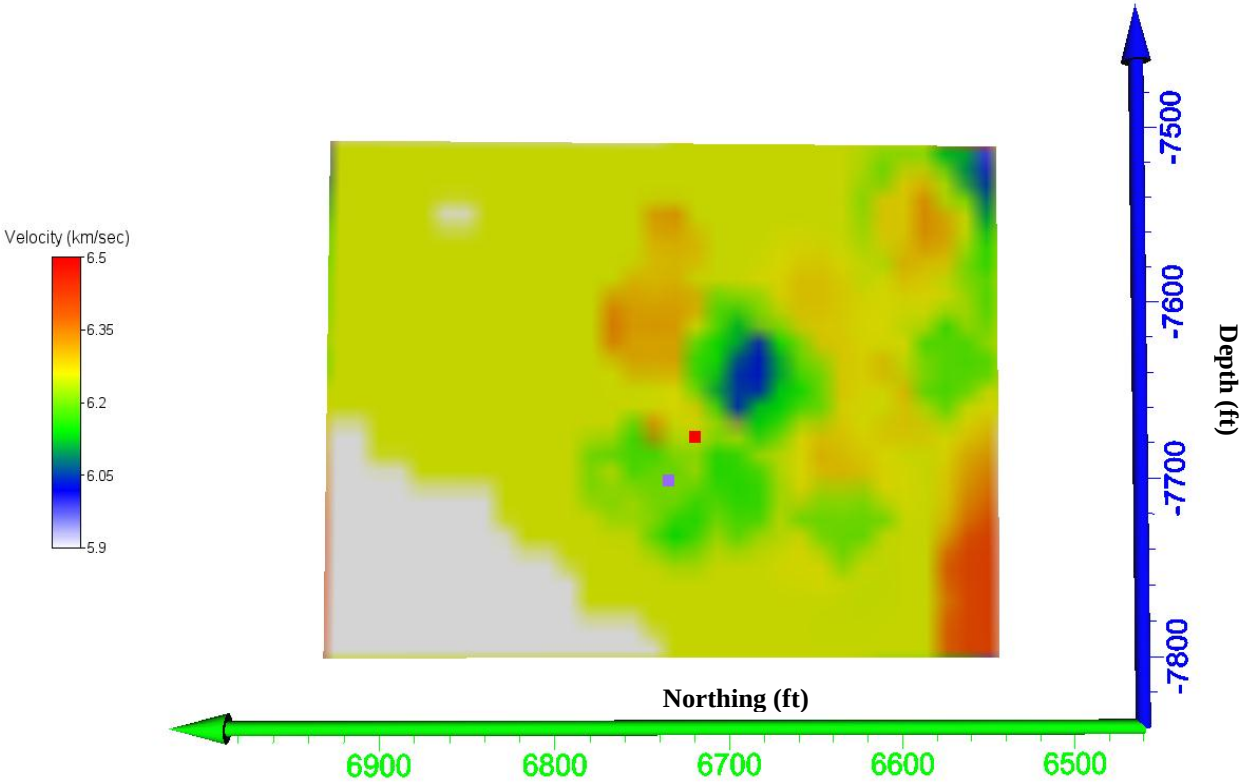

Figure F.6: YZ tomogram of the first grouping of events in the cluster after the events.

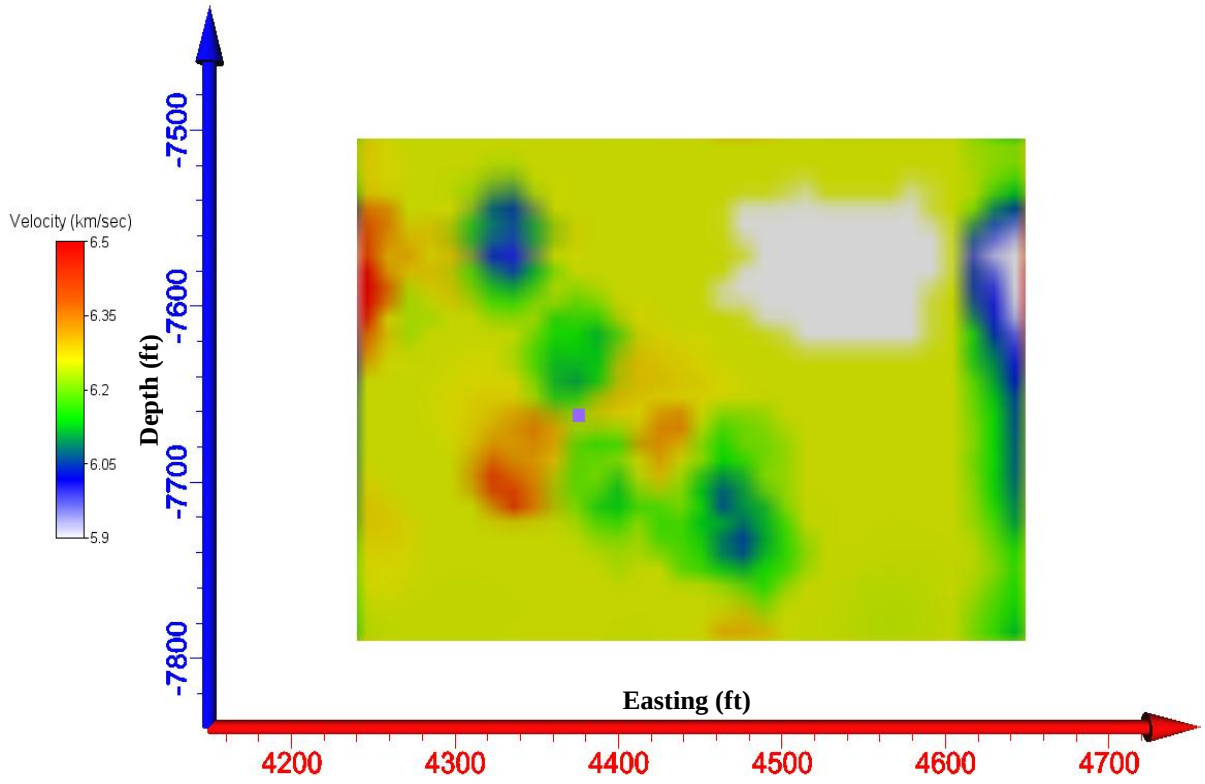

Figure F.7: XZ tomogram of the second grouping of events in the cluster prior to the events.

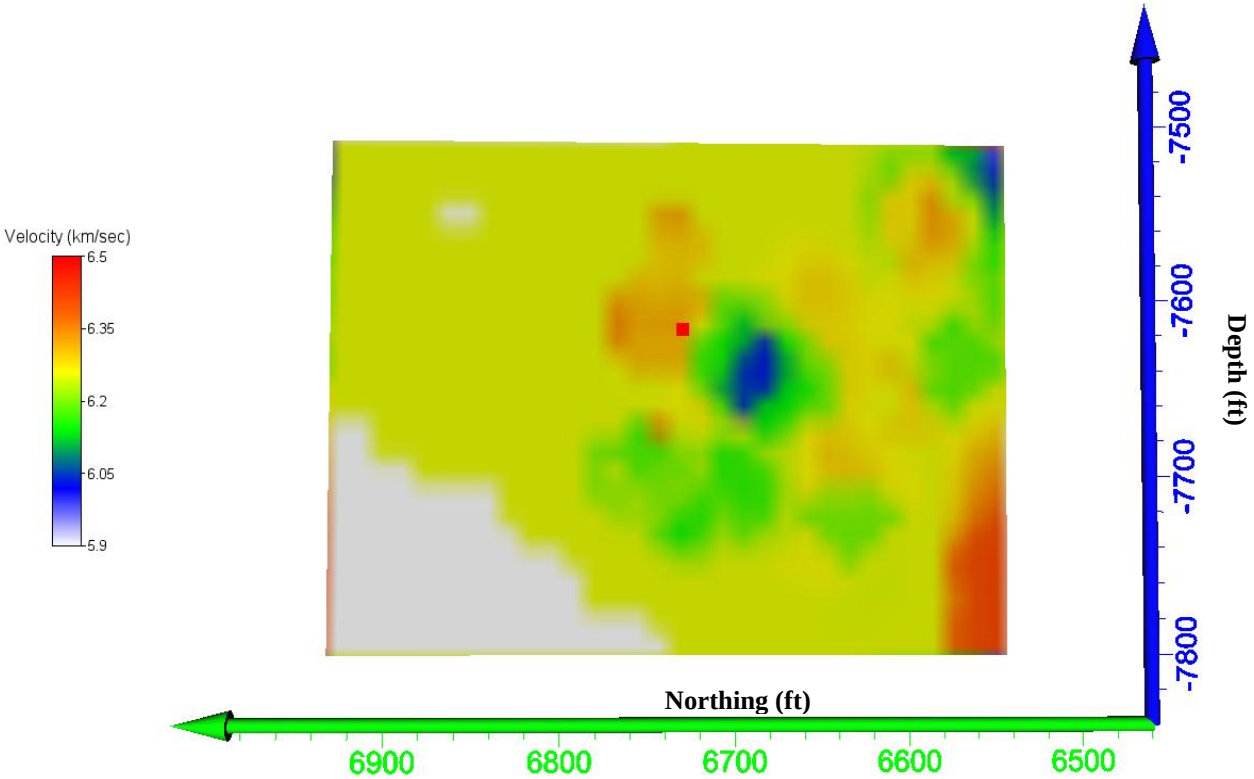

Figure F.8: YZ tomogram of the second grouping of events in the cluster prior to the events.

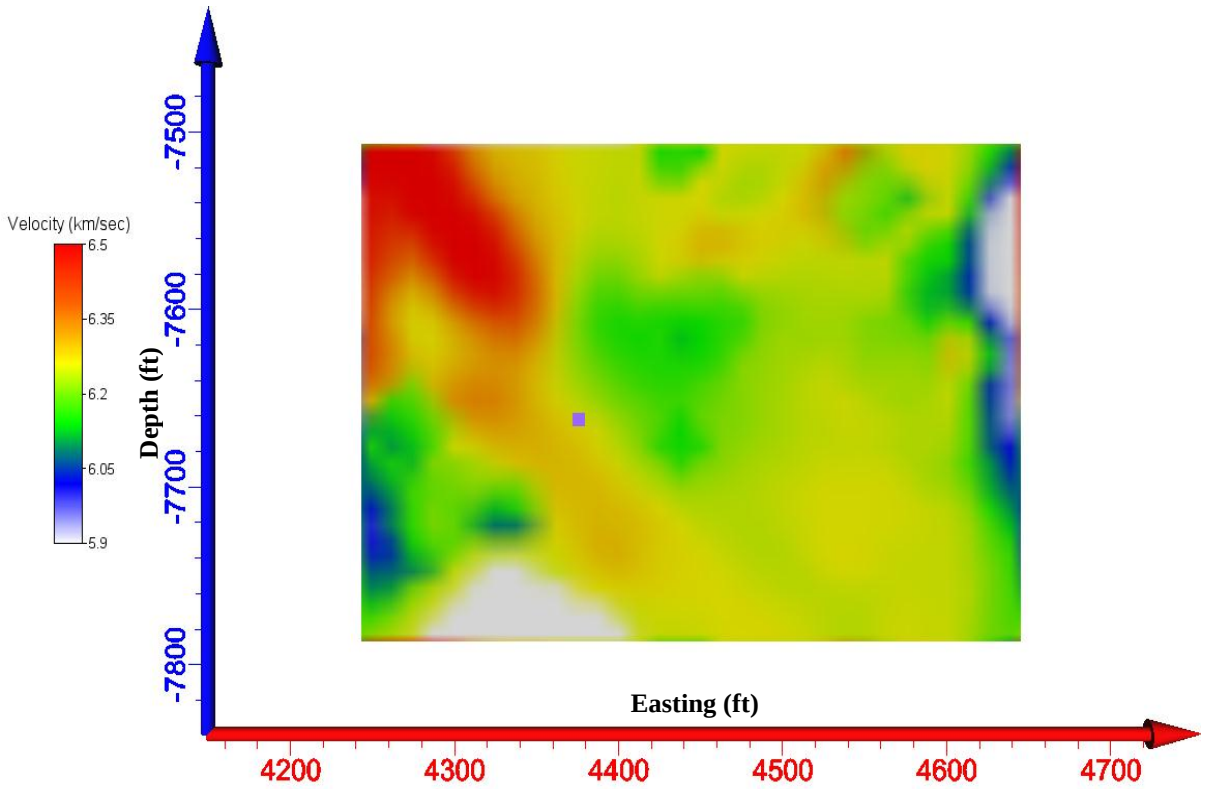

Figure F.9: XZ tomogram of the second grouping of events in the cluster during the events.

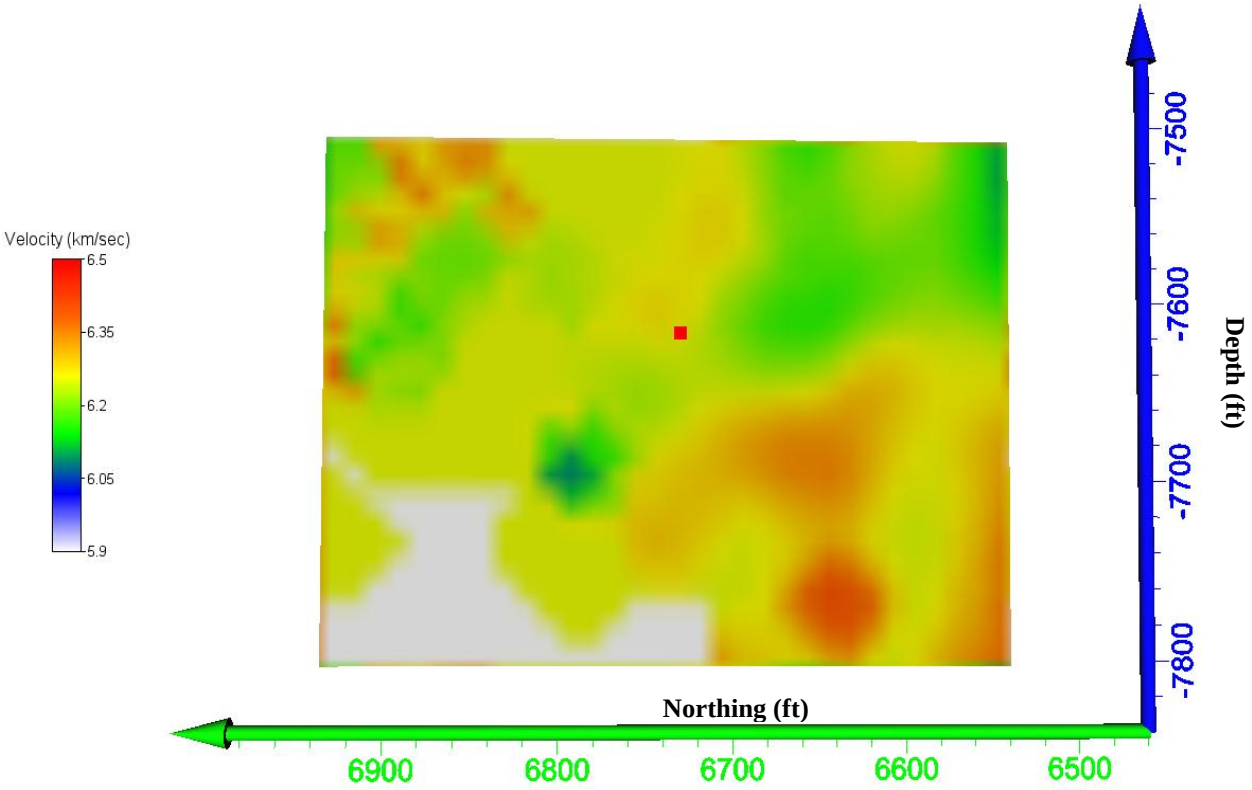

Figure F.10: YZ tomogram of the second grouping of events in the cluster during the events.

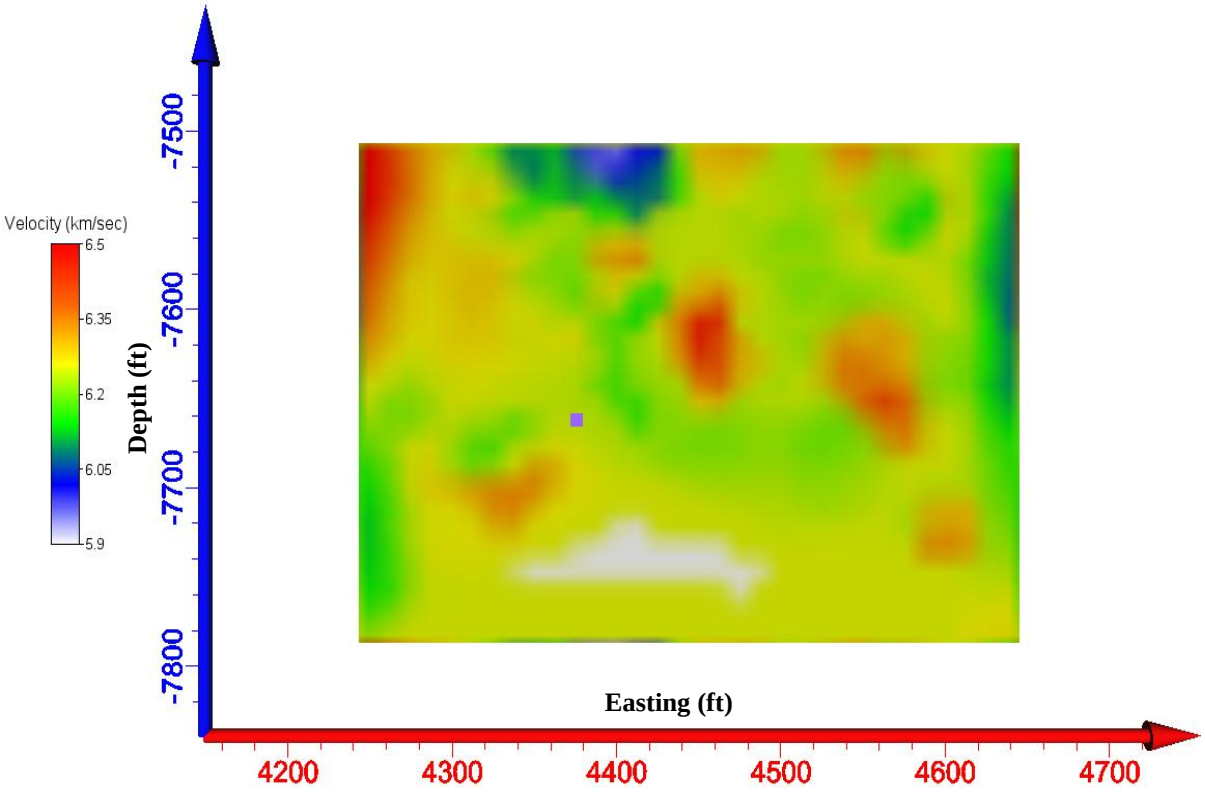

Figure F.11: XZ tomogram of the second grouping of events in the cluster after the events.

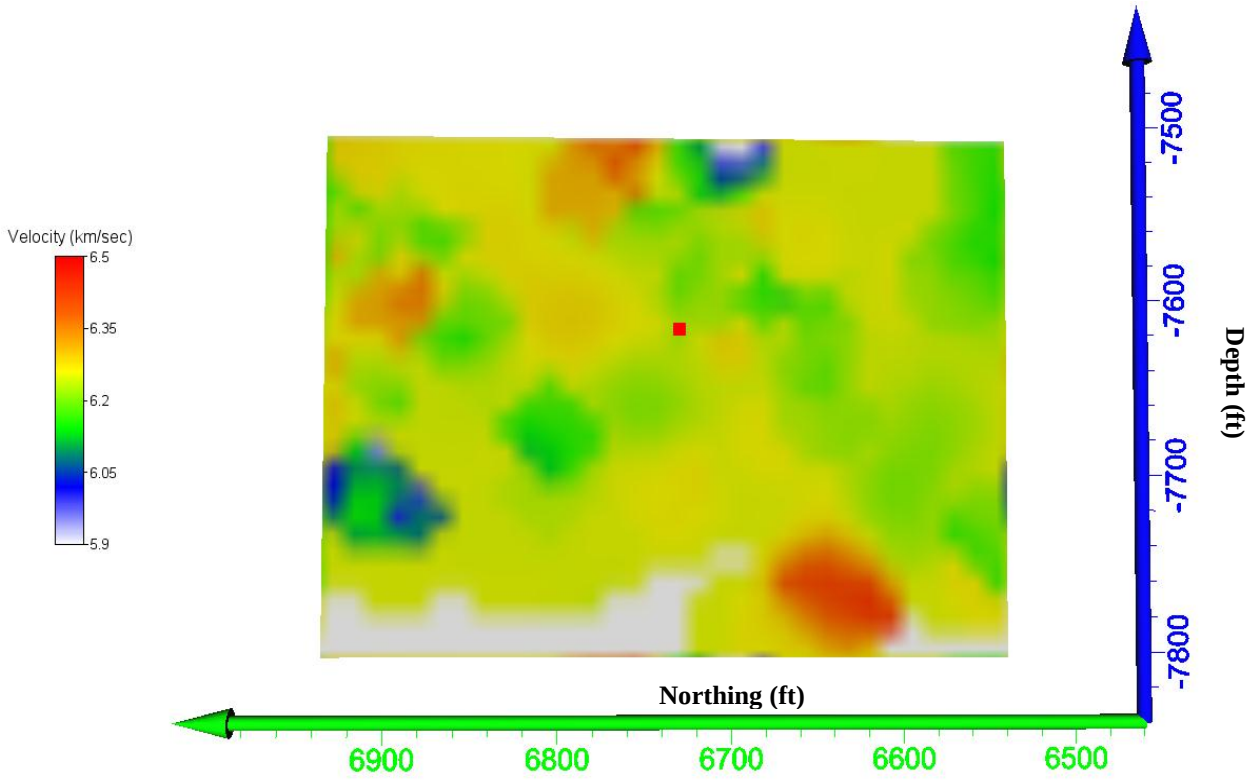

Figure F.12: YZ tomogram of the second grouping of events in the cluster after the events.